

---

Exploring Structure- and  
Composition-Activity Correlations of Mixed  
Cobalt Iron Perovskites and Spinels in  
Oxidation Catalysis

---

Dissertation

Zur Erlangung des akademischen Grades eines  
Doktors der Naturwissenschaften

– Dr. rer. nat. –

vorgelegt von

**Maik Dreyer**

Fakultät für Chemie  
der  
Universität Duisburg-Essen

April 2022

# DuEPublico

Duisburg-Essen Publications online

UNIVERSITÄT  
DUISBURG  
ESSEN

*Offen im Denken*

**ub** | universitäts  
bibliothek

Diese Dissertation wird via DuEPublico, dem Dokumenten- und Publikationsserver der Universität Duisburg-Essen, zur Verfügung gestellt und liegt auch als Print-Version vor.

**DOI:** 10.17185/duepublico/76069  
**URN:** urn:nbn:de:hbz:465-20220704-111347-4

Alle Rechte vorbehalten.

Diese Arbeit wurde im Zeitraum von Oktober 2018 bis Dezember 2021 an der Fakultät für Chemie der

**Universität Duisburg-Essen**

in der Arbeitsgruppe von

**Prof. Dr. Malte Behrens**

angefertigt.

Tag der Abgabe: 7. April 2022

Tag der Disputation: 9. Juni 2022

**Gutachter:** *Prof. Dr. Malte Behrens*

*Prof. Dr. Martin Muhler*

*Prof. Dr. Stephan Schulz*

**Vorsitzender:** *Prof. Dr. Rainer Meckenstock*



# Danksagung

Ein großer Dank geht an Prof. Dr. Malte Behrens für die Möglichkeit, seit Oktober 2017 in seinem Arbeitskreis in unterschiedlichen Rollen forschen zu dürfen. Für die stets gute Zusammenarbeit, die Freiheiten, vielen Ratschläge, guten Ideen und die Möglichkeit im Ruhrgebiet bleiben zu dürfen, bin ich Dir sehr dankbar!

Ebenso danken möchte ich Prof. Dr. Martin Muhler für die Übernahme des Koreferats und die stets freundlichen und produktiven Diskussionen im Rahmen der Zusammenarbeit im Sonderforschungsbereich 247 im Tandemprojekt A1.

Prof. Dr. Stephan Schulz danke ich dafür, dass er als dritter Gutachter zur Verfügung steht. Außerdem danke ich ihm für die gute Zusammenarbeit im Sonderforschungsbereich 247 sowie gute Gespräche bei verschiedenen Anlässen über Wissenschaft und Themen darüber hinaus sowie stets positive Kritik im gemeinsamen Gruppenseminar.

Für seine großartige Unterstützung insbesondere bei der Planung und beim Aufbau der SFB-Oxidationsanlagen – oder neuerdings MultiCat-Anlagen – danke ich Dr. Klaus Friedel Ortega. Ebenso danke ich Dir für die vielen anregenden Diskussionen und eingebrachten Ideen.

A special thanks goes to Dr. Sharif Najafishirtari for taking the lead of our small subgroup in Duisburg, many intense discussions, your guidance, feedback, and lots of reading of my English writing, including this thesis. Furthermore, thanks for contributing to this thesis and the papers with the DRIFTS work.

Anna Rabe danke ich für eine wunderbare Zusammenarbeit am selben Projekt, viele Hilfestellungen, Ideen, Messungen, Probenlieferungen, Korrekturvorschläge, mentale Aufbauarbeit, das Korrekturlesen dieser Arbeit und vieles mehr.

Meiner zwischenzeitlichen Duisburger Bürokollegin Jil Gieser danke ich für viele interessante Tage im Büro, bis uns eine Pandemie dazwischenkam. Vielen Dank auch für die Unterstützung durch BET-Messungen und unsere Diskussionen.

Benjamin Mockenhaupt danke ich für seine Ratschläge aus der Sicht eines Ingenieurs, die mir in vielen Situationen aus der Klemme geholfen haben. Vielen, vielen Dank, lieber BeMo auch für die BET-Messungen.

Meinen beiden Studenten Nicolas Cosanne und Moritz Krebs gilt ein besonderer Dank für ihre Arbeit. Die Arbeit mit euch hat viel Spaß gemacht, ihr habt schnell gelernt und wurdet schnell von frisch einzuarbeitenden Studenten zu einer großen Unterstützung. Vielen Dank! Besonders an Nico noch ein großer Dank für die Arbeit als HiWi. Ich weiß, dass das Pressen und Sieben nicht immer Spaß gemacht hat...

Dem Rest unserer Gruppe und ihren ehemaligen Mitgliedern, Stefanie Becker, Gereon Behrendt, Tobias Bochmann, Justus Heese-Gärtlein, Manuel Heimann, Andreas Hüttner, Chakrapani Kalapu, Fatih Özcan, Denise Rein, Alexander Servas und Jonas Sager

danke ich für interessante Gespräche, Tipps, Einarbeitungen, BET-Messungen und eure Unterstützung in unterschiedlichen Phasen meiner Arbeit.

Dem Arbeitskreis Schulz danke ich für die gute Zeit, als ich noch häufig am Campus Essen war.

Beim Team der Werkstatt in Duisburg, besonders Uwe Rettig und Michel Klar, bedanke ich mich für die großartige Arbeit beim Anlagenaufbau und das Beibringen einiger handwerklicher Kniffe.

Ein Dank gilt auch Stefan Behrensmeyer, der trotz Pandemie immer die Stellung im NETZ gehalten hat, und bei technischen Fragen, Problemen oder Gaslieferungen immer direkt zur Stelle war. Ich weiß nicht, wie viel schwerer die Arbeit im NETZ ohne eine gute Seele wie Stefan wäre.

Außerdem möchte ich Sabine Bollmann, Sabine Kiefer, Dr. Franziska Günther, Dr. Carina Marek und Susanne Moser dafür danken, dass mir viele organisatorische Dinge aus der Hand genommen wurden und viele Bestellungen im Rahmen meiner Arbeit bearbeitet wurden.

Dem ganzen Team des Sonderforschungsbereichs 247 möchte ich für die Unterstützung, lustigen Momente, Probenlieferungen, die Probenanalytik und die gemeinsame Arbeit danken. Mein Dank geht an Dr. Steven Angel, Eko Budiyanto, Carsten Placke-Yan, Sascha Saddeler und Swen Zerebecki für die Materialsynthese, an Dr. Ulrich Hagemann, Dr. Markus Heidelmann und Thai Binh Nguyen für XPS und TEM, an Dr. Daniel Cruz und Dr. Patrick Zeller für die NAP-XPS Experimente, und an Dr. Soma Salamon und Dr. Joachim Landers für Magnetometrie und Mössbauer. Prof. Dr. Nils Hartmann danke ich für die gute Zusammenarbeit beim Verfeinern der Pläne für die Comparative Study und die Administration der Charakterisierung. Vielen Dank an Dr. Sven Anke für das Einarbeiten in die Isopropanoloxidation und die Vermittlung seines Wissens. Vielen Dank auch an Julia Büker, Tobias Falk und Daniel Waffel als Team im Projekt A1 für die gute Zusammenarbeit. Ich danke der Deutschen Forschungsgemeinschaft für die Finanzierung meiner Arbeit.

Für den stets gut laufenden XRD-Servicemessbetrieb danke ich Dietrich Tönnes, außerdem Dr. Kateryna Loza und Tobias Bochmann für die SEM-Messungen.

Meiner Familie möchte ich für die Unterstützung und euer Vertrauen in meine Entscheidungen während der vergangenen gut achtjährigen Jahre seit dem Beginn meines Studiums danken. Ich weiß nicht, ob und wenn ja, wie ich an manchen Stellen ohne euren Rückhalt durch das Studium gekommen wäre. Ganz besonders danke ich Opa Dieter, auch wenn er diese Zeile niemals lesen können wird.

Vielen Freunden danke ich für die schöne Zeit innerhalb und außerhalb der Uni, und die vielen schönen Erlebnisse auf Touren mit euch durch Deutschland und Europa. Martin und Nils, diese Dissertation würde es ohne euch nicht geben. Danke für eure ersten

Praxisberichte in den Jahren 2012 und 2013 und die Hilfe bei den ersten Schritten auf dem Campus.

Besonders danke ich meiner Partnerin Linda für die Unterstützung in allen Lebenslagen, ihr Vertrauen in mich und meine Entscheidungen und ganz besonders dafür, mir zu Hause den Rücken freizuhalten, wenn mal wieder sehr viel zu tun war und ich doch mal wieder keinen Urlaub mit Dir gemacht habe.



---

# Abstract

The importance of catalytic oxidation reactions in the gas phase is known, and many catalytic materials are already used for oxidation reactions. However, due to often harsh process conditions, gas phase oxidation reactions may suffer from selectivity problems. Therefore, stepping into liquid phase catalysis at milder conditions is quite reasonable. In the liquid phase, sophisticated analysis methods like near ambient pressure X-ray photoelectron spectroscopy (NAP-XPS) are not yet available. The addition of excess water vapor into the gas feed streams is, therefore, a useful technology to build a bridge between traditional dry gas phase and liquid phase catalysis. In this study, Fe rich  $\text{LaFe}_{1-x}\text{Co}_x\text{O}_3$  perovskites and Co rich  $\text{Co}_{3-x}\text{Fe}_x\text{O}_4$  spinels are studied in the gas phase oxidation of CO as an example for total oxidation catalysis, and dry and wet gas phase selective 2-propanol oxidation. The perovskites are additionally studied in the liquid phase electrochemical water oxidation reaction (OER).

In the gas phase oxidation of CO, a strong correlation between perovskite reducibility and the CO oxidation activity is observed. This effect superimposes a vaguely observed correlation of Co content and activity. The addition of only 5% Co in the Fe sublattice increases the activity strongly. In addition, a pronounced formation of stable carbonates is seen in *operando* diffuse reflectance infrared fourier transform spectroscopy (DRIFTS) for Fe rich perovskites. The carbonate stability decreases with Co content while the  $\text{CO}_2$  formation increases. In the CO oxidation on spinel catalysts, an increasing Fe content decreases the catalyst activity, which shows higher activity of Co than Fe. However, in a cyclic experiment, a pronounced influence of the catalysts (meso)structure is observed. The amount of exposed low-index surface facets has an effect on the ability to generate reactive oxygen species (ROS) in an oxidizing feed gas mixture, since larger particles form less ROS. The ROS formation ability is also observed in the mixed spinels. The activity increase upon ROS formation is most pronounced for mixed FeCo spinels derived from nanocasting. This means that Fe might also play a role in oxygen activation and ROS formation.

In the gas phase 2-propanol oxidation on perovskites, the activity does not scale monotonically with the Co content, and the addition of only 5% Co increases the activity strongly, as also observed in CO oxidation. The materials show a highly active but not stable low-temperature (LT) activity channel and a less active but stable high-temperature (HT) activity channel in dry and wet feed. After adding water into the feed gas stream, the activity in the LT channel is decreased for all materials. There is an activity increase in transient experiments in the HT channel if more than 15% Co are in the perovskite. However, the increase is only temporary since the Co containing materials deactivate slower in wet feed and show less activity under steady-state conditions. In *operando* NAP-XPS

---

at 200 °C in 2-propanol oxidation on a LaFe<sub>0.75</sub>Co<sub>0.25</sub>O<sub>3</sub> perovskite, a reduction of the Co species from Co<sup>3+</sup> to Co<sup>2+</sup> is observed. The reduction might be one explanation for LT/HT channel behavior. Another explanation might be carbonaceous species formation on the surface. In comparison between dry and wet feed, signals for hydroxide and carbonate increase in the wet feed. Similar trends are derived from comparable measurements on spinel catalysts even though there is an activity maximum at doping levels of Fe ( $\leq 4\%$ ) in the Co<sub>3</sub>O<sub>4</sub> structure, that coincides with an more pronounced reduction of the Co<sup>3+</sup> species to Co<sup>2+</sup>, which means that reducibility plays a major role in explaining the beneficial effect. On Co<sub>3</sub>O<sub>4</sub>, the deactivation speed is similar in dry and wet feed on the maximum temperature of the LT channel. However, during an isothermal period of 1 h at 300 °C on the whole substitution series a higher stability in wet conditions was observed.

In the scope of a comparative study with over 90 catalysts studied, a beneficial effect of Co compared to Fe in the materials is observed. This means that Co sites are the more active site. Within materials of the same composition, the activity differs, but parameters to describe the catalyst structure are still being determined. Catalyst deactivation occurs due to surface reduction and formation of carbonaceous species and is reduced under wet conditions.

In the liquid phase electrochemical oxygen evolution reaction (OER), a nonmonotonic trend with Co content and a pronounced activity increase with 5% Co in the structure is observed. Density functional theory with Hubbard  $U$  term confirms this nonmonotonic behavior on (001)-BO<sub>2</sub> terminated perovskites. Furthermore, a contribution of sub-surface metal ions in the OER reaction is observed since they change their oxidation state during the reaction modeling.

---

# Kurzzusammenfassung

Die Bedeutung von katalytischen Oxidationsreaktionen in der Gasphase ist bekannt, und viele Katalysatoren werden bereits für Oxidationsreaktionen eingesetzt. Aufgrund der oft rauen Prozessbedingungen können Oxidationsreaktionen in der Gasphase jedoch unter Selektivitätsproblemen leiden. Daher ist der Umstieg auf Flüssigphasenkatalyse unter milderer Bedingungen sinnvoll. In der Flüssigphase sind allerdings anspruchsvolle Analysemethoden wie die Röntgenphotoelektronenspektroskopie bei Umgebungsdruck (NAP-XPS) noch nicht verfügbar. Die Zugabe von Wasserdampf in den Gaszufuhrstrom ist daher ein nützliches Werkzeug, um eine Brücke zwischen der traditionellen trockenen Gasphasen- und der Flüssigphasenkatalyse zu bauen. In dieser Studie werden Fe-reiche  $\text{LaFe}_{1-x}\text{Co}_x\text{O}_3$ -Perowskite und Co-reiche  $\text{Co}_{3-x}\text{Fe}_x\text{O}_4$ -Spinelle in der Gasphasenoxidation von CO als Beispiel für die totale Oxidationskatalyse sowie in der trockenen und nassen selektiven Gasphasenoxidation von 2-Propanol untersucht. Die Perowskite werden zusätzlich in der elektrochemischen Wasseroxidationsreaktion (OER) in der Flüssigphase untersucht.

Bei der Gasphasenoxidation von CO wird eine starke Korrelation zwischen der Reduzierbarkeit der Perowskite und der CO-Oxidationsaktivität beobachtet. Dieser Effekt überlagert eine vage beobachtete Korrelation zwischen dem Co-Gehalt und der Aktivität. Die Zugabe von nur 5% Co im Fe-Untergitter erhöht die Aktivität stark. Darüber hinaus wird in der *operando* diffusen Reflexions-Fouriertransformationsinfrarotspektroskopie eine ausgeprägte Bildung stabiler Karbonate für Fe-reiche Perowskite beobachtet. Die Karbonatstabilität nimmt mit dem Co-Gehalt ab, während die  $\text{CO}_2$ -Bildung zunimmt. Bei der CO-Oxidation an Spinell-Katalysatoren nimmt mit steigendem Fe-Gehalt die Katalysatoraktivität ab, was eine höhere Aktivität von Co als von Fe zeigt. In einem zyklischen Experiment wird jedoch ein ausgeprägter Einfluss der Katalysator-(Meso-)Struktur und der Menge an freiliegenden Oberflächenfacetten mit niedrigem Index auf die Fähigkeit zur Erzeugung reaktiver Sauerstoffspezies (ROS) in einem oxidierenden Zustromgemisch beobachtet, da Materialien mit hohem Durchmesser weniger ROS bilden. Die Fähigkeit zur ROS-Bildung wird auch bei gemischten Spinellen beobachtet. Der Aktivitätsanstieg bei ROS-Bildung ist bei gemischten FeCo-Spinellen, die durch das Nanogussverfahren hergestellt wurden, am stärksten ausgeprägt. Das bedeutet, dass Fe auch eine Rolle bei der Sauerstoffaktivierung und ROS-Bildung spielen könnte.

Bei der Gasphasenoxidation von 2-Propanol an Perowskiten steigt die Aktivität nicht monoton mit dem Co-Gehalt an, und die Zugabe von nur 5% Co erhöht die Aktivität stark, wie auch bei der CO-Oxidation beobachtet wurde. Die Materialien zeigen einen hoch aktiven, aber nicht stabilen Niedrigtemperatur-Aktivitätskanal (LT) und einen weniger aktiven, aber stabilen Hochtemperatur-Aktivitätskanal (HT) in trockenem und nassem Strom. Nach Zugabe von Wasser in den Gasstrom nimmt die Aktivität im LT-Kanal bei

---

allen Materialien ab. Bei transienten Experimenten kommt es zu einem Aktivitätsanstieg im HT-Kanal, wenn mehr als 15% Co im Perowskit enthalten sind. Dieser Anstieg ist jedoch nur vorübergehend, da die Co-haltigen Materialien in nassem Strom langsamer deaktivieren und unter stationären Bedingungen weniger Aktivität aufweisen. In *operando* NAP-XPS bei 200 °C bei der 2-Propanoloxidation an einem LaFe<sub>0.75</sub>Co<sub>0.25</sub>O<sub>3</sub>-Perowskit wird eine Reduktion der Co-Spezies von Co<sup>3+</sup> zu Co<sup>2+</sup> beobachtet. Diese Reduktion könnte eine Erklärung für das LT/HT-Kanalverhalten sein. Eine andere Erklärung könnte die Bildung von kohlenstoffhaltigen Spezies auf der Oberfläche sein. Im Vergleich zwischen trockenem und nassem Zustrom nehmen die Signale für Hydroxid und Karbonat im nassen Zustrom zu. Ähnliche Trends lassen sich aus vergleichbaren Messungen an Spinellkatalysatoren ableiten, auch wenn es ein Aktivitätsmaximum bei Dotierungen mit Fe ( $\leq 4\%$ ) in der Co<sub>3</sub>O<sub>4</sub>-Struktur gibt. Dieses Aktivitätsmaximum tritt gemeinsam mit einer ausgeprägteren Reduktion von Co<sup>3+</sup>-Spezies zu Co<sup>2+</sup> auf, was bedeutet, dass Reduzierbarkeit eine große Rolle in der Erklärung des positiven Effekts der Eisendotierung spielt. Auf Co<sub>3</sub>O<sub>4</sub> war die Geschwindigkeit der Desaktivierung unter nassen und trockenen Bedingungen bei der Temperatur des Niedrigtemperaturmaximums vergleichbar. Während einer isothermen Zeit von 1 h bei 300 °C wurde eine höhere Stabilität der gesamten Substitutionsreihe unter nassen Bedingungen beobachtet.

Im Rahmen einer Vergleichsstudie mit mehr als 90 untersuchten Katalysatoren wird eine positive Wirkung von Co im Vergleich zu Fe in den Materialien beobachtet. Dies bedeutet, dass die Co-Atome das aktiver Zentrum sind. Innerhalb von Materialien gleicher Zusammensetzung ist die Aktivität unterschiedlich, aber die strukturellen Parameter zur Beschreibung der Katalysatoreigenschaften werden noch ermittelt. Die Deaktivierung des Katalysators erfolgt durch Oberflächenreduktion und Bildung von kohlenstoffhaltigen Spezies und ist unter feuchten Bedingungen geringer.

Bei der elektrochemischen Sauerstoffentwicklungsreaktion (OER) in flüssiger Phase wird ein nichtmonotoner Trend mit dem Co-Gehalt und ein deutlicher Aktivitätsanstieg mit 5% Co in der Struktur beobachtet. Die Dichtefunktionaltheorie mit Hubbard-*U*-Term bestätigt dieses nichtmonotone Verhalten für (001)-BO<sub>2</sub>-terminierte Perowskite. Darüber hinaus wird ein Beitrag der unter der Oberfläche befindlichen Metallionen zur OER-Reaktion beobachtet, da sie ihren Oxidationszustand während der Reaktionsmodellierung ändern.

---

## Abbreviations

<b>ads</b>	adsorbed
<b>AAS</b>	atomic absorption spectroscopy
<b>AO</b>	atomic orbital
<b>BET</b>	Brunauer, Emmett and Teller
<b>BJH</b>	Barrett, Joyner and Halenda
<b>CC BY 4.0</b>	Creative Commons 4.0 International
<b>CC BY-NC-ND 4.0</b>	Creative Commons Attribution-NonCommercial-NoDerivatives 4.0 International
<b>chem</b>	chemisorbed
<b>DFT+<i>U</i></b>	density functional theory with Hubbard <i>U</i> term
<b>DRIFTS</b>	diffuse reflectance infrared fourier transform spectroscopy
<b>EDX</b>	energy dispersive X-ray spectroscopy
<b>ER</b>	Eley-Rideal
<b>E<sub>1cb</sub></b>	elimination unimolecular conjugate base
<b>FTIR</b>	fourier transform infrared spectroscopy
<b>HER</b>	hydrogen evolution reaction
<b>HT</b>	high-temperature
<b>ICSD</b>	inorganic crystal structure database
<b>IR</b>	infrared
<b>LH</b>	Langmuir-Hinshelwood
<b>LT</b>	low-temperature
<b>LSV</b>	linear sweep voltammetry
<b>MvK</b>	Mars-van Krevelen
<b>MFC</b>	mass flow controller
<b>μGC</b>	micro gas chromatograph
<b>MMOs</b>	mixed metal oxides
<b>MO</b>	molecular orbital
<b>NAP</b>	near ambient pressure
<b>NMR</b>	nuclear magnetic resonance
<b>OER</b>	oxygen evolution reaction
<b>PROX</b>	preferential oxidation of CO
<b>RDS</b>	rate determining step
<b>ROS</b>	reactive oxygen species
<b>SEM</b>	scanning electron microscopy
<b>SHE</b>	standard hydrogen electrode
<b>STEM</b>	scanning transmissing electron microscopy
<b>TCD</b>	thermal conductivity detector

---

<b>TEM</b>	transmission electron microscopy
<b>TPD</b>	temperature-programmed desorption
<b>TPO</b>	temperature-programmed oxidation
<b>TPR</b>	temperature-programmed reduction
<b>VOC</b>	volatile organic compounds
<b>XRD</b>	X-ray diffraction
<b>XPS</b>	X-ray photoelectron spectroscopy

## Symbols and Formula Units

$b$	Tafel slope
$c_0$	initial concentration
$\Delta$	difference dry–wet
$\Delta G$	Gibbs free energy
$j$	exchange current density
$\eta$	overpotential
$r_A$	atomic radius of cation A <sup>n+</sup>
$r_B$	atomic radius of cation B <sup>n+</sup>
$r_O$	atomic radius of O <sup>2-</sup>
$S$	selectivity
$t$	factor of tolerance
$x$	degree of inversion
$X$	conversion
$Y$	yield

## Chemistry

<b>Ar</b>	argon
<b>CO</b>	carbon monoxide
<b>CH<sub>4</sub></b>	methane
<b>CO<sub>2</sub></b>	carbon dioxide
<b>H<sub>2</sub></b>	hydrogen
<b>He</b>	helium
<b>N<sub>2</sub></b>	nitrogen
<b>O<sub>2</sub></b>	oxygen
<b>TBHP</b>	<i>tert</i> -butyl hydroperoxide
<b>H<sub>2</sub>O</b>	water

# Table of Contents

<b>1. Introduction</b>	<b>1</b>
<b>2. State of the Art</b>	<b>3</b>
2.1. Metal Oxides . . . . .	3
2.1.1. The Perovskite Structure . . . . .	3
2.1.2. The Spinel Structure . . . . .	5
2.2. Selective and Total Thermal Oxidation Catalysis on Metal Oxides . . . . .	6
2.2.1. Gas Phase CO Oxidation . . . . .	11
2.2.2. Gas Phase Alcohol Oxidation: The Example 2-Propanol . . . . .	14
2.2.3. Transition from Gas Phase to Liquid Phase . . . . .	18
2.3. Electrochemical Oxygen Evolution . . . . .	19
<b>3. Experimental</b>	<b>23</b>
3.1. BELCAT-B . . . . .	23
3.2. MultiCat . . . . .	24
<b>4. The Effect of Co Incorporation on the CO Oxidation Activity of <math>\text{LaFe}_{1-x}\text{Co}_x\text{O}_3</math></b>	<b>27</b>
<b>5. Synergistic Effects of Co and Fe on the Oxygen Evolution Reaction Activity of <math>\text{LaCo}_x\text{Fe}_{1-x}\text{O}_3</math></b>	<b>47</b>
<b>6. The Effect of Water on the 2-Propanol Oxidation Activity of Co-Substituted <math>\text{LaFe}_{1-x}\text{Co}_x\text{O}_3</math> Perovskites</b>	<b>63</b>
<b>7. Dynamics of Reactive Oxygen Species on Cobalt-Containing Spinel Oxides in Cyclic CO Oxidation</b>	<b>83</b>
<b>8. Beneficial Effects of Low Iron Contents on Cobalt-Containing Spinel Catalysts in the Gas Phase 2-Propanol Oxidation</b>	<b>101</b>
<b>9. Summary and Outlook</b>	<b>115</b>
<b>10. Bibliography</b>	<b>123</b>
<b>A. Appendix</b>	<b>135</b>
I. List of Figures . . . . .	135
II. List of Schemes . . . . .	136
III. List of Reactions . . . . .	137

*Table of Contents*

---

IV. SI: The Effect of Co Incorporation on the CO Oxidation Activity of LaFe <sub>1-x</sub> Co <sub>x</sub> O <sub>3</sub> . . . . .	138
V. SI: Synergistic Effects of Co and Fe on the Oxygen Evolution Reaction Activity of LaCo <sub>x</sub> Fe <sub>1-x</sub> O <sub>3</sub> . . . . .	156
VI. SI: The Effect of Water on the 2-Propanol Oxidation Activity of Co-Substituted LaFe <sub>1-x</sub> Co <sub>x</sub> O <sub>3</sub> Perovskites . . . . .	164
VII. SI: Dynamics of Reactive Oxygen Species on Cobalt-Containing Spinel Oxides in Cyclic CO Oxidation . . . . .	183
VIII. SI: Beneficial Effects of Low Iron Contents on Cobalt-Containing Spinel Catalysts in the Gas Phase 2-Propanol Oxidation . . . . .	200
<b>B. Publications</b>	<b>213</b>
<b>C. Curriculum Vitae</b>	<b>216</b>
<b>D. Declaration of Authorship</b>	<b>221</b>

# 1. Introduction

About 25% of all catalytic reactions performed in industry are oxidation reactions of hydrocarbons catalyzed by metal oxide catalysts.<sup>1</sup> Among these reactions are the oxidation of volatile organic compounds (VOC), and the selective oxidation of alcohols.<sup>2</sup> An industrially important alcohol oxidation is the formaldehyde synthesis from the shortest chain alcohol methanol on a mixed iron-molybdenum oxide.<sup>3,4</sup> However, the oxidation of higher alcohols for example to acetals is usually more challenging, and might need further process steps.<sup>5,6</sup> Among the most important industrial oxidations is the production of acrylic acid as a frequently used monomer in polymer chemistry via propylene oxidation. A possible alternative in the liquid phase is the oxidative dehydrogenation of glycerol (propane-1,2,3-triol).<sup>7,8</sup>

Most of the heterogeneous oxidation processes are performed in the gas phase even though the relatively high temperatures lead to intrinsic selectivity problems since the thermodynamically favored oxidation reaction is the total oxidation of the (oxygenated) hydrocarbons to carbon dioxide ( $\text{CO}_2$ ) and water ( $\text{H}_2\text{O}$ ).<sup>9–11</sup> The selective oxidation to higher value products is kinetically controlled and therefore needs a careful process design. A consequence is operation at partial conversion to achieve high product selectivity followed by extensive separation of reactants and products.<sup>12</sup> In the liquid phase, typically less severe reaction conditions are employed, which lead to more selective reactions.<sup>13</sup> Furthermore, molecules with high boiling points are preferably oxidized in the liquid phase.<sup>2,14,15</sup> To gain mechanistic understanding and thereby improve the processes, detailed knowledge about kinetics and intermediates is necessary but we lack the required methods for investigating the phenomena in liquid phase catalysis. Until now, many *operando*, or *in-situ* techniques are still under development for liquid phase catalysis.<sup>16–19</sup> Therefore, a necessity exists to build a bridge between gas phase and liquid phase catalysis to model a solid-liquid interface, and retain the advantages of the sophisticated gas phase experimentation that was developed in the past. A way to bridge the gap might be the addition of an excess of  $\text{H}_2\text{O}$  into the feed gas stream of a catalytic reaction.

Perovskite and spinel materials are among the most studied oxidation catalysts, in the gas phase, liquid phase, and in the electrochemical oxygen evolution reaction (OER) due to their enormous flexibility in the cationic sublattice which allows isomorphous cation substitution.<sup>20,21</sup> Therefore, transition metal oxide spinels and perovskites are considered to replace precious metals, or their oxides because of their usually lower cost and tunable properties. Their real structure differs from the ideal bulk structure, and surface defects like undercoordinated transition metal cations are described as the active site in catalysis.<sup>22,23</sup> Perovskites and spinels were used as catalysts in different oxidation reactions like the oxidation of carbon monoxide ( $\text{CO}$ ),<sup>24,25</sup> the total oxidation of VOC,<sup>26,27</sup> or the selective

oxidation of alcohols like 2-propanol in the gas phase.<sup>28,29</sup> Furthermore, these materials are studied in liquid phase oxidation reactions like oxidation of cyclohexene, cinnamyl alcohol, styrene, or benzyl alcohol.<sup>29–31</sup>

This thesis has the goal of expanding the fundamental knowledge on oxidation catalysis over Co and Fe containing transition metal oxides. One aspect is the application of the same catalyst in different reactions to find similarities between different reactions. Another objective of this thesis is building a bridge between conventional gas phase and liquid phase catalysis by adding water into the process gas stream.

To fulfill these tasks, the thesis focuses on four pillars: (1) the synthesis of mixed  $\text{LaCo}_{1-x}\text{Fe}_x\text{O}_3$  perovskites, (2) catalytic testing of these perovskites, and  $\text{Co}_{3-x}\text{Fe}_x\text{O}_4$  spinels in the gas phase oxidation of CO, (3) the catalytic gas phase oxidation of 2-propanol with and without the addition of  $\text{H}_2\text{O}$  into the feed on perovskites and spinels, and (4) the determination of OER activity on  $\text{LaCo}_{1-x}\text{Fe}_x\text{O}_3$  perovskites. The gas phase 2-propanol oxidation part of this thesis is based on previous works by Dr. Sven Anke in the group of Prof. Dr. Martin Muhler at the Ruhr University in Bochum, who showed that the reaction is a suitable probe reaction for the investigation of redox and acid-base properties.<sup>22,28,32,33</sup>

In the gas phase catalysis, the attempt will be made to derive composition-activity correlations which can be a first step into the direction of generating structure-activity correlations with more sophisticated structural analysis performed on selected sample series. In the context of CO oxidation, the effect of carbonate species on perovskites will be addressed, and the effect of morphology and composition on reactive oxygen species (ROS) formation in the spinel system. For the 2-propanol oxidation, the effect of phase segregation will be addressed on perovskites, while on spinel catalysts a doping effect of Fe will be investigated. In both studies, the effect of  $\text{H}_2\text{O}$  in the feed is investigated to generate knowledge about surface hydration and induced effects by  $\text{H}_2\text{O}$ . In the chapter focusing on the OER on perovskites, synergistic effects between Fe and Co will be investigated by experimental studies and density functional theory with Hubbard  $U$  term (DFT+ $U$ ) studies in collaboration with the groups of Prof. Dr. Rossitza Pentcheva from the University of Duisburg-Essen and Prof. Dr. Wolfgang Schuhmann from the Ruhr University Bochum.

The catalyst materials will be studied by different methods such as atomic absorption spectroscopy (AAS), X-ray diffraction (XRD), nitrogen ( $\text{N}_2$ ) physisorption followed by Brunauer, Emmett and Teller (BET) and Barrett, Joyner and Halenda (BJH) analysis, fourier transform infrared spectroscopy (FTIR), X-ray photoelectron spectroscopy (XPS), near ambient pressure (NAP) XPS, (*operando*) diffuse reflectance infrared fourier transform spectroscopy (DRIFTS), magnetometry, Mössbauer spectroscopy, transmission electron microscopy (TEM), scanning transmissing electron microscopy (STEM), scanning electron microscopy (SEM) and temperature-programmed reduction (TPR).

## 2. State of the Art

This chapter presents a brief overview of the most relevant topics addressed by the submitted thesis and the underlying concepts. A detailed introduction into the specific research field and the individual research questions are given within each chapter.

### 2.1. Metal Oxides

Mixed metal oxides (MMOs) are inorganic compounds containing at least two different metal cations and oxide anions. They are often used as catalysts since they provide high thermal stability, are often favorable in cost, and have a higher resistance to poisoning than noble metals. MMOs are an essential material class with multiple applications, for example, in fuel cells, as sensors, or as catalysts due to their acid-base and redox properties.<sup>34–36</sup> Generally, transition metal oxides are used in several industrial contexts like oil refining or the production of bulk chemicals.<sup>37</sup> One industrially relevant process in which oxide catalysts are used is the selective oxidation of methanol to formaldehyde.<sup>2–4</sup> However, the potential of mixed metal oxides is not only limited to oxidation reactions but also dehydrogenation, the water gas shift reaction, and even reduction reactions are catalyzed by MMOs.<sup>37</sup> Usually, metal oxides terminate by the oxide anion  $O^{2-}$  which is typically larger in size than the metal cations  $M^{n+}$ . The symmetry breaks at the surface of metal oxides, and metal cations are under-coordinated on the surface. The undercoordinated cations might adsorb water vapor which leads to the formation of OH species on the surface. Also alcohols will dissociate heterolytically when adsorbing on MMOs.<sup>38</sup> In addition, metal oxide surfaces can contain additional defect sites like edges or steps.<sup>37</sup> Oxides can be classified as either crystalline or amorphous. There are various crystalline metal oxides such as perovskites, spinels, scheelites, and palmeirites in which different oxygen polyhedra coordinate the metal cations. For the connection of the oxygen polyhedra, there are many possible ways like chains, corner-sharing, or edge-sharing. The cation arrangement is influenced by the nature of the element and its neighbors. The arrangement affects the type and the strength of bonding.<sup>36</sup>

#### 2.1.1. The Perovskite Structure

The general perovskite sum formula is  $ABO_3$  where A is a large cation like a lanthanide, alkali metal, or alkaline earth metal, and the B cation typically is a transition metal. A typical example of perovskites is the  $A^{3+}B^{3+}O_3$  perovskite in which both cations have a  $M^{3+}$  oxidation state like in  $LaFeO_3$  and  $LaCoO_3$ . The perovskite structure is very versatile

and can host more than 90% of the metallic elements from the periodic table of elements and therefore allows tuning of its properties by changing the composition.<sup>20,39</sup>

The crystal structure of perovskites depends on the ratio of the atomic radius of cation A<sup>n+</sup> ( $r_A$ ), the atomic radius of cation B<sup>n+</sup> ( $r_B$ ), and atomic radius of O<sup>2-</sup> ( $r_O$ ) and is reflected in the factor of tolerance ( $t$ ), as defined in Equation 2.1. The ideal perovskite structure is cubic and has a tolerance factor of 1.

$$t = \frac{r_A + r_B}{\sqrt{2} \cdot (r_B + r_O)} \quad (2.1)$$

In the ideal structure, the A cation is the center of a cube formed by the B cations with the oxygen atoms on the middle of the cube edges, which leads to octahedral coordination of the B cations with eight oxygen atoms and dodecahedral coordination of the A cation with twelve oxygen atoms.<sup>20,39</sup> The structure's stability is determined by geometrical constraints of octahedral and dodecahedral sites, and if  $t$  drops below 0.75, a distortion occurs leading to orthorhombic or rhombohedral crystal structures.<sup>20</sup> The orthorhombic crystal structure of LaFeO<sub>3</sub> is shown in Figure 2.1a, the rhombohedral crystal structure of LaCoO<sub>3</sub> in Figure 2.1b. There are three main mechanisms for perovskite distortion: tilting of the BO<sub>6</sub> octahedra, reordering of A- and B-sites, and formation of vacancies of either A, B or O.<sup>40</sup>



**Figure 2.1:** Projection of the crystal structure of the orthorhombic LaFeO<sub>3</sub> perovskite along the [110] viewing direction, reproduced from inorganic crystal structure database (ICSD) collection code 93611 (a).<sup>41</sup> Projection of the crystal structure of the rhombohedral LaCoO<sub>3</sub> perovskite along the [110] viewing direction, reproduced from ICSD collection code 93611 (b).<sup>42</sup> La ions are shown in blue, Fe ions and their hexagonal oxygen coordination polyhedra are shown in yellow, Co ions and their hexagonal oxygen coordination polyhedra are shown in orange. O ions are shown in red. The images were created with VESTA.<sup>43</sup>

In addition, the potential of oxygen vacancy formation makes perovskites a versatile class of catalysts for several oxidation reactions. When substituting the La<sup>3+</sup> cation with a Sr<sup>2+</sup> cation, oxygen vacancies are formed in the perovskite.<sup>20,44</sup> The A cation is typically considered catalytically inactive and the B cation as the active one.<sup>45</sup> Often, La is used as the A cation in oxide perovskites, and a variation of the B cation enables a comparison of the activity of different active cations.

## 2.1.2. The Spinel Structure

Metal oxide spinels generally follow the sum formula  $AB_2O_4$  and crystallize in the cubic spinel structure, which is named after the spinel mineral  $MgAl_2O_4$ . Often, the A cation is divalent, and the B cation is trivalent. 32 oxygen anions (eight formula units) in a cubic close-packed structure span the structure's unit cell. Interstitial sites are partially filled with the cations between the oxygen ions, namely tetrahedral and octahedral sites. Four oxygen anions surround tetrahedral sites in a tetrahedral geometry. Six oxygen anions surround octahedral sites. In total, 64 tetrahedral and 32 octahedral sites are formed in spinels, but only 8 tetrahedral and 16 octahedral sites are filled and are labeled A-sites and B-sites, respectively.<sup>46–48</sup> The structure of the cubic  $Co_3O_4$  spinel is shown in Figure 2.2a.

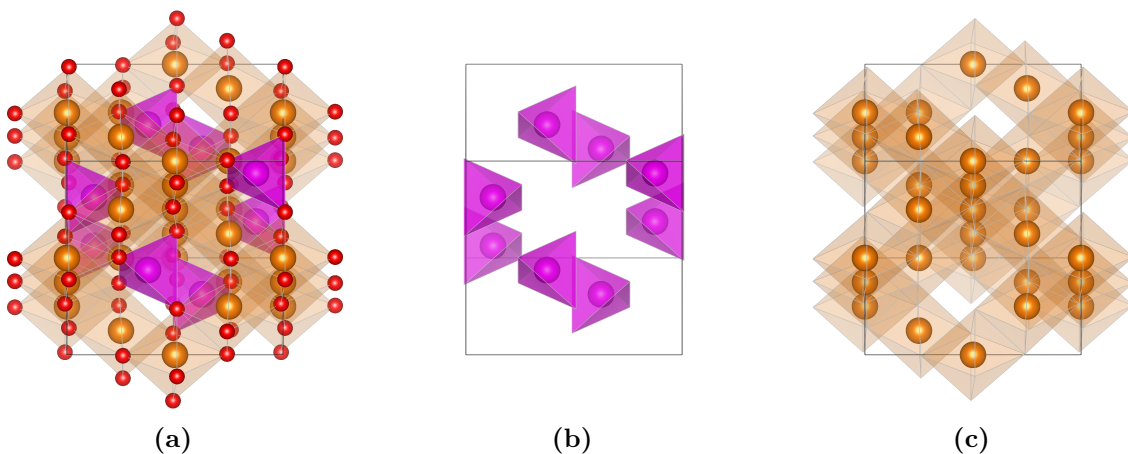


**Figure 2.2:** (a) Projection of the crystal structure of the cubic  $Co_3O_4$  normal spinel along the [024] viewing direction, reproduced from ICSD collection code 9362.<sup>49</sup> (b) Projection of the crystal structure of the cubic  $Co_3O_4$  normal spinel along the [024] viewing direction and its tetrahedral sites. (c) Projection of the crystal structure of the cubic  $Co_3O_4$  normal spinel along the [024] viewing direction and its octahedral sites.  $Co^{2+}$  ions and their tetrahedral oxygen coordination polyhedra are shown in magenta,  $Co^{3+}$  ions and their octahedral oxygen coordination polyhedra are shown in orange. O ions are shown in red. The image was created with VESTA.<sup>43</sup>

Within the spinels, normal spinels like  $Co_3O_4$  and inverse spinels like  $CoFe_2O_4$  are distinguished on the occupation of different sites in the spinel structure. In a normal spinel, the tetrahedral A sites (Figure 2.2b) are filled by the  $A^{2+}$  cations and the octahedral B sites (Figure 2.2c) by the  $B^{3+}$  cations. However, in an inverse spinel, the tetrahedral A sites are filled with eight  $B^{3+}$  cations, and the B sites are filled with eight  $A^{2+}$  cations and the remaining eight  $B^{3+}$  cations.<sup>46–48</sup> There are also intermediate cation distributions that are described by the degree of inversion ( $x$ ) in the sum formula  $(A_x^{2+}B_{1-x}^{3+})[A_{1-x}^{2+}B_{1+x}^{3+}]O_4^{2-}$  whereas the A sites are given in parenthesis and B sites are given in square brackets. For a normal spinel,  $x$  is 0, for an inverse spinel  $x$  is 1 and a  $x$  of  $\frac{2}{3}$  describes a random distribution of cations.<sup>46–48</sup>

The cation distribution in spinels is determined by, for example, ionic size, Madelung constant, and ligand field stabilization energy. In terms of size, tetrahedral sites are smaller

than octahedral sites, and the smaller cation should occupy the tetrahedral site.<sup>48</sup> Usually, the B cation is smaller due to its higher charge and should occupy the tetrahedral sites, leading to an inverse spinel structure. However, interaction of cations within the structure leads to a preferred occupation of the larger octahedral B sites with the  $B^{3+}$  cations. The Madelung constant measures the electrostatic potential of an ion in a crystal and depends on the molecular volume, lattice parameters, and distances between the cations.<sup>48</sup>

The ligand field stabilization energy is higher for nearly every octahedral configuration than tetrahedral configuration, and the higher stabilization energy is decisive for normal or inverse spinel formation, which depends on the remaining electrons in the d shell. Octahedral and tetrahedral fields are energetically equal. only for  $d^5$  high spin like  $Fe^{3+}$  and  $d^{10}$  configurations, both labeled as spherically symmetric.<sup>48</sup> Those spherically symmetric ions usually form normal spinels if they are in  $M^{2+}$  oxidation state, and inverse spinels in the  $M^{3+}$  oxidation state.<sup>48</sup>

With all these considerations made, the degree of inversion can be theoretically calculated by quantum mechanics.<sup>46,50,51</sup> Several experimental techniques are used for the determination of the cation distribution, such as XRD, Mössbauer spectroscopy, Raman spectroscopy, and nuclear magnetic resonance (NMR) spectroscopy.<sup>46</sup> It might be essential to know the degree of inversion of spinels since the cation distribution is also reflected on the oxide surface, and different cations might be exposed in mixed metal spinels.<sup>52,53</sup>

## 2.2. Selective and Total Thermal Oxidation Catalysis on Metal Oxides

In large-scale thermal oxidation processes like oxo-functionalization or oxidative dehydrogenation, reactants undergo a reaction with molecular oxygen ( $O_2$ ) and the selectivity of these reactions is an important parameter. The thermodynamically favored total oxidation of the reactants to  $CO_2$  and  $H_2O$  must be prevented. At the same time, the selectivity of functionalized products formed by kinetic control should be high, which is a challenge for industry and catalysis science.<sup>35</sup> Typically, heterogeneously catalyzed gas-solid oxidation reactions are performed at high temperatures, which favors the total oxidation.

The “seven pillars” of oxidation catalysis introduced by Grasselli are empirical rules for the design of catalysts for selective oxidation reactions.<sup>11,54</sup> Those pillars or principles are lattice oxygen, metal-oxygen bond strength, host structure, redox properties, multi-functionality of active sites, site isolation, and phase cooperation.<sup>54</sup> Active oxygen species like oxide anions  $O^{2-}$ , superoxide  $O_2^-$ , peroxide  $O_2^{2-}$ , and metal-oxo  $O^-$  are among the most influential parameters in catalyst design that derived from the phenomenological studies. The molecular orbital (MO) diagram of  $O_2$  is shown in Figure 2.3a and reveals the paramagnetic behavior of the triplet ground state molecular  $O_2$ . The atomic orbital (AO)

diagram for  $\text{O}^-$  is shown in Figure 2.3b, for  $\text{O}^{2-}$  in Figure 2.3c. The atomic orbital schemes reveal a radical character for  $\text{O}^-$  and a nucleophilic character of the  $\text{O}^{2-}$  species. The MO diagrams for the superoxide  $\text{O}_2^-$  and peroxide  $\text{O}_2^{2-}$  anions are shown in Figure 2.4a and Figure 2.4b, respectively. The superoxide has a clear radical character with a single unpaired electron, and the peroxide has a rather weak oxygen–oxygen single bond that is prone to decomposition and formation of a metal-oxo species.

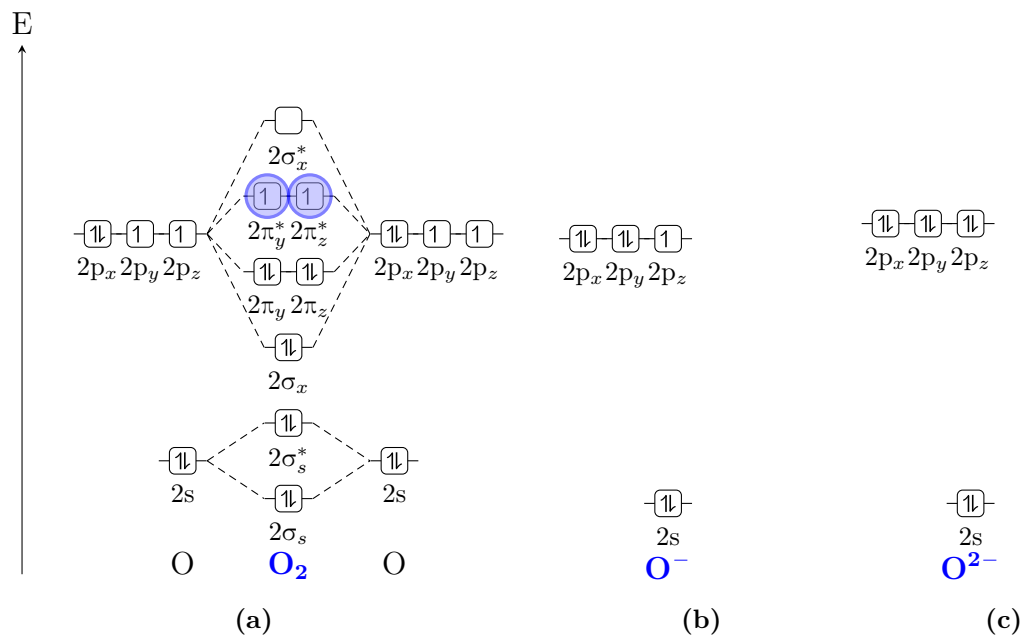


**Figure 2.3:** Molecular orbital diagram for di-oxygen  $\text{O}_2$  (a), atom orbital diagram for the metal-oxo ion  $\text{O}^-$  (b), and for the oxide anion  $\text{O}^{2-}$  (c).

The activation and use of  $\text{O}_2$  molecules are crucial for oxidation of alkanes, alcohols, and small molecules like CO and VOC. The activation of the catalyst leads to redox species that act selectively in C–H activation and the addition of oxygen to the carbon backbone.<sup>11</sup> On copper oxide, Grasselli reported that lattice oxygen species present in excess on the surface favor unselective oxidation of propene while at low abundance of lattice oxygen, highly selective oxidation towards acrolein is observed.<sup>11,54</sup> Consequently, a catalyst design principle was developed: The structure of the active catalyst can control the abundance of lattice oxygen atoms. Thereby the selectivity and the amount of  $\text{O}_2$  available should be limited to the amount needed for the stoichiometric catalytic reaction.<sup>11</sup>

Furthermore, to prevent an over-stoichiometric reaction, no exchange of oxygen species between different active sites should be allowed. No exchange implicitly means that the geometric structure of the catalyst must remain unchanged during the catalytic cycle even though an oxygen transfer to the organic substrate and reoxidation by  $\text{O}_2$  occur.<sup>11</sup> The surface oxygen and the gas phase  $\text{O}_2$  are in an equilibrium that is controlled by the chemical potential of the  $\text{O}_2$  in the gas phase. Activation of gas phase  $\text{O}_2$  is happening in a dynamic equilibrium between many different types of oxygen species that are shown

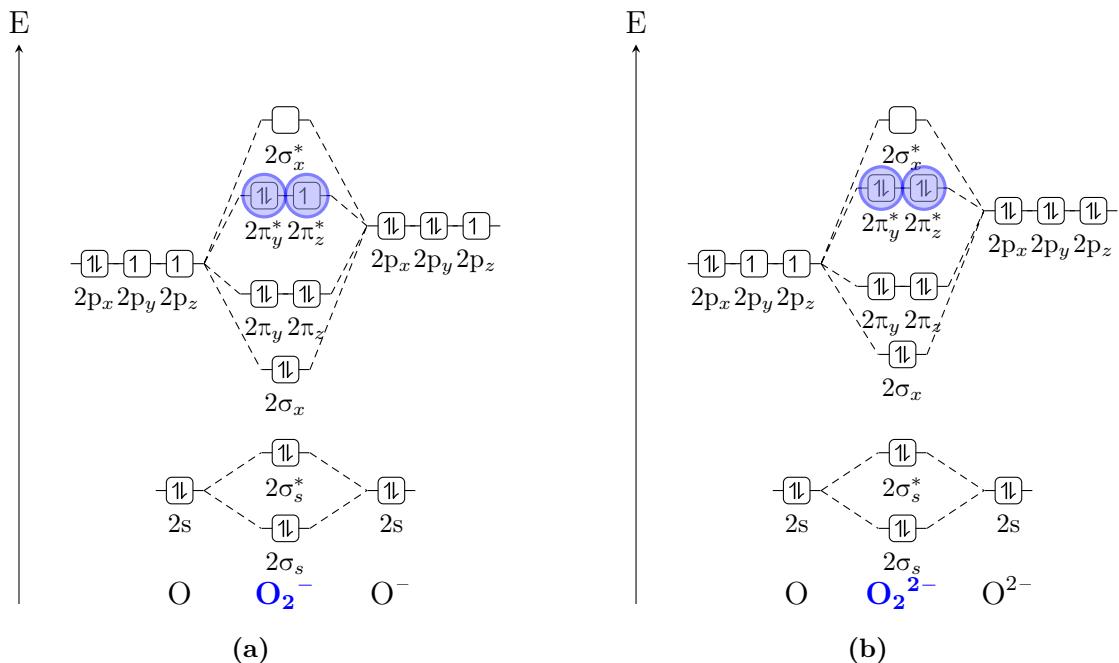
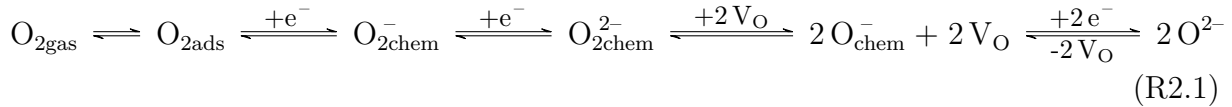


**Figure 2.4:** Molecular orbital diagrams for (a) the superoxide anion  $O_2^-$  and (b) the peroxide anion  $O_2^{2-}$ .

in Equation R2.1 which leads to several oxygen species present at the catalyst surface at the same time. The reverse elementary steps happen in the case of oxygen desorption. In the reaction equation, the abbreviations for adsorbed (ads) and chemisorbed (chem) are used.<sup>55</sup>



The surface coverage with different oxygen species depends on the gas phase's O<sub>2</sub> pressure, rate constants, and temperature. At low temperatures, maybe only the surface layer is equilibrated. At high temperatures, defects created at the surface might diffuse to the bulk. The oxide anions O<sup>2-</sup> are strongly nucleophilic, and the activated oxygen forms superoxide O<sub>2</sub><sup>-</sup>, peroxide O<sub>2</sub><sup>2-</sup>, and metal-oxo O<sup>-</sup> – which are summarized as ROS – have radical character and are strongly electrophilic, as can be seen from the MO diagrams in Figure 2.3a, Figure 2.4a, and Figure 2.4b and the AO diagram in Figure 2.3b.<sup>55</sup> The electrophilic oxygen molecules initiate radical reaction mechanisms after contact with hydrocarbons and can lead to total oxidation products. Nucleophilic oxide anions have no oxidizing properties but the potential to insert into activated molecules which leads to the formation of oxygenated products.<sup>55</sup> Haber introduced the before-mentioned concept of nucleophilic and electrophilic oxygen.<sup>56</sup> For many processes, the O<sub>2</sub> reaction order is

low and leads to the assumption that generation of active oxygen species is not part of a kinetically difficult step but still important.<sup>11</sup>

The reaction mechanism that involves nucleophilic oxide anions is called Mars-van Krevelen (MvK) mechanism, and most gas phase oxidations on reducible oxides proceed via this mechanism.<sup>57</sup> It describes the oxidation of adsorbed activated hydrocarbons with lattice oxygen, and proceeds via the formation of oxygen vacancies at reduced cationic sites. The vacancies are filled by gas phase O<sub>2</sub>, and the cationic sites are oxidized again. However, the reoxidation does not necessarily take place at the same site since oxygen ions can be transported through the lattice.<sup>55</sup> In the MvK mechanism, the O<sub>2</sub> reaction order is expected to be 0. Electrophilic oxygen species participate in the second type of mechanism called Langmuir-Hinshelwood (LH) mechanism. It describes the adsorption of hydrocarbon and oxygen on neighboring sites and their bimolecular reaction on the surface, and the O<sub>2</sub> reaction order is expected to be positive.<sup>58,59</sup> More exotic and less common in gas phase catalysis is the Eley-Rideal (ER) mechanism.<sup>60,61</sup> It describes the reaction of an adsorbed molecule with a non-adsorbed molecule directly from the gas phase.

These fundamental mechanistic and empirical considerations might very well be only a minor part of the overall reaction mechanism picture and are part of the before mentioned “seven pillars” of oxidation catalysis. The oxide systems are not only sharing electrons between atoms, but oxides might also terminate their surface as active clusters supported on a bulk semiconductor parent oxide system. For complex oxides, it is essential to know the crystallographic structure since active sites might be part of it.<sup>11,62</sup>

Therefore, Robert Schlögl suggested redefining the concept of lattice oxygen:<sup>11</sup> Lattice oxygen availability, as well as the availability of ROS, should be restricted to the active site, and there should be chemically effective boundaries for oxygen mobility. The active site is then considered as an atom cluster, including substrate conversion and site regeneration. Furthermore, Schlögl suggests that sub-surface oxygen species should not be postulated as active anymore.<sup>11</sup> However, all concepts mentioned before cannot be used as a predictive tool, which is why Schlögl suggests an evolution of the conceptual basis into a closer link to physical concepts and knowledge-based experimentation.<sup>11</sup> The catalyst is seen as an enabling entity for a reaction network being executed. Mutual interactions between the catalyst and reactants control the functionality of the catalyst, whose electronic structure is defined as a bulk-semiconductor and its surface state arises from a terminating overlayer that differs from the bulk structure.<sup>11</sup> Consequently, *in situ* analytical methods are needed to identify the structures, and the methods then form a feedback loop to find which structures are responsible for selectivity in the reaction network.<sup>11</sup> The concept to be defined is then based on physical observables.<sup>11</sup> In the end, it might allow finding a design strategy based on kinetic descriptions combining inter-reactant interactions and interactions between reactants and catalysts, which is not available yet. However, many of the missing parameters are accessible by *in situ* techniques.<sup>11</sup>

Not only O<sub>2</sub> activation and redox properties are important in oxidation catalysis but also acid-base properties of the oxide surfaces are of relevance for product distribution in catalysis since also acid-base reactions can occur.<sup>37,63,64</sup> Metal oxides with strong acid-base properties are often used in refining and petrochemistry.<sup>37,65</sup>

Two different kinds of acids and bases are distinguished: Brønsted and Lewis acid-base pairs. The Brønsted concept defines acids as proton donors and bases as proton acceptors, while the Lewis concept defines acids as electron-pair acceptors and bases as electron pair donors.<sup>65</sup> Followingly, organic molecules are activated by acids and the creation of a carbocation either by proton transfer to the organic substrate or electron transfer to a Lewis site. The basic activation either occurs by proton abstraction or coordination to an area with high electron density like a carbonyl (C=O) bond. However, cooperative action of acids and bases is often necessary for a specific reaction to take place.<sup>65</sup> The acid-base properties of catalysts can be probed by many physical methods, including FTIR after adsorption of probe molecules like pyridine, their temperature-programmed desorption (TPD), TPD of ammonia, NMR, the zeta potential, and test reactions like alcohol dehydration or dehydrogenation.<sup>37,63,65</sup>

Dehydration of alcohols leads to the elimination of a H<sub>2</sub>O molecule and alkene production, while dehydrogenation leads to the formation of a ketone or aldehyde function and a hydrogen (H<sub>2</sub>) molecule. Usually, dehydration is caused by a strongly acidic center, while dehydrogenation is driven by basic centers.<sup>65,66</sup> It is proposed that oxygen vacancies can also lead to dehydration by oxygen abstraction.<sup>67</sup> On acidic oxides, competitive adsorption of water and alcohols is observed.<sup>66</sup> Based on the product spectrum and the results of adsorption-desorption experiments, metal oxides are also classified into basic and acidic. Basic oxides like La<sub>2</sub>O<sub>3</sub> are sensitive to atmospheric CO<sub>2</sub> by carbonate formation, while acidic oxides like protonic zeolites or silica-alumina adsorb water vapor.<sup>68,69</sup> In general, spinels and perovskites are seen as rather basic oxides.<sup>68</sup>

Another research topic including metal oxides is the total oxidation of VOC like CO, methane (CH<sub>4</sub>) and longer chain compounds into CO<sub>2</sub> and H<sub>2</sub>O that is important in the field of depollution.<sup>37,70</sup> It is stated that mixed oxides exhibit superior performance than single element oxides because of active M<sub>1</sub>/M<sub>2</sub> redox couples or in the case of perovskites with hardly reducible A cations even M<sub>2</sub>/M<sub>2</sub> redox couples like Co<sup>2+</sup>/Co<sup>3+</sup> in LaCoO<sub>3</sub> stabilized by the La cations.<sup>20,37,45,70,71</sup> C–H bond activation in hydrocarbons is crucial, there the example of methane oxidation requires high temperatures above 400 °C on oxides like Co<sub>3</sub>O<sub>4</sub> is briefly discussed. As described before, increased activity is linked to oxygen vacancies that activate either O<sub>2</sub> or the oxidizable compound. That activity depends on the exposed crystal facets and the shape.<sup>70,72</sup>

Often, in a cubic spinel structure primarily the most stable (100) and (111) lattice planes are exposed but not the less stable and more active (110) plane.<sup>73–75</sup> Work from the Sojka group shows that with increasing temperature, there is a shift from a suprafacial ER

mechanism at 400 °C to an interfacial MvK mechanism at 600 °C on the (100) facet. On the (111) surface, three surface states are reported.<sup>76,77</sup> Up to 450 °C – 500 °C, superoxo and metaloxo species are reported, up to 550 °C – 600 °C a bare surface, and oxygen vacancies are reported for temperatures >600 °C, which confirms a transition from suprafacial into the interfacial mechanism.<sup>77</sup>

Mechanistic studies on (100) nanocubes from the Sojka group show two pathways for C–H bond activation, namely a suprafacial mechanism on oxygen covered surfaces and an interfacial mechanism on bare surfaces. The dissociation of the first C–H bond is the kinetically relevant step.<sup>78</sup> In terms of oxygen species contribution, oxo species are mainly active in the suprafacial C–H activation, whereas peroxy species participate in the intermediate reaction steps.<sup>78</sup> In the interfacial activation, dual Co–O sites might activate the C–H bonds cooperatively.<sup>78</sup> Previously, already a significant contribution on the (110) termination of twofold coordinated lattice oxygen was reported.<sup>79,80</sup> On LaCoO<sub>3</sub> the bulk oxygen mobility is of great importance.<sup>70,81</sup>

In the following, the CO oxidation and the oxidation of alcohols with the example of 2-propanol are discussed in further detail.

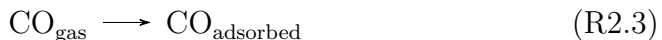
### 2.2.1. Gas Phase CO Oxidation

The simplest molecule to study total oxidation on is CO. The primary reaction equation of the CO oxidation is given in Equation R2.2 and yields only one gaseous product: CO<sub>2</sub>. The reaction is studied often in the literature as a probe reaction for the catalyst surface and catalyst activity since it has only one rate-determining step, and its gaseous product is interacting less strongly with the surface than the reactant CO.<sup>82,83</sup> The product CO<sub>2</sub> is usually considered inert, but the hypothesis is only valid if no reducing species are co-adsorbed on the surface.<sup>82</sup>



The reaction equation itself might seem not very complex. However, CO oxidation still has the potential to give useful insights into fundamental processes since three entities (CO, O<sub>2</sub>, and the surface) have to interact under particular conditions, and the reaction is spin-forbidden even though the catalyst might enable the reaction.<sup>82</sup> The kinetically effective reaction steps are given in Equation R2.3 to Equation R2.5, from which only

the CO adsorption R2.3 is an elementary reaction and the other reactions are composed reactions with complex details and kinetics.<sup>82</sup>



However, the mechanism of CO oxidation is still not fully understood. On noble metal catalysts, clear evidence for LH kinetics was found already in early work by the group of Ertl.<sup>82,84,85</sup> On metal oxides, the situation might be more complex since there are also contributions from oxide species. A potent catalyst for CO oxidation should exhibit a limited ability for back-donation into the CO–σ\* orbital and an intermediate capability of forming M–O bonds.<sup>82</sup> Cobalt is among the elements that exhibit the required electronic structure, which is why recent work on Co<sub>3</sub>O<sub>4</sub> and Co containing perovskites is reported here.

Co<sub>3</sub>O<sub>4</sub> catalysts exhibit high activity in the CO oxidation and reach complete conversion even below room temperature, as early works show.<sup>86</sup> Later, full conversion was even achieved in the region of –80 °C.<sup>87,88</sup> However, the oxides often suffer from deactivation at low temperatures. Jansson et al. report that there is no direct responsibility of formed carbonate species for the deactivation but rather an effect of surface reconstruction hindering the redox couple Co<sup>2+</sup>/Co<sup>3+</sup>. The activity can be restored upon oxidative treatment at 250 °C.<sup>25</sup> In work by Xie et al., an increase in activity was found when spherical particles were substituted by needles which have a higher ratio of (110) planes exposed that are rich in Co<sup>3+</sup> sites,<sup>87</sup> which was confirmed by Hu et. al.<sup>89</sup> Iablokow et al. reported a structure-sensitivity relationship and demonstrated the crucial role of Co<sup>3+</sup>.<sup>90</sup> Another study highlighting the role of a high amount of Co<sup>3+</sup> is from Ding et al., who synthesized flower-like Co<sub>3</sub>O<sub>4</sub> catalysts.<sup>91</sup>

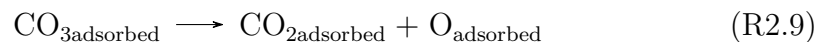
Recent studies focus on mechanistic details and oxygen species participating in the reaction cycle. Singh et al. performed an extensive study on the CO oxidation on Co<sub>3</sub>O<sub>4</sub> surfaces. They developed a detailed reaction pathway based on DRIFTS analysis as well as a detailed kinetic study.<sup>92</sup> According to their proposal, at low temperatures, CO oxidation occurs without the formation of carbonates and superoxide anions, and Co<sup>3+</sup> is the active site.<sup>92</sup> Furthermore, they state that lattice oxygen formation is the rate determining step (RDS),<sup>92</sup> while other reports state that oxygen abstraction from the superoxide is the RDS.<sup>80,88,93</sup>

Detailed investigations of the preferential oxidation of CO (PROX) in a CO and H<sub>2</sub> containing gas stream on Co<sub>3</sub>O<sub>4</sub>,<sup>94</sup> the CO oxidation on Co<sub>3</sub>O<sub>4</sub>,<sup>95</sup> and CO oxidation on CoO<sup>96</sup> were performed in the Rupprechter group. In PROX they report that the surface appears fully oxidized up to 250 °C. Still, pure CO reduces the surface starting from 100 °C

by a reaction with lattice oxygen that is easily replenished by gas phase O<sub>2</sub> which suggests a MvK mechanism.<sup>94</sup> In the second study, they unfolded a complex network of the MvK mechanism, carbonate formation, and their decomposition as well as CO dissociation followed by carbon oxidation at temperatures above 100 °C. The LH mechanism could not be excluded due to activity even without oxygen vacancies detected.<sup>95</sup> On CoO, they report re-oxidation to Co<sub>3</sub>O<sub>4</sub> on the surface and the subsurface during CO oxidation at above 150 °C.<sup>96</sup>

On (111) terminated Co<sub>3</sub>O<sub>4</sub>, the Sojka group reports that CO mainly gets oxidized by a suprafacial mechanism by diatomic superoxide or cobalt-oxo species.<sup>77</sup> On (100) terminated Co<sub>3</sub>O<sub>4</sub>, Liu et al. report a B layer termination and superoxide formation. The superoxide desorbs from a vacancy-free surface at low temperatures. It is not active in CO oxidation, whereas, on an oxygen vacancy-containing surface, superoxide species can oxidize CO at shallow temperatures and remain stable until 0 °C. Furthermore, the vacancies are not filled by superoxide species.<sup>97</sup>

The potential of perovskite catalysts in the CO oxidation is known, for example, for perovskites containing Co and Fe.<sup>20,45</sup> The mechanism is considered to follow mainly the suprafacial LH type.<sup>83,98</sup> Early work by Tascon et al. on LaCoO<sub>3</sub> indicates the adsorption of CO and CO<sub>2</sub> on the same sites, which are proposed to be oxide anions, and O<sub>2</sub> adsorbs on oxygen vacancies.<sup>99</sup> Furthermore, they offer the following steps during the reaction mechanism:<sup>100</sup>

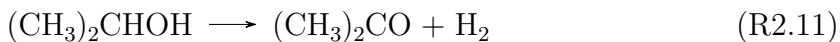


In this kinetic model, carbonate formation in Equation R2.8 is the rate-determining step, and the carbonates are initially bidentate. They are formed from adsorbed oxygen which indicates a suprafacial LH mechanism between 100 °C and 300 °C.<sup>100</sup> However, during the course of the reaction, the overall concentration of oxygen vacancies on the perovskite is becoming the controlling factor of the reaction, and also with increasing temperature, the contribution of bulk oxygen is reported to increase.<sup>83</sup> For Mn containing perovskites, participation of lattice oxygen is reported, indicating a MvK mechanism.<sup>101–104</sup> More recent works on LaCoO<sub>3</sub> reveal that oxygen mobility is triggered at 350 °C.<sup>105</sup>

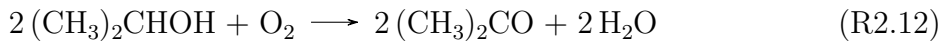
## 2.2.2. Gas Phase Alcohol Oxidation: The Example 2-Propanol

The alcohol oxidation is discussed using the example of the oxidation of 2-propanol as a probe reaction. As mentioned before, different reactions can take place on different sites of oxide surfaces. On strongly acidic sites, the dehydration reaction is observed, and on strongly basic sites, the dehydrogenation reaction takes place. However, for both reactions, another site with weakly adverse properties in the vicinity is necessary.<sup>66</sup> The reaction equation for the dehydrogenation of 2-propanol is given in Equation R2.11, the oxidative dehydrogenation in Equation R2.12, the dehydration in Equation R2.13 and the total oxidation that occurs at high temperatures in Equation R2.14.<sup>66</sup>

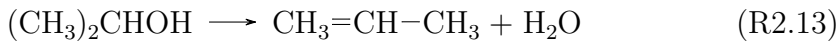
Dehydrogenation reaction to acetone:



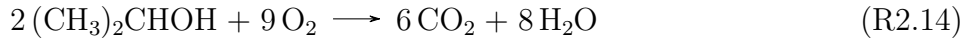
Oxidative dehydrogenation reaction to acetone:



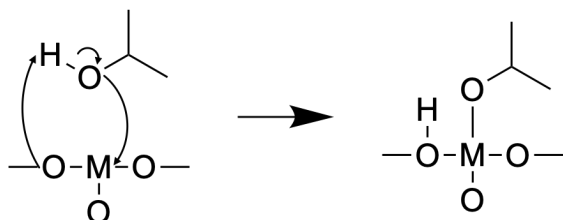
Dehydration reaction to propene:



Total oxidation reaction to CO<sub>2</sub>:

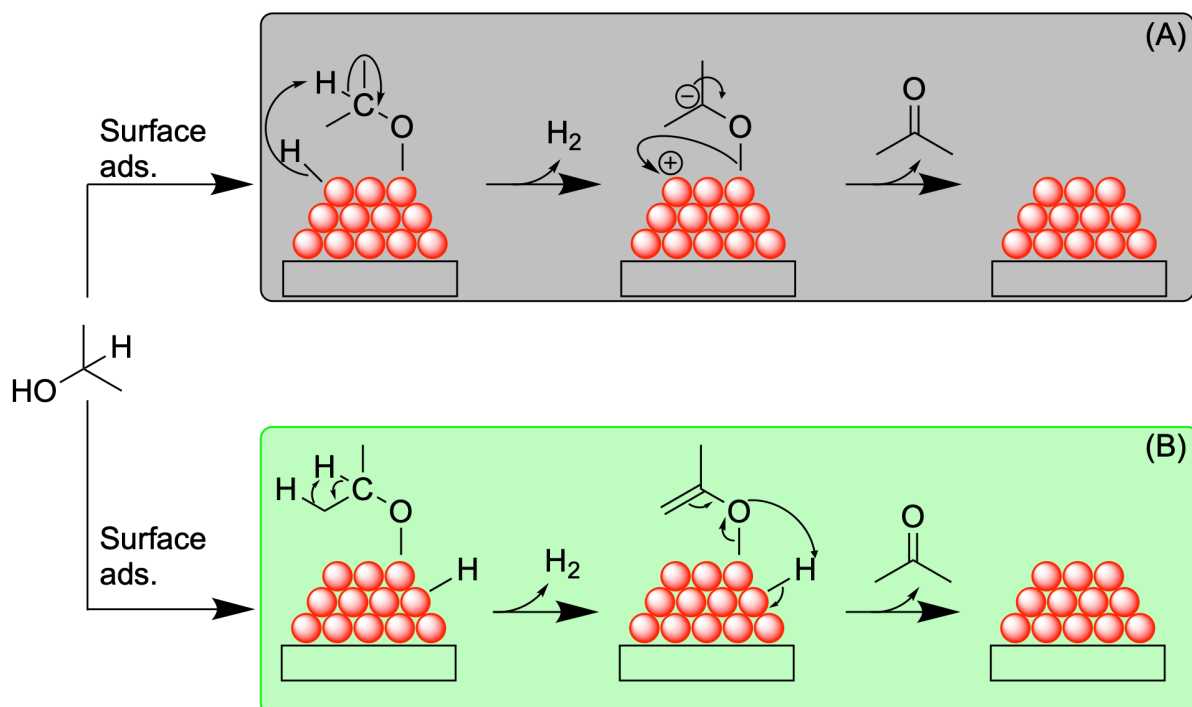


For the oxidation reaction to happen, the 2-propanol must be adsorbed first, as is shown in Scheme R2.1. The adsorption is assumed to take place dissociatively forming a molecule of 2-propoxide and an adsorbed hydrogen atom, and was shown to occur on metal oxide surfaces such as Au(111),<sup>106</sup> Rh(111)-O,<sup>107</sup> Pd/Al<sub>2</sub>O<sub>3</sub>,<sup>108</sup> Mo(110),<sup>109</sup> O/Pd(111),<sup>110</sup> Pd(111),<sup>110</sup> and nanocrystalline CoFe<sub>2</sub>O<sub>4</sub> particles.<sup>32</sup> However, by surface-sensitive vibrational sum frequency spectroscopy, only molecular adsorption of 2-propanol was reported on TiO<sub>2</sub>.<sup>38</sup>



**Scheme 2.1.:** Schematic adsorption of 2-propanol on a catalyst surface, adapted from [66].

The activation of the C–H bond on the  $\alpha$ -carbon is the RDS and can happen differently, as is shown in Scheme R2.2 as an example for the dehydrogenation.<sup>2,66</sup> In one case, called the carbonyl mechanism, the hydrogen is removed from the  $\alpha$ -carbon atom either in one concerted or in two steps, shown as (A). In the other case, the enolic mechanism, the hydrogen is removed from the  $\beta$ -carbon atom, as shown in (B) where the enolic form rearranges to the corresponding acetone. However, by isotopic labeling, the direct participation of the  $\beta$ -carbon was excluded.<sup>111–113</sup> The RDS is the formation of the H<sub>2</sub> molecule.<sup>66</sup> During the process, the intermediate stays adsorbed via the oxygen. Theoretical calculations support the activation via the hydrogen bond to the  $\alpha$ -carbon,<sup>111,114</sup> whereas initial adsorption without dissociation with an intact hydroxy group results in activation of the hydrogen attached to the  $\beta$ -carbon which can also easily lead to dehydration yielding propene.<sup>115</sup> Another explanation for the formation of propene is a high metal–oxygen bond strength of transition metals that lead to a C–O bond cleavage.<sup>106,109</sup>



**Scheme 2.2.:** Ways of conversion of activated 2-propanol to acetone along the carbonyl mechanism (A) as well as along the enolic mechanism (B) under O<sub>2</sub> free conditions, idea from [2].

The oxidation of 2-propanol has been studied in research before,<sup>22,23,28,32,106,116–120</sup> and also finds industrial relevance in the Wacker-Hoechst process if 2-propanol is formed as an intermediate in acetone production.<sup>121</sup> Also, industrial acetone production proceeds through the gas phase dehydrogenation of 2-propanol.<sup>122</sup> 2-Propanol is not only suited for in-depth studies due to its industrial use. The molecule can further be used to determine principle reaction mechanisms in selective oxidation catalysis and acid/base properties under reaction conditions as a measure of product ratio between acetone and propene.<sup>123–128</sup>

Furthermore, 2-propanol was used as a probe molecule to measure the acid/base properties, for example in DRIFTS analysis.<sup>32,119,129,130</sup>

2-Propanol oxidation on spinels was studied in the literature with two main purposes: the study of selective oxidation and the purpose of total oxidation as an example for an oxygenated VOC. In the last decade of the previous century, the group of Lorenzelli worked with spinels and 2-propanol. They studied 2-propanol adsorption on  $\text{Co}_3\text{O}_4$  in the framework of propane total oxidation and showed the formation of acetone and acetate species when increasing the temperature.<sup>131</sup> Furthermore, they studied the catalytic oxidation of 2-propanol over  $\text{MgCr}_2\text{O}_4$  and  $\text{Co}_3\text{O}_4$ . There, they found higher activity for  $\text{Co}_3\text{O}_4$  with conversion starting from around 200 °C and high initial selectivity to acetone. The conversion increased with increasing temperature, but the acetone selectivity decreased in favor of total oxidation. In infrared (IR) spectroscopy, they found that acetates are formed as intermediates of acetone oxidation. In addition, they concluded nucleophilic oxygen species are the active species in total and selective oxidation.<sup>132,133</sup> In another study on  $\text{Mn}_3\text{O}_4$ ,  $\text{MgCr}_2\text{O}_4$  and  $\text{Co}_3\text{O}_4$ , they observed dehydration forming propene starting from 180 °C on  $\text{Mn}_3\text{O}_4$ , and confirmed the decrease in selectivity towards acetone. Further detected products were acetaldehyde and traces of acetic acid.<sup>134</sup>

More recent studies were performed by Hosseini starting from 2011 on  $\text{CoMn}_2\text{O}_4$ ,  $\text{NiMn}_2\text{O}_4$ , and  $\text{CuMn}_2\text{O}_4$ , where the Ni containing spinel showed the highest activity due to a synergistic effect between  $\text{Mn}^{3+}$  and  $\text{Ni}^{2+}$  as shown by TPR. All three materials showed already 20% conversion at 150 °C. The full conversion was reached at 250 °C for the Ni-containing spinel and between 300 °C and 350 °C for the other two spinels. The product distribution was not determined, but the reaction was proposed to follow the MvK mechanism.<sup>135</sup> In another study, they studied  $\text{CoCr}_2\text{O}_4$ ,  $\text{CuCr}_2\text{O}_4$  and  $\text{ZnCr}_2\text{O}_4$ .  $\text{ZnCr}_2\text{O}_4$  had the highest activity of over 75% conversion at 150 °C and 100% conversion at 300 °C due to excess oxygen on the surface,  $\text{Cr}^{3+}\text{--Cr}^{6+}$  redox couples and a synergistic effect between the spinel and formed  $\text{ZnO}$ .<sup>136</sup>

Another recent study by Dissanayake et al. studies the total oxidation of 2-propanol on  $\text{Co}_3\text{O}_4$  and describes a dependency of the activation energy on the synthesis conditions. The synthesis conditions are correlated with more surface oxygen species, a higher amount of  $\text{Co}^{3+}$  on the surface, larger pore volumes, and better low-temperature (LT) reducibility. Furthermore, surface carbonates and carbonyl species are observed DRIFTS. They also added water vapor to the feed, which shifts the temperature of 90% conversion up by 8 °C.<sup>119</sup>

The most recent works on 2-propanol oxidation on spinels were published by the Muhler group.<sup>22,23,28,32,33,120</sup> In 2017, the selectivity in 2-propanol oxidation was investigated on  $\text{CoFe}_2\text{O}_4$  in comparison between a commercial catalyst and a catalyst synthesized by co-precipitation of a crystalline precursor and subsequent thermal decomposition. The catalyst prepared by the crystalline precursor decomposition approach, mainly exposing

the (111) facet due to topotactic transformation, had a higher selectivity to propene. In contrast, the commercial catalyst nearly exclusively catalyzed the dehydrogenation, which indicates a structure-activity correlation in acidity.<sup>28</sup> In another study on Co<sub>3</sub>O<sub>4</sub> nanoparticles, they introduced the concept of a LT and a high-temperature (HT) activity channel since the activity decreases between heating and cooling in a transient experiment due to reduction of the Co species and carbonaceous deposit formation. An oxidative treatment can restore the initial activity. Furthermore, they found that active Co<sup>3+</sup> species are involved in combination with surface-bound ROS. DFT+U calculations indicate that 5-fold-coordinated octahedral surface Co<sub>5c</sub><sup>3+</sup> is the active site on the [100] facet and that the LH mechanism leads to the highest energy gain.<sup>22</sup>

On CoFe<sub>2</sub>O<sub>4</sub> nanoparticles, they investigated the reversible deactivation and the phenomenon of LT and HT activity channels. The main product was acetone via oxidative dehydrogenation. The deactivation occurs due to the formation of carbonaceous species from which they consider carbonates acting as spectators in the reaction and acetates as poisons for the catalysts. The reduction of cobalt is another cause for deactivation.<sup>32</sup> A recent study on the comparison of Co<sub>3</sub>O<sub>4</sub> nanoparticles of different sizes shows that the (110) facet is the most active, and on this facet, the preferred path from DFT+U is the MvK mechanism. The model of the deactivation is refined, and temperature-programmed oxidation (TPO) experiments show that during the reaction, multilayer coke deposition and reduction of the Co occur.<sup>120</sup> A recent study by Libuda et al. on a (111) terminated Co<sub>3</sub>O<sub>4</sub> surface shows that surface reduction takes place by total oxidation and that the product distribution changes towards propene with the degree of reduction of Co<sub>3</sub>O<sub>4</sub>(111). Also, carbonaceous deposits were found.<sup>137</sup>

Also, perovskite oxides were studied in the oxidation of 2-propanol, and the product ratios were investigated. Early works by Radha et al. used La<sub>2</sub>MnMO<sub>6</sub> perovskites with M = Co, Ni, and Cu. They showed selective dehydrogenation of 2-propanol and a linear correlation between activation energy and electrical conduction.<sup>138</sup> Kubo et al. investigated BaMoO<sub>3</sub> and SrMoO<sub>3</sub> synthesized by reduction of Scheelite-type oxides in the oxidation of 2-propanol and found that dehydration to propene mainly occurs over Mo<sup>6+</sup> while Mo<sup>4+</sup> promotes the dehydrogenation to acetone.<sup>139</sup> Hosseini et. al. studied LaMn<sub>y</sub>Co<sub>1-y</sub>O<sub>3</sub> perovskites for optimization of 2-propanol total oxidation.<sup>140</sup>

In recent times, the Wu group studied the acid-base properties of their perovskites using 2-propanol oxidation. On A-terminated perovskites, they report that the surface is basic. Therefore, mainly dehydrogenation occurs, and both reactions follow the elimination unimolecular conjugate base (E<sub>1cb</sub>) elimination from the alkoxy intermediate to acetone or propene.<sup>141</sup> The E<sub>1cb</sub> proceeds through the abstraction of a rather acidic proton, and intermediate carbanion formation. In a second step, the OH<sup>-</sup> or another proton is abstracted. In a study on differently shaped nanocrystals, they report surface reconstruction during oxidative pretreatment and propose that step sites, introduced during the pretreatment, are

the active sites. Like in spinels, it is suggested that the (110) facet is more active because it leads to more step sites compared to (100).<sup>142</sup> In a combined kinetic and spectroscopic study, Tan et al. investigated 2-propanol on the SrTiO<sub>3</sub>(110) surface. They mainly see acetone formation and the formation of propene at elevated temperatures. They assume an orientation where the hydrogen at the  $\alpha$ -carbon atom points directly towards the surface, which facilitates the activation and following abstraction.<sup>143</sup>

In terms of the influence of the A-cations, Zhang et al. performed oxidation of 2-propanol on LaMnO<sub>3</sub>(100), and La<sub>0.7</sub>Sr<sub>0.3</sub>MnO<sub>3</sub>(100) thin films with propene as the main product for both catalysts, and the pure La perovskite is more active than the La<sub>0.7</sub>Sr<sub>0.3</sub>MnO<sub>3</sub>. It is proposed that oxygen vacancies can also lead to dehydration by oxygen abstraction.<sup>67</sup> Another recent study by Büker et al. showed that A-site substitution in La<sub>1-x</sub>Sr<sub>x</sub>CoO<sub>3</sub> perovskites leads to an increase in 2-propanol oxidation activity up to 20% of Sr in the structure due to more oxygen vacancies on the surface. When increasing the Sr amount further, too many Co<sup>2+</sup> species on the surface were formed.<sup>29</sup>

### **2.2.3. Transition from Gas Phase to Liquid Phase**

Oxidation processes in the liquid phase are usually conducted at less harsh conditions than processes in the gas phase which usually leads to more selective oxidation products.<sup>2,13</sup> However, many *operando* or *in situ* techniques are still under development for liquid phase catalysis,<sup>16–19</sup> and techniques like NAP XPS are only available in the gas and not in the liquid phase. Therefore, the co-feed of water into the gas phase feed of an oxidation reaction can be a bridge between traditional dry gas phase and liquid phase catalysis.

The effect of water was studied on different alcohols using Pt-catalysts in gas phase reactions by the Somorjai group. In the ethanol oxidation, conversions and selective oxidation selectivity decreased,<sup>144</sup> for 1-propanol, a steady conversion decay and an increase in activation energy with increasing water content were observed but no clear trend in selectivity,<sup>145</sup> and in the oxidation of 2-propanol, there was a steady conversion decay with increasing water content.<sup>80</sup> Also in the 2-propanol oxidation, Dissanayake et al. showed a slightly negative effect on the conversion upon water co-feeding on the conversion with the goal of total oxidation.<sup>119</sup> Falk et al. showed that the HT and LT channel behavior remains present even with water present in the feed. However, water changes the onset of the reaction to higher temperatures and the position and the magnitude of the LT maximum shift to higher temperatures. During cooling, the curve is shifted to lower temperatures which means higher activity.<sup>23</sup>

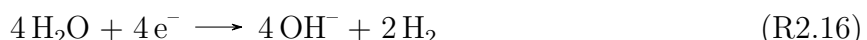
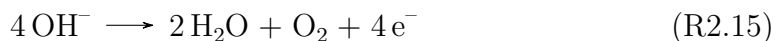
In other oxidation reactions such as CO and toluene total oxidation, water decreases the conversion on La<sub>0.6</sub>La<sub>0.4</sub>MnO<sub>3</sub> perovskites.<sup>146</sup> A dependency of the effect of water was found in methane oxidation over La<sub>1-x</sub>Sr<sub>x</sub>FeO<sub>3</sub>, where a negative effect on the conversion was reported at lower temperatures. In contrast, there is no detrimental effect at elevated

temperatures.<sup>147</sup> In *n*-butane oxidation over vanadium phosphorous oxide, competitive adsorption of water and O<sub>2</sub> influences the O<sub>2</sub> activation.<sup>148</sup> Another study suggests a filling of oxygen vacancies by water which was taken as an explanation for an activity loss. The extent of deactivation was more severe for LaFeO<sub>3</sub> than for LaCoO<sub>3</sub> but was depressed with increasing temperature.<sup>149</sup> In CO oxidation, the activity decreases upon water co-feeding on spinels,<sup>150,151</sup> which is attributed to the formation of surface hydroxyl groups that hinder O<sub>2</sub> activation,<sup>150,152</sup> or water adsorption blocking Co<sup>3+</sup> sites.<sup>150</sup> Detrimental effects in the activity of spinel catalysts are also present in propane total oxidation,<sup>153</sup> and other hydrocarbon oxidation.<sup>151</sup>

Despite all reports about lower activity in the gas phase upon water co-feeding, there are also similarities between gas and liquid phase catalysis. Similar 2-propanol oxidation activation energies were found by Falk et al. on Co<sub>3</sub>O<sub>4</sub> in the liquid phase as well as in the gas phase with water co-feeding during heating.<sup>23</sup> Another study by Büker et al. showed similar activity patterns in gas phase 2-propanol oxidation and in liquid phase cyclohexene oxidation.<sup>29</sup> Another interesting report by Waffel et al. showed the importance of the oxygen species used for liquid phase oxidation of styrene, benzyl alcohol, and cinnamyl alcohol on a Co<sub>3-x</sub>Fe<sub>x</sub>O<sub>4</sub> spinel series synthesized via nanocasting. In the cinnamyl alcohol oxidation, doping with Fe had a positive effect if *tert*-butyl hydroperoxide (TBHP) was used as the oxidizing agent. In contrast, it had a detrimental effect if O<sub>2</sub> was used as the oxidizing agent. The difference is attributed to O<sub>2</sub> activation via spin transfer and TBHP activation via partial decomposition.<sup>31</sup> The synergistic effect was also observed in a LaCo<sub>1-x</sub>Fe<sub>x</sub>O<sub>3</sub> substitution series in cinnamyl oxidation with TBHP as the oxidant.<sup>30</sup>

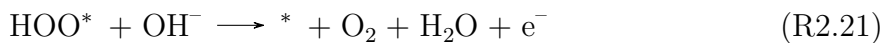
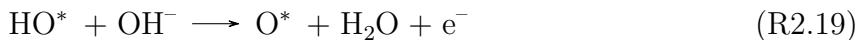
## 2.3. Electrochemical Oxygen Evolution

An important oxidation reaction in the framework of a potential future hydrogen economy is the electrochemical OER.<sup>154,155</sup> It is the kinetically more demanding step of water splitting occurring together with the hydrogen evolution reaction (HER) mostly in a conventional electrochemical setup that consists of an electrolysis cell, a conducting electrolyte, and two redox electrodes for oxidation and reduction. Both reaction equations in an alkaline medium are given in Equation R2.15 at the anode and Equation R2.16 at the cathode, respectively. The overall reaction is Equation R2.17<sup>154</sup>



The OER is more demanding since the number of transmitted electrons is twice the number as in the HER, and the potential thermodynamically required against the standard hydrogen electrode (SHE) are 1.23 V for the OER and  $-0.83$  V (in basic, 0.00 V in acidic) for the HER. Complex charge and mass transport processes occur in both reactions, and therefore, the real potential differs from the ideal potential. Therefore, an additional activation barrier exists. This additional potential is called overpotential ( $\eta$ ). During experimentation, additional phenomena like surface blockage by gas bubbles, electrolyte resistance, external circuit resistance, and transport of charge and ions from the bulk electrolyte to the anode surface are contributing to increase the overpotential.<sup>154,156</sup> Since experimental setups differ including for example the counter electrode and potentiostats used, there is a need for comparison by objective benchmark data. Often, comparison of catalysts is made during a linear sweep voltammetry (LSV) measurement at a current density of  $10 \text{ mA cm}^{-2}$  or current density normalized to the electrochemically active surface area.<sup>157</sup>

The mechanism of the OER usually involves the same three adsorbed intermediates  $\text{OH}^*$ ,  $\text{O}^*$ , and  $\text{OOH}^*$  even though there are different suggestions for the exact mechanism. Under basic conditions, all proposed mechanisms include  $\text{OH}^*$  formation by the elementary step of hydroxide coordination to the active site.<sup>158</sup> The following mechanism is widely accepted for the OER under basic conditions:<sup>158,159</sup>



In addition to measurements of the overpotential of the OER, Rossmeisl and Nørskov developed a theoretical description of the OER allowing the theoretical prediction that includes the intermediates mentioned above to understand the thermodynamics of each OER reaction step. Their suggestions include a Gibbs free energy ( $\Delta G$ ) for each reaction step, and the largest value is the overpotential of the reaction.<sup>160</sup> In addition, Sabatier's principle was used to construct volcano curves which show a plot of the OER overpotential against a binding strength descriptor  $\Delta G_{\text{O}^*}^0 - \Delta G_{\text{HO}^*}^0$ .<sup>158,161</sup> These offer pathways to improving catalyst design and composition since the maximum of the volcano is a maximum in reactivity. At the left side of the maximum, the binding strength of oxygen is too weak, at the right side too strong, which both lead to sluggish reaction kinetics.<sup>158</sup>

Kinetic parameters to judge the OER performance are the Tafel slope ( $b$ ) and exchange current density ( $j$ ), which are connected to  $\eta$  over the Tafel Equation 2.2.<sup>158,162,163</sup> The Tafel slope can be used to deduce the kinetic rate and the mechanism of the electrocatalytic

reaction. A smaller value of  $b$  suggests faster charge carrier kinetics. A high value of  $j$  indicates a higher activity for water splitting.<sup>158</sup> Like in thermal catalysis, the stability of a catalyst is also important in electrocatalysis, which can, for example, be determined by LSV. In that case, many reaction cycles are performed, and the overpotential at a current density of  $10 \text{ mA cm}^{-2}$  is evaluated to determine the catalytic stability. Another possibility is the determination via chronopotentiometry and chronoamperometry in which at a current density of  $10 \text{ mA cm}^{-2}$  is kept constant, and the potential variation is measured. Stable catalysts endure – depending on the definition – more than  $10 \text{ mA cm}^{-2}$  for over  $10 \text{ h}$  or more than 5000 cycles.<sup>158</sup>

$$\eta = b \cdot \log j \quad (2.2)$$

Among other very promising transition metal oxide catalysts for OER anode materials are Co containing spinels and perovskites.<sup>164–172</sup> During the process of an OER experiment on  $\text{Co}_3\text{O}_4$ ,  $\text{CoO}_x(\text{OH})_y$  forms reversibly as the active phase,<sup>173</sup> but the activity is correlated with the other cations incorporated in the structure because of different oxyhydroxide stabilization ability.<sup>174</sup> In a recent study, Rabe et al. showed in a spinel substitution series that  $\text{Co}^{3+}$  plays a major role in the OER activity.<sup>168</sup> Recent studies by Saddeler et al. showed an effect of surface termination on the activity,<sup>171</sup> and phase transition from cobalt-rich wüstite nanoparticles into spinels during the catalytic process and maximum activity for a  $\text{Co}_{2.25}\text{Fe}_{0.75_x}\text{O}_4$  spinel.<sup>172</sup> A similar activity increase with Fe doping was observed by Budiyanto et. al.<sup>166</sup> Perovskite catalysts are assumed to be especially active in the OER if they are mixed on the A- and B-site combined.<sup>164,169</sup> A suitable descriptor for the activity was the occupation of the  $e_g$  orbital in perovskites that tunes the B–O binding energy.<sup>175</sup> It was predicted that  $\text{LaFeO}_3$  is less active than  $\text{LaCoO}_3$ ,<sup>176–180</sup> and it is assumed that the covalency of the Co–O bond plays a crucial role in the OER,<sup>181–183</sup> and that oxygen vacancies and high Co spin state stabilization are further important parameters.<sup>176,181,182,184,185</sup>



# 3. Experimental

A detailed experimental section is given in each following chapter. However, the setups used for catalytic experiments and the determination of activity and selectivity are briefly discussed in this chapter. Two different kinds of setups were used, a commercial catalyst analyzer, and a pair of home-built devices that are equipped for multiple catalytic experiments.

## 3.1. BELCAT-B

The majority of CO oxidation experiments was performed using a commercial catalyst analyzer (BELCAT-B, MicrotracBEL Corp., Suminoe-ku, Osaka, Japan). Gas analytics were performed with an online micro gas chromatograph ( $\mu$ GC) 490 (Agilent Technologies, 490, Santa Clara, CA, USA) equipped with a 5 Å molecular sieve and a Pora Plot Q column with helium (He) as the carrier gas. A schematic scheme of the system is shown in Figure 3.1 and was taken as a screenshot from the setups control software.

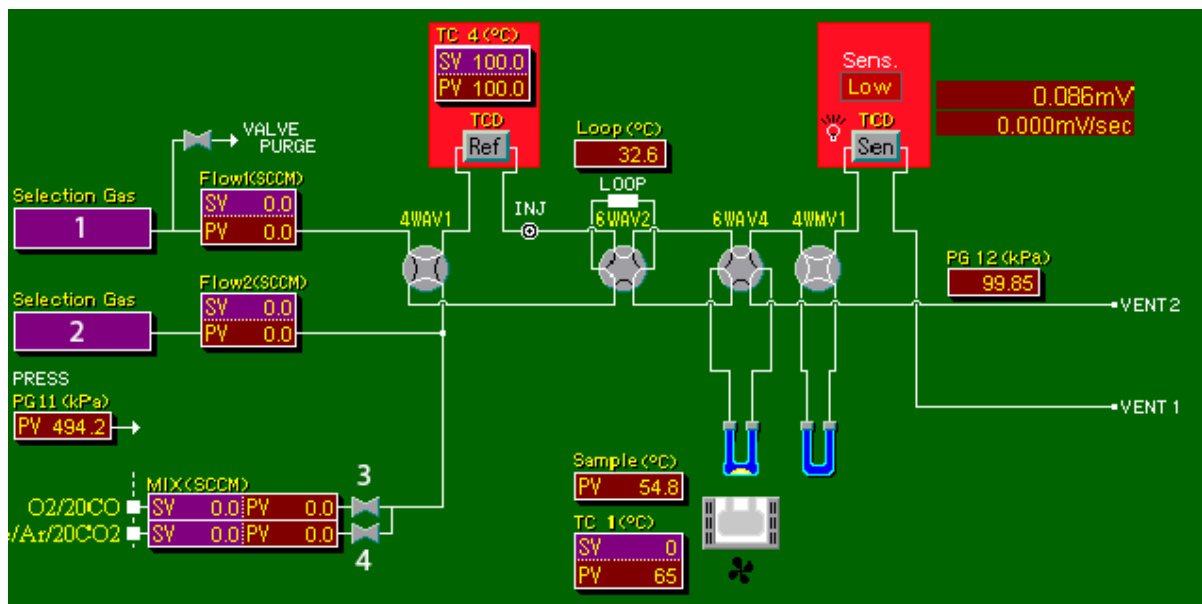


**Figure 3.1:** Screenshot of the user interface of the BELCAT-B system.

The BELCAT provides two different gas streams. One consists of only one mass flow controller (MFC) (1), the second consists of three MFCs. Reactive gas mixtures are passed through the second gas stream. MFC 2 carries a mixture of CO in He, MFC 3 carries O<sub>2</sub> and MFC 4 carries He to dilute the gas mixture. Via a pneumatic 4-way valve, the reaction mixture can either be passed towards the U-shaped quartz reactor or towards a thermal conductivity detector (TCD). If the gas flows towards the reactor, a pneumatic

6-way valve can be switched to set the reactor online which means a flow through the catalyst bed that is placed on a quartz wool support. The reactor is placed inside an oven. The catalyst bed temperature is measured via a thermocouple type K. The gas analytics via  $\mu$ GC is connected to the VENT 1 gas outlet. H<sub>2</sub> TPR experiments are also possible in the BELCAT-B setup and can be monitored via the online TCD. To perform this experiment, a manual 4-way valve should enable the flow of the gas mixture through an U-shaped reactor filled with a molesieve to remove H<sub>2</sub>O formed during the reduction of oxide compounds. The TCD was calibrated using different amounts of copper oxide.

### 3.2. MultiCat

Within this thesis, two similar MultiCat setups were built. All gas-carrying lines are made of stainless steel, the reactor is made of quartz. Goal of the device setup is to allow the execution of gas phase oxidation reactions in a broad range of gas phase compositions containing two different liquids. The used liquids in the scope of this thesis are 2-propanol and H<sub>2</sub>O. Within this study, not only the oxidation of 2-propanol with and without H<sub>2</sub>O was performed in this setup but also the oxidation of CO and the TPR with H<sub>2</sub>. The flow scheme of the setups is shown in Figure 3.2.

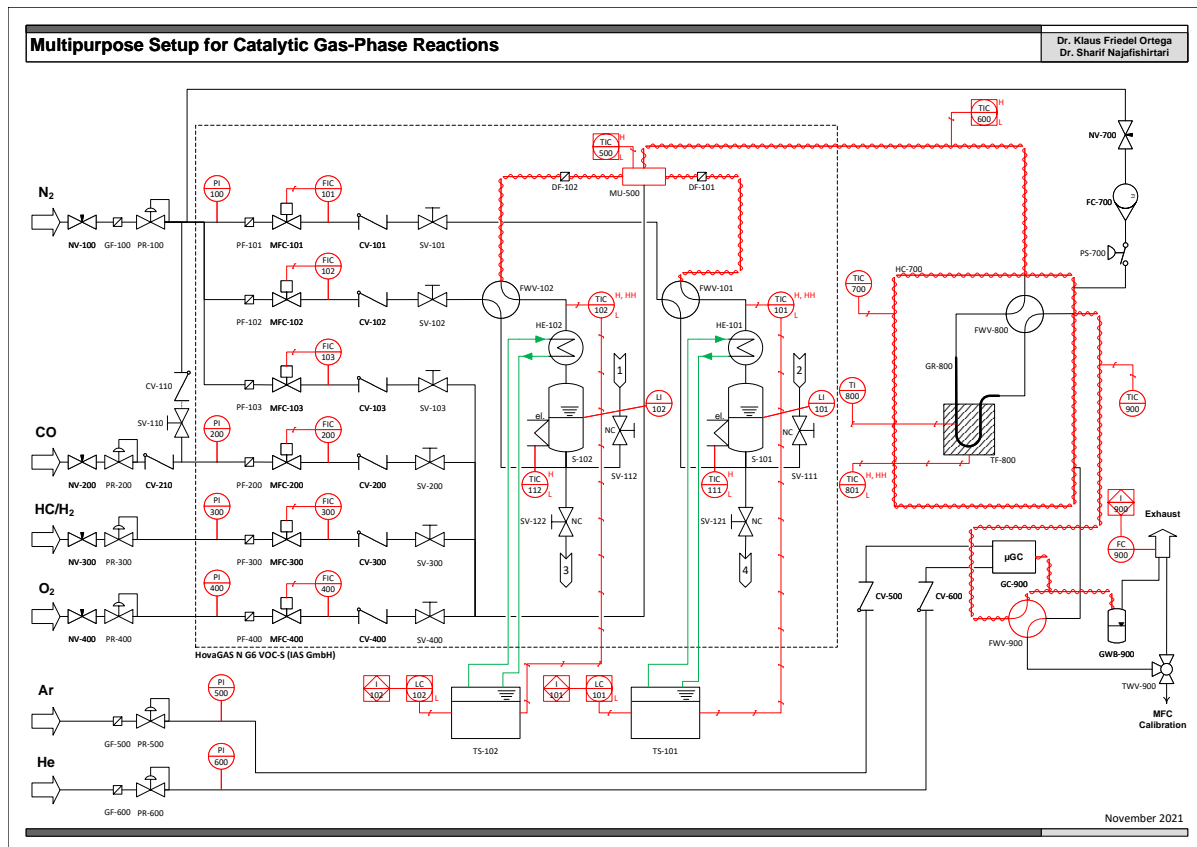


**Figure 3.2:** Piping and Instrumentation Diagram of the MultiCat system.

The gas dosing was performed via a HovaGAS N G6 VOC-S (IAS GmbH, Oberursel, Germany). The dosing unit contains two two-step saturators whose second-step temperature was regulated by a thermostat Ministat 125 (Peter Huber Kältemaschinenbau AG, Offenburg, Germany). The system contains six gas-carrying lines controlled with MFCs, each line equipped with a particle filter to prevent contamination with particles. There are three  $N_2$  streams, two of which are passed through two saturators each filled with either an organic compound (2-propanol) or  $H_2O$ . Via a manual valve, the saturators can be switched online or offline which means gas passing through the saturator or not. From the saturator to the dosing unit outlet, each line is heated to 110 °C. The third  $N_2$  line is mixed with gases coming from three different MFCs. Depending on the experiment performed, the 4<sup>th</sup> MFC carries a mixture of CO in  $N_2$  (CO oxidation) or  $N_2$  (2-propanol oxidation). The 5<sup>th</sup> MFC carries a mixture of  $H_2$  in  $N_2$  for TPR experiments. The oxidizing agent is provided via a 6<sup>th</sup> MFC that is either operated with  $O_2$  (CO oxidation) or synthetic air (2-propanol oxidation). All gas flow rates are controlled by a software provided by the manufacturer IAS GmbH. The three different gas streams are mixed with a cross piece and passed from the dosing unit towards the dosing unit towards the reactor unit.

The quartz reactor is placed inside a silicon carbide tube in a tube furnace MTF 10/25/130 (Carbolite Gero, Neuhausen, Germany). The furnace unit itself is positioned in a heating cabinet Thermocenter TC100 (SalvisLab, Rotkreuz, Switzerland). The temperature of the heating cabinet is set to 40 °C and the heating cabinet is permanently flushed with  $N_2$  at a flow rate of 3 L min<sup>-1</sup>. Via a manual valve, the reactor can be set online or offline which means that the gas is flowing through the reactor and the catalyst bed or bypasses it. The oven temperature is monitored and set via a LabVIEW environment, the temperature is controlled by a EUROTHERM E3216P1 controller. The catalyst bed is supported by a quartz wool plug and the bed temperature is monitored by a type K thermocouple and logged by a PicoLog TC-08 (Pico Technology, St Neots, United Kingdom).

Conversion ( $X$ ), Selectivity ( $S$ ) and yield ( $Y$ ) are determined via an online  $\mu$ GC (Fusion Micro GC, Inficon GmbH Bad Ragaz, Switzerland) equipped with four separation modules (2× Rt-Molsieve 5 Å, 1× Stabilwax DB, 1× Rt-Q Bond). One Rt-Molsieve 5 Å uses argon (Ar) as the carrier gas, to detect He, the other Rt-Molsieve 5 Å column uses He as the carrier gas due to higher sensitivity. The  $\mu$ GC is connected via a T-piece to the line going to the exhaust. In the exhaust region, two gas washing bottles are installed to remove liquids from the gas phase.

For data evaluation, the different files for furnace temperature, reactor temperature and  $\mu$ GC data are merged on their timestamp and  $X$ ,  $S$  and  $Y$  are calculated by a Python data evaluation script. As the initial concentration ( $c_0$ ), the last 4  $\mu$ GC runs in the reaction gas mixture were used.

Several safeguards are implemented into the setup. First, the whole setup is constructed in a housing with permanent ventilation. If the ventilation stops, a flow monitor is triggered and causes a loss of power supply to all devices except for the  $\mu$ GC and line heating. Second, the IAS software prevents feeding an explosive mixture to the reactor by a calculation of the actual concentration. If the actual concentration is within the limits of an explosion triangle for more than 10 s, the flow is stopped automatically. Third, the inside of the heating cabinet is permanently purged with N<sub>2</sub> to prevent danger in case of a broken reactor.

## 4. The Effect of Co Incorporation on the CO Oxidation Activity of $\text{LaFe}_{1-x}\text{Co}_x\text{O}_3$

**Title:** “The Effect of Co Incorporation on the CO Oxidation Activity of  $\text{LaFe}_{1-x}\text{Co}_x\text{O}_3$ ”

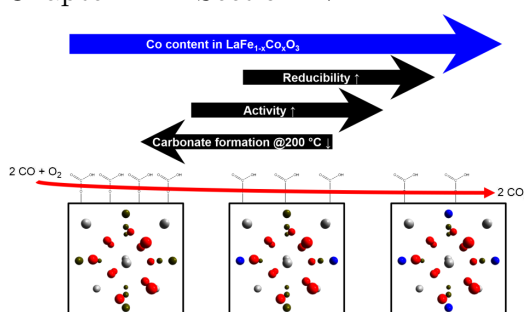
**Authors:** Maik Dreyer, Moritz Krebs, Sharif Najafishirtari, Anna Rabe, Klaus Friedel Ortega, Malte Behrens

**Citation:** Dreyer, M.; Krebs, M.; Najafishirtari, S.; Rabe, A.; Friedel Ortega, K.; Behrens, M., *Catalysts* **2021**, 11 (5), 550.<sup>186</sup>

**DOI:** 10.3390/catal11050550

The Supporting Information can be accessed under <https://www.mdpi.com/2073-4344/11/5/550/s1> and is shown in Chapter A in Section IV.

**Graphical Abstract:**



Maik Dreyer wrote the first manuscript draft and partially prepared the catalyst materials. In addition, he was responsible for and planned the data collection within the in-depth practical course of Moritz Krebs which was summarized in the report “Synthesis of Hydroxycarbonates and Perovskites of the Lanthanum Iron Cobalt System by co-precipitation” and performed the evaluation of particle sizes, catalytic data and XRD as well as the integration of the DRIFTS data. Sharif Najafishirtari performed the DRIFTS experiments and their evaluation and contributed by reading and editing the paper. Anna Rabe took care of the Rietveld analysis, and contributed by reading and editing the paper. Klaus Friedel Ortega participated in conceptualization, reading and editing. Malte Behrens acquired the funding, conceptualized and supervised the work, and contributed by reading and editing.

The work was reprinted without changes under the Creative Commons 4.0 International (CC BY 4.0) licence. © 2021 by the authors. Licensee MDPI, Basel, Switzerland.



Article

## The Effect of Co Incorporation on the CO Oxidation Activity of LaFe<sub>1-x</sub>Co<sub>x</sub>O<sub>3</sub> Perovskites

Maik Dreyer <sup>1</sup>, Moritz Krebs <sup>1,2</sup>, Sharif Najafishirtari <sup>1</sup> , Anna Rabe <sup>1</sup> , Klaus Friedel Ortega <sup>2</sup> and Malte Behrens <sup>1,2,3,\*</sup>

<sup>1</sup> Faculty for Chemistry, Inorganic Chemistry, University of Duisburg-Essen, 45141 Essen, Germany; maik.dreyer@uni-due.de (M.D.); mkrebs@ac.uni-kiel.de (M.K.); sharif.najafishirtari@uni-due.de (S.N.); anna.rabe@uni-due.de (A.R.)

<sup>2</sup> Institute for Inorganic Chemistry, Christian-Albrechts-Universität zu Kiel, 24118 Kiel, Germany; kfriedel@ac.uni-kiel.de

<sup>3</sup> CENIDE, Center for Nanointegration, University of Duisburg-Essen, 47057 Duisburg, Germany

\* Correspondence: mbehrens@ac.uni-kiel.de

**Abstract:** Perovskite oxides are versatile materials due to their wide variety of compositions offering promising catalytic properties, especially in oxidation reactions. In the presented study, LaFe<sub>1-x</sub>Co<sub>x</sub>O<sub>3</sub> perovskites were synthesized by hydroxycarbonate precursor co-precipitation and thermal decomposition thereof. Precursor and calcined materials were studied by scanning electron microscopy (SEM), attenuated total reflection Fourier transform infrared spectroscopy (ATR-FTIR), thermogravimetric analysis (TG), and X-ray powder diffraction (XRD). The calcined catalysts were in addition studied by transmission electron microscopy (TEM) and N<sub>2</sub> physisorption. The obtained perovskites were applied as catalysts in transient CO oxidation, and in operando studies of CO oxidation in diffuse reflectance infrared Fourier transform spectroscopy (DRIFTS). A pronounced increase in activity was already observed by incorporating 5% cobalt into the structure, which continued, though not linearly, at higher loadings. This could be most likely due to the enhanced redox properties as inferred by H<sub>2</sub>-temperature programmed reduction (H<sub>2</sub>-TPR). Catalysts with higher Co contents showing higher activities suffered less from surface deactivation related to carbonate poisoning. Despite the similarity in the crystalline structures upon Co incorporation, we observed a different promotion or suppression of various carbonate-related bands, which could indicate different surface properties of the catalysts, subsequently resulting in the observed non-linear CO oxidation activity trend at higher Co contents.



**Citation:** Dreyer, M.; Krebs, M.; Najafishirtari, S.; Rabe, A.; Friedel Ortega, K.; Behrens, M. The Effect of Co Incorporation on the CO Oxidation Activity of LaFe<sub>1-x</sub>Co<sub>x</sub>O<sub>3</sub> Perovskites. *Catalysts* **2021**, *11*, 550. <https://doi.org/10.3390/catal11050550>

Academic Editor: Simone Mascotto

Received: 31 March 2021

Accepted: 26 April 2021

Published: 27 April 2021

### 1. Introduction

Perovskites ABO<sub>3</sub> are exciting materials for oxidation catalysis as they provide considerable flexibility regarding their compositions and the possibility to implement oxygen vacancies with a selective modification of the cationic sublattice [1–3]. The potential use of perovskites in catalysis is extensive as they can be employed, e.g., in oxygen reduction [4], oxygen evolution [5], CO and hydrocarbon gas-phase oxidation [6], total oxidation of Volatile Organic Compounds (VOC) [7], or selective oxidation of substrates like benzyl alcohol [8] or cinnamyl alcohol [9]. These materials are accessible through a variety of synthetic approaches, such as ceramic methods [10,11], complexation with, e.g., citric acid followed by thermal decomposition [12,13], freeze-drying [14], spray-flame synthesis [15,16], or co-precipitation at increasing pH [17], decreasing pH [18], with manually adjusted constant pH [19] or automatically controlled constant pH [20]. Often, precursor compounds are formed at low temperatures. For crystallization of the material, thermal treatment of at least 500 °C is necessary [1]. Perovskite oxides with lanthanum (La) as the A-site cation



**Copyright:** © 2021 by the authors. Licensee MDPI, Basel, Switzerland. This article is an open access article distributed under the terms and conditions of the Creative Commons Attribution (CC BY) license (<https://creativecommons.org/licenses/by/4.0/>).

and cobalt (Co) and iron (Fe) as the B-site cations have been synthesized via thermal decomposition of propionates [21], the Pechini method [22], or the sol-gel approach [23]. The synthesis of LaFe<sub>x</sub>Co<sub>1-x</sub>O<sub>3</sub> via co-precipitation assisted by microwaves has been reported [24]. Another synthesis route to LaFeO<sub>3</sub> follows a solid-state reaction between Ancylite (La<sub>2</sub>(CO<sub>3</sub>)<sub>2</sub>(OH)<sub>2</sub>) and Fe<sub>2</sub>O<sub>3</sub> [25].

Since Fe and Co are abundant elements, there is motivation to incorporate them as B-site cations in perovskites to obtain active and thermally stable catalysts that do not require noble metals. Furthermore, the perovskite structure is tolerant to the formation of anionic and cationic vacancies, which can tune the catalytic properties of the materials. It has been shown that an increasing Co content in LaFe<sub>1-x</sub>Co<sub>x</sub>O<sub>3</sub> perovskites leads to enhanced catalytic activity, e.g., in VOC oxidation [7,26], soot combustion [27], and exhaust gas decomposition [23]. In NO and N<sub>2</sub>O containing atmosphere, a pronounced effect of incorporating Co into the perovskite structure has been found, but there was no linear scaling of the activity in N<sub>2</sub>O conversion with the Co content for a NO concentration of 0.5% in the feed. In a feed containing a tenfold higher NO concentration, however, such a trend was observable with LaCo<sub>0.8</sub>Fe<sub>0.2</sub>O<sub>3</sub> being the most active catalyst [23].

The oxygen activation and dissociation capabilities at perovskite surfaces are strongly correlated to the composition and number of oxygen vacancies [28,29]. It has been shown that such vacancies can promote the formation of monoatomic oxygen (O<sup>-</sup>), which would act as the primary type of oxygen in the system [30]. One straightforward approach to determine catalytic activity and oxygen activation capability is the CO oxidation reaction as a prototypical reaction for heterogeneous processes [31]. The reaction only has a single gaseous product, which interacts with metal oxides either strongly or weakly. For Co<sub>3</sub>O<sub>4</sub>, no adsorption of CO<sub>2</sub> on the surface was found [32], whereas an adsorption capacity has been reported for Al<sub>2</sub>O<sub>3</sub> [33]. Furthermore, this reaction pathway is involved in the total oxidation mechanism of hydrocarbons and oxygenated molecules, which leads to a decrease in selectivity towards valuable intermediates. The effect of Co incorporation into oxides and LaFeO<sub>3</sub> perovskite on CO oxidation catalysis has also attracted attention. For example, including only 1% Co has been shown to increase the CO oxidation activity of NiO significantly, but no steady conversion increase with Co incorporation has been observed [34]. On Sr- and Co-doped LaFeO<sub>3</sub>, extrema at intermediate Co level were observed for transition metal surface content, oxygen storage capacity, reducibility, and methanol oxidation activity [35].

In this work, we report on the synthesis of a series of LaFe<sub>1-x</sub>Co<sub>x</sub>O<sub>3</sub> perovskites with  $0 \leq x \leq 0.30$  derived from amorphous precursors containing the corresponding Fe:Co ratios. The catalysts were prepared by constant-pH co-precipitation according to a procedure previously reported [20]. Furthermore, we systematically studied the activities of the synthesized materials in CO oxidation. We tracked the product evolution during CO oxidation by operando diffuse reflectance infrared Fourier transform spectroscopy (DRIFTS) to gain insights into changes of the surface properties induced by Co incorporation.

## 2. Results

### 2.1. Co-Precipitation and Precursor Characterization

Syntheses were conducted in a semi-automatized laboratory workstation for co-precipitation, and the parameters were precisely controlled. Computer-controlled simultaneous dosing of the metal salt solution and the basic precipitating agent allowed to maintain a constant pH during co-precipitation. Temperature, pH, and dosage of the metal salt solution were monitored. The corresponding synthesis protocols of the series during co-precipitation are displayed in Figures S1–S7 in the Supplementary Material. The pH values at the beginning of the dosing showed a small offset, which decreased with time as the buffer system was formed in the suspension. Figure 1a shows an exemplarily SEM image of the washed and dried co-precipitate with  $x = 0.05$ . An overview of SEM images of the complete sample series is shown in Figure S8. Aggregates of small and relatively uniform spherical particles in the 50–60 nm range are visible, although the particles in the

calcined samples appear to be sintered to some extent. The sample morphology can be described as a sponge-like network (also note the similarity between the  $x = 0.20$  and  $0.30$  despite having different Co contents). An increase of the Co content beyond a threshold of  $x = 0.10$  favors the formation of larger plate-like structures with sizes of  $100\text{--}300\text{ nm}$ , which is shown as an example for  $x = 0.15$  with arrows pointing towards anisotropic regions in Figure 1b.

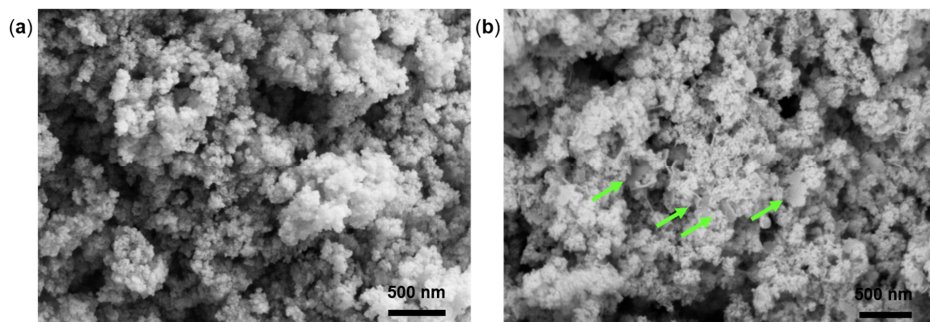


**Figure 1.** (a) SEM image of the  $x = 0.05$  sample after co-precipitation, washing, and drying. (b) The SEM image of the sample with  $x = 0.15$  shows the formation of hexagonal platelet structures, highlighted by green arrows.

The X-ray powder patterns of the co-precipitated particles are shown in Figure 2a. The particles are X-ray amorphous as similarly reported for a hydroxycarbonate precursor employed in the synthesis of co-precipitated precursors used to obtain LaNiO<sub>3</sub> [19]. With increasing Co content, already at a nominal value of  $x = 0.10$ , a hydrotalcite-like structure is additionally formed as inferred from the low-intensity (003) reflection of the CoFe-hydrotalcite at  $2\theta = 12^\circ$  (ICSD reference for MgAl-LDH: 6296 [36]), which is more pronounced for sample  $x = 0.30$ . This observation is well in line with larger plate-like structures encountered during SEM analysis. However, based on the weak intensity of the (003) reflection, the total amount of the impurity is considerably low. This finding is supported by the negligible fraction of hexagonal platelet structures encountered in a minority of the SEM images. The actual Co contents in the precipitates determined by AAS are lower than the nominal values, as shown by the parity plot Figure 2b. As this deviation scales with the Co content, a possible cause is an under-estimated degree of hydration of the Co nitrate salt used in the synthesis resulting in a systematic error during the reactant weighing.

In ATR-FTIR spectroscopy shown in Figure 2c, characteristic absorption bands of hydroxyl and carbonyl groups can be seen as comparable to those found for La(OH)CO<sub>3</sub> in literature [37]. The broad band at  $3375\text{ cm}^{-1}$  corresponds to stretching and bending vibrations of hydroxyl groups, whereas the band at  $1640\text{ cm}^{-1}$  is representative for molecular interlayer water molecules [38]. Carbonate ion modes are present at  $1070\text{ cm}^{-1}$  ( $\nu_1$ ),  $850\text{ cm}^{-1}$  ( $\nu_2$ ),  $1470$  and  $1390\text{ cm}^{-1}$  ( $\nu_3$ ) as well as  $730$  to  $690\text{ cm}^{-1}$  ( $\nu_4$ ) [37,38]. Below  $700\text{ cm}^{-1}$ , the vibrations of hydroxide and oxide bonds can be seen [39]. In Figure S9a, the wavenumbers at the position of the corresponding transmission minimum are displayed. A steady shift towards higher wavenumbers with increasing Co content is visible at around  $447\text{ cm}^{-1}$ . However,  $x = 0.15$  is an outlier featuring the lowest wavenumber of the minimum. In literature, a similar trend is found for Co-Fe-hydroxycarbonates which is explained by a weaker force constant of the Co(II)-O bond compared to the Fe(III)-O bond [39]. With increasing Co content, the intensity at the transmission minimum in the M-OH and M-O region ( $<580\text{ cm}^{-1}$ ) remains nearly constant, as can be seen in Figure S9b.

Thermogravimetric analysis of the precursors in a 21% O<sub>2</sub>/Ar atmosphere is shown in Figure 2d. A steady mass loss can be seen for all samples attributed to the evolution of

H<sub>2</sub>O followed by a two-step CO<sub>2</sub> formation, as reported by Kühl et al. [20]. The last abrupt mass loss was attributed to a sharp CO<sub>2</sub> evolution in the temperature range of 580 °C to 620 °C depending on the Co content. The mass remains stable above 650 °C with an overall mass loss of about 25%. No extra mass loss indicating the formation of a secondary phase upon calcination is detected. Even for the highest Co content ( $x = 0.30$ ), no characteristic mass loss at 900 °C for the thermal reduction of a potential Co<sub>3</sub>O<sub>4</sub> by-phase to CoO can be seen [40].

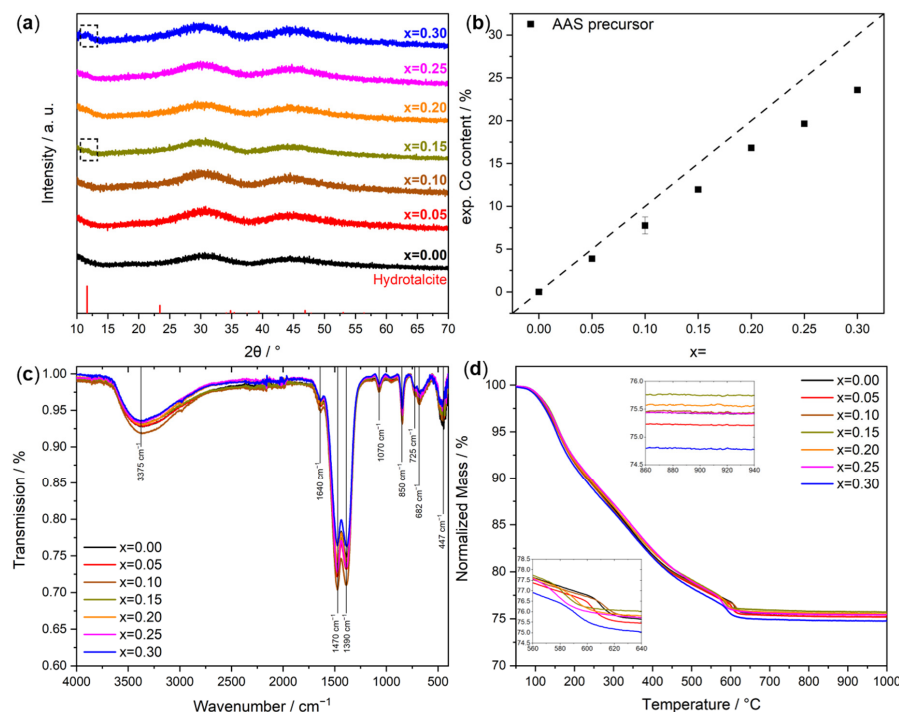


**Figure 2.** (a) XRD powder patterns of the as-prepared sample series. (b) Co contents in the samples before calcination. (c) ATR-FTIR spectra of the samples before calcination. (d) Thermogravimetry mass losses.

## 2.2. Catalyst Characterization

After thermal decomposition of the amorphous precursors during calcination at 800 °C, XRD powder patterns were recorded. The corresponding diffractograms, shown in Figure 3a, are compared to orthorhombic LaFeO<sub>3</sub> (ICSD: 93611 [41]) with indications of the most intensive (hkl) assignments. The patterns can be fully described by the one calculated for the perovskite structure, which further confirms the absence of secondary crystalline phases. The reflections are shifted to higher angles with increasing Co content, which is indicative of the incorporation of Co into the crystal structure. This is related to replacing Fe accompanied by a decrease of the d-spacing associated with the smaller effective ionic radius of low-spin Co<sup>3+</sup> (0.545 Å) compared to Fe<sup>3+</sup> (0.645 Å) in the high-spin configuration [42], which in the latter case is the ground state electronic structure of octahedrally coordinated trivalent Fe cations in LaFeO<sub>3</sub> [43]. The formation of phase-pure perovskites from non-phase-pure materials is known, which is relevant to consider in view of the hydrotalcite-like by-phase encountered for higher Co contents in the precursor

stage. For example, the formation of phase-pure LaFeO<sub>3</sub> was reported as well from Fe<sub>2</sub>O<sub>3</sub> and La<sub>2</sub>(CO<sub>3</sub>)<sub>2</sub>(OH)<sub>2</sub> [25]. As the homogeneity of the amorphous precursor is unknown, and a hydrotalcite-like by-phase was observed in some samples, perovskite formation from a multi-phase precursor system must also be assumed for our synthesis approach.

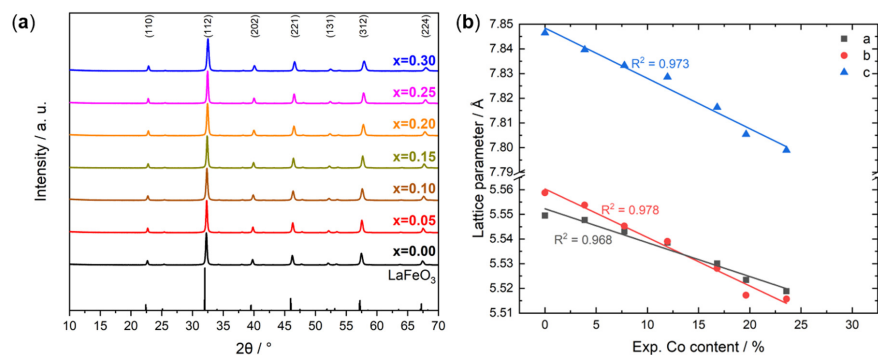


**Figure 3.** (a) XRD powder patterns of the samples after calcination. (b) Lattice parameters of the samples from Rietveld refinement plotted against the experimental Co content.

A plot of the lattice parameters derived from Rietveld refinement [44] with increasing Co content is shown in Figure 3b. The encountered trend is in line with the qualitative analysis of changes in the d-spacing upon isomorphic transition metal cation substitution. As expected, lattice parameters decrease monotonously with increasing the degree of Co substitution, which is in agreement with Vegard's law [21,23]. Meanwhile, the refinement results are reported in Table 1. The crystallite size was determined as the volume-weight mean column height from integral breadth, the obtained sets of Rietveld fit parameters are summarized in Table S1. The corresponding plots are shown in Figure S10. This quantitative analysis further supports the phase purity of the samples.

**Table 1.** Characterization data of the samples after calcination, including Rietveld refinement, surface area, pore-volume, and particle size. The crystallite size was determined as the volume-weight mean column height from integral breadth.

x =	a [Å]	b [Å]	c [Å]	Cell Volume [Å <sup>3</sup> ]	Crystallite Size (LVol-IB) [nm]	SA <sub>BET</sub> [m <sup>2</sup> g <sup>-1</sup> ]	Pore Volume [cm <sup>3</sup> g <sup>-1</sup> ]	Particle Size (TEM) [nm]	Particle Size (SEM) [nm]
0.00	5.5494 (7)	5.5587 (2)	7.8464 (6)	242.0473	46.6	16	0.13	32.4 ± 14.5	51.2 ± 8.6
0.05	5.5477 (0)	5.5537 (6)	7.8396 (2)	241.5441	45.7	18	0.12	35.1 ± 11.9	49.4 ± 9.5
0.10	5.5429 (5)	5.5452 (7)	7.8332 (7)	240.7734	33.2	24	0.16	26.4 ± 7.8	41.9 ± 7.5
0.15	5.5385 (1)	5.5390 (2)	7.8286 (1)	240.1664	34.4	17	0.16	29.5 ± 10.2	58.7 ± 9.7
0.20	5.5300 (8)	5.5280 (7)	7.8163 (2)	238.9508	32.3	18	0.15	36.6 ± 10.0	42.2 ± 7.6
0.25	5.5234 (3)	5.5172 (5)	7.8054 (2)	237.8637	45.4	15	0.04	53.3 ± 15.9	78.2 ± 11.9
0.30	5.5188 (9)	5.5157 (3)	7.7989 (8)	237.4070	33.8	25	0.26	39.6 ± 10.8	48.2 ± 7.2

The mostly spherical particle morphology remains unchanged upon calcination, as confirmed by SEM analysis. Figure 4a shows the isotropic character of the particles corresponding to sample x = 0.05, which have a mean diameter of 50 nm. This value is in good agreement with the crystallite size derived from XRD analysis. Differences are still to be expected as the calculated values are attributed to the size of the coherently diffracting domains, which are not necessarily equal to the crystallite size. SEM images of the entire sample series in the as-prepared and calcined state are shown in Figure S8. After calcination, the samples still show a spongy morphology, but x = 0.20 and x = 0.25 had a slightly more sintered structure, while x = 0.00 and x = 0.30 maintain their visual similarity. The corresponding

particle size distributions in the calcined state are depicted in Figure S11. The particles appear to be partially sintered after calcination, which is also visible in the TEM image of sample  $x = 0.05$  (Figure 4b). TEM images of the perovskite series are summarized in Figure S12. Particle size distributions derived from a detailed TEM evaluation are depicted in Figure S13. The analysis shows that the mean particle size changes, although the broadening of the statistical distribution is comparable within the sample series.

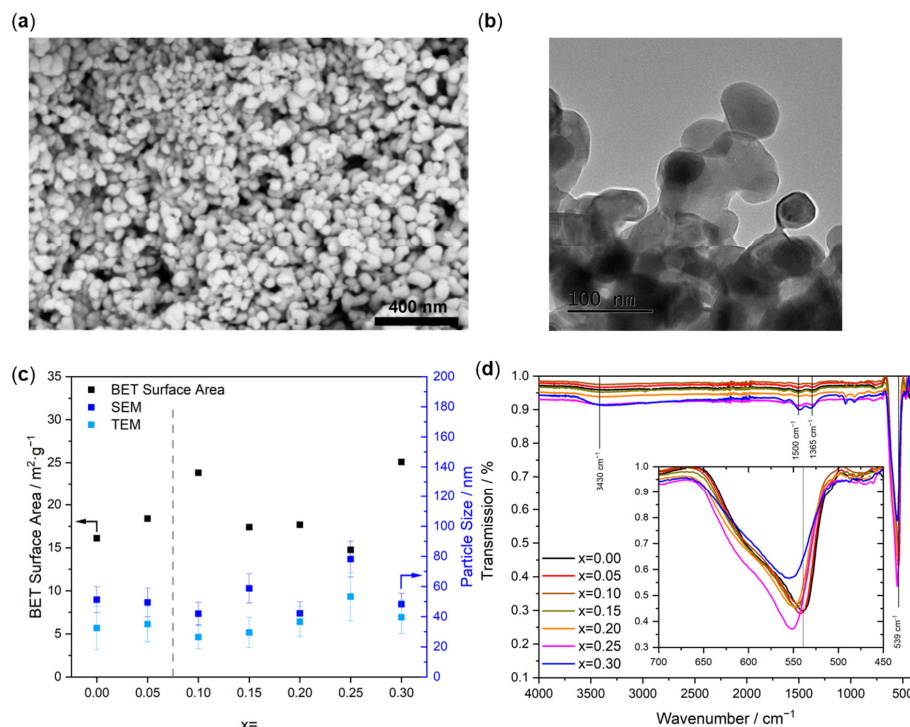


**Figure 4.** (a) SEM image of the sample with  $x = 0.05$  after calcination. (b) TEM image of the sample with  $x = 0.05$  after calcination. (c) BET surface areas compared to the particle diameters. (d) ATR-FTIR spectra of the samples after calcination.

Evidently, the individual roundish particles are not dispersed but appear fused due to sintering. HR-TEM analysis (Figure S12) further confirms the high degree of crystallinity of the obtained perovskites as expected from the sharp reflections in the corresponding XRD patterns. The particles mostly exhibit isotropic faceted shapes.

The average particle sizes determined by SEM and TEM are shown in Figure 4c. The diameters are similar for all samples, with systematically slightly larger values seen in SEM. Evidently, the mean particle size is not affected by the isomorphic substitution of Fe with Co into the crystal structure. TEM particle sizes are in the range of 30 nm to 53 nm, whereas the SEM particle size is determined in a range from 48 to 70 nm. The difference might be an effect of the lower resolution of the SEM image, making a differentiation between single and fused particles challenging. The BET surface areas are inversely following the differences in particle sizes as observed in SEM and TEM, indicating low porosity of the agglomerates. Nitrogen adsorption-desorption isotherms, which are characterized by a type IVa hysteresis loop, are shown in Figure S14. The corresponding pore size distributions, which were obtained applying the BJH method on the desorption branch of the

isotherms, are depicted in Figure S15. A bimodal pore size distribution can be seen with some minor pores inside the particles and the majority of the pores in the range of 20 nm, indicating mainly interparticle voids. The sample with  $x = 0.10$  shows the smallest particle size and the second highest BET surface area of around  $24 \text{ m}^2 \text{ g}^{-1}$ .

ATR-FTIR spectra of the perovskites are depicted in Figure 4d, showing the remaining hydroxide ( $3430$  and  $1500 \text{ cm}^{-1}$ ) and carbonate bands ( $1365 \text{ cm}^{-1}$ ) [37,38]. As TG in Figure 2d did not show any mass loss at higher temperatures than  $800^\circ\text{C}$ , these bands can be attributed to the re-adsorption of H<sub>2</sub>O and CO<sub>2</sub> from the atmosphere. Samples  $x = 0.10$ ,  $x = 0.20$  and  $x = 0.30$  show additional bands at  $1050 \text{ cm}^{-1}$ . In the metal oxide vibration region, the bands became more pronounced below  $600 \text{ cm}^{-1}$  than before the thermal treatment. The maximum for the LaFeO<sub>3</sub> perovskites is observed at  $539 \text{ cm}^{-1}$  and confirms the presence of FeO<sub>6</sub> octahedra and their characteristic Fe-O stretching vibration. The maximum band position is shifted to higher wavenumbers with increasing Co content in the calcined state, as displayed in Figure S9a. The shift indicates a distortion in the orthorhombic perovskite structure upon introducing Co<sup>3+</sup> ions, which affects the Fe-O bond strength [45]. The bond strength argument is backed up by temperature-programmed reduction (H<sub>2</sub>-TPR). The reduction of Fe<sup>3+</sup> to Fe<sup>0</sup> in LaFeO<sub>3</sub> is described in the literature as a two-step mechanism that takes place at temperatures above  $800^\circ\text{C}$  [46]. However, reduction phenomena have also been reported at considerably lower temperatures, which have been ascribed to an increased oxygen release from Fe-Co-perovskites [47,48].

H<sub>2</sub>-TPR curves are shown in Figure S16a, which show a two-step reduction behavior in a lean hydrogen atmosphere (7% H<sub>2</sub>/N<sub>2</sub>). For LaFeO<sub>3</sub>, a first smaller reduction peak is observed at  $420^\circ\text{C}$ , followed by a pronounced maximum at  $892^\circ\text{C}$ . For all Co containing samples, the position of the first maximum is shifted to lower temperatures by at least  $34^\circ\text{C}$  compared to LaFeO<sub>3</sub>. The shift proves the enhanced reducibility of the perovskite structure in the presence of Co in the temperature range below  $500^\circ\text{C}$ , but there is no linear correlation between the Co content and the peak position, as highlighted in Figure S16b. The reducibility in the low-temperature region shows the following order in  $x$ :  $0.15 > 0.05 > 0.25 > 0.10 > 0.20 > 0.30 > 0.00$ . In contrast, the second maximum shifts to higher temperatures with Co incorporation, while similar to the first maximum, the second does not show a clear correlation with Co content.

A similar non-linear behavior in the high-temperature region upon cation substitution has also been observed on La<sub>1-x</sub>Sr<sub>x</sub>FeO<sub>3</sub> perovskites, which was attributed to increased consumption of surface oxygen at lower temperatures originating from enhanced oxygen mobility upon Sr incorporation [48]. As a consequence, the oxygen availability at higher temperatures decreases and results in the shift of the second maximum to higher temperatures [48]. For samples with a higher oxygen activation barrier, the low-temperature peak is less pronounced, while the availability of easier-to-reduce oxygen species at higher temperatures is increased [48].

In terms of Co incorporation into LaFe<sub>1-x</sub>Co<sub>x</sub>O<sub>3</sub> perovskites, the ratio of lattice oxygen to adsorbed oxygen decreases, resulting in higher total oxidation activity in CH<sub>4</sub> oxidation [3]. Furthermore, Zhao et al. attributed the two-step reduction of perovskites to the stepwise reduction of adsorbed oxygen accompanied by Fe<sup>4+</sup> to Fe<sup>3+</sup> reduction and Co<sup>3+</sup> to Co<sup>2+</sup> followed by total bulk reduction of reducible cations [3].

### 2.3. CO Oxidation Activity

Temperature-programmed CO oxidation reaction was performed in the temperature range between room temperature and  $500^\circ\text{C}$ . Conversions as a function of reaction temperature are shown in Figure 5a. The reaction rates normalized by the BET surface area were calculated up to a conversion of 65% and plotted in Figure 5b. A pronounced increase in CO oxidation rate was observed in our experiments by Co incorporation as low as 5% into the perovskite structure, lowering the  $T_{50}$  by  $42^\circ\text{C}$ . An even stronger effect was observed during CO oxidation upon the incorporation of small amounts of Co into NiO [34]. Thus, a positive impact on the catalytic activity in the presence of Co is expected. Co<sup>3+</sup> acts as

an active site for CO adsorption, while Co<sup>2+</sup> at oxygen vacancies preferentially adsorbs molecular oxygen, as was shown for LaCoO<sub>3</sub> perovskites [49].

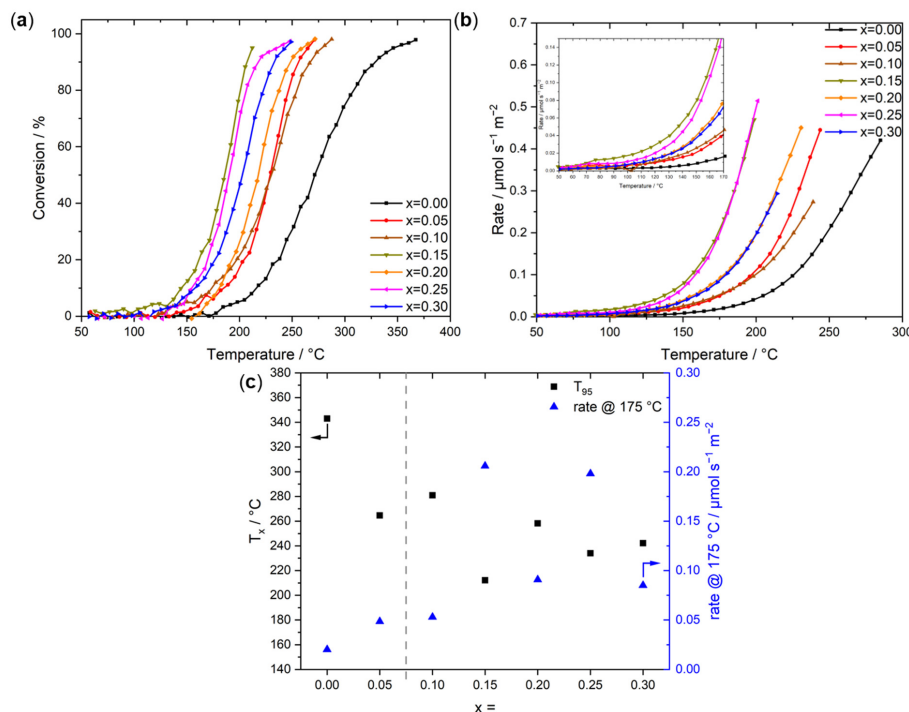


**Figure 5.** (a) CO oxidation conversions of the perovskites from 50 to 500 °C in the reaction mixture of 2% CO + 20% O<sub>2</sub> balanced in He. (b) Rates of the sample series up to a conversion of 65% in the same reaction mixture. (c) Comparison between CO oxidation conversions for 95% conversion and rates at 175 °C derived from (a,b).

Interestingly, after this activity boost, neither the conversion nor the reaction rate linearly follows the Co incorporation. Regarding conversion,  $x = 0.15$  and  $x = 0.25$  are the most active samples, followed by  $x = 0.30$ . After rate-normalization, the curves for  $x = 0.15$  and  $x = 0.25$  converge as well as the curves for  $x = 0.20$  and  $x = 0.30$ . A similar non-linear scaling of the activity with the Co content was observed for exhaust gas decomposition containing NO and N<sub>2</sub>O on LaFe<sub>x</sub>Co<sub>1-x</sub>O<sub>3</sub> [23] and CO oxidation on Co-doped NiO [34]. Furthermore, on Sr- and Co-doped LaFeO<sub>3</sub>, extrema at intermediate Co contents were found for the methanol oxidation activity [35]. For the two samples emerging from the purely amorphous precursor without minor contributions from the anisotropic CoFe-LDH by-phase ( $x = 0.00$  and  $x = 0.05$ ), the activity increase with Co incorporation is evident, as discussed before. Nonetheless, several factors such as surface termination, surface composition, and oxygen vacancies should be taken into account to understand the non-linear change in activity with a variation of the Co content. A more detailed structural analysis is needed to address this effect. Interestingly, TPR indicates a strong correlation between the position of the reduction peak below 500 °C and the catalytic activity. The catalysts  $x = 0.15$  and  $x = 0.25$  are easier to reduce under reaction conditions compared to  $x = 0.20$  and  $x = 0.30$  and more active in the catalytic oxidation of CO.

When comparing the temperatures of 95% conversion ( $T_{95}$ ) within the series as shown in Figure 5c, the same behavior as before becomes evident. The incorporation of only small

Co amounts increases the activity drastically, whereas  $x = 0.15$  shows the lowest  $T_{95}$  followed by  $x = 0.25$  and  $x = 0.3$ . In the literature, a temperature of 95% conversion ( $T_{95}$ ) is not expected before 500 °C for LaFeO<sub>3</sub>, which is higher than our result of 343 °C [50]. However, there are also examples showing  $T_{90}$  values of 400 °C [51], of about 370 °C [52], or near 430 °C [53]. This gap, however, might be related to differences in the experimental conditions of the catalytic testing in terms of CO concentrations and GHSVs. In comparison to LaFeO<sub>3</sub> catalysts from spray-flame synthesis, the exposed BET surface area in the presented study is decreased by a factor of 5 for reported high surface area catalysts and comparable to low surface area catalysts [15]. The activity at 300 °C of about 73% for the sample derived from a co-precipitated precursor is increased compared to the sample obtained by spray-flame synthesis, which featured at least 30% conversion in a less oxidizing atmosphere (3% CO, 6% O<sub>2</sub>). Here, we compare our results to a study in which different amounts of ethanol as fuel were used during gas-phase synthesis. After rate-normalization, LaFeO<sub>3</sub> synthesized in this study features 0.493 μmol s<sup>-1</sup> m<sup>-2</sup>, whereas the spray-flame synthesized materials show rates of 0.302 (pure EtOH, 15 m<sup>2</sup> g<sup>-1</sup>), 0.117 (35% EtOH, 92 m<sup>2</sup> g<sup>-1</sup>), and 0.075 μmol s<sup>-1</sup> m<sup>-2</sup> (50% EtOH, 89 m<sup>2</sup> g<sup>-1</sup>) at 300 °C [15].

For the rate comparison at 175 °C Figure 5c, a general trend towards higher activity can be observed as a function of the Co content with the exceptions of  $x = 0.15$  and  $x = 0.25$ , which show extraordinarily high activities.

In Figure S17a, transient CO oxidation curves of two batches of  $x = 0.00$  are shown. A good reproducibility of the conversion profile can be seen even among different synthesis batches. The observed offset for  $T_{50}$  and  $T_{95}$  was 7.2 °C and 12.3 °C, respectively, which is considered as an error bar estimation also for the other syntheses and measurements. In addition, we performed a reusability test of the same batch ( $x = 0.00$ ), which is shown in Figure S17b. Prior to each reproduction run, a temperature-programmed oxidation (TPO) up to 300 °C in 20% O<sub>2</sub> and N<sub>2</sub> was performed. After the oxidative treatment, the activity was slightly enhanced compared to the initial activity, which can be explained by surface cleaning and oxygen adsorption. The two runs after a TPO perfectly overlap, which proves the reproducibility of the results as well as the re-usage stability of the catalysts under these reaction conditions.

Additionally, the stabilities with time on stream of the samples  $x = 0.00$  and  $x = 0.25$  were investigated under steady conditions at 200 °C. The results are displayed in Figure S17c. The stability measurement of  $x = 0.00$  indicates the pre-treated catalyst goes through a short period of deactivation but reaches a steady state after 6 h of exposure to the reaction mixture. In the deactivation period, a loss in conversion from 16.3% to 7.6% could be observed. The  $x = 0.25$ , on the other hand, showed only a slight deactivation from 99% to 95.6%, after which it reached the steady-state conversion. The decrease in conversion is thus less pronounced for  $x = 0.25$  compared to  $x = 0.00$  at the same temperature, suggesting that the addition of Co does not only help the activity but also has a positive effect on stability.

#### 2.4. Operando DRIFTS during CO Oxidation

In order to investigate the surface properties of the catalysts, samples with nominal Co contents of  $x = 0.00$ ,  $x = 0.05$ ,  $x = 0.20$ ,  $x = 0.25$ , and  $x = 0.30$  were studied in the CO oxidation monitored by Diffuse Reflectance Infrared Fourier Transform Spectroscopy (DRIFTS). The selected samples include the least active catalyst ( $x = 0.00$ ) and three samples with similar activities despite different Co contents ( $x = 0.05$ ,  $x = 0.20$ ,  $x = 0.30$ ), and one sample with extraordinarily high activity ( $x = 0.25$ ). Initially, the DRIFTS spectra during a transient experiment were collected while the catalyst was exposed to the reaction mixture. The spectra at selected temperatures are illustrated in Figure 6a for  $x = 0.25$ , as one of the most active samples when looking at the normalized rate, and for other samples in Figure S18a–d.

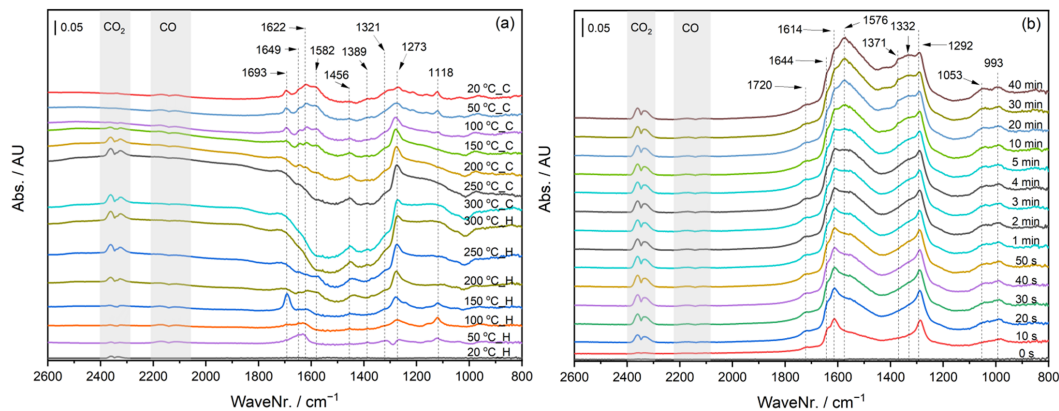


**Figure 6.** (a) DRIFTS spectra of sample  $x = 0.25$  exposed to the reaction mixture of 0.2% CO + 2% O<sub>2</sub> balanced in He, after a He-treatment at 150 °C during a transient experiment (b) DRIFTS spectra of sample  $x = 0.25$  exposed to the reaction mixture of 0.2% CO + 2% O<sub>2</sub> balanced in He, after an oxidative treatment during 40 min of steady-state condition at 200 °C.

The progressive formation of CO<sub>2</sub> at higher temperatures can be observed in all cases by the intensity of the gas-phase CO<sub>2</sub> bands. However, it is not straightforward to internally compare the spectra due to different absorption intensities and the bending of the baseline at higher temperatures (also note the difference in the scale bars of the graphs). The activity significantly changes by incorporating Co, as observed in the catalytic experiments. It can be qualitatively compared by the intensity of the gas-phase CO vs. CO<sub>2</sub> among the samples, which is in line with the MS signal (not shown). Several bands were observed below 1710 cm<sup>-1</sup>, which can be related to symmetric and asymmetric vibration of different carbonates, including monodentate, bidentate, bridged, polydentate, and bicarbonates [54,55]. Although detailed band assignment in these cases requires extensive assumptions about the coordination of the atoms on the surface as well as support from theoretical calculations and therefore is not reported here, there are still interesting trends to discuss. In all cases, the formation of carbonates is progressed as the temperature increases during the heating segment and stays the same during cooling. As the atmosphere is significantly richer in oxygen than in CO, this indicates that the formation of carbonates is limited by the number of adsorption sites as well as the amount of CO present in the reaction mixture, wherefore the carbonates are not built up anymore after a certain level. The former case is seen for the lower Co contents where we still see the gas-phase CO contribution while the carbonate contribution is at its highest intensity. On the other hand, the limiting factor of CO concentration is seen especially for the higher Co contents where we see that the contribution of the gas-phase CO at higher temperatures is totally diminished. This is consistent with the higher normalized rates that had been observed for the sample  $x = 0.25$ . The bands show minor shifts that could indicate different electronic properties at the surface. Indeed, the isomorphous substitution of Fe with Co in the bulk structure will induce changes in the surface composition and subsequently result in different electronic states of the adsorption sites on the surface. In addition, the presence of Co in the sample seems to suppress or promote some bands stronger than others. For instance, the band shifting among the sample between 1572–1582 cm<sup>-1</sup>, which can be attributed to asymmetric vibration of mono and/or bridged carbonates, is promoted up to  $x = 0.20$  Co incorporation. The most active sample with  $x = 0.25$  Co shows the lowest tendency to become poisoned at the surface by the carbonates. It is evident that Co incorporation changes the surface properties during the transient test despite similar crystal structures.

To further analyze the stability of the catalyst surface under steady-state conditions, the samples were studied after an oxidative treatment for 40 min at 200 °C upon exposure to the reaction mixture. The resulting spectra are shown in Figure 6b for  $x = 0.25$  and for other samples in Figure S19a–d. Evidently, there was a progressive formation and build-up of carbonate-based species as soon as the catalysts were exposed to the reaction mixture. Two simultaneous pathways can be considered to form carbonates on these catalysts. One would be the result of reducing the 3+ cations at the surface by CO, especially known for Co<sup>3+</sup> when O<sub>2</sub> is not present, which may result in the direct formation of carbonates on the surface [56]. Simultaneously, if the catalyst has some CO oxidation activity, the produced CO<sub>2</sub> molecules can be adsorbed on the surface and subsequently form carbonates, especially if the surface has weak Lewis basic sites, as reported for example for Al<sub>2</sub>O<sub>3</sub> and Mg<sub>2</sub>SiO<sub>2</sub> [33,57]. Depending on the conditions of the experiment, one or the other could be dominant, but neither could be ruled out. In the case of the herein studied perovskite catalysts, it is reasonable to assume that the formation of carbonate is mainly due to the surface reaction of CO with the two active O<sup>-</sup>, as reported for Co<sub>3</sub>O<sub>4</sub> catalysts [58]. The positive correlation of the extent of the reaction with the Co content can be qualitatively inferred by the gas phase CO and CO<sub>2</sub> intensities. Like the transient test, similar bands are observed in the steady-state, some of which are promoted or suppressed over time. To better compare this, the DRIFTS spectra at 40 min are depicted in Figure 7a. Here, the band at 1728 cm<sup>-1</sup>, possibly related to C=O in bidentate coordination, is promoted by the Co content. The same is observed for bands at 1641, 1572, 1288 cm<sup>-1</sup>, while the band at 1439 cm<sup>-1</sup> seems to be suppressed. The spectra were also compared in the upper range of the wavenumber, which showed a very weak yet similar interaction of CO<sub>2</sub> with the hydroxyl group at 3633 cm<sup>-1</sup> (see Figure S20) [59]. The similarity of the band intensity and position among the samples would suggest that the possible contribution of the OH groups of the catalyst in the CO oxidation activity was most likely insignificant and not responsible for the observed activity trend. Nevertheless, it is similar among the samples showing the same activity, particularly among  $x = 0.20$  and  $0.30$ , which suggest a similar surface structure for these samples despite different Co contents. The CO<sub>2</sub> formation normalized by He intensity, sample mass, and BET surface area monitored using MS (see Figure 7b) indicated a significant promoting effect of Co. Interestingly, the deactivation of the catalysts, as indicated by a gradual decline of the CO<sub>2</sub> signal, was suppressed at the higher Co contents. In other words, the more Co in the sample, the less significant deactivation could be observed, in line with the observations during the transient DRIFTS measurements and during the kinetic steady-state measurements of the catalysts  $x = 0.25$  and  $x = 0.00$  at 200 °C (Figure S17c). This could be backed up by analyzing the DRIFTS spectra in the carbonate region, i.e., in the wavenumber range of 1150–1700 cm<sup>-1</sup>. To this aim, the spectra were integrated within the specified range during the whole isothermal segment and normalized based on the BET surface area. As depicted in Figure 7c, the carbonates were formed as soon as the catalysts were exposed to the reaction mixture but their build-up was suppressed by the higher Co content in the sample. The trend between the activity observed from the transient catalytic experiments and the carbonate build-up during the transient and isothermal DRIFTS measurements were consistent (i.e.,  $x = 0.25 > x = 0.30, x = 0.20 > x = 0.05 > 0.00$ ). This is also in line with most of the normalized CO<sub>2</sub> formation MS signals, with the  $x = 0.05$  being an outlier by showing a sharp CO<sub>2</sub> signal at the beginning, which is then diminished later on by time on stream. The inverse correlation between CO<sub>2</sub> and carbonate formation could indicate the blocking of active sites due to a larger amount of carbonate species preferentially formed by increasing the Fe content. On the other hand, one could hypothesize that the Co incorporation enhances the decomposition of the carbonates, which are formed as reaction intermediates rather than surface poisoning species.

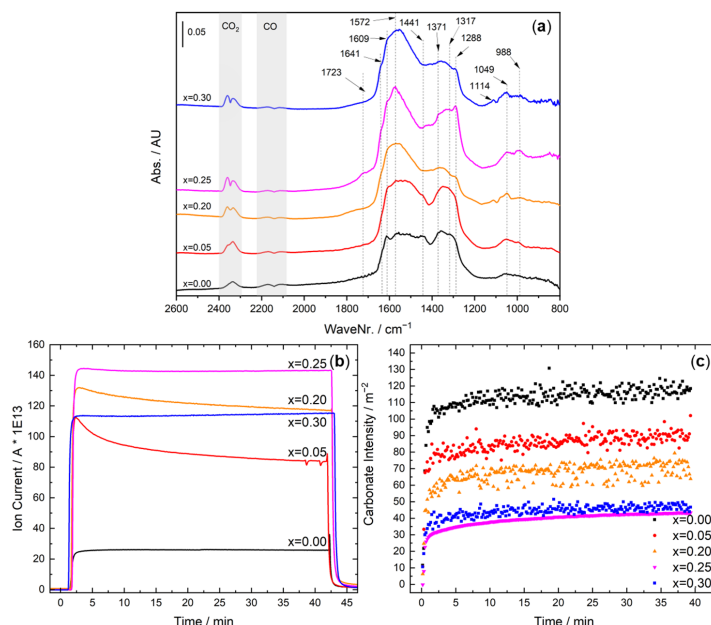


**Figure 7.** (a) DRIFTS spectra of the selected 20% O<sub>2</sub>-treated catalysts after 40 min of exposure to the reaction mixture of 0.2%CO + 2% O<sub>2</sub> in He at 200 °C. The labels represent the Co content in the catalysts. (b) MS CO<sub>2</sub> traces during the isothermal holding period in the reaction mixture of 0.2% CO + 2% O<sub>2</sub> balanced in He. (c) Integrals of the carbonate region normalized on exposed BET surface area in the spectra during the experiment in the reaction mixture of 0.2% CO + 2% O<sub>2</sub> balanced in He.

The CO probe gas interaction with the adsorption sites was additionally investigated at 10 °C, and the results during 40 min of exposure are plotted in Figure S21. As the extent of the reaction is limited at this temperature, the formation and build-up of carbonates can be attributed more dominantly to the reduction of the 3+ cations. However, the contribution of CO<sub>2</sub> adsorption, whether as the product of the reaction or impurity of the CO mixture, cannot be totally excluded. Indeed, there is a positive correlation between the Co content and the build-up of the carbonates (inferred by the relative intensities of gas-phase CO and the carbonates), which is consistent with the reduction of Co<sup>3+</sup> by CO. Additionally, our previous hypothesis in the discussion about the steady-state data can be supported in the sense that Co<sup>3+</sup> promotes the formation of the carbonates. However, it also enhances their decomposition in an O<sub>2</sub>-rich environment. The Co-free sample shows a similar behavior, although with much lower intensities. The 40 min spectra of the catalyst are stacked in Figure 8 for better comparison. Several bands can be observed in the range of 1620 to 1053 cm<sup>-1</sup>, while others show different relative intensities. For instance, there is a positive correlation between the relative intensities of the bands at 1620, 1396, and 1121 cm<sup>-1</sup>. In summary, Co content has a positive effect on the formation of the carbonates in an O<sub>2</sub>-free environment, consistent with the higher population of reducible surface Co<sup>3+</sup> species. On the other hand, when the atmosphere is O<sub>2</sub>-rich, the adsorption of CO is enhanced by the incorporation of Co, leading to the formation of carbonates as reaction intermediates, but their decomposition is also promoted by Co. In the end, this leads to a more active catalyst in CO oxidation, which is yet more resistant to surface poisoning. The small changes in the type of carbonates in all DRIFTS experiments could reflect minor differences in the surface properties, which could have an impact on the reaction pathway

and the overall catalytic activity. The similarity of the surface properties among those samples with a comparable morphology, especially  $x = 0.20$  and  $0.30$ , is also consistent with the similar observed activity trend.

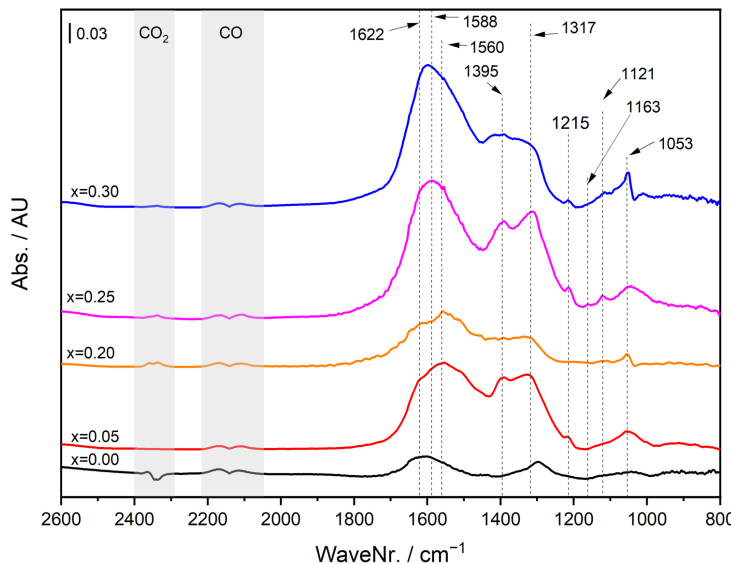


**Figure 8.** DRIFTS spectra of the selected 20% O<sub>2</sub>-treated catalysts after 40 min of exposure to the probe gas of 0.2% CO in He at 10 °C. The labels represent the Co content in the catalysts.

### 3. Materials and Methods

#### 3.1. Raw Materials

For the synthesis of the investigated catalysts, commercially available reagents were used without additional purification: lanthanum(III) nitrate hexahydrate (99.9% La, abcr GmbH, Karlsruhe, Germany), iron(III) nitrate nonahydrate ( $\geq 96\%$ , Carl Roth GmbH, Karlsruhe, Germany), cobalt(II) nitrate hexahydrate ( $\geq 98\%$ , Carl Roth GmbH, Karlsruhe, Germany), sodium hydroxide (98.5%, Carl Roth GmbH, Karlsruhe, Germany), and sodium carbonate ( $\geq 99.5\%$ , VWR International GmbH, Darmstadt, Germany).

#### 3.2. Synthesis and Sample Preparation

The synthesis via co-precipitation included the preparation of metal salt stock solutions with a total ionic concentration M<sup>x+</sup> of 0.8 mol L<sup>-1</sup> with the general composition La<sup>3+</sup>/Fe<sup>3+</sup>/Co<sup>2+</sup> = 1:1-x:x. The value of x was varied in the range between 0 and 0.3. The precipitation agent was a solution consisting of 1.2 M NaOH and 0.18 M Na<sub>2</sub>CO<sub>3</sub>.

The syntheses were performed in an automated OptiMax 1001 (Mettler Toledo GmbH, Greifensee, Switzerland) synthesis workstation. The setup consists of a single-walled glass reactor fixed inside a solid-state thermostat for accurate temperature control. During precipitation and aging steps, N<sub>2</sub> flow was employed, and the prefill volume of the reactor was purged with N<sub>2</sub> for 30 min. The co-precipitation experiments have been performed isothermally at 10 °C and a constant pH of 9.5. A universal control box equipped with a precision balance allowed gravimetric dosing of the metal salt solutions of 75 g in 36 min. Control over the pH was achieved by simultaneous computer-controlled dosing of the metal salt solution and the precipitation agent via two ProMinent gamma/L metering pumps. The pH was monitored and adjusted using an InLab Semi-Micro-L electrode before

each experiment. A pitched blade impeller rotating at a constant speed of 300 rpm was used to avoid concentration and temperature gradients. After the precipitation was finished, an aging step at 10 °C for 60 min was performed. After aging, the precipitate was isolated by centrifugation (6000 rpm, 2 min) and washed with deionized water until the conductivity of the supernatant was below 0.1 mS cm<sup>-1</sup> in two consecutive runs. Afterwards, the samples were dried in static air at 80 °C for 12 h. The precursors were calcined at 800 °C for 3h ( $\beta = 2\text{ }^{\circ}\text{C min}^{-1}$ ) in stagnant air in a muffle furnace (B150, Nabertherm, Lilienthal, Germany). The calcined samples were characterized as powders and pressed with a hydraulic press by Perkin-Elmer (5 t, 2 min, Überlingen, Germany), pestled, and sieved with stainless steel sieves from ATECHNIK (ISO 3310-1, Leinburg, Germany). A sieve fraction of 250–355 µm was used for the kinetic analysis with a BELCAT-B (MicrotracBEL Corp., Haradanaka Toyonaka, Japan) catalyst analyzer.

### 3.3. Catalyst Characterization

Fe and Co contents in the precursors were determined by atomic absorption spectroscopy (M-Series, Thermo Electron Corporation, Waltham, MA, USA).

Thermogravimetric measurements (TG) were performed in a NETZSCH STA 449F3 thermal analyzer (NETZSCH-Gerätebau GmbH, Selb, Germany). For TG measurements, 50 mg of precursor material was heated in a corundum crucible in 21% O<sub>2</sub> in Ar from 30 °C to 1000 °C with a linear heating rate of 5 °C min<sup>-1</sup>.

N<sub>2</sub> adsorption-desorption experiments were performed with a NOVA3000e setup (Quantachrome Instruments, Boynton Beach, Florida, USA) at -196 °C after degassing the samples at 80 °C for 2 h in a vacuum. BET (Brunauer Emmet Teller) surface areas were calculated from  $p/p_0$  data between 0.05 and 0.3. Total pore volumes were determined at  $p/p_0 = 0.99$ .

Powder XRD patterns in the 2θ range from 5° to 90° were recorded on a Bruker D8 Advance (Bruker, Billerica, MA, USA) diffractometer in Bragg–Brentano geometry using a position-sensitive LYNXEYE detector (Ni-filtered CuK<sub>α</sub> radiation, Bruker, Billerica, MA, USA) applying a counting time of 0.3 s and step size of 0.018. Samples were mounted using dispersion in ethanol on a glass disc inserted in a round PMMA holder. The latter was subject to gentle rotation during scanning after removing the ethanol by drying. For structure analysis and calculation of lattice parameters, Rietveld refinement [44] was applied using the TOPAS software (Bruker, Billerica, MA, USA).

Scanning electron microscopy (SEM) studies were performed on a Apreo S LoVac Thermo Scientific (ThermoFisher, Waltham, MA, USA) microscope with a Thermo Scientific UltraDry EDS X-ray detector (ThermoFisher, Waltham, MA, USA).

High-resolution scanning transmission electron microscopy (STEM) studies were carried out on a Jeol JEM 2200 fs microscope (Akishima, Japan) equipped with a probe-side Cs-corrector operated at 200 kV acceleration voltage. Micrographs were taken in a high-angle annular darkfield (HAADF). EDX elemental mappings were acquired with a X-Max 100 detector (Oxford Instruments, Abingdon, United Kingdom. For particle size estimation, 50 particle diameters were counted using the software ImageJ.

IR spectra were obtained in a Bruker Platinum ATR Diamond spectrometer (Bruker, Billerica, MA, USA) in a spectral range between 400 cm<sup>-1</sup> to 4000 cm<sup>-1</sup>. The step size was set to 0.1 cm<sup>-1</sup>.

### 3.4. Catalytic CO Oxidation at Ambient Pressure

For catalytic testing in a BELCAT-B catalyst analyzer (MicrotracBEL Corp., Japan), 100 mg (sieve fraction 250–355 µm) of each calcined catalyst sample diluted with 500 mg of silicon carbide (>355 µm) was placed inside a U-shaped quartz tube reactor (inner diameter = 8 mm). Each sample was cleaned by heating at 3 °C min<sup>-1</sup> in He (99.9999%, Air Liquide) from room temperature to 100 °C, kept constant for 1 hr. After that, the sample was cooled down in He to 50 °C. Before starting the temperature-programmed catalytic experiments, the catalyst/SiC mixture was purged for 15 min with 2% CO and 20% O<sub>2</sub> in

He to equilibrate the gas composition. After that, the temperature was increased to 500 °C at a heating rate of 3 °C min<sup>-1</sup>. The total gas flow was 80 mL min<sup>-1</sup>. The reactor outlet stream was analyzed with a MicroGC 490 (Agilent Technologies, Santa Clara, CA, USA) equipped with a 5-Å molecular sieve and a Pora Plot Q column to detect CO, O<sub>2</sub>, and CO<sub>2</sub>.

### 3.5. Operando DRIFTS during CO Oxidation

DRIFTS was performed using an FTIR spectrometer from ThermoFisher Scientific (Waltham, MA, USA), i.e., Nicolet™ iS20, equipped with a DRIFTS cell (Praying Mantis™, Harrick Scientific Products Inc., Pleasantville, New York, USA) and a Mercury Cadmium Telluride detector (MCT) cooled with liquid nitrogen. The DRIFTS cell outlet gas stream was analyzed continuously during the experiment by an on-line mass spectrometer (Omnistar GSD 320, Pfeiffer Vacuum, Wetzlar, Germany). Using a four-port selector valve, the inlet gas was switched between two different streams, one for He-purging and/or pretreatments (He or 20% v/v O<sub>2</sub> in He) and the other containing the probe gas (0.2% v/v CO in He or the reaction mixture of 0.2% v/v CO, 2% v/v O<sub>2</sub> balanced in He). A flow-through configuration was applied in all segments with a total flowrate of 80 mL min<sup>-1</sup>. At first, the loaded samples (~30–40 mg fine powder) were pretreated by He at 150 °C for 1 h (at a heating rate of 10 °C/min), after which the cell was cooled down to 20 °C at the same rate. After stabilizing the temperature, the background spectrum was collected in He. Then, the samples were exposed to the reaction mixture while ramping the temperature to 300 °C at a rate of 10 °C/min and collecting the spectra every 1 min (corresponding to 10 °C intervals). The samples were dwelled for 10 min at 300 °C and subsequently cooled down to 20 °C at the same rate while collecting spectra every 1 min. In the second part of the experiment, the samples were pretreated in 20% O<sub>2</sub> for 1 h at 350 °C to clean the surface from the formed carbonate species and then cooled down to 200 °C. After stabilizing the temperature, the gas was changed to He, and the system was purged for 10 min to collect the new background. Subsequently, the catalysts were exposed to the reaction mixture for 40 min while collecting the spectra every 10 s. The first spectrum was collected before switching the gas, so it represents the time 0. In the final part of the experiment, the catalysts were pretreated in 20% O<sub>2</sub> again at similar conditions stated above and then cooled down to 10 °C. After temperature stabilization and collecting a new He background, the samples were exposed to 0.2% CO probe gas for 40 min, and the spectra were collected every 10 s.

## 4. Conclusions

Synthesis of LaFe<sub>1-x</sub>Co<sub>x</sub>O<sub>3</sub> perovskites was performed by co-precipitation of mostly amorphous precursors and thermal decomposition towards phase-pure perovskites. The precursor materials contain a minor contribution from a hydrotalcite-like secondary phase for x ≥ 0.10. In ATR-FTIR spectroscopy, indications for a weaker force constant of the Co(II)-O bond compared to that of the Fe(III)-O bond in the hydroxycarbonate precursors are observed. After thermal decomposition, the perovskites feature sintered particles with a size of ~50 nm. The BET surface area inversely follows the size of the particles, which is an indication for mainly interparticle porosity. ATR-FTIR spectroscopy of the calcined materials revealed an influence of the Co incorporation on the MO<sub>6</sub> octahedra, indicating a distortion in the orthorhombic perovskite, which affects the Fe-O bond strength.

Strong pronounced promotion of only 5% Co incorporation is observed in transient CO oxidation, which could be related to enhancing the reducibility as inferred by the H<sub>2</sub>-TPR and ATR-FTIR results. Further Co incorporation generally enhanced the activity compared to the pure iron sample, although no linear trend could be observed with the Co content. The promoted reducibility of Co<sup>3+</sup> compared to Fe<sup>3+</sup> might have led to enhanced redox properties, that are not linearly following the Co content in the samples. Nevertheless, a correlation between the low-temperature TPR peak and CO oxidation activity was observed. From the CO oxidation monitored by surface-sensitive operando DRIFTS measurements, we found that the formation of carbonates in presence of the reaction

mixture was suppressed at a higher Co content, while the CO<sub>2</sub> formation was boosted. In other words, the carbonates on the catalyst with lower Co contents were more stable and possibly not acting as reaction intermediates but rather as surface poisoning species. However, minor surface modification upon Co incorporation, especially at higher loadings, could not be ruled out. Indeed, despite comparable crystalline structures, Co incorporation could result in minor distortion, as revealed by ATR-FTIR, which resulted in changes of the surface properties, which might have had an impact on the CO oxidation activity. In this regard, the samples with similar morphology and surface properties showed similar activity in spite of different Co contents. In our upcoming research work, we will perform further mechanistic studies on the CO oxidation on these perovskites and also test the catalysts in different oxidation reactions.

**Supplementary Materials:** The following are available online at <https://www.mdpi.com/article/10.3390/catal11050550/s1>, Figure S1. Synthesis protocol of sample  $x = 0.00$ , Figure S2. Synthesis protocol of sample  $x = 0.05$ , Figure S3. Synthesis protocol of sample  $x = 0.10$ , Figure S4. Synthesis protocol of sample  $x = 0.15$ , Figure S5. Synthesis protocol of sample  $x = 0.20$ , Figure S6. Synthesis protocol of sample  $x = 0.25$ , Figure S7. Synthesis protocol of sample  $x = 0.30$ , Figure S8. SEM images of the precursors (left column) and the calcined materials (right column), Figure S9. (a) Positions of the transmission minimum in the M-O and M-OH region ( $<580\text{ cm}^{-1}$ ) in the IR spectra. (b) Transmission minimum in IR spectra in the M-O and M-OH region ( $<580\text{ cm}^{-1}$ ) corresponding to the minimum positions shown in (a), Table 1. Criteria of fit for the Rietveld Refinements of the X-ray diffraction patterns of the calcined samples. Figure S10. (a) Rietveld plots of  $x = 0.00$ . (b) Rietveld plots of  $x = 0.05$ . (c) Rietveld plots of  $x = 0.10$ . (d) Rietveld plots of  $x = 0.15$ . (e) Rietveld plots of  $x = 0.20$ . (f) Rietveld plots of  $x = 0.25$ . (g) Rietveld plots of  $x = 0.30$ . Grey: experimental pattern; red: calculated pattern; blue: difference plot; black: Bragg peak position, Figure S11. SEM particle size counts of all samples after calcination from 100 particles per sample, Figure S12. TEM images in the magnifications 60 k (left column), 300 k (middle column), and 10 M (right column), Figure S13. TEM particle size counts of all samples after calcination from 100 particles per sample, Figure S14. BET isotherms of all samples, Figure S15. Pore size distribution of all samples, Figure S16. (a) H<sub>2</sub>-TPR profiles of the sample series. (b) Positions of the maxima below 500 °C (labelled low temperature) and above 500 °C (labelled high temperature) derived from the TPR curves in (a). Figure S17. (a) Conversion curves of  $x = 0.00$  derived from two different synthesis batches in the reaction mixture of 2% CO + 20% O<sub>2</sub> balanced in He. (b) Reusability and reproducibility curves on CO oxidation of sample  $x = 0.00$  after storage in air and reproducibility tests of sample  $x = 0.25$  in the reaction mixture of 2% CO + 20% O<sub>2</sub> balanced in He or N<sub>2</sub>. (c) Stability test of  $x = 0.00$  and  $x = 0.25$  at 200 °C and of  $x = 0.25$  at 100 °C in the reaction mixture of 2% CO + 20% O<sub>2</sub> balanced in N<sub>2</sub>. Figure S18. DRIFTS spectra of the selected catalysts exposed to the reaction mixture of 0.2% CO + 2% O<sub>2</sub> balanced in He, after a He-treatment at 150 °C during a transient experiment; (a)  $x = 0.00$ , (b)  $x = 0.05$ , (c)  $x = 0.20$  and (d)  $x = 0.30$  Co incorporation. In the legends, H and C designate the heating and cooling segments, respectively. Figure S19. DRIFTS spectra of the selected catalysts exposed to the reaction mixture of 0.2% CO + 2% O<sub>2</sub> balanced in He, after an oxidative treatment during 40 min of steady-state condition at 200 °C; (a)  $x = 0.00$ , (b)  $x = 0.05$ , (c)  $x = 0.20$  and (d)  $x = 0.30$  Co incorporation, Figure S20. OH-region DRIFTS spectra of the selected catalysts exposed to the reaction mixture of 0.2% CO + 2% O<sub>2</sub> balanced in He, after an oxidative treatment during 40 min of steady-state condition at 200 °C, Figure S21. DRIFTS spectra of the selected catalysts exposed to the probe gas of 0.2% CO in He, after an oxidative treatment during 40 min of steady-state condition at 10 °C; (a)  $x = 0.00$ , (b)  $x = 0.05$ , (c)  $x = 0.20$ , (d)  $x = 0.25$  and (e)  $x = 0.30$  Co incorporation.

**Author Contributions:** Conceptualization, M.B. and K.F.O.; methodology, A.R. and S.N.; validation, M.K. and M.D.; investigation, M.K., M.D. and S.N.; resources, M.K., M.D., S.N. and A.R.; writing—original draft preparation, M.D. and S.N.; writing—review and editing, M.K., A.R., K.F.O. and M.B.; visualization, M.K., M.D. and S.N.; supervision, M.B.; project administration, M.B.; funding acquisition, M.B. All authors have read and agreed to the published version of the manuscript.

**Funding:** This work was funded by the Deutsche Forschungsgemeinschaft (DFG, German Research Foundation)—388390466—TRR 247 within projects A1 and C1.

**Acknowledgments:** The authors thank Markus Heidelmann from the “Interdisciplinary Center for Analytics on the Nanoscale (ICAN)”, a core facility funded by the German Research Foundation (DFG, reference RI\_00313) for the TEM measurements. The authors also acknowledge Kateryna Loza for SEM measurements and Robin Meya and Beate Römer for providing AAS measurements. Furthermore, we acknowledge support by the Open Access Publication Fund of the University of Duisburg-Essen.

**Conflicts of Interest:** The authors declare no conflict of interest.

## References

- Royer, S.; Duprez, D.; Can, F.; Courtois, X.; Batiot-Dupeyrat, C.; Laassiri, S.; Alamdar, H. Perovskites as substitutes of noble metals for heterogeneous catalysis: Dream or reality. *Chem. Rev.* **2014**, *114*, 10292–10368. [\[CrossRef\]](#) [\[PubMed\]](#)
- Kayaalp, B.; Lee, S.; Klauke, K.; Seo, J.; Nodari, L.; Kornowski, A.; Jung, W.; Mascotto, S. Template-free mesoporous La<sub>0.3</sub>Sr<sub>0.7</sub>Tl<sub>1-x</sub>Fe<sub>x</sub>O<sub>3±δ</sub> for CH<sub>4</sub> and CO oxidation catalysis. *Appl. Catal. B Environ.* **2019**, *245*, 536–545. [\[CrossRef\]](#)
- Zhao, K.; He, F.; Huang, Z.; Wei, G.; Zheng, A.; Li, H.; Zhao, Z. Perovskite-type oxides LaFe<sub>1-x</sub>CoO<sub>3</sub> for chemical looping steam methane reforming to syngas and hydrogen co-production. *Appl. Energy* **2016**, *168*, 193–203. [\[CrossRef\]](#)
- Suntivich, J.; Gasteiger, H.A.; Yabuuchi, N.; Nakanishi, H.; Goodenough, J.B.; Shao-Horn, Y. Design principles for oxygen-reduction activity on perovskite oxide catalysts for fuel cells and metal-air batteries. *Nat. Chem.* **2011**, *3*, 546–550. [\[CrossRef\]](#)
- Suntivich, J.; May, K.J.; Gasteiger, H.A.; Goodenough, J.B.; Shao-Horn, Y. A perovskite oxide optimized for oxygen evolution catalysis from molecular orbital principles. *Science* **2011**, *334*, 1383–1385. [\[CrossRef\]](#)
- Peña, M.A.; Fierro, J.L. Chemical structures and performance of perovskite oxides. *Chem. Rev.* **2001**, *101*, 1981–2017. [\[CrossRef\]](#) [\[PubMed\]](#)
- Szabo, V.; Bassir, M.; van Neste, A.; Kaliaguine, S. Perovskite-type oxides synthesized by reactive grinding: Part II: Catalytic properties of LaCo(1-x)Fe<sub>x</sub>O<sub>3</sub> in VOC oxidation. *Appl. Catal. B Environ.* **2002**, *37*, 175–180. [\[CrossRef\]](#)
- Sumathi, R.; Johnson, K.; Viswanathan, B.; Varadarajan, T.K. Selective oxidation and dehydrogenation of benzyl alcohol on ABB'03 (A=Ba, B=Pb, Ce, Ti and B'=Bi, Cu, Sb)-type perovskite oxides—temperature programmed reduction studies. *Appl. Catal. A Gen.* **1998**, *172*, 15–22. [\[CrossRef\]](#)
- Waffel, D.; Alkan, B.; Fu, Q.; Chen, Y.-T.; Schmidt, S.; Schulz, C.; Wiggers, H.; Muhler, M.; Peng, B. Towards Mechanistic Understanding of Liquid-Phase Cinnamyl Alcohol Oxidation with tert-Butyl Hydroperoxide over Noble-Metal-Free LaCo<sub>1-x</sub>Fe<sub>x</sub>O<sub>3</sub> Perovskites. *ChemPlusChem* **2019**, *84*, 1155–1163. [\[CrossRef\]](#)
- Voorhoeve, R.J.; Remeika, J.P.; Johnson, D.W. Rare-Earth manganites: Catalysts with low ammonia yield in the reduction of nitrogen oxides. *Science* **1973**, *180*, 62–64. [\[CrossRef\]](#)
- Voorhoeve, R.J.H.; Remeika, J.P.; Trimble, L.E. Defect chemistry and catalysis in oxidation and reduction over perovskite-type oxides. *Ann. N. Y. Acad. Sci.* **1976**, *272*, 3–21. [\[CrossRef\]](#)
- Baythoun, M.S.G.; Sale, F.R. Production of strontium-substituted lanthanum manganite perovskite powder by the amorphous citrate process. *J. Mater. Sci.* **1982**, *17*, 2757–2769. [\[CrossRef\]](#)
- Taguchi, H.; Yamada, S.; Nagao, M.; Ichikawa, Y.; Tabata, K. Surface characterization of LaCoO<sub>3</sub> synthesized using citric acid. *Mater. Res. Bull.* **2002**, *37*, 69–76. [\[CrossRef\]](#)
- Gallagher, P.K.; Johnson, D.W.; Remeika, J.P.; Schrey, F.; Trimble, L.E.; Vogel, E.M.; Voorhoeve, R. The activity of La<sub>0.7</sub>Sr<sub>0.3</sub>MnO<sub>3</sub> without Pt and La<sub>0.7</sub>Pb<sub>0.3</sub>MnO<sub>3</sub> with varying Pt contents for the catalytic oxidation of CO. *Mater. Res. Bull.* **1975**, *10*, 529–538. [\[CrossRef\]](#)
- Angel, S.; Neises, J.; Dreyer, M.; Friedel Ortega, K.; Behrens, M.; Wang, Y.; Arandian, H.; Schulz, C.; Wiggers, H. Spray-flame synthesis of La(Fe, Co)O<sub>3</sub> nano-perovskites from metal nitrates. *AIChE J.* **2019**, *10*, 441. [\[CrossRef\]](#)
- Alkan, B.; Cychy, S.; Varhade, S.; Muhler, M.; Schulz, C.; Schuhmann, W.; Wiggers, H.; Andronescu, C. Spray-Flame-Synthesized LaCo<sub>1-x</sub>Fe<sub>x</sub>O<sub>3</sub> Perovskite Nanoparticles as Electrocatalysts for Water and Ethanol Oxidation. *ChemElectroChem* **2019**, *6*, 4266–4274. [\[CrossRef\]](#)
- Junwu, Z.; Xiaojie, S.; Yanping, W.; Xin, W.; Xujie, Y.; Lude, L. Solution-Phase Synthesis and Characterization of Perovskite LaCoO<sub>3</sub> Nanocrystals via A Co-Precipitation Route. *J. Rare Earths* **2007**, *25*, 601–604. [\[CrossRef\]](#)
- Choudhary, V.R.; Upadhe, B.S.; Belhekar, A.A. Oxidative Conversion of Methane to Syngas over LaNiO<sub>3</sub>Perovskite with or without Simultaneous Steam and CO<sub>2</sub>Reforming Reactions: Influence of Partial Substitution of La and Ni. *J. Catal.* **1996**, *163*, 312–318. [\[CrossRef\]](#)
- Sim, Y.; Yoo, J.; Ha, J.-M.; Jung, J.C. Oxidative coupling of methane over LaAlO<sub>3</sub> perovskite catalysts prepared by a co-precipitation method: Effect of co-precipitation pH value. *J. Energy Chem.* **2019**, *35*, 1–8. [\[CrossRef\]](#)
- Kühl, S.; Düdder, H.; Girsdis, F.; Kähler, K.; Muhler, M.; Behrens, M. Perovskites as Precursors for Ni/La<sub>2</sub>O<sub>3</sub> Catalysts in the Dry Reforming of Methane: Synthesis by Constant pH Co-Precipitation, Reduction Mechanism and Effect of Ru-Doping. *Z. Anorg. Allg. Chem.* **2017**, *643*, 1088–1095. [\[CrossRef\]](#)
- Bedel, L.; Roger, A.; Estournes, C.; Kiennemann, A. Co<sub>0</sub> from partial reduction of La(Co, Fe)O<sub>3</sub> perovskites for Fischer-Tropsch synthesis. *Catal. Today* **2003**, *85*, 207–218. [\[CrossRef\]](#)
- Derakhshi, Z.; Tamizifar, M.; Arzani, K.; Baghshahi, S. Synthesis and Characterization of LaCoxFe<sub>1-x</sub>O<sub>3</sub> (0≤x≤1) Nano-Crystal Powders by Pechini Type Sol-Gel Method. *Synth. React. Inorg. M.* **2016**, *46*, 25–30. [\[CrossRef\]](#)

23. Wu, Y.; Cordier, C.; Berrier, E.; Nuns, N.; Dujardin, C.; Granger, P. Surface reconstructions of LaCo<sub>1-x</sub>Fe<sub>x</sub>O<sub>3</sub> at high temperature during N<sub>2</sub>O decomposition in realistic exhaust gas composition: Impact on the catalytic properties. *Appl. Catal. B Environ.* **2013**, *140–141*, 151–163. [[CrossRef](#)]
24. Yang, Y.; Shi, K. Preparation of LaFe<sub>x</sub>Co<sub>1-x</sub>O<sub>3</sub> Perovskite by Coprecipitation. *Open J. Nat. Sci.* **2016**, *4*, 378–383. [[CrossRef](#)]
25. Kaiwen, Z.; Xuehang, W.; Wenwei, W.; Jun, X.; Siqi, T.; Sen, L. Nanocrystalline LaFeO<sub>3</sub> preparation and thermal process of precursor. *Adv. Powder Technol.* **2013**, *24*, 359–363. [[CrossRef](#)]
26. Kaliaguine, S.; Szabo, V.; van Neste, A.; Gallot, J.E.; Bassir, M.; Muzychuk, R. Perovskite-Type Oxides Synthesized by Reactive Grinding. *Appl. Catal. A Gen.* **2001**, *24*, 39–56. [[CrossRef](#)]
27. Xu, J.; Liu, J.; Zhao, Z.; Zheng, J.; Zhang, G.; Duan, A.; Jiang, G. Three-dimensionally ordered macroporous LaCo<sub>x</sub>Fe<sub>1-x</sub>O<sub>3</sub> perovskite-type complex oxide catalysts for diesel soot combustion. *Catal. Today* **2010**, *153*, 136–142. [[CrossRef](#)]
28. Staykov, A.; Téllez, H.; Akbay, T.; Druce, J.; Ishihara, T.; Kilner, J. Oxygen Activation and Dissociation on Transition Metal Free Perovskite Surfaces. *Chem. Mater.* **2015**, *27*, 8273–8281. [[CrossRef](#)]
29. Seo, M.H.; Park, H.W.; Lee, D.U.; Park, M.G.; Chen, Z. Design of Highly Active Perovskite Oxides for Oxygen Evolution Reaction by Combining Experimental and ab Initio Studies. *ACS Catal.* **2015**, *5*, 4337–4344. [[CrossRef](#)]
30. Yang, J.; Hu, S.; Fang, Y.; Hoang, S.; Li, L.; Yang, W.; Liang, Z.; Wu, J.; Hu, J.; Xiao, W.; et al. Oxygen Vacancy Promoted O<sub>2</sub> Activation over Perovskite Oxide for Low-Temperature CO Oxidation. *ACS Catal.* **2019**, *9*, 9751–9763. [[CrossRef](#)]
31. Freund, H.-J.; Meijer, G.; Scheffler, M.; Schlögl, R.; Wolf, M. CO oxidation as a prototypical reaction for heterogeneous processes. *Angew. Chem. Int. Ed.* **2011**, *50*, 10064–10094. [[CrossRef](#)]
32. Lukashuk, L.; Yigit, N.; Rameshan, R.; Kolar, E.; Teschner, D.; Hävecker, M.; Knop-Gericke, A.; Schlögl, R.; Föttinger, K.; Rupprecht, G. Operando Insights into CO Oxidation on Cobalt Oxide Catalysts by NAP-XPS, FTIR, and XRD. *ACS Catal.* **2018**, *8*, 8630–8641. [[CrossRef](#)]
33. Föttinger, K.; Schlögl, R.; Rupprecht, G. The mechanism of carbonate formation on Pd-Al<sub>2</sub>O<sub>3</sub> catalysts. *Chem. Commun.* **2008**, *3*, 320–322. [[CrossRef](#)]
34. Yi, Y.; Zhang, P.; Qin, Z.; Yu, C.; Li, W.; Qin, Q.; Li, B.; Fan, M.; Liang, X.; Dong, L. Low temperature CO oxidation catalysed by flower-like Ni-Co-O: How physicochemical properties influence catalytic performance. *RSC Adv.* **2018**, *8*, 7110–7122. [[CrossRef](#)]
35. Kuhn, J.; Ozkan, U. Surface properties of Sr- and Co-doped LaFeO<sub>3</sub>. *J. Catal.* **2008**, *253*, 200–211. [[CrossRef](#)]
36. Allmann, R.; Jepsen, H.P. Die Struktur des Hydrotalkits. *Neues Jahrb. Miner. Mon.* **1969**, *1969*, 544–551.
37. Xie, J.; Wu, Q.; Zhang, D.; Ding, Y. Biomolecular-Induced Synthesis of Self-Assembled Hierarchical La(OH)CO<sub>3</sub> One-Dimensional Nanostructures and Its Morphology-Held Conversion toward La<sub>2</sub>O<sub>3</sub> and La(OH)<sub>3</sub>. *Cryst. Growth Des.* **2009**, *9*, 3889–3897. [[CrossRef](#)]
38. del Arco, M.; Trujillano, R.; Rives, V. Cobalt-iron hydroxycarbonates and their evolution to mixed oxides with spinel structure. *J. Mater. Chem.* **1998**, *8*, 761–767. [[CrossRef](#)]
39. Uzunova, E.; Klissurski, D.; Mitov, I.; Stefanov, P. Cobalt-iron hydroxide carbonate as a precursor for the synthesis of high-dispersity spinel mixed oxides. *Chem. Mater.* **1993**, *5*, 576–582. [[CrossRef](#)]
40. Wang, C.-B.; Lin, H.-K.; Tang, C.-W. Thermal Characterization and Microstructure Change of Cobalt Oxides. *Catal. Lett.* **2004**, *94*, 69–74. [[CrossRef](#)]
41. Sangaletti, L.; Depere, L.E.; Allieri, B.; Nunziante, P.; Traversa, E. An X-ray study of the trimetallic LaxSm<sub>1-x</sub>FeO<sub>3</sub> orthoferrites. *J. Eur. Ceram. Soc.* **2001**, *21*, 719–726. [[CrossRef](#)]
42. Shannon, R.D. Revised effective ionic radii and systematic studies of interatomic distances in halides and chalcogenides. *Acta Cryst.* **1976**, *32*, 751–767. [[CrossRef](#)]
43. Gaikwad, V.M.; Acharya, S.A. Novel perovskite–spinel composite approach to enhance the magnetization of LaFeO<sub>3</sub>. *RSC Adv.* **2015**, *5*, 14366–14373. [[CrossRef](#)]
44. Rietveld, H.M. Line profiles of neutron powder-diffraction peaks for structure refinement. *Acta Cryst.* **1967**, *22*, 151–152. [[CrossRef](#)]
45. Cui, H.; Zayat, M.; Levy, D. Epoxide assisted sol-gel synthesis of perovskite-type LaMxFe<sub>1-x</sub>O<sub>3</sub> (M=Ni,Co) nanoparticles. *J. Non-Cryst. Solids* **2006**, *352*, 3035–3040. [[CrossRef](#)]
46. Faye, J.; Baylet, A.; Trentesaux, M.; Royer, S.; Dumeignil, F.; Duprez, D.; Valange, S.; Tatibouët, J.-M. Influence of lanthanum stoichiometry in La<sub>1-x</sub>FeO<sub>3-δ</sub> perovskites on their structure and catalytic performance in CH<sub>4</sub> total oxidation. *Appl. Catal. B Environ.* **2012**, *126*, 134–143. [[CrossRef](#)]
47. Mihai, O.; Chen, D.; Holmen, A. Chemical looping methane partial oxidation: The effect of the crystal size and O content of LaFeO<sub>3</sub>. *J. Catal.* **2012**, *293*, 175–185. [[CrossRef](#)]
48. Chang, H.; Bjørgum, E.; Mihai, O.; Yang, J.; Lein, H.L.; Grande, T.; Raaen, S.; Zhu, Y.-A.; Holmen, A.; Chen, D. Effects of Oxygen Mobility in La-Fe-Based Perovskites on the Catalytic Activity and Selectivity of Methane Oxidation. *ACS Catal.* **2020**, *10*, 3707–3719. [[CrossRef](#)]
49. Khan, S.; Oldman, R.J.; Corà, F.; Catlow, C.R.A.; French, S.A.; Axon, S.A. A computational modelling study of oxygen vacancies at LaCoO<sub>3</sub> perovskite surfaces. *Phys. Chem. Chem. Phys.* **2006**, *8*, 5207–5222. [[CrossRef](#)]
50. Lu, H.; Zhang, P.; Qiao, Z.-A.; Zhang, J.; Zhu, H.; Chen, J.; Chen, Y.; Dai, S. Ionic liquid-mediated synthesis of meso-scale porous lanthanum-transition-metal perovskites with high CO oxidation performance. *Chem. Commun. (Camb.)* **2015**, *51*, 5910–5913. [[CrossRef](#)]

51. Ciambelli, P.; Cimino, S.; de Rossi, S.; Lisi, L.; Minelli, G.; Porta, P.; Russo, G. AFeO<sub>3</sub> (A=La, Nd, Sm) and LaFe<sub>1-x</sub>Mg<sub>x</sub>O<sub>3</sub> perovskites as methane combustion and CO oxidation catalysts: Structural, redox and catalytic properties. *Appl. Catal. B Environ.* **2001**, *29*, 239–250. [[CrossRef](#)]
52. Zhang, X.; Li, H.; Li, Y.; Shen, W. Structural Properties and Catalytic Activity of Sr-Substituted LaFeO<sub>3</sub> Perovskite. *Chin. J. Catal.* **2012**, *33*, 1109–1114. [[CrossRef](#)]
53. Li, P.; Hu, X.; Zhang, L.; Dai, H.; Zhang, L. Sol-gel nanocasting synthesis of patterned hierarchical LaFeO<sub>3</sub> fibers with enhanced catalytic CO oxidation activity. *Nanoscale* **2011**, *3*, 974–976. [[CrossRef](#)] [[PubMed](#)]
54. Hwang, J.; Rao, R.R.; Katayama, Y.; Lee, D.; Wang, X.R.; Crumlin, E.; Venkatesan, T.; Lee, H.N.; Shao-Horn, Y. CO<sub>2</sub> Reactivity on Cobalt-Based Perovskites. *J. Phys. Chem. C* **2018**, *122*, 20391–20401. [[CrossRef](#)]
55. Coenen, K.; Gallucci, F.; Mezari, B.; Hensen, E.; van Sint Annaland, M. An in-situ IR study on the adsorption of CO<sub>2</sub> and H<sub>2</sub>O on hydrotalcites. *J. CO<sub>2</sub> Util.* **2018**, *24*, 228–239. [[CrossRef](#)]
56. Hadjivanov, K.I.; Vayssilov, G.N. *Characterization of oxide surfaces and zeolites by carbon monoxide as an IR probe molecule*; Elsevier: Amsterdam, The Netherlands, 2002; pp. 307–511. ISBN 9780120078479.
57. Signorile, M.; Zamirri, L.; Tsuchiyama, A.; Ugliengo, P.; Bonino, F.; Martra, G. On the Surface Acid–Base Properties of Amorphous and Crystalline Mg<sub>2</sub>SiO<sub>4</sub> as Probed by Adsorbed CO, CO<sub>2</sub>, and CD<sub>3</sub>CN. *ACS Earth Space Chem.* **2020**, *4*, 345–354. [[CrossRef](#)]
58. Wang, X.; Li, X.; Mu, J.; Fan, S.; Chen, X.; Wang, L.; Yin, Z.; Tadé, M.; Liu, S. Oxygen Vacancy-rich Porous Co<sub>3</sub>O<sub>4</sub> Nanosheets toward Boosted NO Reduction by CO and CO Oxidation: Insights into the Structure–Activity Relationship and Performance Enhancement Mechanism. *ACS Appl. Mater. Interfaces* **2019**, *11*, 41988–41999. [[CrossRef](#)]
59. Drenchev, N.L.; Chakarova, K.K.; Lagunov, O.V.; Mihaylov, M.Y.; Ivanova, E.Z.; Strauss, I.; Hadjivanov, K.I. In situ FTIR Spectroscopy as a Tool for Investigation of Gas/Solid Interaction: Water-Enhanced CO<sub>2</sub> Adsorption in UiO-66 Metal-Organic Framework. *J. Vis. Exp.* **2020**, *156*. [[CrossRef](#)]

## 5. Synergistic Effects of Co and Fe on the Oxygen Evolution Reaction Activity of $\text{LaCo}_x\text{Fe}_{1-x}\text{O}_3$

**Title:** “Synergistic Effects of Co and Fe on the Oxygen Evolution Reaction Activity of  $\text{LaCo}_x\text{Fe}_{1-x}\text{O}_3$ ”

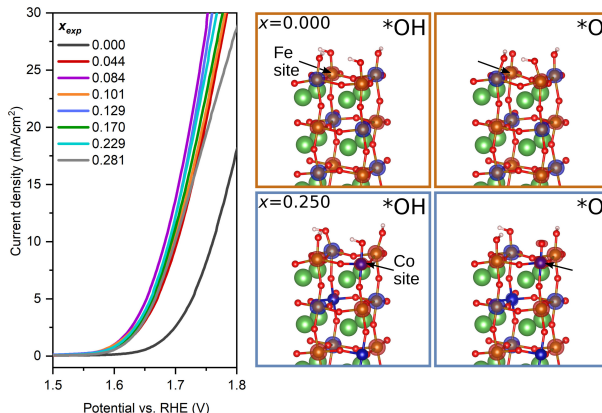
**Authors:** Achim Füngerlings\*, Adarsh Koul\*, Maik Dreyer\*, Anna Rabe, Dulce M. Morales, Wolfgang Schuhmann, Malte Behrens, Rossitza Pentcheva; \* contributed equally

Füngerlings, A.; Koul, A.; Dreyer, M.; Rabe, A.; Morales, D. M.; Schuhmann, W.; Behrens, M.; Pentcheva, R.,

*Chem. Eur. J.* **2021**, 27 (68), 17145–17158.<sup>187</sup>

**DOI:** 10.1002/chem.202102829

The Supporting Information can be accessed under [https://chemistry-europe.onlinelibrary.wiley.com/action/downloadSupplement?doi=10.1002%2Fchem.202102829&file=chem202102829-sup-0001-misc\\_information.pdf](https://chemistry-europe.onlinelibrary.wiley.com/action/downloadSupplement?doi=10.1002%2Fchem.202102829&file=chem202102829-sup-0001-misc_information.pdf) and is shown in Chapter A in Section V.



**Graphical Abstract:**

Maik Dreyer contributed to writing parts of the original draft and performed editing and review of the manuscript. He performed the materials synthesis, and was responsible for the coordination of materials characterization and its evaluation. Achim Füngerlings performed the theoretical calculation, wrote original draft parts, and contributed by editing and reviewing the manuscript. Adarsh Koul did the electrochemical measurements, wrote original draft parts, and contributed by editing and reviewing the manuscript. Anna Rabe performed the Rietveld refinements, read and edited the paper in the writing process. Dulce M. Morales assisted in writing and supervised the electrochemical measurements. Wolfgang Schuhmann, Malte Behrens, and Rossitza Pentcheva conceptualized the work,

had the supervision over the project, acquired the funding, and contributed in the writing process by review and editing.

© 2021 The Authors. Chemistry - A European Journal published by Wiley-VCH GmbH. Reprinted without changes under the Creative Commons Attribution-NonCommercial-NoDerivatives 4.0 International (CC BY-NC-ND 4.0) licence.

## Synergistic Effects of Co and Fe on the Oxygen Evolution Reaction Activity of $\text{LaCo}_x\text{Fe}_{1-x}\text{O}_3$

Special Issue

Achim Füngerlings<sup>[a]</sup>, Adarsh Koul<sup>[b]</sup>, Maik Dreyer<sup>[c]</sup>, Anna Rabe<sup>[c]</sup>, Dulce M. Morales<sup>[d]</sup>, Wolfgang Schuhmann<sup>[b]</sup>, Malte Behrens<sup>[c, e]</sup> and Rossitza Pentcheva<sup>\*[a]</sup>

**Abstract:** In a combined experimental and theoretical study we assess the role of Co incorporation on the OER activity of  $\text{LaCo}_x\text{Fe}_{1-x}\text{O}_3$ . Phase pure perovskites were synthesized up to  $x = 0.300$  in 0.025/0.050 steps. HAADF STEM and EDX analysis points towards  $\text{FeO}_2$ -terminated (001)-facets in  $\text{LaFeO}_3$ , in accordance with the stability diagram obtained from density functional theory calculations with a Hubbard  $U$  term (DFT+ $U$ ). Linear sweep voltammetry conducted in a rotating disk electrode setup shows a reduction of the OER overpotential and a nonmonotonic trend with  $x$ , with double layer capacitance measurements indicating an intrinsic nature of activity. This is supported by DFT+ $U$  results that show

reduced overpotentials for both Fe and Co reaction sites with the latter reaching values of 0.32–0.40 V, ~0.3 V lower than for Fe. This correlates with a stronger reduction of the binding energy difference of the  $^*\text{O}$  and  $^*\text{OH}$  intermediates towards an optimum value of 1.6 eV for  $x = 0.250$ , the OH deprotonation being the potential limiting step in most cases. Significant variations of the magnetic moments of both surface and subsurface Co and Fe during OER demonstrate that the beneficial effect is a result of a concerted action involving many surrounding ions, which extends the concept of the active site.

### 1. Introduction

The development and commercialization of water electrolysis technologies for the sustainable production of hydrogen face currently a need for high-performance catalysts based on earth-abundant elements that are able to drive the oxygen evolution reaction (OER) at low overpotentials. Transition metal oxide-based catalysts have been extensively studied and have shown promising OER activity in alkaline media.<sup>[1–4]</sup> Besides low cost and high abundance, their ability to obtain various oxidation states and adapt to different coordination environments represent some of the key ingredients enabling tunable electrocatalytic performance. Lately, it has been observed that a combination of different transition metal cations may be beneficial to reduce the overpotentials for oxidation processes.<sup>[5–7]</sup> These effects have been attributed to the tuning of adsorption energy differences,<sup>[8]</sup> consequently affecting the potential-limiting step, as well as to differences in electrical conductivity.<sup>[9]</sup> Notably, the combination of Fe and Co has shown evidence for improved electrochemical activity in metal oxides,<sup>[10–13]</sup> in particular in Co and Fe containing spinels,<sup>[7,14–18]</sup> phosphides,<sup>[10,19]</sup> borides and nitrides.<sup>[20–24]</sup>

Perovskites (chemical formula  $\text{ABO}_3$ ) represent another interesting class of metal oxides that allows for broad tuning of properties through variation of the A- and B-cations.<sup>[25]</sup> Several reviews address their activity for the oxygen evolution reaction.<sup>[1,26,27]</sup> Individual and combined A- and B-site mixing, as e.g. in  $(\text{Ba},\text{Sr})\text{Co}_x\text{Fe}_{1-x}(\text{BSFO})$  or  $\text{La}_x\text{Sr}_{1-x}\text{CoO}_3$  has emerged as a promising strategy for optimizing anode materials for OER.<sup>[5,28]</sup> Here the  $e_g$  orbital occupation was identified as a descriptor of OER activity,<sup>[29]</sup> where the improved performance of BSCFO was ascribed to an optimum occupation of the  $e_g$  orbitals of 1.2

[a] A. Füngerlings,\* R. Pentcheva

Department of Physics,  
Theoretical Physics and Center of Nanointegration (CENIDE),  
University of Duisburg-Essen,  
47057 Duisburg, Germany  
E-mail: rossitza.pentcheva@uni-due.de

[b] A. Koul,\* W. Schuhmann

Analytical Chemistry-Center for Electrochemical Sciences (CES),  
Faculty of Chemistry and Biochemistry,  
Ruhr University Bochum,  
44780 Bochum, Germany

[c] M. Dreyer,\* A. Rabe, M. Behrens

Faculty for Chemistry,  
Inorganic Chemistry and Center of Nanointegration (CENIDE),  
University of Duisburg-Essen,  
45141 Essen, Germany

[d] D. M. Morales

Nachwuchsgruppe Gestaltung des Sauerstoffentwicklungsmechanismus,  
Helmholtz-Zentrum Berlin für Materialien und Energie GmbH,  
Hahn-Meitner-Platz 1, 14109 Berlin, Germany

[e] M. Behrens

Institute for Inorganic Chemistry,  
Christian-Albrechts-Universität zu Kiel,  
24118 Kiel, Germany

[†] Contributed equally

[‡] Supporting information for this article is available on the WWW under  
<https://doi.org/10.1002/chem.202102829>

[§] Part of a Special Issue on Contemporary Challenges in Catalysis.

© 2021 The Authors. Chemistry - A European Journal published by Wiley-VCH GmbH. This is an open access article under the terms of the Creative Commons Attribution Non-Commercial NoDerivs License, which permits use and distribution in any medium, provided the original work is properly cited, the use is non-commercial and no modifications or adaptations are made.

which tunes the B–O binding energy.<sup>[26]</sup> Furthermore, the critical role of the Co 3d – O 2p covalency as a function of Sr substitution at the A site,<sup>[26,30,31]</sup> the role of oxygen vacancies and the stabilization of higher spin states of Co in nanoparticles have been recognized.<sup>[26,30,32–34]</sup> Previous theoretical studies on  $\text{LaXO}_3$  suggest that  $\text{LaCoO}_3$  has a higher OER activity than  $\text{LaFeO}_3$ .<sup>[32,35–38]</sup> Here, we focus particularly on the effect of cation mixing at the B-site and present a combined theoretical and experimental study of the  $\text{LaFeO}_3\text{-LaCoO}_3$  series as an OER catalyst to gain insight into possible synergy effects between Co and Fe.

$\text{LaCo}_x\text{Fe}_{1-x}\text{O}_3$  (LCFO) has previously been synthesized and studied as a catalyst for various reactions involving hydrocarbons.<sup>[39–41]</sup> The synthesis of LCFO by thermal decomposition of amorphous precursor materials by constant pH co-precipitation was recently reported.<sup>[42]</sup> While previous studies have concentrated on the Co-rich limit,<sup>[34]</sup> here we concentrate on the Fe-rich phases with samples synthesized in small steps of 0.025 to 0.050 in the range up to  $x = 0.300$  to avoid the formation of secondary phases. Rotating disk electrode voltammetry is applied to study the OER activity with Co substitution. The nature of the observed effects is probed by double layer capacitance experiments. To investigate the role of Co incorporation on the OER overpotential and the origin of the non-monotonic trend and shed light on the underlying mechanisms, we have performed density functional theory calculations with a Hubbard  $U$  term. Prior to assessing the OER activity, we discuss the properties of bulk LCFO and identify the relevant surface orientations and terminations in the framework of *ab initio* thermodynamics. Moreover, the coverage of the surface with O- and OH-groups under reaction conditions as a function of applied voltage and pH is compiled in a Pourbaix diagram. The calculated OER overpotentials are compared to the experimental data and correlated to the binding energy difference of  ${}^{\circ}\text{O}$  and  ${}^{\circ}\text{OH}$ . To gain further understanding, the energetic trends are traced back to the changes in electronic properties in terms of variation of the oxidation state of the reaction site and its neighbors during OER.

## 2. Results and Discussion

### 2.1. Catalyst Synthesis and Characterization

$\text{LaCo}_x\text{Fe}_{1-x}\text{O}_3$  perovskites were obtained through thermal decomposition of amorphous precursor materials synthesized by constant pH co-precipitation in a semi-automatized lab reactor system as reported previously.<sup>[42]</sup> The materials in this study were freshly synthesized in steps of 0.025 to 0.050 difference in Co content determined by the  $\text{Co}/(\text{Co}+\text{Fe})$  ratio, in order to study the effect of composition differences on the catalytic properties in small steps.

Powder X-ray diffraction (XRD) patterns of the co-precipitated precursors are shown in the Supporting Information in Figure S1. For  $x > 0.050$ , the formation of a crystalline secondary phase corresponding to the (003) reflection of the CoFe-hydrotalcite (ICSD collection code 6296) was observed at 12

$2\theta$ ,<sup>[43]</sup> as reported before,<sup>[42]</sup> which increased with the nominal Co content in the metal salt solution used in synthesis. The precursor materials were slightly Co deficient compared to Fe, as was observed in the experimentally determined  $\text{Co}/(\text{Co}+\text{Fe})$  ratio ( $x_{\text{exp}}$ ) from atomic absorption spectroscopy (AAS), as shown in Table S1. The deficiency in Co matched well with the lattice parameters after Rietveld refinement of the perovskite catalysts derived after thermal decomposition and is slightly less pronounced compared to the previous report.<sup>[42]</sup>

In Figure 1(a), the XRD patterns of the materials after thermal treatment at 800 °C are shown. Sample  $x = 0.000$  corresponds to orthorhombic  $\text{LaFeO}_3$  (ICSD: 93611).<sup>[44]</sup> With increasing Co content, the reflections were shifted to higher angles (indicated by the dotted line at the most intensive (112) reflection, see also zoom-in of this peak in Figure 1(b)) showing that the incorporation of Co into the orthorhombic perovskite structure is accompanied by a decrease in the lattice spacings due to the smaller effective ionic radius of low-spin  $\text{Co}^{3+}$  in comparison to  $\text{Fe}^{3+}$  in octahedrally coordinated sites.<sup>[45,46]</sup> The reduction of the lattice parameters with  $x$  is supported also by the DFT +  $U$  calculation, a comparison is shown in Figure 3. From our previous work, also a distortion of the  $M\text{-O}_6$  octahedra is expected, that results in a weaker force constant of the transition metal oxygen bond.<sup>[42,47]</sup>

From transmission electron microscopy (TEM), faceted crystalline particles were detected, as also reported in a previous study.<sup>[42]</sup> An exemplary image for  $x = 0.000$  is shown in Figure 1(c). The high-angle annular darkfield (HAADF) scanning TEM (STEM) image in Figure 1(d) with a viewing direction along the [110] direction and an overlay of the crystal structure indicates a (001) termination of the particle at the upper right row of the image indicated by a red arrow. From energy-dispersive X-ray spectroscopy (EDX) elemental mapping, the A and B cation layers can be identified and the image suggests a B-termination of this  $\text{LaFeO}_3$  particle, as shown in Figure 1(e). The pattern of the Fe and La ions follow the contrast changes in the right side of the image in the not-mapped area.

Adsorption isotherms for the calcined perovskite samples are displayed in Figure S2(a),  $\text{N}_2$  in the Supporting Information. All isotherms were described by a type IVa hysteresis loop.<sup>[48]</sup> The corresponding pore-size distributions are shown in Figure S2(b). The distributions were derived via the BJH method from desorption data. The pore size distributions showed a maximum in the range of 20–30 nm for the samples, indicating mainly interparticle pores. In Table S1, BET surface areas calculated from  $p/p_0$  data between 0.05 and 0.3, average pore sizes determined by the BJH method during desorption and total pore volumes determined at  $p/p_0 = 0.99$  are listed. None of them showed a clear trend with Co content. The pore volumes seemed to be increasing up to  $x = 0.100$ , but decreased again beyond this value. The same applied to the BET surface area, with an outlier at  $x = 0.250$ . Overall, there is no clear correlation between the adsorption-desorption behavior and the Co content.

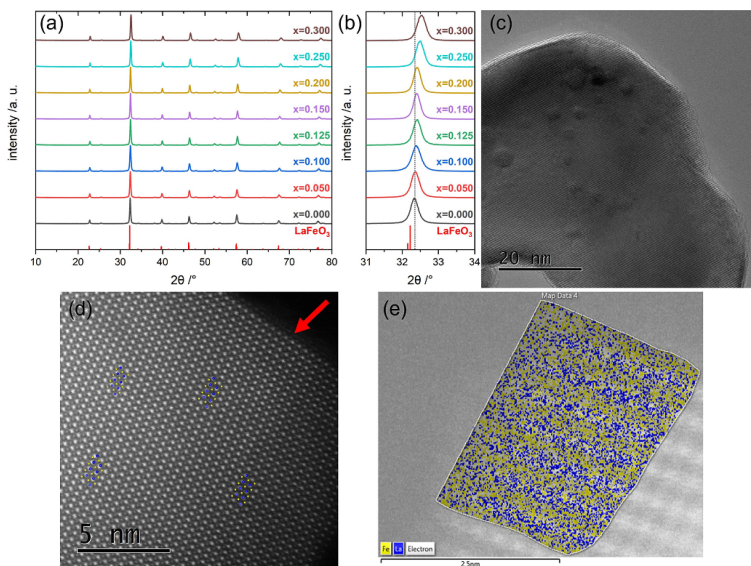


**Figure 1.** (a) XRD powder patterns of the calcined materials. (b) XRD powder patterns of the (112) reflections. (c) HR-TEM micrograph of  $x = 0.000$ . (d) HAADF-STEM micrograph of  $x = 0.000$  with insets of the  $\text{LaFeO}_3$  lattice along the [110] direction, lanthanum ions are shown in blue, iron ions in yellow. (e) STEM elemental mapping in a selected area showing the A and B cation layers, oriented along the (001)-direction, lanthanum ions are shown in blue, iron ions in yellow.

## 2.2. Catalytic Activity Measurements

Investigation of the OER activity of the different perovskite samples was conducted by rotating disk electrode voltammetry. The averages of three independent measurements are shown in Figure 2(a). Evidently, the sample with the lowest activity in terms of overpotential and current density was  $\text{LaFeO}_3$ . A substantial decrease in the OER overpotentials is observed even with a minor addition of Co to the perovskite structure. In order to evaluate the OER activity in relation to the cobalt content, the potentials required to reach a current density of  $10 \text{ mA}/\text{cm}^2$ ,  $E_{J=10}$ , were extracted from the voltammograms shown in Figure 2(a) as a function of the composition with increasing cobalt content  $x$ , Figure 2(b). The obtained values are summarized in Table S2. Since the data show no clear correlation between measured overpotentials and BET, the effect of BET surface area on the electrochemical reaction can be neglected, whereas the Co content is decisive. For the pristine Fe perovskite, i.e.,  $\text{LaFeO}_3$ ,  $E_{J=10}$  was 1.760 V. For the samples with  $x = 0.05, 0.10$ ,  $E_{J=10}$  values of 1.702 and 1.682 V were obtained, which are lower by about 60 and 80 mV than that of  $\text{LaFeO}_3$ , respectively. Similar trends of increased activity upon incorporation of small amounts of Co into a Fe oxide structure have been observed previously.<sup>[49,50]</sup> However, further Co incorporation led to an overall increase in overpotentials, rendering  $\text{LaCo}_{0.1}\text{Fe}_{0.9}\text{O}_3$  ( $x = 0.100$ ) the perovskite with the lowest overpotential (1.682 V) among the investigated catalysts.

It may be speculated that the observed increase in the OER overpotentials at  $x > 0.100$  could be caused by a decrease in electrical conductivity due to a lower Fe content, since it has been reported that Fe has a favorable impact on the electrical conductivity.<sup>[9,51]</sup> Assuming that the differences in electrical conductivities become more evident at larger electrode potentials according to Ohm's law, the current densities measured at a potential of 1.8 V vs RHE ( $J_{1.8}$ ) were extracted from the voltammograms shown in Figure 2(a) and compared as a function of the Co content, Figure 2(c). The obtained values are summarized in Table S2. The cobalt-free perovskite exhibited the lowest current of  $J_{1.8} \approx 19 \text{ mA}/\text{cm}^2$ , whereas  $\text{LaCo}_{0.1}\text{Fe}_{0.9}\text{O}_3$  displayed the largest current density, with  $J_{1.8} \approx 45 \text{ mA}/\text{cm}^2$ . Further increase in Co content led to lower current densities. Even though similar activity trends were displayed with the activity parameters  $E_{J=10}$  and  $J_{1.8}$ , for the latter a more pronounced nonmonotonic trend was observed at larger Co contents. Thereby, differences in electrical conductivity alone cannot explain the observed activity trend in relation to the composition.

Differences in the electrochemically active surface area (ECSA) may also play a role in the observed activity trend. To investigate this, double layer capacitance,  $C_{DL}$ , which is proportional to the ECSA, was determined for the different samples by scan rate-dependent cyclic voltammetry following a procedure reported recently.<sup>[52]</sup> An example of collected CVs and the resulting charging current vs scan rate plot is shown in the

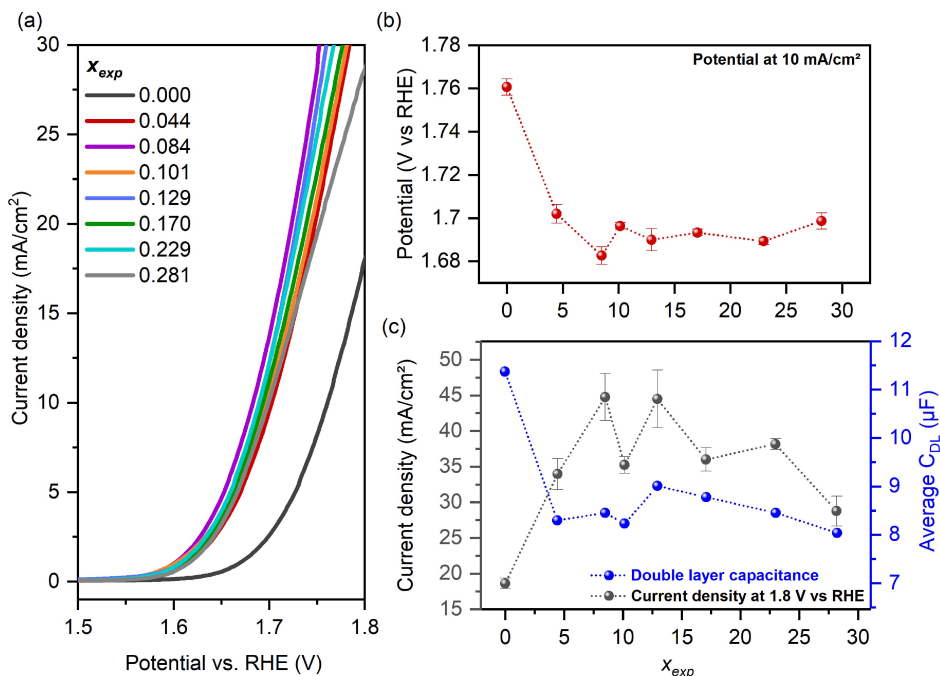


**Figure 2.** (a) Linear sweep voltammograms of  $\text{LaCo}_x\text{Fe}_{1-x}\text{O}_3$  perovskites recorded at a scan rate of 5 mV/s and electrode rotation of 1600 rpm in Ar-saturated 1 M KOH as electrolyte, and the corresponding (b) potentials measured at 10 mA/cm<sup>2</sup>, and (c) current densities attained at 1.8 V vs. RHE and average double layer capacitance ( $C_{DL}$ ). Error bars in (b) and (c) represent the standard deviation.

Supporting Information (Figure S3). The average  $C_{DL}$  values obtained for each of the samples using the allometric regression model are reported in Table S3 along with their respective coefficient of determination,  $R^2$ , and exponent,  $\alpha$ , and are additionally shown in Figure 2(c). The  $C_{DL}$  values exhibited by the different perovskite samples were rather similar, ranging from 8 to 11 μF. However, the  $C_{DL}$  plot also follows a nonmonotonic trend in the  $x$  range between 0.05 and 0.2, which could explain the nonmonotonic pattern seen for the activity parameters  $E_{f-10}$  and  $J_{1.8}$  in this same cobalt content range. Yet, the highest capacitance (~11 μF) was obtained with the sample  $x = 0$ , which was also the perovskite that exhibited the lowest OER currents and largest overpotentials, indicating that the observed differences in activities are not only due to differences in ECSA or electrical conductivity, as discussed earlier, but also to differences in intrinsic activity.

### 2.3. DFT + U calculations

In order to explore the origin of improved OER activity of  $\text{LaCo}_x\text{Fe}_{1-x}\text{O}_3$  with Co incorporation and the nonmonotonic dependence on concentration, we performed density functional

theory calculations with a Hubbard  $U$  term. The OER performance of  $\text{LaCo}_x\text{Fe}_{1-x}\text{O}_3$  was investigated for four different Co concentrations: with  $x = \{0, 0.125, 0.250, 0.500\}$ . In a first step, we assessed the bulk properties of  $\text{LaCo}_x\text{Fe}_{1-x}\text{O}_3$  for these concentrations. Transition metal cations, in particular Co, can exist in different spin states: high (HS), intermediate (IS) or low spin (LS) state.<sup>[53–56]</sup> Moreover, the B cations' spins can order either ferro- or antiferromagnetically. Furthermore, different arrangements of the Co and Fe-cations are possible. All possible B-cation arrangements within a  $2 \times 2 \times 2$  unit cell in combination with possible magnetic configurations as well as high and low spin states were examined and the relative stability of these configurations as a function of  $x$  are listed in Table S6 in the SI. The lowest energy configuration across all concentrations turned out to be Co having only Fe nearest neighbors (G-type cation order), with all Co-ions being  $\text{Co}^{3+}$  LS with nearly quenched magnetic moment ( $0.11\text{--}0.28 \mu_B$ ) and all Fe-ions in  $\text{Fe}^{3+}$  HS with a magnetic moment of  $\sim 4.1 \mu_B$  and G-type antiferromagnetic (G-AF) order (i.e. nearest Fe-neighbors with opposite spin). Only for  $x = 0.500$  the latter competes with a ferromagnetic configuration. Furthermore, for  $x = 0.250$  we observed a close competition between the different cation orders, but most importantly also the Co HS configuration lies

close in energy. A similar effect was reported previously for the Co-rich limit ( $x = 0.900$ ).<sup>[34]</sup> The spin densities of the most stable configurations for each concentration are shown in Figure 3(a). The measured and calculated lattice parameters are displayed in Figure 3(b) and exhibit a decrease as a function of cobalt concentration, albeit the theoretical values are slightly lower, which is likely related to the choice of the PBEsol exchange correlation functional. Moreover, we determined the B–O–B bond angles as a measure of the lattice distortion and octahedral tilts and rotations (the stronger the deviation from 180°, the stronger the distortion). While in LFO the calculated Fe–O–Fe angles are ~155°, they are slightly lowered to ~154° for  $x = 0.125$  and subsequently increase to ~156° for  $x = 0.250$ . Likewise, also the Co–O–Fe angles show a non-monotonic trend varying from ~158° for  $x = 0.125$  to ~156° for  $x = 0.250$  and ~161° for  $x = 0.500$ .

For an initial assessment of changes of bulk conductivity due to Co mixing in LCFO, we report the DFT+U projected density of states and band gaps for the studied concentrations (see Figure S5 in SI). The band gaps are substantially reduced from 2.15 eV for  $\text{LaFeO}_3$  to 1.68 eV ( $x = 0.125$ ), 1.64 ( $x = 0.250$ , here the Co HS state has a lower gap of 1.07 eV due to a localized state in the gap) and 1.47 eV ( $x = 0.500$ , here the FM configuration has a similar band gap of 1.42 eV).

In order to select the most relevant surface orientations and terminations for the OER modelling, we determine their stability in the framework of *ab initio* thermodynamics,<sup>[57,58]</sup> using Eq. (5), as described in the Methods Section. The surface phase diagram was constructed for the (001), (110) and (111) orientations with two possible terminations each.

Figure 4 displays the most stable favorable orientations and terminations as a function of the chemical potentials of La and O. The relevant synthesis conditions coincide with a region of

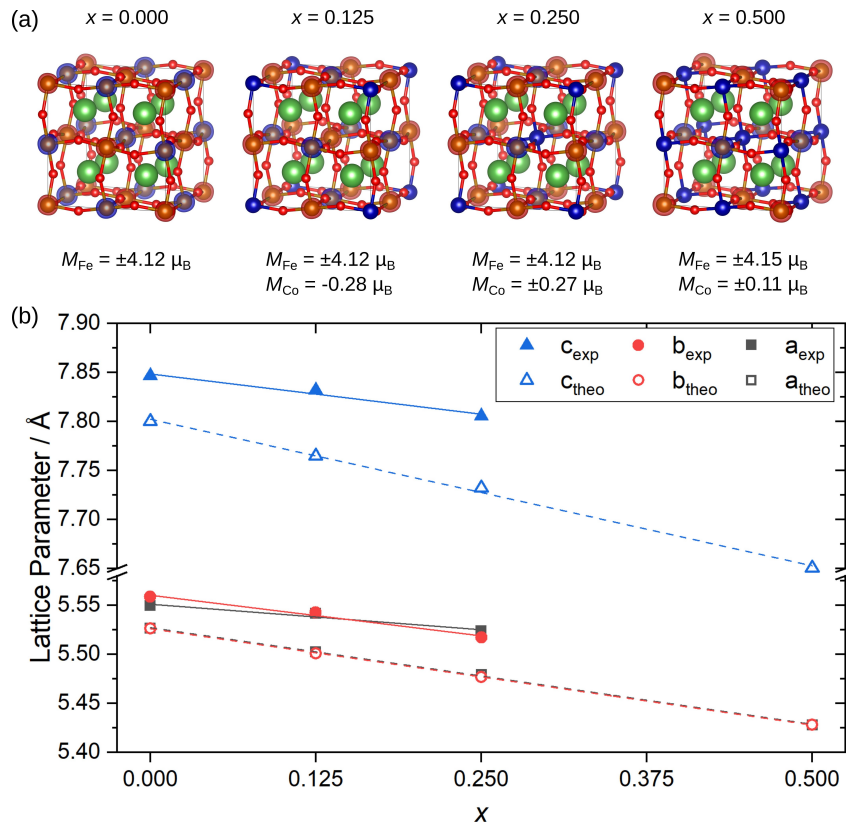


**Figure 3.** (a) Relaxed structures of the most stable configurations of bulk  $\text{LaCo}_x\text{Fe}_{1-x}\text{O}_3$  (G-type cation and antiferromagnetic order with Fe (HS) and Co (LS)) together with the spin-densities for the different Co concentrations. Green, bronze, blue and red spheres denote La, Fe, Co and O, respectively. Red and blue clouds indicate positive and negative spin densities in the antiferromagnetically coupled systems. Additionally, the magnetic moments of Fe and Co are given. (b) Comparison of experimental and theoretical lattice constants as a function of Co/Co + Fe ratio.

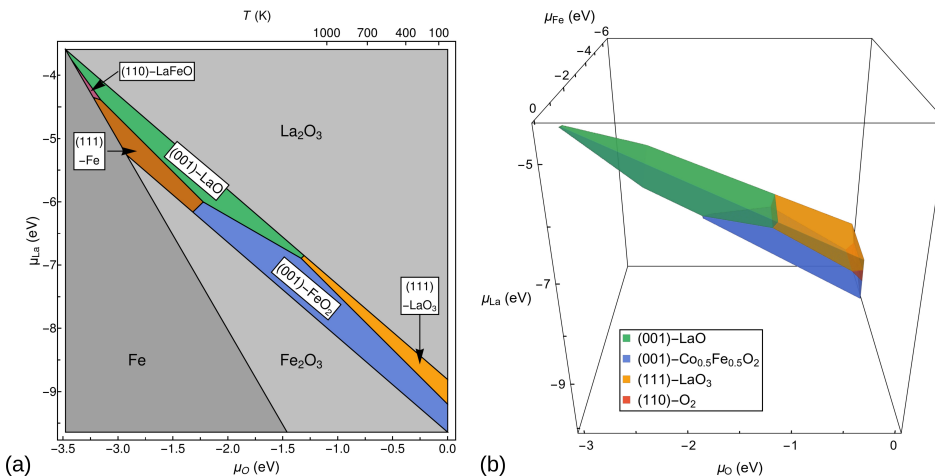


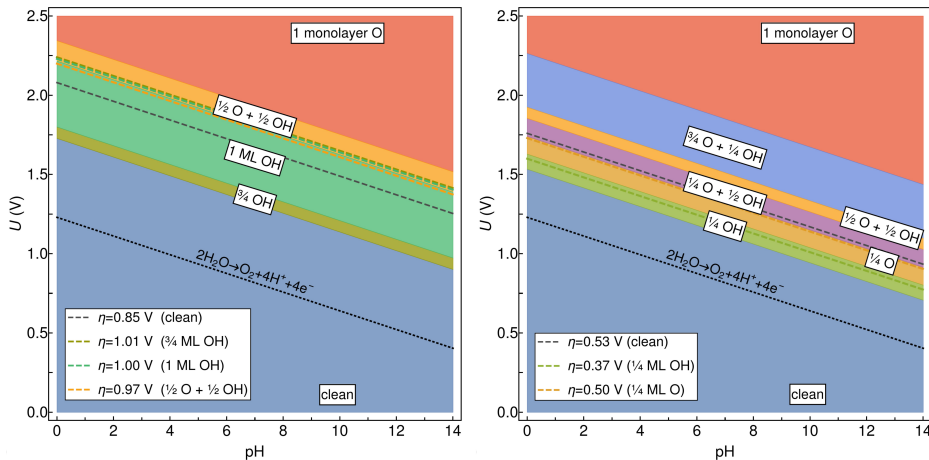
**Figure 4.** Surface stability diagrams for (a)  $\text{LaFeO}_3$  and (b)  $\text{LaCo}_{0.5}\text{Fe}_{0.5}\text{O}_3$  showing the most stable orientations and terminations as a function of  $\mu_{\text{La}}$  and  $\mu_{\text{O}}(T, p_{\text{O}_2})$ . On the top axis the latter is converted into  $T$  for  $p_{\text{O}_2} = 1 \text{ atm}$ .

stability of the  $\text{BO}_2$ -termination of the (001) surface. This is also consistent with the (001) orientation and the Fe enrichment at the surface obtained from TEM (cf. Figure 1(e)). Therefore in the following we focus on the  $\text{BO}_2(001)$  termination to study the OER activity.

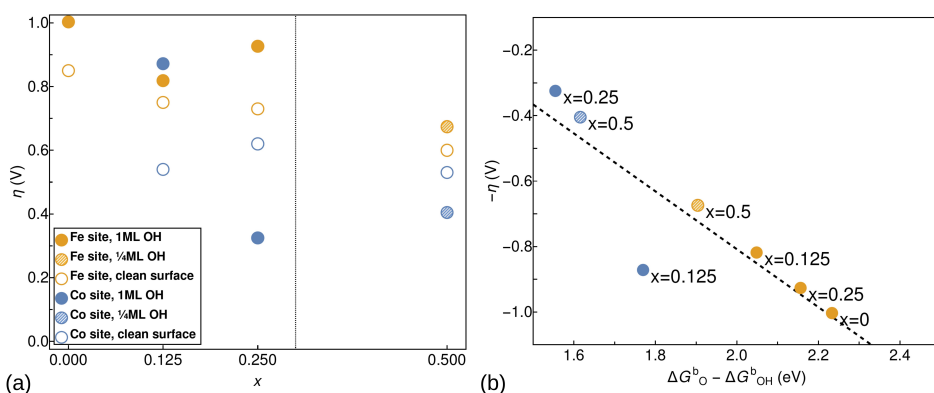
When the catalyst's surface is in contact with an aqueous solution, oxo- and hydroxyl-groups are expected to form, the extent and composition depending on the solution's pH as well as on the applied voltage. A surface Pourbaix diagram was constructed to explore the stability of surface functional groups using Eq. (6), as described in the Computational Section, see also Ref. [59]. The four B-cation sites at the surface were covered by one to four  ${}^{\circ}\text{O}$  and/or  ${}^{\circ}\text{OH}$  corresponding to one quarter to a full monolayer (ML) in all possible combinations regarding also the order of cations at the B-sites. From all studied combinations the system with the lowest free energy was selected. The Pourbaix diagrams for  $\text{LaFeO}_3(001)$  and  $\text{LaCo}_{0.5}\text{Fe}_{0.5}\text{O}_3(001)$  in Figure 5 show a broad region of stability of the clean surface up to 1.7 V and 1.5 V for the former and latter, respectively, followed by an increasing coverage by hydroxyl groups and subsequently mixed and oxygenated surfaces with increasing voltage. The calculated OER potentials,  $\phi_{\text{OER}}$ , derived from Eq. (12), are also shown in Figure 5 by dashed lines. For  $\text{LaCo}_{0.5}\text{Fe}_{0.5}\text{O}_3(001)$ ,  $\phi_{\text{OER}}$  of the precovered surfaces lies in the region of corresponding coverage, 1/4 ML OH and 1/4 ML O. For  $\text{LaFeO}_3(001)$ , the region of stability 1 ML OH is broader and  $\phi_{\text{OER}}$  lies slightly above the border to a mixed OH and O coverage. Since also the experimentally applied voltage (1.76 V at pH 13) lies in this region, we have investigated the OER for 1 ML OH-coverage besides the clean surface. This coverage was also adopted for  $x = 0.125$  and  $x = 0.250$ .

Figure 6(a) shows the overpotentials  $\eta$  (see Eq. (14) in the Methods section) for the clean and precovered surfaces of  $\text{LaCo}_{1-x}\text{Fe}_x\text{O}_3(001)$  with  $\text{BO}_2$  termination as a function of Co contents for both Fe and Co reaction sites. For both reaction sites a reduction of the overpotential with  $x$  is observed compared to the end member  $\text{LaFeO}_3$  ( $\eta = 1.0 \text{ V}$ ), demonstrating the favorable role of Co substitution. Overall, the overpotentials for Co reaction sites are lower than for Fe. The precovered surfaces tend to have higher overpotentials, except for a Co site at the surface covered by 1 ML OH at  $x = 0.250$ , where the lowest overpotential of 0.32 V is obtained. Furthermore, the trend is overall nonmonotonic, with the above mentioned minimum for a Co reaction site for the precovered surface at  $x = 0.250$  and subsequent slight increase (the minimum for the uncovered surface is at  $x = 0.125$ ). For Fe as the reaction site the overpotential decreases from initially 1.0 V ( $x = 0.000$ ) to 0.82 V ( $x = 0.125$ ), then increases to 0.93 V ( $x = 0.250$ ) and subsequently decreases to 0.63 V for  $x = 0.500$ . The nonmonotonic trend in the calculated OER overpotentials is consistent with the experimental observation in Figure 2(b) and the presence of an outlier at  $x = 0.250$ .

To gain more insight, in Figure 6(b) we have plotted the overpotential as a function of the binding energy difference  $G_{\text{O}}^b - G_{\text{OH}}^b$ , the so-called volcano plot.<sup>[35]</sup> The results show that all cases lie on the strong binding leg and reflect both the nonmonotonic trend with coverage, but in particular the improvement of  $\eta$  with the reduction of the binding energy difference towards an optimum value below 1.6 eV,<sup>[16,18]</sup> achieved for the Co site at the fully hydroxylated surface at  $x = 0.250$ . Interestingly, values of  $\eta$  for Co and Fe sites are well separated, the latter lying at much higher binding energy differences between 2.2 and 2.4 eV.



**Figure 5.** Pourbaix diagrams for (a)  $\text{LaFeO}_3(001)$  and (b)  $\text{LaCo}_{0.5}\text{Fe}_{0.5}\text{O}_3(001)$  showing the most stable coverage as a function of applied voltage and pH value. Dashed lines indicate the highest reaction free energy that determines the overpotential for OER, which can be plotted as a function of pH, according to Eq. (12), as described in the Methods section.



**Figure 6.** (a) OER overpotential as a function of Co concentration. The dashed vertical line at  $x = 0.3$  indicates the threshold up to which phase-pure perovskite samples could be synthesized and OER activity was measured experimentally (see Figure 2(b)). (b) Overpotential as a function of the difference of  ${}^*\text{O}$  and  ${}^*\text{OH}$  adsorption energies for covered surfaces with linear fit to the data with slope: 0.88 V/eV.

In order to gain further understanding of the effect of Co mixing and the nonmonotonic trend of the overpotential with  $x$ , we have plotted in Figure 7 the cumulative reaction free energies of Fe- and Co-sites for all compounds.  $\Delta G_i$  and  $\eta$  are also listed in Table 1 (the individual steps are defined in Equations (7)–(10) in the Methods section). In most cases the potential determining step turns out to be  ${}^*\text{OH} \rightarrow {}^*\text{O}$  (step 2), except for a Fe site at the clean and a Co site at the precovered surface for  $x = 0.125$ , where  $\Delta G_1$  – the formation of  ${}^*\text{OH}$  – is highest. Overall, the potential determining steps for Fe reaction sites are  $\sim 0.2 - 0.3$  eV higher than for Co and increase by

$\sim 0.2$  eV for the hydroxylated surface, resulting overall in higher overpotentials for Fe sites than for Co. For the latter, hydroxylation reduces the overpotential by 0.30 and 0.13 eV for  $x = 0.250$  and  $x = 0.500$ , respectively. The Co site at the hydroxylated surface for  $x = 0.125$  marks the only case where the overpotential of a Co site is increased and comparable to the ones of the Fe sites. Altogether, especially for the higher concentrations of Co, the heights of the individual intermediate steps become comparable, which is a desirable feature for optimum OER activity<sup>[35]</sup> and has also been predicted for spinel surfaces,  $\text{CoFe}_2\text{O}_4(001)$  and  $\text{Co}_3\text{O}_4(001)$ .<sup>[16,18]</sup>

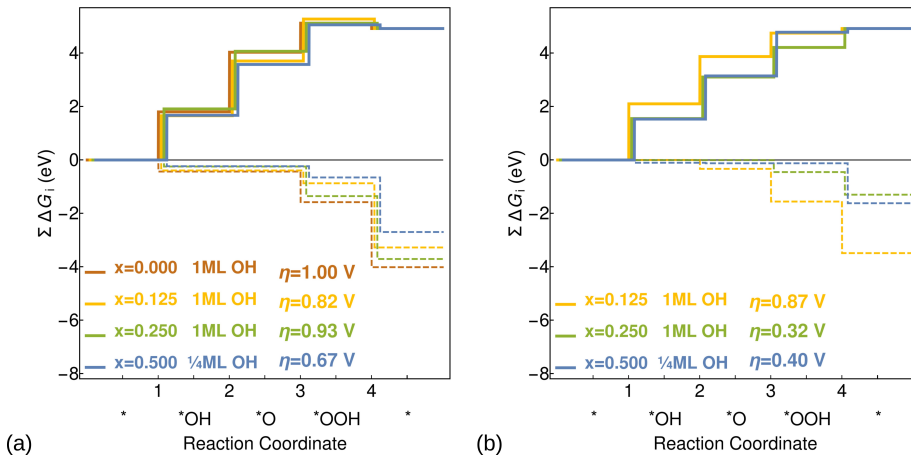


**Figure 7.** Cumulative reaction free energies of the OER intermediates (solid lines) for covered surfaces at (a) Fe- and (b) Co-reaction sites. The values under applied external potential  $\phi$  are denoted by dashed lines.

<b>Table 1.</b> Reaction free energies of intermediates and the resulting overpotential for Fe and Co reaction sites at the clean and hydroxylated $\text{LaCo}_x\text{Fe}_{1-x}\text{O}_3(001)$ surface. Potential determining steps are emphasized with bold font.					
<i>x</i>	$\Delta G_1$ (eV)	$\Delta G_2$ (eV)	$\Delta G_3$ (eV)	$\Delta G_4$ (eV)	$\eta$ (V)
Fe site (clean surface)					
0	1.80	<b>2.08</b>	1.27	-0.24	0.85
0.125	<b>1.97</b>	1.81	1.01	0.12	0.74
0.25	1.49	<b>1.96</b>	1.15	0.33	0.73
0.5	1.67	<b>1.83</b>	1.26	0.15	0.60
Fe site (hydroxylated)					
0	1.80	<b>2.23</b>	1.09	-0.20	1.00
0.125	1.66	<b>2.05</b>	1.57	-0.35	0.82
0.25	1.91	<b>2.16</b>	1.05	-0.20	0.93
0.5	1.67	<b>1.90</b>	1.48	-0.14	0.67
Co site (clean surface)					
0.125	1.11	<b>1.77</b>	1.15	0.89	0.54
0.25	1.17	<b>1.85</b>	1.43	0.47	0.62
0.5	1.53	<b>1.63</b>	1.76	-0.00	0.53
Co site (hydroxylated)					
0.125	<b>2.10</b>	1.77	0.88	0.17	0.87
0.25	<b>1.55</b>	<b>1.55</b>	1.11	0.71	0.32
0.5	1.53	<b>1.62</b>	<b>1.63</b>	0.14	0.40

We next correlate the energetic trends with the underlying electronic properties. Figures 8 and 9 show the side views of the structures, spin density and magnetic moments of cations for the OER intermediates for different Co concentrations and Fe and Co reaction sites, respectively. We start with the Fe reaction site in Figure 8: For  $x = 0.000$  the hydroxylated surface (except for the reaction site) prior to adsorption (\*) shows bulk-like behavior with  $\text{Fe}^{3+}$  (magnetic moment  $\sim 4.1 \mu_B$ ) in the third layer and an increasing fraction of  $\text{Fe}^{2+}$  (magnetic moment  $\sim 3.5 - 3.6 \mu_B$ ) in the subsurface (50%) and surface layers

(75%), with antiferromagnetic order in all layers. For the  $^*\text{OH}$  intermediate, which corresponds to a fully hydroxylated surface, the top layer is exclusively  $\text{Fe}^{2+}$ , whereas the charge states of Fe for the  $^*\text{O}$  and  $^*\text{OOH}$  intermediates resemble more strongly the ones at \*, except for the  $\text{Fe}^{4+}$  (magnetic moment  $2.36 \mu_B$ ) at the reaction site for 'O'.

With Co incorporation, significant changes occur in the magnetic moments, signalling changes in valence and/or spin state. In contrast to bulk  $\text{LaCo}_x\text{Fe}_{1-x}\text{O}_3$  where  $\text{Co}^{3+}$  LS prevails, at LCFO(001) Co acquires a finite magnetic moment even in the third layer ( $0.68 - 2.90 \mu_B$ ). Unlike  $x = 0.000$ , for  $x = 0.125$  the Fe reaction site is  $\text{Fe}^{2+}$  (\*), changes to  $\text{Fe}^{3+}$  ( $^*\text{OH}$ ),  $\text{Fe}^{4+}$  for  $^*\text{O}$  and back to  $\text{Fe}^{3+}$  for  $^*\text{OOH}$ . Overall the presence of Co enhances the  $\text{Fe}^{3+}$  fraction in  $\text{LaCo}_x\text{Fe}_{1-x}\text{O}_3(001)$ , albeit in the subsurface layer the  $\text{Fe}^{2+}$  fraction varies from 0 (\*), to 1/4 ( $^*\text{OH}$  and  $^*\text{O}$ ) and 1/2 ( $^*\text{OOH}$ ). For  $x = 0.250$  the charge states of the reaction site resemble rather those at  $x = 0.000$ , whereas the variation of charge states at the Fe reaction site for  $x = 0.500$  are similar to the ones for  $x = 0.125$ . This may explain the nonmonotonic trend in the overpotentials of the Fe reaction site with an initial decrease and subsequent increase of  $\eta$  both in the predicted and measured values at  $x = 0.250$ . Interestingly, for  $x = 0.500$  Co in the third layer is low spin ( $\sim 0.1 \mu_B$ ), but the Co magnetic moment increases to  $\sim 1.0 - 1.2 \mu_B$  in the subsurface layer and to  $2.2 - 2.97 \mu_B$  in the surface layer which indicates a higher fraction of  $\text{Co}^{2+}$  at the surface.

Turning now to the Co reaction site in Figure 9, for  $x = 0.125$  its magnetic moment is reduced from initially  $-2.13 \mu_B$  (\*) to  $-1.26 \mu_B$  ( $^*\text{OH}$  and  $^*\text{O}$ ) and subsequently increased to  $-1.58 \mu_B$  ( $^*\text{OOH}$ ). For  $x = 0.250$  its magnetic moment is  $-0.65 \mu_B$  at \* and increases to  $-1.80 \mu_B$  for the remaining intermediate steps. Finally, for  $x = 0.500$  the Co reaction site has a magnetic moment of  $2.23 \mu_B$  for all

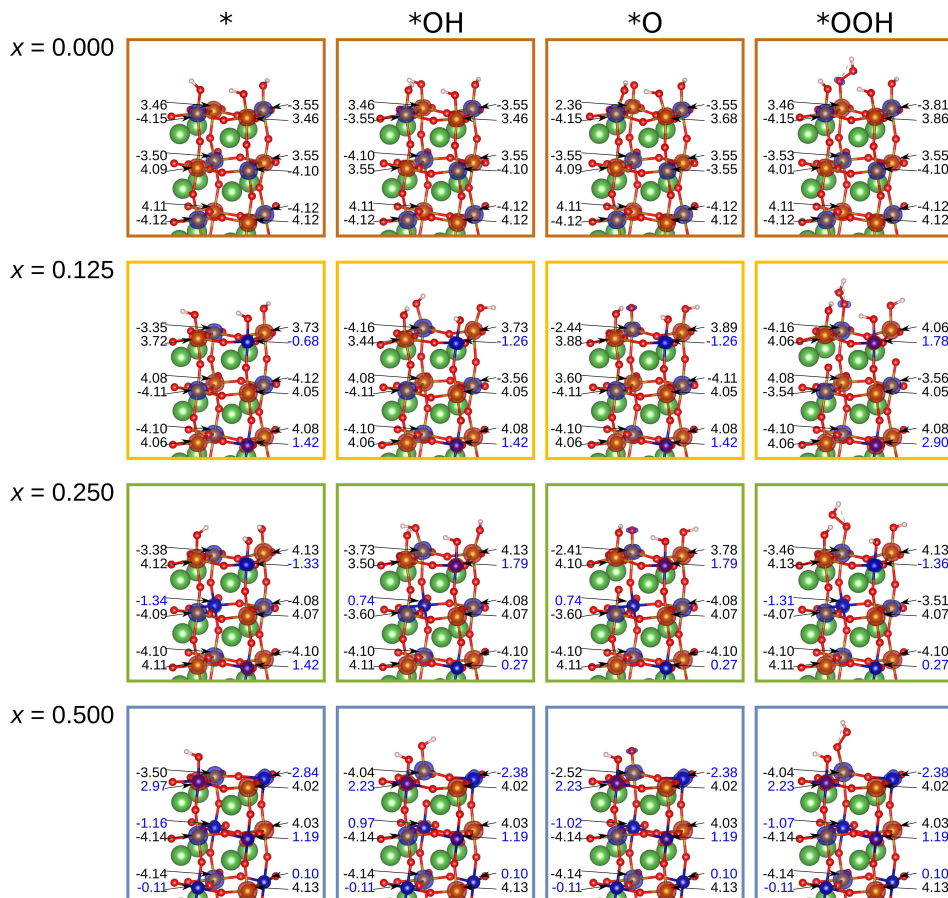


**Figure 8.** Side view of the relaxed structures together with the spin density of the hydroxylated surface for the four OER steps of a Fe reaction site at  $\text{LaCo}_x\text{Fe}_{1-x}\text{O}_3(001)$  with different concentrations  $x$ . Additionally, the magnetic moments of the Fe (black) and Co-cations (blue) in the three topmost layers are given in  $\mu_{\text{B}}$ .

intermediates except for  $^*\text{OOH}$ , where it is  $1.15 \mu_{\text{B}}$ . We note that due to the antiferromagnetic order of  $\text{LaCo}_x\text{Fe}_{1-x}\text{O}_3$ , the active site has in some cases a positive and in some a negative magnetic moment. How the orientation of the magnetic moment may affect the OER activity is an important question that needs to be addressed in further studies.

While the magnetic moment of the Co reaction site shows less variation, more pronounced changes occur at the subsurface Co-sites with changes between 0.28 and  $1.43 \mu_{\text{B}}$  for  $x = 0.125$  and 0.250. For  $x = 0.500$ , the magnetic moments of subsurface Co vary from 0.10 and  $2.57 \mu_{\text{B}}$ , whereas the third layer contains almost exclusively  $\text{Co}^{3+}$  LS.  $\text{Fe}^{2+}$  is present in the surface and, to a lesser extent, subsurface layer, but its fraction

decreases noticeably with  $x$ , leading to an overall stabilization of  $\text{Fe}^{3+}$ .

Altogether, the fraction of bulk-like  $\text{Fe}^{3+}$  HS and  $\text{Co}^{3+}$  LS increases with  $x$  which may correlate with the nonmonotonic trend and subsequent increase of  $\eta$ . On the other hand, the substantial changes in magnetic moments at  $\text{LaCo}_x\text{Fe}_{1-x}\text{O}_3(001)$  during OER involve multiple ions also further away from the reaction site. In some cases the changes in magnetic moment are even more pronounced at the neighboring sites than at the reaction site, implying a concerted process with involvement of several coordination shells. This indicates that the concept of the active site goes significantly beyond the single reaction site and the surrounding cations, including deeper layers, play an important role and give important hints towards the synergy

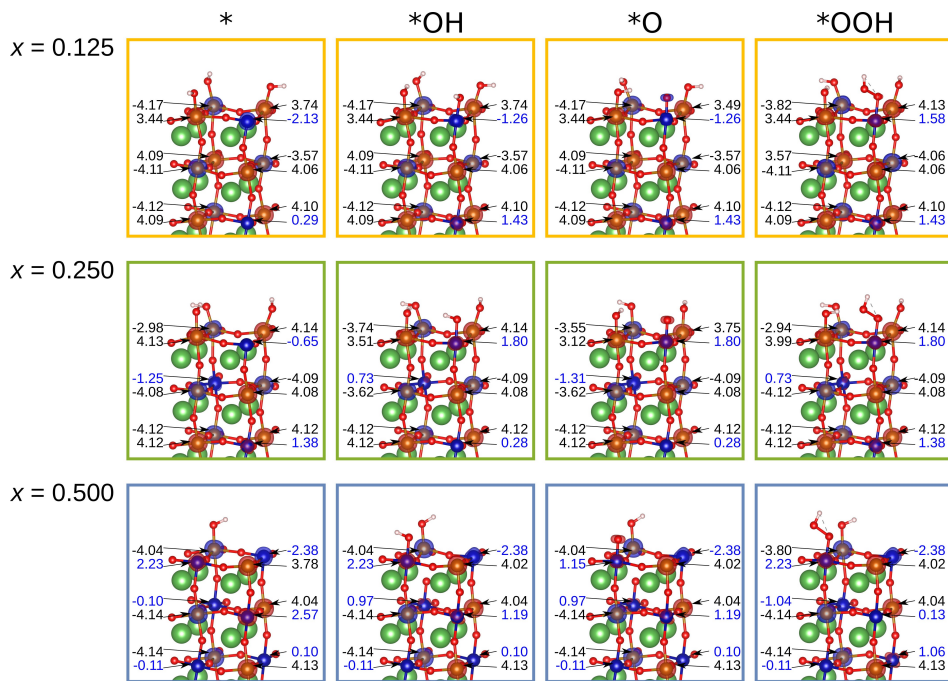


**Figure 9.** Side view of the relaxed structures together with the spin density of the hydroxylated surface for the four OER steps of a Co reaction site at  $\text{LaCo}_x\text{Fe}_{1-x}\text{O}_3(001)$  with different concentrations  $x$ . Additionally, the magnetic moments of the Fe (black) and Co-cations (blue) in the three topmost layers are given in  $\mu_{\text{B}}$ .

effects between Co and Fe in LCFO as an anode material for OER.

### 3. Conclusions

In a combined experimental and theoretical study we explored the OER activity of  $\text{LaCo}_x\text{Fe}_{1-x}\text{O}_3$  as a function of Co concentration. Rotating disc electrode voltammetry of phase pure perovskites with a  $\text{Co}/(\text{Co} + \text{Fe})$  ratio of up to 0.300, shows a substantial overpotential decrease of about 70 meV for even the smallest Co admixture of  $x = 0.05$ . Double layer capacitance measurements showing a slightly higher electrochemically active surface area for  $\text{LaFeO}_3$  than for the Co-containing compounds suggest that the increase in OER-activity is intrinsic. The positive effect of Co incorporation and the nonmonotonic trend with  $x$  are confirmed by DFT+ $U$  calculations at  $\text{BO}_2^-$ -terminated  $\text{LaCo}_x\text{Fe}_{1-x}\text{O}_3(001)$  surfaces. This surface termination was found to be stable at the relevant synthesis conditions, according to the surface phase diagram and is also supported by TEM measurements. The calculations show that the OER overpotentials are reduced for both Fe and Co reaction sites with Co incorporation, but those of Co are significantly lower,

reaching values of 0.32–0.40 V, compared to 0.60–0.67 V for Fe. This correlates with a lowering of the binding energy difference between  ${}^*\text{O}$  and  ${}^*\text{OH}$  to below 1.6 eV for Co at  $x = 0.250$ . We note that the deprotonation of  ${}^*\text{OH}$  comprises the potential limiting step in the majority of cases considered. The non-monotonic trend in the calculated microscopic overpotentials is correlated to the electronic and magnetic properties. We observe strong changes of the magnetic moments during OER, in particular with Co incorporation, indicative of changes in oxidation state, as found previously at spinel surfaces, e.g.  $\text{CoFe}_2\text{O}_4$  and  $\text{Co}_3\text{O}_4(001)$ .<sup>[16,18]</sup> While a significant fraction of  $\text{Fe}^{2+}$  is present at the  $\text{LaFeO}_3(001)$  surface and subsurface layer, Co enhances the fraction of  $\text{Fe}^{3+}$ , in particular in the deeper layers. Increase of the Co concentration reduces the variation in magnetic moments at the Co reaction site during OER, which seems to have a beneficial effect on the overpotential. In contrast to spinels where the neighboring sites are much less affected and the changes are concentrated at the reaction site,<sup>[16,18]</sup> for  $\text{LaCo}_x\text{Fe}_{1-x}\text{O}_3$  the changes in magnetic moments are by far not limited to the reaction site, but occur in several coordination shells up to the third layer. This may indicate a significant difference between perovskites and spinels. Moreover, it demonstrates that the surroundings of the reaction site

plays an active role in the catalytic performance, pointing towards a generalization of the concept of the active site.

## Experimental Methods

### Raw Materials

For catalyst synthesis, commercially available reagents were used without further purification: iron(III) nitrate nonahydrate ( $\geq 98\%$ , Sigma-Aldrich GmbH, St. Louis, Missouri, USA), lanthanum(III) nitrate hexahydrate (99.9% La, abcr GmbH, Karlsruhe, Germany), cobalt(II) nitrate hexahydrate ( $\geq 98\%$ , Carl Roth GmbH, Karlsruhe, Germany), sodium carbonate ( $\geq 99.5\%$ , VWR International GmbH, Darmstadt, Germany), and sodium hydroxide (98.5%, Carl Roth GmbH, Karlsruhe, Germany).

### Synthesis

The synthesis via co-precipitation was reported before,<sup>[42]</sup> and included the preparation of metal salt stock solutions with a total ionic concentration  $M^{n+}$  of  $0.8 \text{ mol L}^{-1}$  with the composition  $\text{La}^{3+}:\text{Fe}^{3+}:\text{Co}^{2+} = 1:(1-x)x$  in deionized water. The value of  $x$  was varied in the range between 0 and 0.25. The precipitation agent consisted of  $1.2 \text{ M NaOH}$  and  $0.18 \text{ M Na}_2\text{CO}_3$  in deionized water.

The syntheses were conducted in an automated synthesis workstation OptiMax 1001 (Mettler Toledo GmbH, Greifensee, Switzerland). The setup consisted of a single-walled glass reactor fixed inside a solid-state thermostat for accurate temperature control. During precipitation and aging steps,  $\text{N}_2$  flow was employed, and the prefill volume of the reactor was purged with  $\text{N}_2$  for 30 min. Co-precipitations were performed at a constant pH of 9.5 and an isothermal temperature of 10 °C. A precision balance controlled by a universal control box allowed gravimetric dosing of the metal salt solutions of 75 g in 36 min. Control over the pH was achieved by simultaneous computer-controlled dosing of the metal salt solution and the precipitation agent via two ProMinent gamma/L metering pumps. The pH was monitored and adjusted using an InLab Semi-Micro-L electrode before each experiment. A pitched blade impeller rotating at a constant speed of 300 rpm was used to avoid concentration and temperature gradients. After the precipitation was finished, an aging step at 10 °C for 60 min was performed. After aging, the precipitate was isolated by centrifugation (6000 rpm, 2 min) and washed with deionized water until the conductivity of the supernatant was below  $0.1 \text{ mScm}^{-1}$  in two consecutive runs. Conductivity was measured using a Multi-Range Conductivity Meter HI 9033 (Hanna Instruments, Graz, Austria), which was held in the supernatant in the middle of the centrifuge tube. Afterward, the samples were dried in static air at 80 °C for 12 h. The precursors were calcined at 800 °C for 3 h ( $\beta=2 \text{ C min}^{-1}$ ) in stagnant air in a muffle furnace (B150, Nabertherm, Lilienthal, Germany). The calcined samples were characterized as powders.

### Sample Characterization

Fe and Co contents in the precursors were determined by atomic absorption spectroscopy (M-Series, Thermo Electron Corporation, Waltham, Massachusetts, United States of America).

$\text{N}_2$  adsorption and desorption experiments were conducted after degassing the samples at 80 °C for 2 h in a vacuum with a NOVA3000e setup (Quantachrome Instruments, Boynton Beach, Florida, United States of America) at  $-196$  °C. BET (Brunauer Emmet Teller) surface areas were calculated from  $p/p_0$  data between 0.05

and 0.3. Total pore volumes were determined at  $p/p_0=0.99$ . Pore size distributions were determined using the BJH method during desorption.

Powder XRD patterns in the  $2\theta$  range from 5° to 90° were recorded on a Bruker D8 Advance (Bruker, Billerica, Massachusetts, USA) diffractometer in Bragg–Brentano geometry using a position-sensitive LYNXEYE detector (Ni-filtered  $\text{CuK}_\alpha$  radiation, Bruker, Billerica, Massachusetts, USA) applying a counting time of 0.3 s and step size of 0.018°. Samples were mounted using dispersion in ethanol on a glass disc inserted in a round PMMA holder. The latter was subject to gentle rotation during scanning after removing the ethanol by drying.

High-resolution scanning transmission electron microscopy (STEM) studies were carried out on a Jeol JEM 2200 FS microscope (Akishima, Japan) equipped with a probe-side Cs-corrector operated at 200 kV acceleration voltage. Micrographs were taken in conventional bright field as well as in high-angle annular darkfield (HAADF) mode. In addition, EDX elemental mappings were acquired with an X-Max 100 detector (Oxford Instruments, Abingdon, United Kingdom).

### Electrochemical Measurements

All electrochemical measurements were conducted with a three-electrode cell configuration setup using Metrohm Autolab PGSTAT potentiostat equipped with a rotator (Metrohm). A double-junction Ag/AgCl electrode (Metrohm) filled with 3 M KCl and 1 M KOH solution at the inner and outer compartments, respectively, was used as the reference electrode. A platinum mesh was used as the counter electrode, and was kept in a compartment separated by a glass frit during the measurements. A catalyst ink was prepared by dispersing 1 mg of catalyst powder in  $200 \mu\text{L}$  of a solution comprising water, ethanol and Nafion solution (49:49:2 volume ratio). The working electrode was prepared by drop-casting  $4.8 \mu\text{L}$  of catalyst ink over a glassy carbon rotating disk electrode of  $0.1134 \text{ cm}^2$  geometric area to obtain a total catalyst loading of  $210 \mu\text{g}/\text{cm}^2$ . Prior to drop-casting, the glassy carbon substrate was polished using  $0.05 \mu\text{m}$  alumina paste until a mirror finishing was attained. Argon-saturated 1 M KOH was used as the electrolyte. The electrolyte was purified using a chelating ion resin (Chelex 100, Bio-Rad) to remove metal impurities. A stream of argon was flushed over the electrolyte during the measurements to maintain gas saturation.

Prior to activity tests, cyclic voltammetry was conducted in the potential window from  $-0.2$  to  $0.4 \text{ V}$  vs Ag/AgCl/KCl at a scan rate of  $0.1 \text{ V/s}$  until reproducible voltammograms (CVs) were obtained. Subsequently, galvanostatic electrochemical impedance spectra were recorded at  $0 \text{ A}$  in the frequency range from  $100 \text{ kHz}$  to  $100 \text{ Hz}$  with an AC amplitude of  $10 \mu\text{A}$  (RMS). From the resulting Nyquist plots, the uncompensated resistance ( $R$ ) was determined and was used to iR-drop-correct the measured potentials according to Eq. (1), considering the measured current ( $I$ ).

$$E_{\text{corrected}} = E_{\text{measured}} - I \cdot R \quad (1)$$

To investigate the OER activity, linear sweep voltammetry (LSV) was conducted in the potential range from  $0.1$  to  $0.8 \text{ V}$  vs Ag/AgCl/KCl at a scan rate of  $0.005 \text{ V/s}$  and electrode rotation speed of  $1600 \text{ rpm}$ . All measurements were conducted in triplicate. The obtained currents were normalized with respect to the geometric area of the electrode. The measured potentials were converted to the reversible hydrogen electrode (RHE) scale using Eq. (2).

$$E_{\text{RHE}} = E_{\text{Ag}/\text{AgCl}/\text{KCl}} + 0.207 + 0.059 \cdot \text{pH} \quad (2)$$

The pH of the KOH solution was calculated using Eq. (3), considering the activity of water ( $a_w$ ) in KOH as reported in the literature.<sup>[60,61]</sup>

$$\text{pH} = 14 + \log[\text{OH}^-] + \log a_w \quad (3)$$

Double layer capacitance ( $C_{DL}$ ) was determined for all perovskites following a procedure reported recently.<sup>[52]</sup> CVs were recorded in a potential window of about 0.4 V centered at the open circuit potential (OCP) at scan rates of 0.10, 0.25, 0.50, 0.75 and 1.00 V/s until reproducible voltammograms were obtained. OCP values and potential windows used for each of the samples are shown in Table S4. Charging currents measured at the potential corresponding to OCP ( $\phi$ ) were extracted from the anodic and cathodic sweeps of the last recorded CVs and plotted as a function of the scan rate ( $v$ ). The allometric regression model was used for determining  $C_{DL}$  according to Eq. (4).

$$I_C = C_{DL} v^\alpha \quad (4)$$

## Computational Methods and Details

### DFT calculations

The density functional theory calculations were carried out with the VASP code using pseudopotentials and the projector augmented wave (PAW) method.<sup>[62–65]</sup> The PBEsol exchange-correlation functional was used together with an effective Hubbard parameter  $U_{\text{eff}} = U - J$  within the Dudarev approach with  $U_{\text{eff}} = 4$  eV for Fe and 3.3 eV for Co<sup>[66,67]</sup> obtained by fitting to bulk oxide formation enthalpies.<sup>[68,69]</sup> A plane wave cutoff of 520 eV and a  $4 \times 4 \times 4$ -Monkhorst-Pack k-point mesh were used for bulk LaCo<sub>x</sub>Fe<sub>1-x</sub>O<sub>3</sub><sup>[70]</sup> which was modelled using a  $2 \times 2 \times 2$  pseudocubic unit cell to take into account different B-cation arrangements as well as octahedral tilts and distortions. The (001) oriented surfaces were modelled by slabs with a  $2 \times 2 \times 13$  geometry and separated by 15.6 Å of vacuum in z-direction to avoid interaction between the slabs and the periodic images. For these a  $4 \times 4 \times 1$  k-mesh was used. All systems were relaxed until the residual forces were below 0.01 eV/Å. Since the adsorption was only modeled on one surface, a dipole-correction in the vertical direction was applied.

### Surface stability and Pourbaix diagram

In the framework of *ab initio* thermodynamics,<sup>[57,58]</sup> the surface energy of a slab is given by:

$$\gamma = \frac{1}{2A} (E_* - M \cdot E_{\text{bulk}} - N_i \mu_i) \quad (5)$$

where  $E_*$  is the total energy of the slab with two surfaces with area  $A$  each,  $M$  the number of bulk units contained in the slab (3 in this case),  $E_{\text{bulk}}$  the bulk energy of the oxide, and  $N_i$  the number of excess ions of each species  $i$  (La, Co, Fe, O) in the slab and  $\mu_i$  the corresponding chemical potentials. The chemical potentials are not independent but are related by the condition that the bulk oxide is stable, which defines the oxygen-poor conditions, beyond which the perovskite would decompose into binary oxides and, finally, into elemental compounds. These boundaries are determined by the formation enthalpies of the corresponding bulk materials. This allows to reduce the dimensionality of the surface phase diagram

and plot it as a function of the chemical potentials of La and O for LaFeO<sub>3</sub> and additionally Fe for LaCo<sub>x</sub>Fe<sub>1-x</sub>O<sub>3</sub>. The oxygen-rich conditions are determined by the binding energy of a gas-phase oxygen molecule. Furthermore, the chemical potential of oxygen can be related to the synthesis conditions by converting it to temperature for a given oxygen partial pressure.

The Pourbaix diagram allows to determine the coverage of the surface with functional groups for given applied voltage  $U$  and pH.<sup>[59]</sup> The free energy of the surface covered by varying amounts of \*O and \*OH groups as a function of applied voltage  $U$  and pH is expressed by:

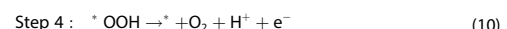
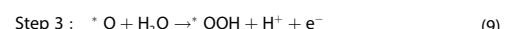
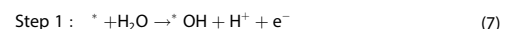
$$\Delta G = E^*_{+N_O+N_{OH}} - E^* - (N_O + N_{OH}) \Delta H_{H_2O}^f + \left( N_O + \frac{1}{2} N_{OH} \right) \Delta H_{H_2}^f \quad (6)$$

$$+ \Delta ZPE - T \Delta S - (2N_O + N_{OH}) (eU + k_B T \ln(10) \text{pH})$$

( $E^*_{+N_O+N_{OH}} - E^*$ ) is the difference in total energy of the clean and covered slab,  $N_{O,OH}$  the number of \*O and \*OH adsorbates,  $H_{H_2O}^f$  and  $H_{H_2}^f$  the formation enthalpies of water and hydrogen, and  $\Delta ZPE$  is the change in zero point energy and  $T \cdot \Delta S$  the entropy loss upon adsorption.

### Modelling of OER

The overpotential was calculated following the approach of Nørskov and Rossmeisl.<sup>[71]</sup> Herein, the OER is divided into four coupled electron-proton transfer steps:



where \* denotes the pristine surface with the reaction site and \*OH, \*O and \*OOH are the three reaction intermediates. The intermediates' binding energy  $\Delta G_{ads}^b$  is given by:

$$\Delta G_{ads}^b = E_* - E_{ads} + N_O \cdot H_{H_2O}^f - \left( N_O - \frac{1}{2} N_H \right) \cdot H_{H_2}^f + \Delta ZPE + T \cdot \Delta S - n_{ads} e \phi \quad (11)$$

$E_* - E_{ads}$  is the total energy difference of the slab without and with adsorbate,  $N_O$  and  $N_H$  are the amounts of O and H atoms of the adsorbate,  $n_{ads}$  is the number of electron transfers taking place at the respective step,  $e$  the elementary charge and  $\phi$  is the applied potential. Previous studies have shown that  $\Delta ZPE$  and  $T \cdot \Delta S$  do not change significantly at different transition metal oxide surfaces<sup>[72]</sup> thus we adopted the values reported in this work. Under electrochemical standard conditions and in relation to the standard hydrogen electrode (SHE), the steps between these intermediates are given by:

$$\Delta G_i = \Delta G_{ads_2}^b - \Delta G_{ads_1}^b + k_B T \ln(10) \text{ pH} \quad (12)$$

where  $\Delta G_{ads_1,2}^b$  are two consecutive intermediates' adsorption energies. The minimal external potential  $\phi$  that makes all  $\Delta G_i$  negative, and thus the whole reaction energetically downhill is thus given by the potential-determining step:

$$\phi_{OER} = \max[\Delta G_i]/e \quad (13)$$

The overpotential is accordingly calculated as:

$$\eta = \phi_{OER} - 1.23 \text{ V} \quad (14)$$

### Acknowledgement

We acknowledge gratefully funding by the Deutsche Forschungsgemeinschaft (DFG, German Research Foundation) – 388390466 – TRR 247 within projects A1, A2, B4 and C1, as well as the Mercator Research Center Ruhr (MERCUR, Pe-2018-0034). The authors thank Robin Meya and Beate Römer for providing AAS measurements and Dietrich Tönnes for the XRD measurements. The authors also acknowledge Dr. Markus Heidelmann for TEM measurements. Furthermore, we acknowledge computational time at SuperMUC at the Leibniz Rechenzentrum (project pr87ro) and at MagnitUDE at UDE (DFG grant INST 20876/209-1 FUGG) and support by the Open Access Publication Fund of the University of Duisburg-Essen. Open Access funding enabled and organized by Projekt DEAL.

### Conflict of Interest

The authors declare no conflict of interest.

- [1] W. T. Hong, M. Risch, K. A. Stoerzinger, A. Grimaud, J. Suntivich, Y. Shao-Horn, *Energy Environ. Sci.* **2015**, *8*, 1404–1427.
- [2] Y. Cheng, S. P. Jiang, *Prog. Natl. Sci.* **2015**, *25*, 545–553.
- [3] S. Kalantarifard, S. I. Allakhverdiev, M. M. Najafpour, *Int. J. Hydrogen Energy* **2020**, *45*, 33563–33573.
- [4] L. Zhang, Q. Fan, K. Li, S. Zhang, X. Ma, *Sustain. Energy Fuels* **2020**, *4*, 5417–5432.
- [5] J. Suntivich, K. J. May, H. A. Gasteiger, J. B. Goodenough, Y. Shao-Horn, *Science* **2011**, *334*, 1383–1385.
- [6] A. Dutta, S. Mutyalal, A. K. Samantara, S. Bera, B. K. Jena, N. Pradhan, *ACS Energy Lett.* **2017**, *3*, 141–148.
- [7] C. Xiao, X. Lu, C. Zhao, *Chem. Commun.* **2014**, *50*, 10122–10125.
- [8] O. Diaz-Morales, I. Ledezma-Yanez, M. T. Koper, F. Calle-Vallejo, *ACS Catal.* **2015**, *5*, 5380–5387.
- [9] D. A. Corrigan, *J. Electrochem. Soc.* **1987**, *134*, 377.
- [10] J. Xu, J. Li, D. Xiong, B. Zhang, Y. Liu, K.-H. Wu, I. Amorim, W. Li, L. Liu, *Chem. Sci.* **2018**, *9*, 3470–3476.
- [11] H. Jin, S. Mao, G. Zhan, F. Xu, X. Bao, Y. Wang, *J. Mater. Chem. A* **2017**, *5*, 1078–1084.
- [12] M. S. Burke, M. G. Kast, L. Trotocaud, A. M. Smith, S. W. Boettcher, *J. Am. Chem. Soc.* **2015**, *137*, 3638–3648.
- [13] D. Guo, H. Kang, P. Wei, Y. Yang, Z. Hao, Q. Zhang, L. A. Liu, *CrysEngComm* **2020**, *22*, 4317–4323.
- [14] K. Chakrapani, G. Bendt, H. Hajiyani, I. Schwarzkopf, T. Lunkenbein, S. Salamon, J. Landers, H. Wende, R. Schlägl, R. Pentcheva, M. Behrens, S. Schulz, *ChemCatChem* **2017**, *9*, 2988–2995.
- [15] K. Chakrapani, G. Bendt, H. Hajiyani, T. Lunkenbein, M. T. Greiner, L. Masliuk, S. Salamon, J. Landers, R. Schlägl, H. Wende, R. Pentcheva, S. Schulz, M. Behrens, *ACS Catal.* **2018**, *8*, 1259–1267.
- [16] H. Hajiyani, R. Pentcheva, *ACS Catal.* **2018**, *8*, 11773–11782.
- [17] E. Budiyanto, M. Yu, M. Chen, S. DeBeer, O. Rüdiger, H. Tüysüz, *ACS Appl. Energ. Mater.* **2020**.
- [18] Y. Peng, H. Hajiyani, R. Pentcheva, *ACS Catal.* **2021**, *11*, 5601–5613.
- [19] J. Han, G. Chen, X. Liu, N. Zhang, S. Liang, R. Ma, G. Qiu, *Chem. Commun. (Camb.)* **2019**, *55*, 9212–9215.
- [20] Y. Li, X. Jiang, M. Tang, Q. Zheng, Y. Huo, F. Xie, D. Lin, *Int. J. Hydrogen Energy* **2020**, *45*, 28586–28597.
- [21] S. Klemenz, J. Schuch, S. Hawel, A.-M. Zieschang, B. Kaiser, W. Jaegermann, B. Albert, *ChemSusChem* **2018**, *11*, 3150–3156.
- [22] D. Li, Y. Xing, R. Yang, T. Wen, D. Jiang, W. Shi, S. Yuan, *ACS Appl. Mater. Interfaces* **2020**, *12*, 29253–29263.
- [23] Y. Wang, D. Liu, Z. Liu, C. Xie, *Chem. Commun. (Camb.)* **2016**, *52*, 12614–12617.
- [24] L. Wu, D. Shi, S. Yan, W. Qiao, W. Zhong, Y. Du, *Int. J. Hydrogen Energy* **2021**, *46*, 2086–2094.
- [25] D. Royer, D. Duprez, F. Can, X. Courtois, C. Batiot-Dupeyrat, S. Laassiri, H. Alamdar, *Chem. Rev.* **2014**, *114*, 10292–10368.
- [26] J. Hwang, R. R. Rao, L. Giordano, Y. Katayama, Y. Yu, Y. Shao-Horn, *Science* **2017**, *358*, 751–756.
- [27] D. Antipin, M. Risch, *J. Phys. Energy* **2020**, *2*, 032003.
- [28] M. H. Seo, H. W. Park, D. U. Lee, M. G. Park, Z. Chen, *ACS Catal.* **2015**, *5*, 4337–4344.
- [29] A. Vojvodic, J. K. Nørskov, *Science* **2011**, *334*, 1355–1356.
- [30] J. T. Mefford, X. Rong, A. M. Abakumov, W. G. Hardin, S. Dai, A. M. Kolpak, K. P. Johnston, K. J. Stevenson, *Nat. Commun.* **2016**, *7*, 1–11.
- [31] A. Grimaud, O. Diaz-Morales, B. Han, W. T. Hong, Y.-L. Lee, L. Giordano, K. A. Stoerzinger, M. T. Koper, Y. Shao-Horn, *Nat. Chem.* **2017**, *9*, 457–465.
- [32] J. S. Yoo, X. Rong, Y. Liu, A. M. Kolpak, *ACS Catal.* **2018**, *8*, 4628–4636.
- [33] Y. Zhu, W. Zhou, J. Yu, Y. Chen, M. Liu, Z. Shao, *Chem. Mater.* **2016**, *28*, 1691–1697.
- [34] Y. Duan, S. Sun, S. Xi, X. Ren, Y. Zhou, G. Zhang, H. Yang, Y. Du, Z. Xu, *Chem. Mater.* **2017**, *29*, 10534–10541.
- [35] I. C. Man, H.-Y. Su, F. Calle-Vallejo, H. A. Hansen, J. I. Martinez, N. G. Inoglu, J. Kitchin, T. F. Jarillo, J. K. Nørskov, J. Rossmeisl, *ChemCatChem* **2011**, *3*, 1159–1165.
- [36] Y.-L. Lee, M. J. Gadre, Y. Shao-Horn, D. Morgan, *Phys. Chem. Chem. Phys.* **2015**, *17*, 21643–21663.
- [37] X. Rong, J. Parolin, A. M. Kolpak, *ACS Catal.* **2016**, *6*, 1153–1158.
- [38] V. Tripkovic, H. A. Hansen, J. M. Garcia-Lastra, T. Vegge, *J. Phys. Chem. C* **2018**, *122*, 1135–1147.
- [39] K. Zhao, F. He, Z. Huang, G. Wei, A. Zheng, H. Li, Z. Zhao, *Appl. Energy* **2016**, *168*, 193–203.
- [40] L. Bedel, A. Roger, C. Estournes, A. Kiennemann, *Catal. Today* **2003**, *85*, 207–218.
- [41] J. Xu, J. Liu, Z. Zhao, J. Zheng, G. Zhang, A. Duan, G. Jiang, *Catal. Today* **2010**, *153*, 136–142.
- [42] M. Dreyer, M. Krebs, S. Najafovisharti, A. Rabe, K. Friedel Ortega, M. Behrens, *Catalysts* **2021**, *11*, 550.
- [43] R. Altmann, H. P. Jepsen, *Neues Jahrb. Mineral. Monatsh.* **1969**, *12*, 544 A’ 551.
- [44] L. Sangiotti, L. E. Depero, B. Allieri, P. Nunziante, E. Traversa, *J. Eur. Ceram. Soc.* **2001**, *21*, 719–726.
- [45] R. D. Shannon, *Acta Crystallogr. Sect. A* **1976**, *32*, 751–767.
- [46] V. M. Gaikwad, S. A. Acharya, *RSC Adv.* **2015**, *5*, 14366–14373.
- [47] H. Cui, M. Zayat, D. Levy, *J. Non-Cryst. Solids* **2006**, *352*, 3035–3040.
- [48] M. Thommes, K. Kaneko, A. V. Neimark, J. P. Olivier, F. Rodriguez-Reinoso, J. Rouquerol, K. S. Sing, *Pure Appl. Chem.* **2015**, *87*, 1051–1069.
- [49] K. Elumeeva, M. A. Kazakova, D. M. Morales, D. Medina, A. Selyutin, G. Golubtsov, Y. Ivanov, V. Kuznetsov, A. Chuvilin, H. Antoni, *ChemSusChem* **2018**, *11*, 1204–1214.
- [50] S. He, H. Lin, *Nanoscale* **2019**, *11*, 10348–10357.
- [51] L. Trotocaud, S. L. Young, J. K. Ranney, S. W. Boettcher, *J. Am. Chem. Soc.* **2014**, *136*, 6744–6753.
- [52] D. M. Morales, M. Risch, *J. Phys. Energy* **2021**, *3*, 034013.
- [53] A. M. Ritzmann, M. Pavone, A. B. Muñoz-García, J. A. Keith, E. A. Carter, *J. Mater. Chem. A* **2014**, *2*, 8060–8074.
- [54] J. Buckeridge, F. Taylor, C. Catlow, *Phys. Rev. B* **2016**, *93*, 155123.
- [55] H. Hsu, P. Blaha, R. M. Wentzcovitch, C. Leighton, *Phys. Rev. B* **2010**, *82*, 100406.
- [56] B. Geisler, R. Pentcheva, *Phys. Rev. B* **2020**, *101*, 165108.
- [57] K. Reuter, M. Scheffl, *Phys. Rev. B* **2001**, *65*, 035406.
- [58] K. Krishnaswamy, C. Dreyer, A. Janotti, C. Van de Walle, *Phys. Rev. B* **2014**, *90*, 235436.
- [59] H.-Y. Su, Y. Gorlin, I. C. Man, F. Calle-Vallejo, J. K. Nørskov, T. F. Jarillo, J. Rossmeisl, *Phys. Chem. Chem. Phys.* **2012**, *14*, 14010–14022.
- [60] M. Knobel, *J. Am. Chem. Soc.* **1923**, *45*, 70–76.
- [61] L. A. Bromley, *AIChE J.* **1973**, *19*, 313–320.
- [62] G. Kresse, J. Hafner, *Phys. Rev. B* **1993**, *47*, 558.
- [63] G. Kresse, J. Furthmüller, *Comput. Mater. Sci.* **1996**, *6*, 15–50.
- [64] G. Kresse, J. Furthmüller, *Phys. Rev. B* **1996**, *54*, 11169.
- [65] P. E. Blöchl, *Phys. Rev. B* **1994**, *50*, 17953.

- [66] S. Dudarev, G. Botton, S. Savrasov, C. Humphreys, A. Sutton, *Phys. Rev. B* **1998**, *57*, 1505.  
[67] G. I. Csonka, J. P. Perdew, A. Ruzsinszky, P. H. Philipsen, S. Lebègue, J. Paier, O. A. Vydrov, J. G. Ángyán, *Phys. Rev. B* **2009**, *79*, 155107.  
[68] L. Wang, T. Maxisch, G. Ceder, *Phys. Rev. B* **2006**, *73*, 195107.  
[69] Y.-L. Lee, J. Kleis, J. Rossmeisl, D. Morgan, *Phys. Rev. B* **2009**, *80*, 224101.  
[70] H. J. Monkhorst, J. D. Pack, *Phys. Rev. B* **1976**, *13*, 5188.  
[71] J. Rossmeisl, Z.-W. Qu, H. Zhu, G.-J. Kroes, J. K. Nørskov, *J. Electroanal. Chem.* **2007**, *607*, 83–89.  
[72] P. Liao, J. A. Keith, E. A. Carter, *J. Am. Chem. Soc.* **2012**, *134*, 13296–13309.

Manuscript received: August 3, 2021  
Accepted manuscript online: September 8, 2021  
Version of record online: October 27, 2021

## 6. The Effect of Water on the 2-Propanol Oxidation Activity of Co-Substituted $\text{LaFe}_{1-x}\text{Co}_x\text{O}_3$ Perovskites

**Title:**

“The Effect of Water on the 2-Propanol Oxidation Activity of Co-Substituted  $\text{LaFe}_{1-x}\text{Co}_x\text{O}_3$  Perovskites”

**Authors:**

Maik Dreyer, Daniel Cruz, Ulrich Hagemann, Patrick Zeller, Markus Heidelmann, Soma Salamon, Joachim Landers, Anna Rabe, Klaus Friedel Ortega, Sharif Najafishirtari, Heiko Wende, Nils Hartmann, Axel Knop-Gericke, Robert Schlögl, Malte Behrens

Dreyer, M.; Cruz, D.; Hagemann, U.; Zeller, P.; Heidelmann, M.; Salamon, S.; Landers, J.; Rabe, A.; Ortega, K. F.; Najafishirtari, S.; Wende, H.; Hartmann, N.; Knop-Gericke, A.; Schlögl, R.; Behrens, M., *Chem. Eur. J.* **2021**, 27 (68), 17127-17144.<sup>188</sup>

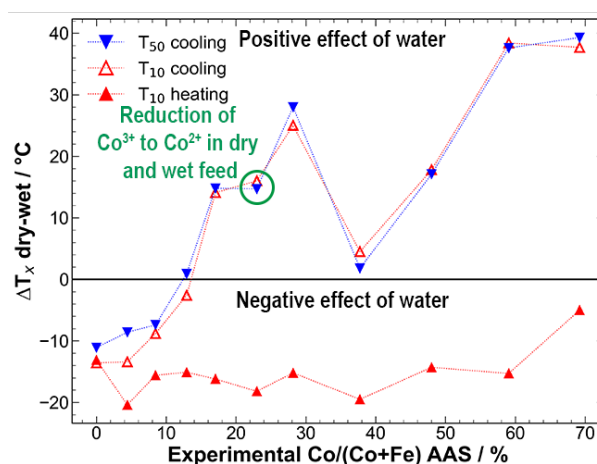
**DOI:**

10.1002/chem.202102791

The Supporting Information can be accessed under [https://chemistry-europe.onlinelibrary.wiley.com/action/downloadSupplement?doi=10.1002%2Fchem.202102791&file=chem202102791-sup-0001-misc\\_information.pdf](https://chemistry-europe.onlinelibrary.wiley.com/action/downloadSupplement?doi=10.1002%2Fchem.202102791&file=chem202102791-sup-0001-misc_information.pdf) and is shown in Chapter A in Section VI.

**Supporting Information:**

**Graphical Abstract:**



Maik Dreyer wrote the major part of the first manuscript draft and synthesized the materials. Furthermore, he organized the characterization of the materials and performed the evaluation despite the XPS analysis. Maik Dreyer also performed the measurements in gas phase 2-propanol oxidation and took care of the data analysis. Daniel Cruz and Patrick Zeller performed the *operando* NAP-XPS measurements, evaluated the results, and wrote the NAP-XPS section. Ulrich Hagemann was responsible for lab XPS and its evaluation. Patrick Zeller performed the *operando* NAP-XPS measurements together with Daniel Cruz and evaluated them. Markus Heidelmann operated the TEM and TEM-EDX. Soma Salamon and Joachim Landers performed Mössbauer spectroscopy and magnetometry measurements, and contributed by their evaluation. Anna Rabe took care of the Rietveld refinements. Klaus Friedel Ortega supervised the work and conceptualized parts of it. Sharif Najafishirtari performed the DRIFTS experiments and was responsible for their evaluation, and writing of the original DRIFTS section draft. Furthermore, he took responsibility in supervision and conceptualization. Nils Hartmann, Axel Knop-Gericke, Robert Schlögl, and Malte Behrens acquired the funding, supervised the work, and administrated the project. All authors contributed to review and editing of the original draft.

The work was reprinted without changes under the CC BY 4.0 license. © 2021 The Authors. Chemistry - A European Journal published by Wiley- VCH GmbH.

## The Effect of Water on the 2-Propanol Oxidation Activity of Co-Substituted $\text{LaFe}_{1-x}\text{Co}_x\text{O}_3$ Perovskites

Maik Dreyer,<sup>[a]</sup> Daniel Cruz,<sup>[b, c]</sup> Ulrich Hagemann,<sup>[d]</sup> Patrick Zeller,<sup>[b, e]</sup> Markus Heidelmann,<sup>[d]</sup> Soma Salamon,<sup>[f]</sup> Joachim Landers,<sup>[f]</sup> Anna Rabe,<sup>[a]</sup> Klaus Friedel Ortega,<sup>[g]</sup> Sharif Najafishirtari,<sup>[a]</sup> Heiko Wende,<sup>[f]</sup> Nils Hartmann,<sup>[d]</sup> Axel Knop-Gericke,<sup>[b, c]</sup> Robert Schlögl,<sup>[b, c]</sup> and Malte Behrens<sup>\*[a, g]</sup>

**Abstract:** Perovskites are interesting oxidation catalysts due to their chemical flexibility enabling the tuning of several properties. In this work, we synthesized  $\text{LaFe}_{1-x}\text{Co}_x\text{O}_3$  catalysts by co-precipitation and thermal decomposition, characterized them thoroughly and studied their 2-propanol oxidation activity under dry and wet conditions to bridge the knowledge gap between gas and liquid phase reactions. Transient tests showed a highly active, unstable low-temperature (LT) reaction channel in conversion profiles and a stable, less-

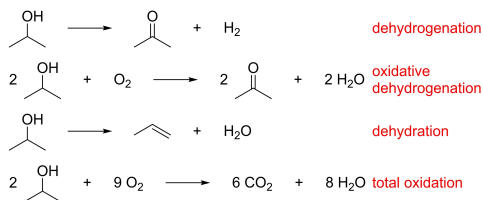
active high-temperature (HT) channel. Cobalt incorporation had a positive effect on the activity. The effect of water was negative on the LT channel, whereas the HT channel activity was boosted for  $x > 0.15$ . The boost may originate from a slower deactivation rate of the  $\text{Co}^{3+}$  sites under wet conditions and a higher amount of hydroxide species on the surface comparing wet to dry feeds. Water addition resulted in a slower deactivation for Co-rich catalysts and higher activity in the HT channel state.

- [a] M. Dreyer, A. Rabe, Dr. S. Najafishirtari, Prof. Dr. M. Behrens  
Faculty for Chemistry and Center for Nanointegration Duisburg-Essen (CENIDE)  
University of Duisburg-Essen  
Universitätsstr. 7, 45141 Essen (Germany)  
E-mail: mbehrens@ac.uni-kiel.de
  - [b] Dr. D. Cruz, Dr. P. Zeller, Dr. A. Knop-Gericke, Prof. Dr. R. Schlögl  
Department of Inorganic Chemistry  
Fritz-Haber-Institut der Max-Planck Gesellschaft  
Faradayweg 4–6, 14195 Berlin (Germany)
  - [c] Dr. D. Cruz, Dr. A. Knop-Gericke, Prof. Dr. R. Schlögl  
Department of Heterogeneous Reactions  
Max Planck Institute for Chemical Energy Conversion  
Stiftstraße 34–36, Mülheim der Ruhr 45470 (Germany)
  - [d] Dr. U. Hagemann, Dr. M. Heidelmann, Prof. Dr. N. Hartmann  
Interdisciplinary Center for Analytics on the Nanoscale (ICAN)  
NanoEnergieTechnikZentrum at University of Duisburg-Essen  
Carl-Benz-Str. 199, 47057 Duisburg (Germany)
  - [e] Dr. P. Zeller  
Helmholtz-Zentrum Berlin für Materialien und Energie GmbH  
BESSY II, Department of Catalysis for Energy  
Albert-Einstein-Straße 15, 12489 Berlin (Germany)
  - [f] Dr. S. Salamon, Dr. J. Landers, Prof. Dr. H. Wende  
Faculty of Physics and CENIDE  
University of Duisburg-Essen  
Lotharstr. 1, 47057 Duisburg (Germany)
  - [g] Dr. K. F. Ortega, Prof. Dr. M. Behrens  
Institute of Inorganic Chemistry  
Christian-Albrechts-Universität zu Kiel  
Max-Eyth-Straße 2, 24118 Kiel (Germany)
-  Supporting information for this article is available on the WWW under <https://doi.org/10.1002/chem.202102791>
-  Part of a Special Issue on Contemporary Challenges in Catalysis.
-  © 2021 The Authors. Chemistry - A European Journal published by Wiley-VCH GmbH. This is an open access article under the terms of the Creative Commons Attribution License, which permits use, distribution and reproduction in any medium, provided the original work is properly cited.

## Introduction

Oxidation catalysis is essential in the chemical industry, either to selectively synthesize products like oxygenates or to remove volatile organic compounds (VOCs) or carbon monoxide (CO) from exhaust gases.<sup>[1]</sup> However, these reactions are often performed using noble metals as catalysts, which are very cost-intensive due to their low abundance. Among potential oxide catalysts to perform those oxidation reactions at a more favorable cost are perovskite oxides with the general empirical formula  $\text{ABO}_3$ .<sup>[2]</sup> Due to their ability to incorporate different redox-active transition metal cations on the B-sites, these compounds are interesting materials to study the effect of composition on the catalytic properties. Additionally, they offer significant structural stability during oxidation catalysis.<sup>[3]</sup> Furthermore, it is possible to tune the oxygen vacancies within their structures and thus the catalytic oxidation properties by manipulating the type and composition of the A-cation, as reported for instance by replacing  $\text{La}^{3+}$  with  $\text{Sr}^{2+}$ .<sup>[4]</sup> As a probe reaction for selective oxidation and the removal of VOCs, the oxidation of 2-propanol was widely studied on precious metals and oxides, as it features the possibility to gain mechanistic insights and to characterize Lewis acidic and Lewis basic surface sites.<sup>[5]</sup>

The main reactions taking place during the gas-phase 2-propanol oxidation are shown in Scheme 1. 2-propanol reacts at strongly basic sites and moderately acidic sites in their vicinity to the desired selective oxidation product, i.e., acetone and hydrogen, via the dehydrogenation pathway. The oxidative dehydrogenation is catalyzed by the same centers but features oxidation to acetone and water as the coupled product. The dehydration is catalyzed by strongly acidic sites in the vicinity

Scheme 1. Possible reactions during the gas-phase 2-propanol oxidation.<sup>[6]</sup>

of weakly basic sites, leading to propene and water as reaction products. Another pathway is total oxidation, in which  $\text{CO}_2$  is formed at high temperatures.<sup>[6]</sup>

Based on the recent work by Anke et al.,<sup>[5b]</sup> the mechanism of gas-phase 2-propanol oxidation on  $\text{Co}_3\text{O}_4$  was described to take place on 5-fold-coordinated octahedral  $\text{Co}^{3+}$  on the surface as the active site for adsorption of both 2-propanol and the reactive oxygen species. Oxidative dehydrogenation was found to be the favored pathway facilitated by the adsorption of atomic oxygen. Furthermore, the reduction of  $\text{Co}^{3+}$  to  $\text{Co}^{2+}$  was observed during the reaction, which led to a deactivation of the catalyst. The reaction showed different pathways, a non-stable low temperature (LT) pathway with high activity only during heating and a stable high-temperature (HT) pathway with lower activity. For spinels, a high amount of exposed (110) surface seems to be beneficial for high activity and stability.<sup>[7]</sup>

By sum-frequency spectroscopy, the adsorption of 2-propanol on  $\text{TiO}_2$  was detected to take place molecularly.<sup>[8]</sup> On a  $\text{SrTiO}_3$  perovskite with a mainly exposed (100) facet, an orientation of the alcohol with the C–H group pointing to the surface was found. The resulting geometry enabled the abstraction of an  $\alpha$ -proton during the dehydrogenation pathway.<sup>[6f]</sup> Reaction selectivity of  $\text{SrTiO}_3$  was dependent on the pretreatment, caused by surface restructuring due to segregation.<sup>[5d,9]</sup>

The effect of water was previously studied in the 2-propanol oxidation reaction on spinels and noble metals. Water adsorption occurs on strongly acidic sites and is expected to suppress dehydration and improve dehydrogenation selectivity for oxide catalysts in oxidation reactions.<sup>[6]</sup> Therefore, water addition should lead to a more pronounced (oxidative) dehydrogenation mechanism due to competitive adsorption on strongly acidic sites. Additionally, by using a wet feed with a high concentration of water, one could take one step further from gas-phase catalysis towards the liquid-phase and therefore facilitate understanding of the liquid-phase oxidation. Similarities between 2-propanol oxidation on  $\text{Co}_3\text{O}_4$  in the liquid phase and the gas phase with water vapor were reported.<sup>[10]</sup> Also, a detrimental effect of water feeding on the low-temperature activity of gas-phase 2-propanol oxidation was found in the same study.<sup>[10]</sup> On Pt catalysts, water in the gas-mixture was studied for different alcohol oxidations. The addition of water resulted in decreasing conversions and selective oxidation selectivity for the oxidation of ethanol.<sup>[11]</sup> For 1-propanol

oxidation, a steady decay in conversion was observed, but no stable trend in the ratio of total and selective oxidation products. In addition, an increase in activation energy was reported for water co-feeding.<sup>[12]</sup> For the oxidation of 2-propanol on Pt nanoparticles, a steady decay in conversion with increasing amount of water in the feed was observed.<sup>[13]</sup>

For perovskites, the influence of water on different oxidation reactions was reported and mostly had the effect of reduced conversion at the same temperature, as will be discussed in more detail in the following paragraph. In CO and toluene oxidation on  $\text{La}_{0.6}\text{Sr}_{0.4}\text{MnO}_3$  perovskites, water decreased the conversion.<sup>[14]</sup> For methane oxidation on  $\text{La}_{1-x}\text{Sr}_x\text{FeO}_3$  catalysts, a decrease in conversion with water concentration was found for lower temperatures, whereas no deactivation was observed at elevated temperatures.<sup>[15]</sup> In ethanol oxidation over an octahedral molecular sieve (OMS-2) catalyst, the addition of 10% water led to a pronounced decrease in activity and was attributed to competitive adsorption of water and ethanol on the active sites.<sup>[16]</sup> A similar conclusion was obtained from *n*-butane oxidation over vanadium phosphorous oxide. However, in this specific case, competitive adsorption of water and oxygen led to a difference in oxygen activation.<sup>[17]</sup> In the parallel oxidation of NO and propane, a loss in activity with water addition was reported and correlated to competitive adsorption of oxygen, NO and water.<sup>[18]</sup> Also, the filling of oxygen vacancies by water was considered a possible explanation for activity reduction. Interestingly, the extent of deactivation of both reactions was less severe for  $\text{LaCoO}_3$  than for  $\text{LaFeO}_3$  and attributed to more abundant anion vacancies in the Co-containing perovskite, and the activity decrease was depressed with rising temperature.<sup>[1c]</sup> In terms of VOC removal, the effect of water is complex, especially at low temperatures, and depends on many factors.<sup>[1c]</sup>

Perovskite oxides can be synthesized in various compositions and by various methods.<sup>[2]</sup> Recently, we presented the synthesis of  $\text{LaFe}_{1-x}\text{Co}_x\text{O}_3$  (LFCO) perovskites by co-precipitation of a mostly amorphous precursor system and subsequent thermal decomposition.<sup>[19]</sup> LFCO materials are interesting oxidation catalysts since the two transition metals Co and Fe are earth-abundant and showed high catalytic activity in various oxidation reactions.<sup>[20]</sup> Further exemplary methods for perovskite synthesis are spray-flame synthesis and ceramic methods.<sup>[3,21]</sup> In these materials, the A-cation is the larger of the two cations, typically a halide or lanthanide element and is considered a weak acidic center in perovskite oxides. The octahedrally coordinated B-cation is often a redox-active metal and is the strong Lewis acidic center. The oxygen anion acts as a Lewis basic center.<sup>[22]</sup>

LSCF (lanthanum strontium cobalt iron) perovskites present acidic and basic surface sites. Upon Fe/Co substitution, non-linear behavior of the surface basicity based on Co content was reported, but in general, a decreased basicity with iron content was found.<sup>[23]</sup> For  $\text{LaCoO}_3$ , an acidic surface was reported based on CO adsorption.<sup>[24]</sup>  $\text{La}_2\text{O}_3$  excess in mixed  $\text{LaFeO}_3$  perovskites leads to an increase in surface basicity in  $\text{LaFeO}_3$  perovskites shown by 2-propanol decomposition, indicating an acidic surface of  $\text{LaFeO}_3$  and basic surface of  $\text{La}_2\text{O}_3$ .<sup>[25]</sup>

In terms of oxidation activity, especially Sr-terminated step sites were found as very active sites in C–H bond activation of methane and CO oxidation which indicates an influence of the A-cations on catalysis.<sup>[26]</sup> Also, the effect of oxygen vacancies created upon Sr-incorporation cannot be neglected.<sup>[26c]</sup>

In order to combine the reported effects of  $\text{Co}^{3+}$  sites on perovskite surfaces, we extended the previously reported synthesis protocol to LFCO materials with a nominal Co content of up to 70% on the B-site in this work.<sup>[19]</sup> Adsorption of 2-propanol was studied on selected materials, and gas-phase 2-propanol oxidation was performed with and without the co-feeding of water vapor to study the effect of water on the catalytic properties as a function of composition. In this regard, two equally important goals were considered in this study, namely the effect of Co content on one hand and the effect of water in the feed on the other hand. In addition, the spent catalysts were characterized by X-ray photoelectron spectroscopy (XPS) and scanning transmission electron microscopy (STEM) and compared to the initial state to gain insight into the dynamic changes of the catalysts during the reaction.

## Results and discussion

### Synthesis and materials characterization

Precursor materials were prepared via constant pH co-precipitation in a semi-automatized laboratory reactor, following the recipe reported in previous publications for a nominal Co content determined by  $x = \text{Co}/(\text{Co} + \text{Fe})$  of  $0.00 \leq x \leq 0.30$ .<sup>[19,27]</sup> In this study, the Co-content was extended up to  $x=0.70$ . The computer-controlled precipitations were performed by simultaneous dosing of metal salt and base solutions, which allowed maintaining a constant pH during co-precipitation. All synthesis protocols are shown in Figure S1.

The freshly prepared precipitated materials for  $x=0.00$  and  $x=0.05$  showed an X-ray amorphous powder pattern, as shown in Figure S2a. For  $x > 0.10$ , the formation of a hydrotalcite-like secondary phase was additionally observed. The presence of the phase was indicated by the evolution of the most prominent (003) reflection of a CoFe-layered double hydroxide (MgAl-LDH structure type, ICSD reference code 6296<sup>[28]</sup>). The intensity of this reflection increased with increasing Co content in the precipitated metal salt solution. The experimental Co/(Co + Fe) ratio derived from atomic absorption spectroscopy of the precursor revealed a slight deficiency of Co compared to Fe in the materials after precipitation, as shown in Figure S2b.

Precursor materials were thermally decomposed by calcination at 800 °C and characterized via XRD with the resulting patterns shown in Figure 1a. The formerly amorphous precursors were transformed into crystalline materials. For  $x < 0.40$ , only the orthorhombic perovskite phase was observed, indicated with a  $\text{LaFeO}_3$  reference (ICSD collection code 93611<sup>[29]</sup>). As reported in our previous study, the (112) reflection shifted to higher angles, indicating the incorporation of the smaller  $\text{Co}^{3+}$  cations into the perovskite lattice.<sup>[19,30]</sup>

For  $x \geq 0.40$ , no phase pure materials were synthesized. Instead, a mixture of three crystalline phases was observed. An orthorhombic phase (like  $\text{LaFeO}_3$ ), a rhombohedral structure (like  $\text{LaCoO}_3$ , ICSD collection code 99369<sup>[31]</sup>) and a spinel (indicated by  $\text{Co}_3\text{O}_4$ , ICSD collection code 9362<sup>[32]</sup>) were observed in the XRD patterns. The evolution of rhombohedral  $\text{LaCoO}_3$  is in good agreement with the literature, where the transition was also reported for  $x \geq 0.40$  in  $\text{LaFe}_{1-x}\text{Co}_x\text{O}_3$ .<sup>[33]</sup> In addition, for  $x > 0.40$ , a minor amount of  $\text{Fe}_{3-x}\text{Co}_x\text{O}_4$  spinel phase was formed. A possible reason for this is cation segregation upon LDH formation. Therefore, there is no homogeneous cation distribution which leads to the spinel formation due to lack of La in the LDH.

The powder diffraction patterns were further analyzed by Rietveld refinement to determine lattice parameters of the different phases and the ratio of phases in the mixture.<sup>[34]</sup> The refinement results are shown for each catalyst in Figure S3, the fit parameters in Table S1. The intermixing of the cationic sublattice was verified by refinement, as shown in Figure 1c. The lattice parameters for all three phases decreased linearly with increasing nominal Co fraction in the solid solution. Even though the XRD pattern of sample  $x=0.40$  barely indicated the presence of the spinel phase, its existence was verified by the refinement. The peak position of the most intense reflection of the spinel phase corresponding to (311) planes in Figure 1b indicated the formation of Co-richer spinels when more Co is precipitated.<sup>[35]</sup> The lattice parameters of the spinel phase shown in Figure 1c indicate a Co-rich spinel as well, but the spinel is not only consisting of Co, based on the literature lattice parameter of 8.065 Å for  $\text{Co}_3\text{O}_4$ .<sup>[32]</sup> The lattice parameter of the spinels show the most prominent change between  $x=0.40$  and  $x=0.50$ , but the general trend in the lattice parameter is also decreasing upon minor changes between  $x=0.50$ ,  $x=0.60$  and  $x=0.70$ . In Table 1, fractions of the phases are displayed. The fraction of orthorhombic perovskite decreases for  $x \geq 0.40$ , while the increasing amount of rhombohedral perovskite and spinel was confirmed by refinement.

$\text{N}_2$  physisorption isotherms and pore size distribution plots determined by the Barrett-Joyner-Halenda (BJH) method during desorption are shown in Figure S4 and Figure S5. All isotherms were characterized as type IVa isotherms.<sup>[36]</sup> A decrease of the adsorbed volume was evident with an increasing amount of Co in the catalysts, even though there was a maximum in the adsorbed volume for  $x=0.10$ . The pore size distributions showed a maximum in the range of 20–30 nm for the samples up to  $x=0.30$ , indicating mainly interparticle pores, similar to what was reported in our previous work for samples up to  $x=0.30$ , where we described round but sintered particles and a BET surface area correlating well with the particle size.<sup>[19]</sup> For the non-phase pure samples  $x > 0.30$ , the uniformity of the pore size distribution was lost, and no clear maximum was observed. For higher Co contents, the pore volume remained unaffected by the amount of cobalt in the material and decreased in this regime compared to the phase pure materials. BET surface area determined by multi-point BET plots and pore volumes determined at  $p/p_0=0.99$  are shown in Table 1 and confirm the trends discussed based on the isotherms.

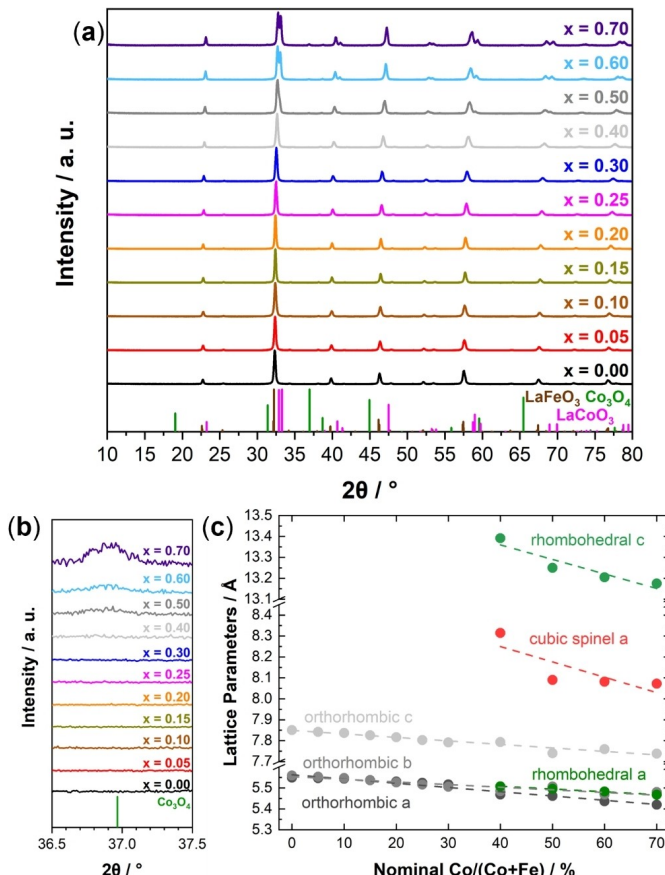


**Figure 1.** (a) XRD patterns of the materials after calcination. (b) Zoom into the XRD patterns after calcination, indicating a secondary spinel phase for  $x > 0.30$ . (c) Evolution of the lattice parameters from Rietveld refinements.

**Table 1.** BET surface area determined by multi-point BET plots, pore volumes determined at  $p/p_0 = 0.99$ , pore sizes determined by the BJH method during desorption, and fractions of different phases derived from Rietveld refinements.

$x =$	BET surface area / $\text{m}^2 \text{g}^{-1}$	Pore volume / $\text{cm}^3 \text{g}^{-1}$	Fraction orthorhombic perovskite / %	Fraction rhombohedral perovskite / %	Fraction spinel / %
0.00	20.0	0.167	100	–	–
0.05	17.3	0.174	100	–	–
0.10	28.9	0.238	100	–	–
0.15	11.7	0.127	100	–	–
0.20	11.0	0.057	100	–	–
0.25	14.4	0.089	100	–	–
0.30	10.6	0.064	100	–	–
0.40	10.1	0.034	74	25	1
0.50	9.5	0.029	60	38	2
0.60	7.0	0.029	36	62	2
0.70	9.5	0.034	34	62	5

To obtain complementary structural information, including the Fe-content of individual phases, as well as on Fe valence states, Mössbauer spectroscopy and magnetometry measurements were performed. Mössbauer spectra recorded at 5 K shown in Figure S6a display the expected sextet structure for the Fe-bearing perovskites. For low Co-contents  $x$ , we observed narrow sextet spectra, proving the complete Fe-bearing material to be in a magnetically ordered state, which was reported to be weakly ferromagnetic<sup>[37]</sup> (WFM), as also indicated in spectra obtained in external magnetic fields of 5 T (Figure S6b). Upon rising  $x$ , the spectra exhibited a minor decrease in sextet splitting (magnetic hyperfine field), with asymmetric line broadening assigned to different local surroundings of the individual Fe atoms and an isomer shift of ca. 0.47 mm s<sup>-1</sup> relative to  $\alpha$ -Fe at room temperature, characteristic of the Fe<sup>3+</sup> state.<sup>[38]</sup> No further additional spectral features were observable that deviate from the hyperfine field or isomer shift of the above discussed perovskite contribution, which would indicate for example the presence of other Fe-bearing phases. This agrees with results from XRD, indicating that the minor parasitic spinel phase is poor in Fe, being close to the  $\text{Co}_3\text{O}_4$  stoichiometry.

In addition to the minor WFM hysteresis, field-dependent magnetometry measurements at 4.3 K and 300 K (Figure S7) displayed a minuscule contribution with low coercive field and a spontaneous magnetization  $\leq 0.5 \text{ Am}^2 \text{ kg}^{-1}$  for some of the sample compositions, latter being especially visible in the 300 K M(H) curves. These could be assigned to a minute fraction (<1%) of parasitic phase of high magnetization, for example, Fe-rich spinels. The temperature-dependent magnetization, normalized for better qualitative comparability and shown in Figure S7c, displayed a distinct shift in the perovskite Néel temperature from >400 K ( $x \approx 0.00$ ) across ca. 300 K ( $x \approx 0.50$ ) down to lower temperatures ( $x > 0.50$ ) based on peak features in the zero-field cooled magnetization and convergence point of the field cooled and zero field cooled branches. The trend in Néel temperatures was similar to previous literature reports<sup>[37b,39]</sup> for varying Co-content in  $\text{LaFe}_{1-x}\text{Co}_x\text{O}_3$ , which further supported the finding that macroscopic stoichiometries are principally preserved in the perovskite phase, which is of primary interest here.

TEM micrographs of the catalysts are shown in Figure S8 and Figure S9. The micrographs revealed the crystallinity of the catalysts and indicated a rather broad particle size distribution. Furthermore, the particles exhibited faceted shapes. Since the bulk composition of the precursor determined by AAS (Figure S2b) suggested only a minor bulk deficiency of Co, ratios of Co/(Co+Fe) and (Co+Fe)/La were determined by STEM-EDX and XPS to gain information on the local and the surface composition of the perovskite catalysts. The Co/(Co+Fe) ratio of the as-prepared materials, i.e., the calcined material prior to any catalytic experiment, is shown in Figure S10a. The surface ratio of Co/(Co+Fe) derived from XPS suggested a Fe-enrichment and Co-deficiency on the surface. Compared to STEM-EDX analysis, which probes the surface and the bulk of the particles, nearly no deviation was observed, while in comparison to the precursors' AAS results, both methods indicated a lower Co/(Co+Fe) ratio. The differences might result from the sample

amount used for the analysis or different systematic errors of the individual measurements. Still, the deviation from the nominal composition might still be within the error of the measurement.

Furthermore, XPS indicated an enrichment of the B-cations on the surface, as displayed in Figure S10b. In general, there are more redox-active B-cations on the surface compared to presumably redox-inert A-cations, inferred by the decrease of the (Co+Fe)/La ratio with increasing nominal Co content in the materials. For the catalysts considered to be phase-pure orthorhombic perovskite ( $0.00 \leq x \leq 0.30$ ), the B-cation excess on the surface decreased strongly with increasing Co content. The decrease was less pronounced for the catalysts that showed the rhombohedral perovskite and spinel phases ( $0.40 \leq x \leq 0.70$ ). It should be mentioned that the  $x=0.00$  catalyst from the same series was studied in a previous work by high-resolution STEM-EDX and found to be B-terminated.<sup>[27]</sup>

The bulk can be considered La rich for the whole range of Co contents ( $0.00 \leq x \leq 0.70$ ), as seen from the STEM-EDX data. In literature, an A-cation enrichment on the perovskite surface is reported based on XPS after hydrothermal synthesis of  $\text{SrTiO}_3$ .<sup>[9]</sup> Low energy ion scattering with increased surface sensitivity indicated domination of A-cations on the surface and a B-cation enriched region below the surface, for example, for  $\text{La}_{0.6}\text{Sr}_{0.4}\text{Co}_{0.2}\text{Fe}_{0.8}\text{O}_3$ . For  $\text{LaFe}_{1-x}\text{Co}_x\text{O}_3$  materials, La enrichment on the surface was reported,<sup>[38b]</sup> as well as on  $\text{LaFeO}_3$ .<sup>[41]</sup> However, STEM-EDX measurements indicated an A-cation enrichment as well on the surface.<sup>[3a]</sup> In contrast, B-cation enrichment is reported for  $\text{La}_{1-x}\text{Sr}_x\text{NiO}_3$  after thermal decomposition of amorphous citrate materials.<sup>[42]</sup> For the catalysts discussed in this study, a B-cation termination was found and reported in another story based on EDX mappings.<sup>[27]</sup> There might be an effect of the synthesis method and perovskite composition on which cations are preferentially exposed on the surface, thus the B-cation enrichment on the surface might evolve from the amorphous precursor decomposition approach.<sup>[42]</sup>

In summary, detailed characterization showed phase segregation for  $x > 0.30$  in orthorhombic perovskite, rhombohedral perovskite, and a spinel phase, as seen by XRD and confirmed by Mössbauer spectroscopy and magnetometry measurements. At lower Co contents, only the orthorhombic perovskite was observed. The phase segregation must be thoroughly considered when discussing catalytic properties. In addition, the materials were slightly Co-deficient on the B-site of the catalysts whereas for  $x \leq 0.30$  an enrichment of B-cations on the surface was observed.

#### Adsorption and desorption of 2-propanol

To investigate the interaction of the catalysts with different Co contents with 2-propanol as one of the main reactants, its adsorption at 20 °C was used as a probe on the selected catalysts, i.e.,  $x=0.00$ ,  $x=0.10$ ,  $x=0.25$ , and  $x=0.70$ , by diffuse reflectance infrared Fourier transform spectroscopy (DRIFTS). The evolution of the surface species for each catalyst during

40 min of adsorption after an oxidative treatment is shown in Figure S11. The presented times were representative of the amount of change that occurred in the spectra. The most prominent change was observed in the initial seconds while after 5 min, mainly gradual changes were observed in the intensity of the evolved species. Due to different IR absorption coefficients of the samples, the spectra were normalized based on their maximum peak intensity at 40 min.

The corresponding normalized spectra at 10 s, 20 s, and 40 min are compared in Figure 2a. The first two times were chosen to show the buildup of the species on the surface in the early state of the experiment, while the latest was chosen to show the maximum coverage of the adsorbed species on the surface. With increasing Co incorporation, the adsorption capacity increased, as was inferred from the intensities of the normalized spectra at initial times. Several bands were observed, which are attributed to different modes of bond vibrations, mainly because of the dissociative adsorption of 2-propanol on the surface of the catalysts. However, the superimposition of the gas-phase 2-propanol bands, especially at longer times, could not be excluded.<sup>[43]</sup>

The bands at  $\sim 2967 \text{ cm}^{-1}$  and  $2931 \text{ cm}^{-1}$  are related to the asymmetric and symmetric stretching of  $-\text{CH}_3$ , respectively,<sup>[44]</sup> while the band at  $2865 \text{ cm}^{-1}$  is attributed to the stretching of C–H bonds. Interestingly, by zooming in the spectra in this wavenumber range (Figure S11, insets), small but detectable variations among the samples were observed. Indeed, by increasing the Co content, two shoulders appeared and became more intense. This could mean that the electronic configuration

of the adsorbed 2-propanol varies among the samples because of their interactions with different adsorption sites. The observation is consistent with having multiple crystalline structures and phase impurities, especially at the highest Co content. Another band was observed at  $1695 \text{ cm}^{-1}$ , attributed to the stretching of  $\text{C}=\text{O}$ , which is indicative of acetone formation. The presence of this band proves that the dehydrogenation path is promoted when more Co is present than is less acidic compared to the Fe-rich sample, as observed by the emerging band for  $x=0.70$  already after 10 s. Interestingly, this band only appears at early times of exposure and disappears on all samples almost after 1 min (Figure S11), which suggests that the acetone is either not stable on the surface or its formation is coverage dependent. The latter is supported by observing the spectra during desorption shown in Figure 2b, where we observed reappearing of the  $\text{C}=\text{O}$  band after 40 min of exposure to He for the Co-containing samples. The time-resolved spectra during desorption for each catalyst additionally showed a decreasing stability trend for the adsorbed 2-propanol, as demonstrated in Figure S12. The insets of Figure S12 highlight the decrease of the stability consistent with less acidity for higher Co contents. The band at  $1589 \text{ cm}^{-1}$  is likely caused by the stretching of the  $\text{C}=\text{C}$  from propene formed through the dehydration path, although its corresponding band during 2-propanol adsorption has been reported at  $\sim 10\text{--}15 \text{ cm}^{-1}$  lower wavenumbers on zirconates and titanates in the perovskite crystal structure.<sup>[5d,9]</sup> Another possibility is a carboxyl vibration from acids like acetic acid as reported by Anke et al. at higher temperatures on  $\text{CoFe}_2\text{O}_4$ .<sup>[43]</sup>

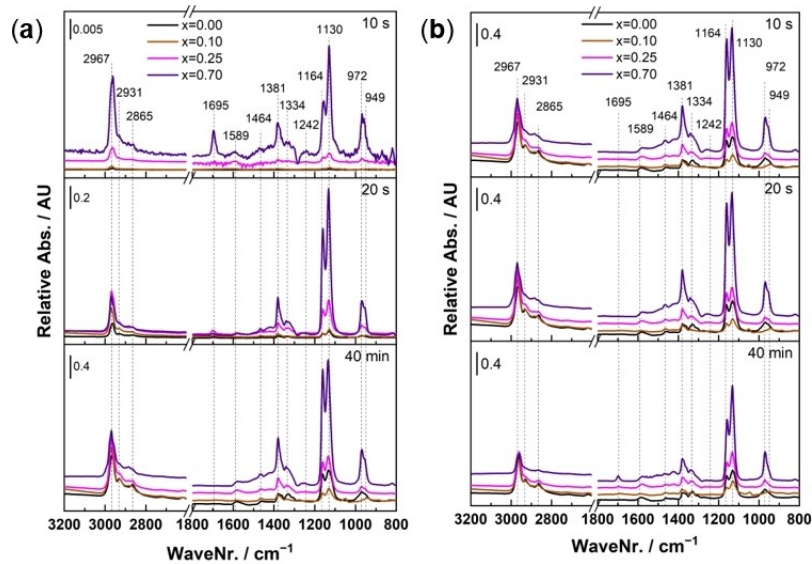
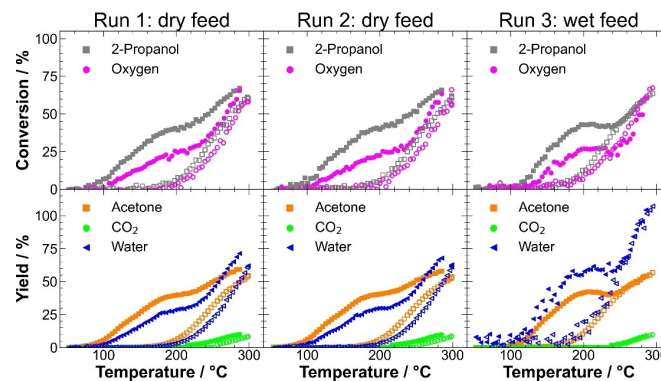


Figure 2. Comparison of DRIFTS spectra at selected times during (a) adsorption and (b) desorption of 2-propanol.

Other features were also observed at  $1464\text{ cm}^{-1}$  and  $1381\text{ cm}^{-1}$  which can be attributed to asymmetric and symmetric scissoring of  $-\text{CH}_3$  and another small band at  $1334\text{ cm}^{-1}$  related to scissoring of C–H bonds of 2-propanol.<sup>[5d,43]</sup> A very small band at  $1242\text{ cm}^{-1}$  could also be detected from the scissoring of O–H bond of the gas-phase or non-dissociative adsorbed 2-propanol.<sup>[44]</sup> Two more bands were progressively developing at  $1164\text{ cm}^{-1}$  and  $1130\text{ cm}^{-1}$ . The former is due to the stretching of the C–C bond, and the latter is related to both the rocking mode of  $-\text{CH}_3$  and stretching of the C–O bond. It should be noted that the C–O bond can be formed by chemisorption of the 2-propanol and the subsequent formation of 2-isopropoxide. Therefore, its relative intensities compared to the C–C band could help to distinguish between the unstable adsorbed 2-propanol (and/or other minor products of dehydrogenation and dehydration paths) and the more-strongly adsorbed 2-isopropoxide or other surface poisoning oxygenated species. The bands at  $972\text{ cm}^{-1}$  and  $949\text{ cm}^{-1}$  are most likely related to the isopropoxide<sup>[45]</sup> and emanating from C–O stretching with hydrogen bonding to the surface<sup>[46]</sup> in contact with  $-\text{OH}$  groups.<sup>[47]</sup> A summary of the bands' assignment is given in Table S2. In conclusion, 2-propanol adsorption DRIFTS showed that the selected catalysts  $x=0.00$ ,  $x=0.10$ ,  $x=0.25$  and  $x=0.70$  adsorb 2-propanol and the position of the asymmetric stretching vibration shifts with Co incorporation into the materials. For  $x=0.70$ , consisting of three crystalline phases, two additional shoulders in the regime were observed. The formation of a C=O bond indicative for acetone formation was seen on all catalysts, although with a higher intensity for the less acidic Co containing catalysts, but the band intensity decreased after  $\sim 1$  min of exposure to 2-propanol which indicates a coverage-dependent formation of acetone since the band intensity increased again during desorption.

#### Catalysis data evaluation procedure

In Figure 3, an obtained example dataset is shown for  $x=0.25$ . The measurement protocol consisted of three consecutive transient experiments on the same catalyst material, two in a dry atmosphere and the third one in a wet atmosphere. The first two runs were performed in a 1:1 mixture of 2-propanol and oxygen diluted with  $\text{N}_2$  without co-feeding of water (dry feed). The second run was performed to check the restorability of the activity of the first run and stability of the catalysts as previously described by Anke and Falk et al.<sup>[5b,7,43,48]</sup> The third run was performed with a 10-fold excess of water compared to 2-propanol and oxygen (wet feed) to build a bridge between gas-phase and liquid-phase catalysis. During initial catalyst activation by temperature-programmed oxidation (TPO) at  $300\text{ }^\circ\text{C}$  in  $10\% \text{ O}_2$  for 2 h,  $\text{CO}_2$  formation was observed, which indicated the formation of carbonates or different adsorbed carbon species formed during storage in air (Figure S13). During the subsequent first run, conversions increased with the temperature proportionally for 2-propanol and oxygen. The oxygen conversion indicates a main contribution of catalytic reactions compared to possible stoichiometric reduction of the catalyst, in which only 2-propanol would be consumed and no oxygen. Since both are consumed, a main contribution of catalysis compared to catalyst reduction can be concluded. A shoulder at  $170\text{ }^\circ\text{C}$  was observed, similar to  $\text{CoFe}_2\text{O}_4$  catalysts.<sup>[43,48]</sup> For 2-propanol oxidation on  $\text{LaFe}_{1-x}\text{Co}_x\text{O}_3$ , high-temperature (HT) and low-temperature (LT) channels were observed, comparable to previous works on  $\text{Co}_3\text{O}_4$ .<sup>[5b,10]</sup> The LT channel persisted during heating to around  $200\text{ }^\circ\text{C}$  and featured selective oxidative dehydrogenation to acetone but is not stable. At different elevated temperatures, secondary product formation was observed,  $\text{CO}_2$  and propene were detected. After an isothermal dwell period of 1 h, the catalyst activity during cooling was significantly decreased, shown in decreased conversion and decreased acetone,  $\text{CO}_2$  and propene yields.



**Figure 3.** Exemplary dataset of  $x=0.25$  obtained from gas-phase 2-propanol oxidation consisting of conversions of 2-propanol and oxygen (top row) and product yields (bottom row) during three consecutive runs. Filled symbols show data points during heating. Empty characters show the behavior during cooling.

Activity loss during cooling was reported before in the literature. The loss was explained by partial stoichiometric reaction of 2-propanol with the catalyst, namely the reduction of  $\text{Co}^{3+}$  to  $\text{Co}^{2+}$  in  $\text{Co}_3\text{O}_4$ ,<sup>[5b]</sup> acetate formation, and carbon deposition on  $\text{CoFe}_2\text{O}_4$ .<sup>[43]</sup>

During TPO between the runs, increased  $\text{CO}_2$  formation was observed, and the  $\text{CO}_2$  formation occurred at higher temperatures compared to the initial activation TPO, exemplarily shown for  $x=0.25$  in Figure S13. The  $\text{CO}_2$  formation indicated buildup of carbonaceous compounds on the catalyst surface during the reaction and their burn-off during TPO. Afterward, the LT activity channel was restored, due to the surface's reoxidation and the removal of carbonaceous compounds and carbon depositions from the surface.<sup>[5b,43,48]</sup> The activity of the second run, during both heating and cooling segments, matched the activity of the first run while the product distribution did not change as well. Indeed, the second run after TPO was performed on all samples to confirm structural stability of the catalysts and the possibility of restoring the activity of the initial freshly loaded catalysts. However, since both dry feed runs were reproducible and overlapped precisely, as shown in Figure S14 for all catalysts, only the first run was considered in the following for further analysis of the dry feed.

Furthermore, the activity of the catalysts upon water co-feeding after a third TPO (Figure S13) showing  $\text{CO}_2$  formation overlapping with the second TPO was studied. Under wet feed conditions, the onset of the reaction was shifted to higher temperatures. In addition, an explicit maximum was observed at 200 °C instead of a broad shoulder in the same temperature range, as clarified in Figure S14e. Still, the main product was acetone as the product of the oxidative dehydrogenation path. In contrast to dry feed, the maximum conversion during wet cooling was not lowered compared to wet heating. While in the dry run, a pronounced activity decay was observed after the isothermal period at 300 °C, in the wet run, heating and cooling curves overlapped for  $T > 250$  °C. This might hint towards a temporary stabilizing effect of water on the catalyst surface structure, preventing either the reduction of active  $\text{Co}^{3+}$  species or the formation of carbonaceous deposits. The HT and LT channels and the instability of the latter remained present under wet conditions, which became evident by the decreased activity of the cooling curve compared to the heating curve at temperatures below 250 °C. In contrast to the heating curves, wet cooling showed higher activity and stability compared to dry cooling. Interestingly, the start of  $\text{CO}_2$  formation during heating was shifted to a higher reaction temperature at 240 °C. The before-mentioned shift in the reaction onset to higher temperatures was in line with the result of adding water vapor to other oxidation reactions due to competitive adsorption of the reactants and water. At higher temperatures, a less severe effect of water in the feed was reported.<sup>[10–18]</sup>

To determine parameters for activity comparison, 2-propanol conversion curves, 2-propanol consumption rates, acetone formation rates, and  $\text{CO}_2$  formation rates were parameterized by fitting the dry and wet data. The heating and cooling curves were fitted with a 20<sup>th</sup> order polynomial and a sigmoidal function, respectively. Figure S15a shows the heating and

cooling curves of 2-propanol conversion during the dry feed run, Figure S15b during the wet feed run. Parameters for comparing the catalysts, such as the temperatures to achieve 10% and 50% conversion ( $T_{10}$  and  $T_{50}$ ), were extracted from the fits.  $T_{10}$  during heating was used to describe the LT reaction channel, while  $T_{10}$  during cooling was used to describe the HT channel of the catalyst after the deactivation of the LT channel.  $T_{50}$  during cooling is used as another parameter to describe the HT channel.

Further parameters for comparison were derived from catalyst mass and BET surface area-normalized rates at 150 °C during heating and 250 °C during cooling for the LT and HT channel, respectively. The methods of determination for these parameters are exemplarily shown for  $x=0.25$  in Figure S15c and d. Both ways are presented to ensure the validity of trends derived from the parameter estimation. In summary, to characterize the LT channel,  $T_{10}$  and rates at 150 °C during heating were taken as activity parameters to compare the different catalysts. As HT channel parameters,  $T_{10}$  and  $T_{50}$ , and rates at 250 °C during cooling were considered. In the following, attempts are presented to correlate these parameters with the materials composition to determine the influence of Co content and phase mixtures.

#### The effect of B-cation substitution on dry feed selective 2-propanol oxidation

In Figure 4a, the 2-propanol conversions of the catalysts in the dry feed are displayed. The conversions of oxygen are shown in Figure S16g. An s-shaped profile was observed for all catalysts during heating. In general, the turning point during heating was shifted to lower temperatures with higher Co content, and the maximum conversion at 300 °C was increased with Co content. All catalysts showed the before-mentioned HT and LT channel and deactivation of the latter during cooling compared to heating. Also, all curves during cooling featured a sigmoidal shape.

With the incorporation of only 5% Co, a substantial increase in activity was observed as reported before for CO oxidation.<sup>[19]</sup> The trend was observed in the LT channel as an initial sharp drop in  $T_{10}$  during heating in Figure 4b. A further more moderate  $T_{10}$  decrease with Co content in the catalysts was seen for all phase-pure catalysts despite local activity maxima for  $x=0.15$  and  $x=0.25$ , which was in line with higher CO oxidation activity and reducibility reported previously.<sup>[19]</sup> In general, judging from  $T_{10}$  for phase-pure samples in dry feed, an activity increase was observed with Co content. No jump in activity was recognized with the formation of secondary phases, but among the non-phase-pure catalysts,  $x=0.50$  featured the lowest  $T_{10}$ , while  $x=0.70$  was the least active sample despite having the highest Co content.

$T_{10}$  and  $T_{50}$  during cooling described the deactivated catalysts activity as parameters for the HT channel, and both showed a parallel evolution (see Figure 4b). For  $0.00 \leq x \leq 0.30$ , a decrease with increasing Co content was detected. The strong activity boost of 5% Co present during heating was not

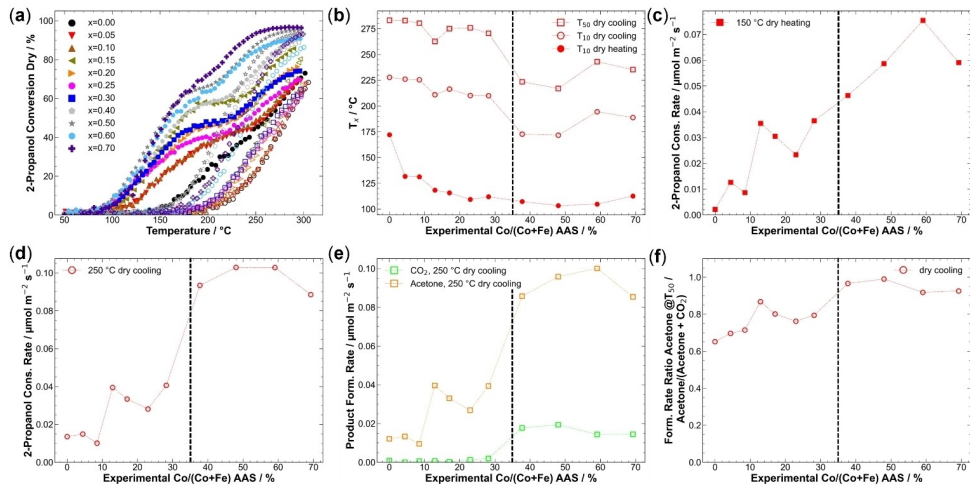


**Figure 4.** (a) 2-Propanol conversions in dry feed. Solid and hollow symbols show data points during heating and during cooling, respectively. (b)  $T_{10}$  values during heating and cooling and  $T_{50}$  during cooling in dry feed plotted against the experimental Co content derived from AAS. (c) Surface-area normalized 2-propanol consumption rates at 150 °C during dry heating. (d) Surface-area normalized 2-propanol consumption rates at 250 °C during dry cooling. (e) Surface-area normalized acetone and  $\text{CO}_2$  formation rates at 250 °C during cooling. (f) Surface-area normalized formation ratio of acetone/(acetone +  $\text{CO}_2$ ) at  $T_{50}$  during cooling. Horizontal lines indicate the formation of the single orthorhombic perovskite phase at low Co contents and the three phase-mixture at higher Co contents.

observed anymore, which might indicate a loss of the beneficial effect of  $\text{Co}^{3+}$  possibly due to reduction leading to similar performance like Co-free  $\text{LaFeO}_3$ , which is in line with the higher reducibility of Co compared to Fe.<sup>[49]</sup> However,  $x=0.15$  was found to be an evident local activity maximum in a volcano-like fashion when considering only the phase-pure samples with  $x < 0.30$ . Since no clear deviation from the intended composition trend was seen for this sample in the previously presented thorough characterization, the reason remains unclear and might be related to the unique (electronic) structure effects of this specific perovskite composition. An extraordinary high activity of this perovskite composition was also reported before for CO oxidation.<sup>[19]</sup> In that work, the position of the low-temperature reduction peak during  $\text{H}_2$ -TPR indicated the highest reducibility for  $x=0.15$  and a correlation between this increased redox activity and the catalytic properties was proposed. Upon the loss of phase purity, a jump to higher activity was observed for  $x \geq 0.40$ , with  $x=0.50$  showing the highest activity suggesting a pronounced effect of the by-phases on the HT channel activity, which was not observed for the LT channel.

2-Propanol consumption rates in dry feed after normalization on exposed BET surface area are displayed in Figure S16c. In comparison to conversion data, differences in the relative reactivity were found after normalization. Rates at 150 °C during heating are shown in Figure 4c. In general, a rather steady increase of the 2-propanol consumption rate with Co content in the catalyst is found, even though no linear

correlation was discovered. The increase between  $x=0.00$  and  $x=0.05$  is not pronounced in this representation, and the volcano-like behavior for the phase-pure samples with a maximum at  $x=0.15$  was observed, which was not as clearly seen for the LT channel in the  $T_{10}$  data. As discussed above, this may be tentatively attributed to higher reducibility of these samples.<sup>[19]</sup> For phase-mixed catalysts, a different trend compared to  $T_{10}$  was observed. Sample  $x=0.60$  showed the highest activity instead of  $x=0.50$ , while  $x=0.70$  still was less active than expected from its bulk Co content. Alike the  $T_{10}$  plot, no abrupt jump in catalytic properties with the presence of by-phases is seen in the rate plot of the LT channel.

The reaction rate at 250 °C during cooling characterizes the HT activity channel and is shown in Figure 4d. Within the phase-pure perovskite samples,  $x < 0.40$ , the volcano-shape with a maximum at  $x=0.15$  from the LT channel was again confirmed in the HT channel. However, the non-phase-pure catalysts showed a pronounced and abrupt activity increase compared to phase-pure ones as observed before for  $T_{50}$  during cooling. The relative activity within the high Co content samples is different compared to the LT channel and the rates for all four catalysts were similar during cooling at 250 °C, with  $x=0.50$  and  $x=0.60$  showing equal and the highest activities. Also, the activity decay for  $x=0.70$  was confirmed.

Product formation rates at 250 °C indicated a jump in  $\text{CO}_2$  formation with the appearance of secondary phases, as is shown in Figure 4e. For acetone formation rates, the same trends as in 2-propanol conversion were seen for all catalysts.

When comparing the selectivity in terms of acetone/(acetone +  $\text{CO}_2$ ) product ratio at  $T_{50}$  during cooling, as shown in Figure 4f, it becomes evident that despite the jump in  $\text{CO}_2$  formation, the selectivity increases rather steadily with Co content even in the presence of by-phases. The local activity maximum at  $x=0.15$  is clearly reflected in a selectivity maximum. The catalyst  $x=0.50$  showed the highest selectivity and selectively catalyzed the formation of acetone at its  $T_{50}$ .

Product yields for all catalysts are shown in Figure S17. For all catalysts, acetone formed via the oxidative dehydrogenation pathway was the main product of the selective oxidation reaction accompanied by the coupled product water. On the other hand, the most prominent undesired oxidation product was  $\text{CO}_2$ . Formation of propene from dehydration in dry feed indicates a more acidic surface of Fe-rich catalysts as  $x=0.00$ ,  $x=0.05$ , and  $x=0.10$  show comparably high yields of propene, which is in line with expectations raised by the literature.<sup>[23,25]</sup> Also, the results agreed with a higher content of B-cations on the materials' surface with low Co-contents found by XPS. This indicates a more acidic surface caused by Fe-excess on the surface. For all other catalysts, the maximum propene yield was less than 1%, the onset temperature shifted to higher temperatures with increasing Co content. Interestingly, the propene formation was not as affected by the deactivation of the catalyst, the yields during heating and cooling were comparable. Other detected products were diisopropyl ether and acetic acid, both of which showing low yields. Ether formation was detected for catalysts with  $x < 0.40$  while acid formation was observed in traces for  $x=0.00$ ,  $x=0.05$ ,  $x=0.10$ ,  $x=0.15$  and  $x=0.30$ .

Summarizing the dry-feed activity, the Co-free sample showed poor activity, whereas Co-incorporation played a dominant role in 2-propanol oxidation activity in the LT channel. In the HT channel, not only the nominal composition but also phase composition was decisive. In the presence of rhombohedral perovskite and spinel, there was an extra activity boost. Within the phase-pure orthorhombic perovskites, a volcano-like behavior was observed with a maximum of 15% Co, which might be superimposed to the composition effect in both channels. A similar non-linear activity increase was reported before in  $\text{CO}$  oxidation and exhaust gas decomposition on  $\text{LaFe}_x\text{Co}_{1-x}\text{O}_3$ <sup>[19,50]</sup> Co-doped  $\text{NiO}$  in  $\text{CO}$  oxidation,<sup>[51]</sup> and  $\text{LaFeO}_3$  with Co and Sr doping.<sup>[23]</sup> For all catalysts, acetone was the main product. Fe-rich catalysts showed the highest propene yields, which indicates that Fe is the more Lewis-acidic site compared to Co.

#### The effect of water vapor on the 2-propanol oxidation

Wet feed 2-propanol conversions of the third run are shown in Figure 5a; wet feed oxygen conversions are shown in Figure S16h. The curves despite  $x=0.00$ ,  $x=0.30$ ,  $x=0.70$  showed a clear local maximum during heating for the LT channel, in contrast to dry feed runs, where only a shoulder was observed. Also, under wet conditions, the deactivation of the LT channel was observed like in the dry feed for all catalysts, and the cooling curve showed a sigmoidal shape without maxima. Compared to the dry runs, the difference between heating and cooling was decreased, which was reflected in cooling curves

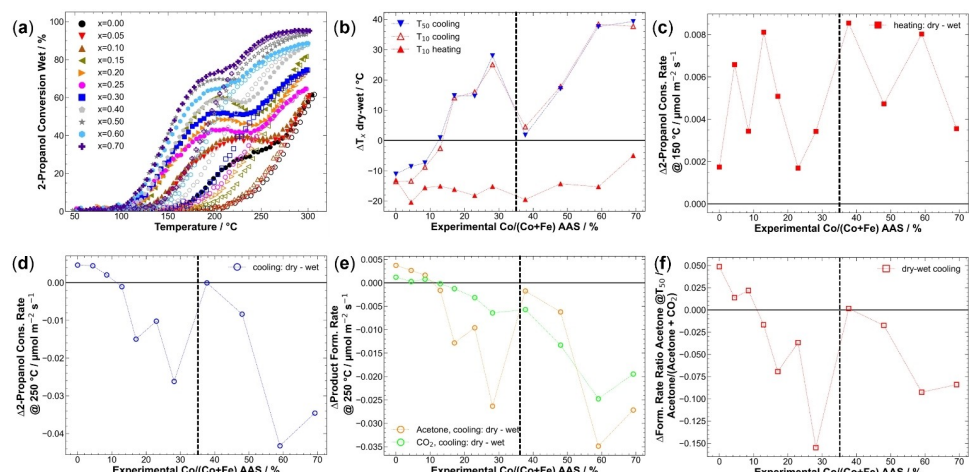


**Figure 5.** (a) 2-Propanol conversions in wet feed. Solid and hollow symbols show data points during heating and during cooling, respectively. (b) Differences between  $T_{10}$  during heating cooling and  $T_{50}$  during cooling for T<sub>dry</sub> and T<sub>wet</sub> differences ( $\Delta = \text{dry-wet}$ ) plotted against the experimental Co content derived from AAS. (c) Differences between surface-area normalized 2-propanol consumption rate at 150 °C during heating. (d) Surface-area normalized 2-propanol consumption rate differences at 250 °C during cooling. (e) Differences in surface-area normalized acetone and  $\text{CO}_2$  formation rates at 250 °C during cooling. (f) The difference in the ratio of acetone/(acetone +  $\text{CO}_2$ ) at  $T_{50}$  during cooling. Horizontal lines indicate the formation of the single orthorhombic perovskite phase at low Co contents and the three phase-mixture at higher Co contents.

shifted to lower temperatures, especially for Co-rich materials. In the HT channel,  $x=0.40$  and  $x=0.50$  showed even an activation and higher activity during cooling than heating until 235 °C and 210 °C indicating a promoting effect of water on the HT channel.

Because of similar curve shapes in dry and wet feed, a comparison based on the previously presented parameters shown in Figure 4 for dry feed is also valid in wet feed. In Figure S18, the mentioned parameters are displayed for dry and wet feed. In the following paragraphs, the differences between dry and wet conditions will be discussed based on the differences between the parameters.

Conversion onset temperature, where the first conversion was observed, during heating was increased for all catalysts from below 100 °C in dry feed to over 100 °C in wet feed. From individual  $T_{10}$  parameters, the lowest  $T_{10}$  in wet feed was 118 °C for  $x=0.50$  and  $x=0.70$ . A parametrized indicator for this rise is the  $\Delta T_{10}$  value between dry and wet conditions, as shown in Figure 5b. A  $\Delta T < 0$  indicates higher temperatures to reach the same conversion and thereby lower activity. As indicated by  $T_{10}$  during heating, the water addition into the feed increased the LT channel onset. The onset of the reaction shifted by at least 12 °C for all catalysts except  $x=0.70$ , for which the onset was only shifted by 5 °C. Also, under wet conditions, the LT boost of only 5% Co was pronounced, as shown in Figure S18a. The activity loss upon water co-feeding can be explained by the competitive pre-adsorption of water on the surface and blocking of active sites, as reported in the literature.<sup>[18]</sup> The water adsorption is considered to take place at the acidic centers of the catalyst surface.<sup>[6]</sup> Also, in methane oxidation, an adverse effect of water on conversion at lower temperatures was observed on  $\text{La}_{1-x}\text{Sr}_x\text{FeO}_3$  catalysts.<sup>[15]</sup> Otherwise, no evident influence of the Co content on the change in LT activity was observed suggesting that above 100 °C, the competitive adsorption does not play a substantial role anymore. Thus, at higher temperatures, the detrimental effect of water addition was less pronounced, as observed also in the literature for other oxidation reactions.<sup>[15,18]</sup>

From Figure S18a, a less-pronounced HT channel boost of  $x=0.15$  in wet feed compared to dry feed can be concluded, along with no major effect of the incorporation of 5% Co as observed in the dry feed. Also, a clear jump in the HT channel between phase-pure and non-phase-pure materials was not observed as strongly as in dry conditions.  $\Delta T_{50}$  and  $\Delta T_{10}$  during cooling characterized the HT activity difference, which revealed similar behaviors (Figure S18a). For Fe-rich catalysts with  $x < 0.15$ , the effect of water on the HT-channel was found to decrease the catalytic activity and higher temperatures were needed for 10% or 50% conversion as is evident from the plot of  $\Delta T_x$  (dry-wet) in Figure 5b. This effect, however, decreased with increasing Co content and the negative  $\Delta T_x$  vanished at  $x=0.15$  for the HT channel, while it persisted in the LT channel. An activity increasing impact of water-addition on the HT activity was observed for  $x > 0.15$  with positive  $\Delta$ -values for the HT channel. A local maximum was reached at  $x=0.30$ , a significant drop for  $x=0.40$  was observed, which indicated a different interaction of different perovskite structures and

spinels upon water addition into the feed. Upon further increase of the Co content and phase segregation, the positive effect of water on the HT channel was even more pronounced. A similar but higher increase of the HT channel activity was previously reported for  $\text{Co}_3\text{O}_4$  spinel catalysts.<sup>[10]</sup> In addition, a more pronounced decrease in the activity of  $\text{LaFeO}_3$  was reported compared to  $\text{LaCoO}_3$  in the oxidation of propane and NO upon co-feeding water.<sup>[18]</sup>

2-Propanol consumption rates in wet feed after normalization on exposed BET surface area are displayed in Figure S16b. To further evaluate activity differences between dry and wet feed, rate differences at 150 °C during heating (HT channel) and 250 °C (LT channel) were compared based on their difference dry-wet ( $\Delta$ ). Positive values indicated higher rates of dry runs and negative values higher rates during wet reactions. Differences at 150 °C as representatives of the LT channel are shown in Figure 5c. Individual dry and wet values in Figure S18b show that the general trend of the dry feed runs was retained for wet runs with a volcano-shaped curve for the phase-pure samples with  $x < 0.40$  with a maximum at  $x=0.15$ . The differences were comparably low between the dry and wet feed, but for all catalysts, the activity in dry feed was slightly higher compared to the wet feed in line with the lower  $T_{10}$  during heating (Figure S18a). There was no systematic effect with Co content on the difference between reaction rates at 150 °C during heating. Like the  $\Delta T_{10}$  heating values the rate differences scatter around an average, indicating a negative effect of water.

On the other hand, water addition strongly affected the HT channel characterized by the 2-propanol consumption rates at 250 °C during cooling, as also observed for  $\Delta T_{50}$ . The difference curve is plotted in Figure 5d, while the individual dry and wet rates are shown in Figure S18c. These indicate a rather constant rate increase with Co incorporation among nearly the whole composition range including the non-phase-pure catalysts until a maximum at  $x=0.60$ . For phase-pure orthorhombic perovskites in wet feed, the superimposed volcano-shaped curve was less clear than in dry conditions and the local maximum was shifted to  $x=0.20$ .

In the rate difference plot (Figure 5d), a decrease in the difference with the Co content was observed, which indicated a beneficial interaction of 2-propanol with the Co-richer surfaces under wet conditions. As seen in the  $\Delta T_{10}$  and  $\Delta T_{50}$  plots for the HT channel, water addition into the feed was detrimental for  $x < 0.15$  as indicated by a positive value for the rate difference, with nearly no effect for  $x=0.15$ , while for higher Co contents, a beneficial and promoting effect was observed with negative rate  $\Delta$ . For the catalysts containing three crystalline phases, the difference between heating and cooling was non-observable for  $x=0.40$ , but with increasing Co content, the beneficial effect of water was also established for these catalysts. The same trend was observed for acetone formation, as shown in Figure 5e. On the other hand, for  $x \leq 0.20$ , the  $\text{CO}_2$  formation was not affected by the co-feeding of water, while for increased Co contents in the catalyst, the increase in  $\text{CO}_2$  formation under wet conditions nearly showed a linear trend up to  $x=0.60$ . Based on the product ratio at  $T_{50}$  during cooling, as shown for

dry and wet feed in Figure S18e and as a difference curve in Figure 5f, for  $x < 0.15$ , a slight loss in selectivity towards selective oxidation in wet feed was found for Fe-rich catalysts, whereas for Co-rich catalysts, the addition of water was beneficial towards a higher ratio of acetone compared to  $\text{CO}_2$ .

The product yields are shown in Figure S17. Like in the dry feed, acetone was the main product for all catalysts accompanied by the couple product water, formed through the oxidative dehydrogenation pathway, while  $\text{CO}_2$  was the main secondary product. The onset of propene yield shifted to higher temperatures with increasing Co content, starting from 235 C ( $x=0.00$ ) in wet feed instead of 185 C in dry feed. Also, the maximum yield of propene was decreased for all catalysts and decreased from 3.6% to 1.6% ( $x=0.00$ ). Only catalysts with  $x < 0.20$  showed the formation of propene in the wet feed, which indicated a higher suppression of water co-feeding on the dehydration pathways compared to oxidative dehydrogenation (acetone) and total oxidation ( $\text{CO}_2$ ). This was in line with the expectation, as the acidic sites for dehydration are competitively adsorbing water and 2-propanol and therefore are partially blocked, whereas the basic sites are still available to perform oxidative dehydrogenation. Also, the formation of diisopropyl ether and acetic acid was influenced by the co-feed of water. While acetic acid was not observed in wet conditions anymore, the onset of ether formation shifted to higher temperatures by ~20 C, and the maximum yield decreased from 0.6% to 0.4%. Ether formation was observed in dry and wet feed for  $x < 0.30$ .

Since, depending on the Co content, wet feed data showed a shift of the HT channel to lower temperatures at the same conversion, a stabilizing effect of water on the HT channel is postulated that might be related to a slower deactivation of the surface by reduction and/or formation of carbonaceous deposits. Therefore, steady-state experiments under dry and wet conditions were performed for  $x=0.00$  and  $x=0.25$  to study the effect of Co addition in the regime of phase-pure perovskites, which are shown in Figure S19 and Figure S20. For  $x=0.00$ , conversion dropped from 52% to 45% within 3 h in dry feed, while under wet conditions, the conversion was stable in the range of 40% from the beginning of the isothermal period. In contrast, in dry feed for  $x=0.25$ , an initial activity decay within 2.5 h in the dry feed from 51% to 23% was observed. Under wet feed conditions, the deactivation took place within 4 h from 54% to 14% conversion. Afterward, the conversion remained constant in both cases in a regime where the activity of the HT-channel during cooling in the transient experiment was observed. This indicates that the low-temperature activity channel is deactivated and can only be seen in a cyclic protocol and restored after another TPO. These experiments supported the argument of the stabilizing effect of water, which leads to a slower deactivation of the Co-containing catalysts, which affects the cooling data in the transient experiments after the isothermal period at 300 C. Also, the experiments showed lower steady-state activity in wet feed, as also reported in the literature.<sup>[10,15]</sup> Potential reasons for the slower deactivation might be suppressed or slower reduction of  $\text{Co}^{3+}$  to  $\text{Co}^{2+}$  due to water adsorption on  $\text{Co}^{3+}$  or

different amounts of carbonaceous species deposition on the catalysts, both shown as deactivation mechanisms for spinel-based catalysts.<sup>[5b,43]</sup> Another possible explanation is the interaction of water molecules with oxygen vacancies. Competitive adsorption of water and oxygen on anion vacancies was reported in the literature and also a hypothesis about a decrease of oxygen vacancies on the catalyst was made.<sup>[18]</sup> However, also a formation of oxygen vacancies in wet feed is possible.

In summary, a detrimental effect of water on the LT channel was seen upon co-feeding water and the onset of the reaction in the LT channel shifted to higher temperatures due to competitive adsorption of water and 2-propanol, while the rates decreased. At the same time, there was a two-fold effect on the HT channel. First, there is an activity decrease for Fe-rich catalysts under wet conditions compared to dry conditions, whereas Co-rich catalysts were more active with water present in the feed in the HT state after deactivation of the LT channel showing how feed and catalyst composition interact for this promoting effect. A likely explanation is that the deactivation of catalysts proceeded slower under the co-feed of water if at least 10% Co is incorporated into the structure, explaining the detrimental effect of water on the HT channel activity for Co-poor materials.

#### Compositional and structural analysis of spent catalysts

In Figure S21, compositional analysis of the surface/bulk B-cation distribution is displayed after catalysis. For the analysis, spent samples were taken from the quartz reactor after cooling down of the wet feed run, stored in air, and characterized. The overall composition trends after reaction (post-catalysis) matched the trends of as-prepared samples before catalysis. As seen on the fresh samples, the catalysts were deficient in Co on the B site on the surface, as derived from XPS, compared with the bulk, as determined by STEM-EDX. In Figure S22a, difference plots of the  $\text{Co}/(\text{Co}+\text{Fe})$  ratio from STEM-EDX and XPS are displayed for direct comparison of the two states, i.e., before and after catalysis. The values are statistically spread around the baseline of 0, indicating no general change among the sample series and no preferred diffusion of Co or Fe to the surface or the bulk during the reaction.

Judging based on the redox-active cation distribution  $\text{Co}/(\text{Co}+\text{Fe})$ , the structure remained largely intact during the reactions, as no indications for systematic compositional changes of the ratio were observed on the surface or in the bulk. XRD after steady-state analysis (shown in Figure S23) strengthened the argument of a retained perovskite structure after catalysis. The perovskite structure remained intact for both cases after two cycles of 24 h reaction time. The only prominent change is the appearance of an increased background in the region between 20 and 35 , that can be attributed to the contribution of quartz wool, used as catalytic bed support. In a previous study on CO oxidation, no bulk changes of  $\text{LaCoO}_3$  were detected by XRD as well.<sup>[3a]</sup> After catalysis, no changes were observed in the ratio of redox-active cations and the bulk-

structure was maintained. The combination of both findings indicates that the characterization of as-prepared catalyst materials may be used as a first approximation for knowledge-based synthesis of perovskite-type oxidation catalysts at temperatures up to 300 °C, since bulk properties and surface composition remain largely unchanged after catalysis at relatively low temperature.

In addition, in High Angular Dark Field (HAADF) STEM analysis of  $x=0.30$  before and after the cyclic catalytic protocol, as shown in Figure 6a in the as-prepared state and in Figure 6b post-catalysis, the orthorhombic perovskite structure remained intact, as indicated by the exemplary crystal structure of the  $\text{LaFeO}_3$  structure along the [110] direction in both subfigures. This supports the argument of an intact perovskite structure after catalysis from a microscopic point of view as well. Altogether, structural characterization after the reaction indicates a stable bulk of the perovskite catalysts even under reaction conditions. However, the surface can be considered as the dynamic part during the reaction, which is supported by the compositional analysis comparing the as-prepared and post-catalysis states.

After catalysis, the trend in B-cation to A-cation distribution with B-cation enrichment remained present, as displayed in Figure S21b. The differences of the STEM-EDX data still indicate a largely unchanged La-enrichment in the bulk of the materials for  $0.00 \leq x \leq 0.70$ . With some deviating data points and an increased error bar compared to one individual measurement, nearly all  $\Delta$  values of the XPS data comparing those measurements before and after catalysis indicate a decrease in the ratio of B- to A-cations in regions near the surface even though the

bulk structure remained unchanged. Effectively, for the phase-pure catalysts up to  $x=0.30$  La enrichment on the surface decreases with increasing Co content until the bulk value is reached. For the catalyst materials with  $x \geq 0.30$  after catalysis, no La surface enrichment is observed anymore (see also Figure S22b). Apparently, migration of La to the catalyst's surface during the reaction or diffusion of Co and Fe into the bulk structure occurred during the reaction. Surface changes in perovskites were also reported in the literature on catalysis and temperature treatment in an oxidizing atmosphere.<sup>[26d,52]</sup> For  $\text{SrTiO}_3$ , an A-cation enrichment on the surface was found upon heat treatment, shown by an increase of  $\text{Sr}/(\text{Sr}+\text{Ti})$  ratio after  $\text{O}_2$  treatment.<sup>[26a]</sup> The same applied for  $\text{BaZrO}_3$  above 500 °C.<sup>[53]</sup>

TEM micrographs after the reaction (Figure S8 and Figure S9, also in comparison with micrographs before the reaction) can be seen as examples for surface dynamics during catalysis, such as surface reconstruction, including surface roughening, surface amorphization, or faceting. The reconstruction to more faceted surfaces was observed in literature upon heat treatment, but at temperatures in the range of 750 °C.<sup>[53]</sup> However, a detailed and statistical analysis of the changes in the STEM images was beyond the scope of the present investigation.

To sum up, according to the comparison of fresh and spent catalysts, the bulk structure remained intact after catalysis. However, the ratio of A-cations to B-cations on the surface, determined by XPS, was changed. Despite the bulk properties of the catalysts seem to be unaffected, changes during catalysis are present at the surface and require operando studies of the catalytic surface, for example in electron microscopy or near ambient pressure X-ray photoelectron spectroscopy (NAP-XPS).<sup>[54]</sup>

#### Operando NAP-XPS: Effect of water on $x=0.25$

The effect of water vapor on the 2-propanol oxidation was studied exemplarily for the  $\text{LaFe}_{0.75}\text{Co}_{0.25}\text{O}_3$  ( $x=0.25$ ) sample, using NAP-XPS, under steady-state conditions, which is comparable to the measurements shown in Figure S20. This technique is potentially able to provide insight into cobalt oxidation states, oxygen defects and adsorbed species at the catalyst surface. Therefore, NAP-XPS upon pretreatment of  $\text{LaFe}_{0.75}\text{Co}_{0.25}\text{O}_3$  ( $x=0.25$ ) up to 250 °C in 0.25 mbar of oxygen was investigated, followed by an investigation in the dry and wet reaction mixtures (total pressure 0.25 mbar) at 200 °C. For each reaction mixture, a fresh catalyst was used. The resulting spectra are shown in Figure 7.

Focus of the analysis was the Co, as this element boosts the catalytic performance and is the redox-active material in this system, and the selected catalyst has a relative high Co content among the phase-pure perovskite catalysts. The corresponding Co 2p spectra are shown in Figure 7a and exhibited a main Co 2p<sub>3/2</sub> signal around a binding energy (BE) of 780 eV together with a satellite structure. The latter is sensitive to the Co oxidation state as the characteristic satellites for  $\text{Co}_3\text{O}_4$  and  $\text{CoO}$  are around 790 eV and 785 eV BE, respectively.<sup>[55]</sup> For pretreat-

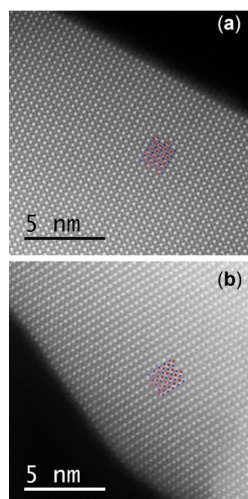


**Figure 6.** (a) HAADF-STEM micrograph of  $x=0.30$  in the as-prepared state. (b) HAADF-STEM micrograph of  $x=0.30$  in the post-catalysis state. The dots on the lattice of both subfigures show the  $\text{LaFeO}_3$  structure along the [110] direction, Fe ions in blue and La ions in red.

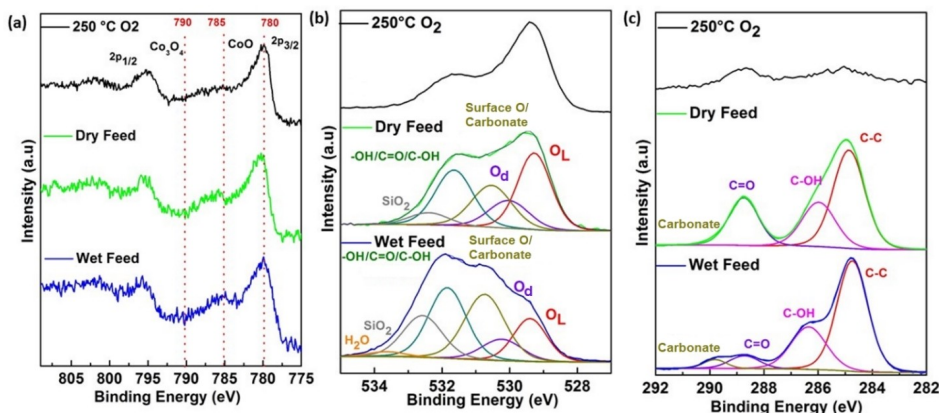


**Figure 7.** Operando NAP-XPS during 2-propanol oxidation under steady state conditions (a) Co 2p spectra ( $h\nu = 930$  eV; KE = 150 eV). (b) Deconvoluted O 1s spectra ( $h\nu = 680$  eV; KE = 150 eV). (c) Deconvoluted C 1s spectra ( $h\nu = 430$  eV; KE = 150 eV). Top, middle, and bottom panel show: the oxidative pretreatment, dry and wet feed conditions.

ment in  $\text{O}_2$  the broad satellite structure between 790 eV and 783 eV BE indicated a partial reduction of  $\text{Co}^{3+}$  to  $\text{Co}^{2+}$ . In contrast, at reaction conditions for both wet and dry feed a single satellite feature around a BE of 783 eV meant a fully reduction to  $\text{Co}^{2+}$ . This is also confirmed by a linear combination fitting using the peak shapes of  $\text{Co}_3\text{O}_4$ ,  $\text{CoO}$  and  $\text{Co}$  (Figure S24) reported by Biesinger et al.<sup>[55]</sup> Close inspection of the peak shape in case of the wet feed revealed some additional peak contribution at 783 eV BE in addition to a slightly broader  $\text{Co} 2p_{3/2}$  signal. This may suggest an additional formation of Co hydroxide species which should have a broad satellite around this region.<sup>[56]</sup>

In the O 1s region of dry and wet feed, a broad signal with overlapping components was detectable. A possible deconvolution is provided in Figure 7b. The components of the substrate can be attributed to oxygen lattice ( $\text{O}_L$ ) at BE = 529.3 eV and to oxygen related to defects ( $\text{O}_d$ ) at BE = 530 eV.<sup>[57]</sup> The defective type oxygen can be understood as a missing oxygen atom, whereas the missing additional charge is compensated by the surrounding oxygen atoms resulting in a peak shift compared the nominal lattice BE of  $\text{O}_L$ . An alternative explanation of this peak at BE = 530 eV could be a contribution of common impurities like molybdates that were found in small amounts on the samples. The peak at BE = 530.7 eV can be attributed to adsorbed and surface oxygen species (surface O).<sup>[57]</sup> In addition, around this binding energy there are also carbonates that were detected in the case of the wet feed in the C 1s spectrum (see below). The signal around BE = 531.8 eV corresponds to carbonyl/alcoholic O as well as to hydroxide formation and could not be resolved into single components. Furthermore, adsorbed water (BE = 533.8 eV) and  $\text{SiO}_2$  contaminations at BE = 532.6 eV can be detected. The main difference between dry and wet feed is an increased intensity of signals related to the

hydroxide formation and the carbonate adsorbates. The first one is in line with the presence of water in the wet feed.

C 1s spectra in Figure 7c after pretreatment indicated no major adsorbed carbon, but under dry conditions, contributions of  $\text{C}=\text{O}$  (BE = 288.7 eV),  $\text{C}-\text{OH}$  (BE = 285.9 eV) and  $\text{C}-\text{C}$  (BE = 284.8 eV) were observed. The signals of  $\text{C}-\text{OH}$  and  $\text{C}-\text{C}$  could arise from adsorbed 2-propanol or some fragments of it. On the other hand, the appearance of  $\text{C}=\text{O}$  can be explained by intermediates of the reaction or even not yet desorbed acetone. Under wet conditions, an additional signal at a BE of 289.8 eV appeared that could be interpreted as carbonate formation. In addition, the carbonyl signal was lowered in intensity and shifted towards lower BE by 0.2 eV. The  $\text{C}-\text{OH}$  signal shifted by 0.3 eV to higher BE. Both shifts may be explained by a different interaction of the adsorbed species with the dry and wet surface.

In summary, a reduction from  $\text{Co}^{3+}$  to  $\text{Co}^{2+}$  was observed in the reaction mixture of gases. According to the sample history with a pre-annealing step and with a temperature of 200 °C, the measurements were performed in the deactivated part of the HT channel. These conditions are in line with the observed reduction of  $\text{Co}^{3+}$  to  $\text{Co}^{2+}$ . It is worth mentioning that during these measurements a formation of acetone,  $\text{CO}_2$  and water was observed via mass spectrometry. The main differences from comparison between dry and wet feed were increased hydroxide and carbonate signals visible in the O 1s spectra. The high amount of adsorbed carbon species on the surface may also explain the deactivation of the catalyst by a blocking of the active sites.

Further operando studies on the selected catalyst are planned and under execution to fully understand the role of water in the reaction mixture and the individual transition metals.

## Conclusion

$\text{LaFe}_{1-x}\text{Co}_x\text{O}_3$  catalysts with an orthorhombic crystal structure were synthesized phase-pure up to  $x=0.30$ . For  $x>0.30$ , a three-phase mixture was found consisting of orthorhombic perovskite and additional rhombohedral perovskite and minor amounts of a spinel structure. By Rietveld refinement, a high content of Co in the spinel was observed. From Mössbauer spectroscopy, the weak ferromagnetism, and typical hyperfine parameters of  $\text{Fe}^{3+}$  ions in the perovskite phase were confirmed, while magnetometry data indicated the preservation of the macroscopic stoichiometry throughout the sample series, with only minute parasitic phase content. The materials are Co deficient on the B-site, both at the surface and in the bulk, particularly at high Co contents, i.e.,  $x\geq 0.30$ . The adsorption of 2-propanol under dry conditions was studied for selected catalysts in a DRIFTS setup during adsorption and desorption of 2-propanol and showed an immediate formation of an acetone band after short exposure to the reaction mixture, but a disappearance of the band at higher surface concentrations of 2-propanol. Also, a higher acidity of Fe-rich surfaces was confirmed during product analysis of the catalytic reaction in a flow-setup.  $\text{LaFe}_{1-x}\text{Co}_x\text{O}_3$  can be considered as active and selective catalysts for gas-phase 2-propanol oxidation in a catalytic flow-reactor. The reaction offers two pathways, a more active unstable pathway (LT-channel) and a less active, but stable pathway (HT-channel). The transition between the two channels can be ascribed to changes in transition metal oxidation state and deposition of carbonaceous compounds on the surface due to stoichiometric reaction instead of catalytic reaction and can be restored by an oxidative treatment in between the oxidation runs. In general, higher Co contents in the perovskites increase the reactivity of the catalysts with the most pronounced boost between  $x=0.00$  and  $x=0.05$ . In HT-activity, a volcano-like behavior was observed among the phase-pure samples with a maximum at  $x=0.15$  which is in line with the lowest TPR peak position presented in a previous study.<sup>[19]</sup> With the evolution of the two secondary phases, another pronounced activity jump was observed. The addition of water into the feed had a negative impact on the LT channel over the whole composition range. For the HT channel, several effects were observed among the phase-pure samples. For catalysts up to  $x=0.10$ , a negative effect of the water co-feed was seen. For  $x=0.15$ , nearly no change was observed, while for  $x>0.15$  there was a positive effect of water. The positive effect of water in the feed might be explained by water adsorption on  $\text{Co}^{3+}$  and therefore preventing the active  $\text{Co}^{3+}$  sites from fast reduction and/or being deactivated quickly due to coking. NAP-XPS showed an increase in hydroxide content on the surface upon the introduction of water into the feed. Furthermore, the reduction of  $\text{Co}^{3+}$  during the reaction cycle in dry and wet feed was shown, which might point toward an only temporary stabilization of the surface in the wet feed in the transient experiment. The comparison of as-prepared samples before catalysis and spent-sample characterization in TEM(-EDX) and XPS indicated that the initial Co deficiency was not changed after catalysis for phase-pure catalysts. The bulk of

the materials generally shows an A-cation enrichment, which is not changed after catalysis. Pronounced B-cation enrichment on the surface is observed that is decreased after the reaction. For the catalysts also featuring secondary phases, B-cation surface enrichment, when compared with bulk value, is significantly less pronounced and vanishes after catalysis. Generally, no large-scale structural changes of nanoparticles like particle size, shape and bulk composition were observed between the samples before and after catalysis, justifying a synthesis approach targeting the rational design of low-temperature oxidation catalysts. In-depth kinetic analysis to fully understand the effect of water in the reaction mixture and the impact on individual transition metals, is currently being done in our consortium for the conditions and materials elaborated in this work and will be reported in an upcoming research paper.

## Experimental Section

### Raw materials

For the synthesis of the investigated catalysts, commercially available reagents were used without additional purification: lanthanum(III) nitrate hexahydrate (99.9% La, abcr GmbH, Karlsruhe, Germany), iron(III) nitrate nonahydrate ( $\geq 98\%$ , Sigma-Aldrich GmbH, Karlsruhe, Germany), cobalt(II) nitrate hexahydrate ( $\geq 98\%$ , Carl Roth GmbH, Karlsruhe, Germany), sodium hydroxide (98.5%, Carl Roth GmbH, Karlsruhe, Germany), and sodium carbonate ( $\geq 99.5\%$ , VWR International GmbH, Darmstadt, Germany).

### Synthesis and sample preparation

The synthesis via co-precipitation included preparing metal salt stock solutions with a total ionic concentration  $M^{n+}$  of  $0.8 \text{ mol L}^{-1}$  with the general composition  $\text{La}^{3+}/\text{Fe}^{3+}/\text{Co}^{2+} = 1:1-x:x$ . The value of  $x$  was varied in the range between 0.00 and 0.70. The precipitation agent was a solution consisting of 1.2 M NaOH and 0.18 M  $\text{Na}_2\text{CO}_3$ .

The syntheses were performed in an automated OptiMax 1001 (Mettler Toledo GmbH, Greifensee, Switzerland) synthesis workstation. The setup consists of a single-walled glass reactor fixed inside a solid-state thermostat for accurate temperature control. During precipitation and aging steps,  $\text{N}_2$  flow was employed, and the 100 mL prefill volume of the reactor was purged with  $\text{N}_2$  for 30 min. The co-precipitation experiments have been performed isothermally at 10 °C and a constant pH of 9.5. A universal control box equipped with a precision balance allowed gravimetric dosing of the metal salt solutions of 75 g in 36 min. Control over the pH was achieved by simultaneous computer-controlled dosing of the metal salt solution and the precipitation agent via two ProMinent gamma/L metering pumps. The pH was monitored and adjusted using an InLab Semi-Micro-L electrode during each experiment. A pitched blade impeller rotating at a constant speed of 300 rpm was used to avoid concentration and temperature gradients. After the precipitation was finished, an aging step at 10 °C for 60 min was performed. After aging, the precipitate was isolated by centrifugation (6000 rpm, 2 min) and washed with deionized water until the conductivity of the supernatant was below  $0.1 \text{ mS cm}^{-1}$  in two consecutive runs. Afterward, the samples were dried in static air at 80 °C for 12 h. Finally, the precursors were calcined at 800 °C for 3 h ( $\beta=2 \text{ °C min}^{-1}$ ) in stagnant air in a muffle furnace (B150, Naber-

therm, Lilienthal, Germany). The calcined samples were characterized as powders and pressed with a hydraulic press by Perkin-Elmer (5 t, 2 min, Überlingen, Germany), pestled, and sieved with stainless steel sieves ATECHNIK (ISO 3310-1, Leinburg, Germany).

#### Catalyst characterization

Fe and Co contents in the precursors were determined by atomic absorption spectroscopy (M-Series, Thermo Electron Corporation, Waltham, Massachusetts, United States of America).

Thermogravimetric measurements (TG) were performed in a NETZSCH STA 449F3 thermal analyzer (NETZSCH-Gerätebau GmbH, Selb, Germany). For TG measurements, 50 mg of precursor material was heated in a corundum crucible in 21%  $\text{O}_2$  in Ar from 30 °C to 1000 °C with a linear heating rate of 5 °C min<sup>-1</sup>.

$\text{N}_2$  adsorption-desorption experiments were performed with a NOVA3000e setup (Quantachrome Instruments, Boynton Beach, Florida, United States of America) at -196 °C after degassing the samples at 80 °C for 2 h in a vacuum. BET (Brunauer Emmet Teller) surface areas were calculated from  $p/p_0$  data between 0.05 and 0.3. Total pore volumes were determined at  $p/p_0 = 0.99$ .

Powder XRD patterns in the 2θ range from 5° to 90° were recorded on a Bruker D8 Advance (Bruker, Billerica, Massachusetts, USA) diffractometer in Bragg-Brentano geometry using a position-sensitive LYNXEYE detector (Ni-filtered  $\text{CuK}_\alpha$  radiation, Bruker, Billerica, Massachusetts, USA) applying a counting time of 0.3 s and step size of 0.018. Samples were mounted using dispersion in ethanol on a glass disc inserted in a round PMMA holder. The latter was subject to gentle rotation during scanning after removing the ethanol by drying. For structure analysis and calculation of lattice parameters, Rietveld refinement [44] was applied using the TOPAS software (Bruker, Billerica, Massachusetts, USA).

X-ray photoelectron spectroscopy (XPS) measurements were performed using a VersaProbe II (Ulvac-Phi, Chanhassen, USA). Al K<sub>α</sub> and Mg K<sub>α</sub> sources were used to investigate the powders.

Mössbauer spectra on selected powder samples were recorded in transmission geometry, using a ~50 mCi <sup>57</sup>Co radiation source mounted on a constant-acceleration driving unit (Wissel GmbH, Ortenberg, Germany). Zero field spectra at low temperatures were recorded with a closed-cycle cryostat (Lake Shore Cryotronics, Westerville, Ohio, USA) while a liquid helium bath cryostat with a superconducting split-pair magnet was utilized for spectra recorded in an applied magnetic field of 5 T parallel to the γ-ray propagation direction.

The macroscopic magnetic properties were characterized with the vibrating sample magnetometer (VSM) option of a PPMS DynaCool (Quantum Design Inc., San Diego, California, USA). Measurements on selected powder samples include magnetic field dependent M(H) loops up to ±9 T at 4.3 K and 300 K, as well as temperature dependent M(T) curves between 5 K and 380 K recorded in the standard zero field cooled – field cooled (ZFC-FC) protocol at an applied magnetic field of 0.1 T.

High-resolution scanning transmission electron microscopy (STEM) studies were carried out on a Jeol JEM 2200 fs microscope (Akishima, Japan) equipped with a probe-side Cs-corrector operated at 200 kV acceleration voltage. Micrographs were taken in conventional bright field as well as in high-angle annular darkfield (HAADF) mode. In addition, EDX elemental mappings were acquired with an X-Max 100 detector (Oxford Instruments, Abingdon, United Kingdom).

#### 2-Propanol adsorption and desorption DRIFTS

DRIFTS was performed using an FTIR spectrometer from Thermo-Fisher Scientific (Waltham, Massachusetts, USA), i.e., Nicolet™ iS20, equipped with a DRIFTS cell (Praying Mantis™, Harrick Scientific Products Inc., Pleasantville, New York, USA) and a Mercury Cadmium Telluride detector (MCT) cooled with liquid nitrogen. The DRIFTS cell outlet gas stream was analyzed continuously during the experiment by an online mass spectrometer (Omnistar GSD 320, Pfeiffer Vacuum, Wetzlar, Germany). Using a four-port selector valve, the inlet gas was switched between two different streams, one for He-purging and/or pretreatments (He or 20% v/v  $\text{O}_2$  in He) and the other containing the probe gas (0.25% v/v 2-propanol in He). A home-built saturator comprising of a double pipe heat exchanger and a submerged static mixer was used to provide 2-propanol with the desired concentration. The temperature of the liquid 2-propanol was maintained by external circulating chilled water flowing through the exchanger's outer tube, while the He flow was thoroughly dispersed in the liquid through the static mixer to maximize the contact between the gas and liquid. The gas streams were flowing through the catalyst bed inside the chamber in all segments with a total flowrate of 80 mL min<sup>-1</sup>. At first, the loaded samples (~30–40 mg fine powder) were pretreated by 20%  $\text{O}_2$  in He at 350 °C for 1 h (at a heating rate of 10 °C min<sup>-1</sup>), after which the cell was cooled down to 20 °C at the maximum rate. After stabilizing the temperature,  $\text{O}_2$  was closed, the chamber and lines were purged with He for 10 min before collecting the background spectrum. Then the samples were exposed to 0.25% 2-propanol in He, and the spectra corresponding to the adsorption were collected for 40 min every 10 s. The first spectrum was collected before switching the gas, so it represents the time 0. Then the gas was automatically switched back to He to record the desorption spectra for another 40 min.

#### Catalytic 2-propanol oxidation

The measurements were performed in a home-built apparatus consisting of a gas dosing unit (HovaGAS N G6 VOC-S, IAS GmbH, Germany) and a Tube Furnace MTF 10/25/130 (Carbolite Gero, Neuhausen, Germany), which is placed in a heating cabinet Thermocenter TC100 (SalvisLab, Rotkreuz, Switzerland). The reaction mixture, either going through or by-passing the reactor, was analyzed on a downstream dual-carrier gas Fusion Micro GC (Inficon GmbH, Bad Ragaz, Switzerland) equipped with four separation modules (2 × Rt-Molsieve 5 A, 1 × Stabilwax DB, 1 × Rt-Q Bond). 100 mg of the catalyst mixture was placed in a quartz reactor (inner diameter = 8 mm).

The reaction consisted of three runs that were performed under the same temperature conditions. Only the reactive gas mixture was changed between the runs. Before each run, temperature-programmed oxidation (TPO) up to 300 °C was performed at a flow rate of 50 mL min<sup>-1</sup> with an  $\text{O}_2$  concentration of 10% (balanced in  $\text{N}_2$ ), the heating rate was set to 3 °C min<sup>-1</sup>. The maximum temperature was kept constant for 2 h. Afterward, the temperature was cooled down to 50 °C with a heating rate of 3 °C min<sup>-1</sup>. The temperature was kept constant for 65 min. During the first 20 min, the remaining  $\text{O}_2$  was purged out by  $\text{N}_2$  (100 mL min<sup>-1</sup>). In the last 45 min, the reaction mixture was purged for stabilization of the MFC flows. Afterward, the temperature was increased to 300 °C in the reaction mixture with a heating rate of 1 K min<sup>-1</sup> up and held constant for 1 h. After the isothermal dwell, the temperature was cooled down to 50 °C with a heating rate of 1 K min<sup>-1</sup> in the reaction mixture. Before the next TPO started, the temperature was dwelled for 10 min and a flow of 100 mL min<sup>-1</sup>  $\text{N}_2$  was applied. The reaction mixture consisted of 0.169% 2-propanol and 0.169%  $\text{O}_2$  balanced in  $\text{N}_2$  (dry mixture) for the first two runs and 0.175% 2-

propanol, 0.172%  $\text{O}_2$ , and 1.88%  $\text{H}_2\text{O}$  in  $\text{N}_2$  for the third run (wet mixture). The flow rate was kept constant at  $100 \text{ mL min}^{-1}$ .

For steady-state experiments, first, a TPO up to 300  $^\circ\text{C}$  was performed at a flow rate of  $50 \text{ mL min}^{-1}$  with an  $\text{O}_2$  concentration of 10% (balanced in  $\text{N}_2$ ), the heating rate was set to  $3 \text{ C min}^{-1}$ . The maximum temperature was kept constant for 2 h. Afterward, the temperature was cooled down to 50  $^\circ\text{C}$  with a heating rate of  $3 \text{ C min}^{-1}$ . The temperature was kept constant for 65 min. During the first 20 min, the remaining  $\text{O}_2$  was purged out by  $\text{N}_2$  ( $100 \text{ mL min}^{-1}$ ). In the last 45 min, the reaction mixture was purged for stabilization of the MFC flows. Afterward, the temperature was increased to 290  $^\circ\text{C}$  (for  $x=0.00$ ) or 190  $^\circ\text{C}$  (for  $x=0.25$ ) in the dry mixture with a heating rate of  $1 \text{ K min}^{-1}$  up and held constant for 24 h. After the isothermal dwell, the temperature was cooled down to 50  $^\circ\text{C}$  with a heating rate of  $1 \text{ K min}^{-1}$  in the dry reaction mixture. Afterward, another cycle with the same temperature and flow conditions was performed. The only difference was the use of the wet instead of the dry reaction mixture.

#### Near ambient pressure XPS studies

Near ambient pressure X-ray photoelectron spectroscopy (NAP-XPS) was performed at the UE56/2-PGM1 (Elliptical Undulator) beamline of the synchrotron radiation facility BESSY II of Helmholtz-Zentrum Berlin, Germany. The used end-station consisted of a near-ambient pressure (NAP) photoelectron analyzer provided by SPECS GmbH (Phoibos 150). To minimize losses of photons and electrons a 50 nm thick  $\text{SiN}_x$  X-ray membrane close to the sample and a differentially pumped electron analyzer with electrostatic lenses were used. Also, it is equipped with a sapphire sample holder, where typically a powder pellet and K-type thermocouple are fixed. The sapphire sample holder is mounted inside the XPS setup near to the aperture of the first differential pumping stage. The heating treatment is carried out through an infrared laser from the rear. The gas composition during the *operando* measurements was monitored by a quadrupole mass spectrometer. Details of the experimental setup can be found in the literature.<sup>[58]</sup>

The pellet was pretreated by annealing in 0.25 mbar  $\text{O}_2$  at 250  $^\circ\text{C}$  using a heating rate of  $5 \text{ C min}^{-1}$  to clean the sample from adsorbed carbon species. Afterward, cooling of the sample to 100  $^\circ\text{C}$  was performed and for the dry feed a mixture of 2-propanol, oxygen and argon was introduced (0.25 mbar,  $1 \text{ mL min}^{-1}$ : $1 \text{ mL min}^{-1}$ : $0.15 \text{ mL min}^{-1}$ ) into the XPS cell. Each partial pressure is controlled by mass flow controllers. Then, the temperature was increased with a heating rate of  $10 \text{ C min}^{-1}$  up to 200  $^\circ\text{C}$  at which the XPS measurements were performed. All core level regions were recorded with a kinetic energy of 150 eV.

For the measurements in wet feed a fresh pellet was used. The procedure was the same as described above, but the reaction gas mixture consisted of water, 2-propanol, oxygen, and argon (0.25 mbar,  $0.7 \text{ mL min}^{-1}$ : $0.7 \text{ mL min}^{-1}$ : $0.7 \text{ mL min}^{-1}$ : $0.1 \text{ mL min}^{-1}$ ).

XPS spectra were analyzed through CasaXPS and Igor Pro. The binding energies were calibrated to the fermi edge of a Pd reference sample. The O1s and C1s spectra were deconvoluted with combined Gaussian and Lorentzian functions after a Shirley + linear background subtraction.

#### Acknowledgements

This work was funded by the Deutsche Forschungsgemeinschaft (DFG, German Research Foundation) – 388390466 – TRR

247 within the projects A1, B2, B7, C1, and S. We also acknowledge the financial support from the Mercator Research Center Ruhr (MERCUR, Pe-2018-0034). The authors also acknowledge Robin Meya and Beate Römer for providing AAS measurements and Dietrich Tönnes for XRD measurements and Benjamin Mockenhaupt as well as Jil Gieser for BET measurements and Nicolas Cosanne for help in performing the syntheses. Furthermore, we acknowledge support by the Open Access Publication Fund of the University of Duisburg-Essen enabled and organized by the Project DEAL. We acknowledge Michael Hävecker and Thomas Götsch for their experimental support and discussions. We thank HZB for synchrotron radiation beamtime at BELChem of BESSY II and to Max Planck Society for financial support. Open Access funding enabled and organized by Projekt DEAL.

#### Conflict of Interest

The authors declare no conflict of interest.

**Keywords:** 2-Propanol · LFCO · Oxidation · Oxygen Vacancies · Perovskite phases

- [1] a) F. Cavani, *Catal. Today* **2010**, *157*, 8–15; b) Z. Guo, B. Liu, Q. Zhang, W. Deng, Y. Wang, Y. Yang, *Chem. Soc. Rev.* **2014**, *43*, 3480–3524; c) He, J., Cheng, X., Zhang, M., Douthwaite, S., Pattisson, Z., Hao, *Chem. Rev.* **2019**, *119*, 4471–4568; d) M. S. Kamal, S. A. Razzak, M. M. Hossain, *Atmos. Environ.* **2016**, *140*, 117–134.
- [2] S. Royer, D. Duprez, F. Can, X. Courtois, C. Batiot-Dupeyrat, S. Laassiri, H. Alamdar, *Chem. Rev.* **2014**, *114*, 10292–10368.
- [3] a) B. Alkan, S. Cychy, S. Varhade, M. Muhler, C. Schulz, W. Schuhmann, H. Wiggers, C. Andronescu, *ChemElectroChem* **2019**, *6*, 4266–4274; b) B. Alkan, D. Medina, J. Landers, M. Heidelmann, U. Hagemann, S. Salamon, C. Andronescu, H. Wende, C. Schulz, W. Schuhmann, H. Wiggers, *ChemElectroChem* **2020**, *7*, 2564–2574; c) J. Büker, B. Alkan, Q. Fu, W. Xia, J. Schulwitz, D. Waffel, T. Falk, C. Schulz, H. Wiggers, M. Muhler, B. Peng, *Catal. Sci. Technol.* **2020**, *10*, 5196–5206; d) D. Waffel, B. Alkan, Q. Fu, Y. T. Chen, S. Schmidt, C. Schulz, H. Wiggers, M. Muhler, B. Peng, *ChemPlusChem* **2019**, *84*, 1155–1163; e) S. Angel, J. Neises, M. Dreyer, K. Friedel Ortega, M. Behrens, Y. Wang, H. Arandian, C. Schulz, H. Wiggers, *AIChE J.* **2019**, *66*, 441.
- [4] J. Park, Y. N. Wu, W. A. Saidi, B. Chorpeling, Y. Duan, *Phys. Chem. Chem. Phys.* **2020**, *22*, 27163–27172.
- [5] a) S. Y. Liu, S. M. Yang, *Appl. Catal. A* **2008**, *334*, 92–99; b) S. Anke, G. Bendt, I. Sinev, H. Hajiyani, H. Antoni, I. Zegkinoglou, H. Jeon, R. Pentcheva, B. Roldan Cuena, S. Schulz, M. Muhler, *ACS Catal.* **2019**, *9*, 5974–5985; c) M. A. Amenta, R. Valdez, R. Silva-Rodrigo, A. Olivas, *Fuel* **2019**, *236*, 934–941; d) G. S. Foo, F. Polo-Garzon, V. Fung, D.-e. Jiang, S.-H. Overbury, Z. Wu, *ACS Catal.* **2017**, *7*, 4423–4434; e) R. Radha, C. S. Swamy, *Surf. Technol.* **1985**, *24*, 157–163; f) S. Tan, M. B. Gray, M. K. Kidder, Y. Cheng, L. L. Daemen, D. Lee, H. N. Lee, Y.-Z. Ma, B. Dougherty, D. A. Lutterman, *ACS Catal.* **2017**, *7*, 8118–8129.
- [6] W. Dai, L. Ren, in *Handbook of Heterogeneous Catalysis*, Vol. 5 (Eds.: G. Ertl, H. Knölzinger, F. Schüth, J. Weitkamp), Wiley-VCH Verlag GmbH & Co. KGaA, Weinheim, Germany, **2008**, p. 2159.
- [7] T. Falk, S. Anke, H. Hajiyani, S. Saddele, S. Schulz, R. Pentcheva, B. Peng, M. Muhler, *Catal. Sci. Technol.* **2021**.
- [8] A. Bera, D. Bullert, M. Linke, E. Hasselbrink, *J. Phys. Chem. C* **2021**, *125*, 7721–7727.
- [9] Z. Bao, V. Fung, F. Polo-Garzon, Z. D. Hood, S. Cao, M. Chi, L. Bai, D.-e. Jiang, Z. Wu, *J. Catal.* **2020**, *384*, 49–60.
- [10] T. Falk, E. Budiyanto, M. Dreyer, C. Pfleiger, D. Waffel, J. Büker, C. Weidenthaler, K. F. Ortega, M. Behrens, H. Tüysüz, M. Muhler, B. Peng, *ChemCatChem* **2021**, *13*, 2942–2951.

- [11] A. Sapi, F. Liu, X. Cai, C. M. Thompson, H. Wang, K. An, J. M. Krier, G. A. Somorjai, *Nano Lett.* **2014**, *14*, 6727–6730.
- [12] F. D. Liu, H. L. Han, L. M. Carl, D. Zherebetsky, K. An, L. W. Wang, G. A. Somorjai, *J. Phys. Chem. C* **2019**, *123*, 7577–7583.
- [13] H. Wang, A. Sapi, C. M. Thompson, F. Liu, D. Zherebetsky, J. M. Krier, L. M. Carl, X. Cai, L. W. Wang, G. A. Somorjai, *J. Am. Chem. Soc.* **2014**, *136*, 10515–10520.
- [14] Y. Liu, H. Dai, J. Deng, X. Li, Y. Wang, H. Arandiyani, S. Xie, H. Yang, G. Guo, *J. Catal.* **2013**, *305*, 146–153.
- [15] C. H. Wang, C. L. Chen, H. S. Weng, *Chemosphere* **2004**, *57*, 1131–1138.
- [16] J. Li, R. Wang, J. Hao, *J. Phys. Chem. C* **2010**, *114*, 10544–10550.
- [17] R. M. Contractor, H. S. Horowitz, G. M. Sisler, E. Bordes, *Catal. Today* **1997**, *37*, 51–57.
- [18] R. Zhang, H. Alamdarri, S. Kaliaguine, *Appl. Catal. B* **2007**, *72*, 331–341.
- [19] M. Dreyer, M. Krebs, S. Najaishiriani, A. Rabe, K. Friedel Ortega, M. Behrens, *Catalysts* **2021**, *11*, 550.
- [20] a) S. Royer, D. Duprez, *ChemCatChem* **2011**, *3*, 24–65; b) P. Granger, S. Kaliaguine, V. I. Părvulescu, W. Prellier, Wiley-VCH, Weinheim, **2016**, pp. Online-Ressource (1 online resource).
- [21] R. J. Voorhoeve, J. P. Remeika, D. W. Johnson, Jr., *Science* **1973**, *180*, 62–64.
- [22] F. Polo-Garzon, Z. Wu, *J. Mater. Chem. A* **2018**, *6*, 2877–2894.
- [23] J. N. Kuhn, U. S. Ozkan, *J. Catal.* **2008**, *253*, 200–211.
- [24] M. M. Natile, E. Ugel, C. Maccato, A. Gisleni, *Appl. Catal. B* **2007**, *72*, 351–362.
- [25] G. Tesquet, J. Faye, F. Hosoglu, A.-S. Mamede, F. Dumeignil, M. Capron, *Appl. Catal. A* **2016**, *511*, 141–148.
- [26] a) F. Polo-Garzon, V. Fung, X. Liu, Z. D. Hood, E. E. Bickel, L. Bai, H. Tian, G. S. Foo, M. Chi, D.-e. Jiang, Z. Wu, *ACS Catal.* **2018**, *8*, 10306–10315; b) L. Bai, F. Polo-Garzon, Z. Bao, S. Luo, B. M. Moskowitz, H. Tian, Z. Wu, *ChemCatChem* **2019**, *11*, 2107–2117; c) X. Wang, K. Huang, J. Qian, Y. Cong, C. Ge, S. Feng, *Sci. Bull.* **2017**, *62*, 658–664; d) F. Polo-Garzon, Z. Bao, X. Zhang, W. Huang, Z. Wu, *ACS Catal.* **2019**, *9*, 5692–5707.
- [27] A. Füngerlings, A. Koul, M. Dreyer, A. Rabe, D. M. Morales, W. Schuhmann, M. Behrens, R. Pentcheva, *Chem. Eur. J.* **2021**.
- [28] R. Allmann, H. P. Jepsen, *Neues Jahrb. Mineral. Monatsh.* **1969**, *1969*, 544–551.
- [29] L. Sangaletti, L. E. Depero, B. Allrieri, P. Nunziante, E. Traversa, *J. Eur. Ceram. Soc.* **2001**, *21*, 719–726.
- [30] R. D. Shannon, *Acta Crystallogr. Sect. A* **1976**, *32*, 751–767.
- [31] O. Haas, R. P. W. J. Struis, J. M. McBreen, *J. Solid State Chem.* **2004**, *177*, 1000–1010.
- [32] I. Kotousová, S. Polyakov, *Kristallografiya* **1972**, *17*, 661–663.
- [33] a) L. Bedel, A. C. Roger, C. Estournes, A. Kiennemann, *Catal. Today* **2003**, *85*, 207–218; b) Z. Derakhshi, M. Tamizifar, K. Arzani, S. Baghshahi, *Synth. React. Inorg. Met.-Org. Nano-Met. Chem.* **2016**, *46*, 25–30.
- [34] H. M. Rietveld, *Acta Crystallogr.* **1967**, *22*, 151.
- [35] T. A. S. Ferreira, J. C. Waerenborgh, M. H. R. M. Mendonça, M. R. Nunes, F. M. Costa, *Solid State Sci.* **2003**, *5*, 383–392.
- [36] M. Thommes, K. Kaneko, A. V. Neimark, J. P. Olivier, F. Rodriguez-Reinoso, J. Rouquerol, K. S. W. Sing, *Pure Appl. Chem.* **2015**, *87*, 1051–1069.
- [37] a) D. V. Karpinsky, I. O. Troyanchuk, M. Kopcewicz, *Phys. Status Solidi B* **2007**, *244*, 1409–1417; b) D. V. Karpinsky, I. O. Troyanchuk, K. Bärner, H. Szymczak, M. Tovar, *J. Phys. Condens. Matter* **2005**, *17*, 7219–7226.
- [38] a) R. R. Kondakindi, A. Kundu, K. Karan, B. A. Peppley, A. Qi, C. Thurgood, P. Schurer, *Appl. Catal. A* **2010**, *390*, 271–280; b) N. A. Merino, B. P. Barbero, P. Ruiz, L. E. Cadús, *J. Catal.* **2006**, *240*, 245–257.
- [39] V. Solanki, S. Das, S. Kumar, M. M. Seikh, B. Raveau, A. K. Kundu, *J. Sol-Gel Sci. Technol.* **2017**, *82*, 536–540.
- [40] J. Druce, H. Téllez, M. Burriel, M. D. Sharp, L. J. Fawcett, S. N. Cook, D. S. McPhail, T. Ishihara, H. H. Brongersma, J. A. Kilner, *Energy Environ. Sci.* **2014**, *7*, 3593–3599.
- [41] a) J. Faye, A. Baylet, M. Trentesaux, S. Royer, F. Dumeignil, D. Duprez, S. Valange, J.-M. Tatibouët, *Appl. Catal. B* **2012**, *126*, 134–143; b) B. P. Barbero, J. A. Gamboa, L. E. Cadús, *Appl. Catal. B* **2006**, *65*, 21–30.
- [42] R. M. García de la Cruz, H. Falcón, M. A. Peña, J. L. G. Fierro, *Appl. Catal. B* **2001**, *33*, 45–55.
- [43] S. Anke, T. Falk, G. Bendt, I. Sinev, M. Havecker, H. Antoni, I. Zegkinoglou, H. Jeon, A. Knop-Gericke, R. Schlögl, B. Roldan Cuena, S. Schulz, M. Muhler, *J. Catal.* **2020**, *382*, 57–68.
- [44] S. A. Fuente, C. A. Ferretti, N. F. Domancich, V. K. Diez, C. R. Pesteguía, J. I. Di Cosimo, R. M. Ferullo, N. J. Castellani, *Appl. Surf. Sci.* **2015**, *327*, 268–276.
- [45] P. A. Christensen, Z. Mashhadani, A. H. B. M. Ali, *Phys. Chem. Chem. Phys.* **2018**, *20*, 9053–9062.
- [46] J. C. Dobrowski, S. Ostrowski, R. Kolos, M. H. Jamróz, *Vib. Spectrosc.* **2008**, *48*, 82–91.
- [47] M. Zaki, *J. Catal.* **1983**, *80*, 114–122.
- [48] K. Friedel Ortega, S. Anke, S. Salomon, F. Özcan, J. Heese, C. Andronescu, J. Landers, H. Wende, W. Schuhmann, M. Muhler, T. Lunkenbein, M. Behrens, *Chemistry* **2017**, *23*, 12443–12449.
- [49] N. Bahlawane, P. H. Ngamou, V. Vannier, T. Kottke, J. Heberle, K. Kohse-Höinghaus, *Phys. Chem. Chem. Phys.* **2009**, *11*, 9224–9232.
- [50] Y. Wu, C. Cordier, E. Berrier, N. Nuns, C. Dujardin, P. Granger, *Appl. Catal. B* **2013**, *140*, 151–163.
- [51] Y. N. Yi, P. Zhang, Z. Z. Qin, C. X. Yu, W. Li, Q. J. Qin, B. Li, M. G. Fan, X. Liang, L. H. Dong, *RSC Adv.* **2018**, *8*, 7110–7122.
- [52] G. S. Foo, Z. D. Hood, Z. Wu, *ACS Catal.* **2017**, *8*, 555–565.
- [53] F. Polo-Garzon, S. Z. Yang, V. Fung, G. S. Foo, E. E. Bickel, M. F. Chisholm, D. e. Jiang, Z. Wu, *Angew. Chem.* **2017**, *129*, 9952–9956; *Angew. Chem. Int. Ed.* **2017**, *56*, 9820–9824.
- [54] S. W. Chee, T. Lunkenbein, R. Schlögl, B. Roldan Cuena, *J. Phys. Condens. Matter* **2021**, *33*, 153001.
- [55] M. C. Biesinger, B. P. Payne, A. P. Grosvenor, L. W. M. Lau, A. R. Gerson, R. S. C. Smart, *Appl. Surf. Sci.* **2011**, *257*, 2717–2730.
- [56] Y. Xu, Z. Liu, D. Chen, Y. Song, R. Wang, *Prog. Nat. Sci.* **2017**, *27*, 197–202.
- [57] G. Koch, M. Hävecker, D. Teschner, S. J. Carey, Y. Wang, P. Kube, W. Hetaba, T. Lunkenbein, G. Auffermann, O. Timpe, F. Rosowski, R. Schlögl, A. Trunschke, *ACS Catal.* **2020**, *10*, 7007–7020.
- [58] A. Knop-Gericke, E. Kleimenov, M. Hävecker, R. Blume, D. Teschner, S. Zafeiratos, R. Schlögl, V. I. Bukhtiyarov, V. V. Kaichev, I. P. Prosvirin, A. I. Nizovskii, H. Blühm, A. Barinov, P. Dudin, M. Kiskinova, in *Advances in Catalysis*, Vol. 52, Academic Press, **2009**, pp. 213–272.

Manuscript received: July 31, 2021

Accepted manuscript online: October 11, 2021

Version of record online: November 8, 2021

## 7. Dynamics of Reactive Oxygen Species on Cobalt-Containing Spinel Oxides in Cyclic CO Oxidation

**Title:**

“Dynamics of Reactive Oxygen Species on Cobalt-Containing Spinel Oxides in Cyclic CO Oxidation”

**Authors:**

Maik Dreyer, Anna Rabe, Eko Budiyanto, Klaus Friedel Ortega, Sharif Najafishirtari, Harun Tüysüz, Malte Behrens

**Citation:**

Dreyer, M.; Rabe, A.; Budiyanto, E.; Friedel Ortega, K.; Najafishirtari, S.; Tüysüz, H.; Behrens, M., *Catalysts* **2021**, 11 (11), 1312.<sup>189</sup>

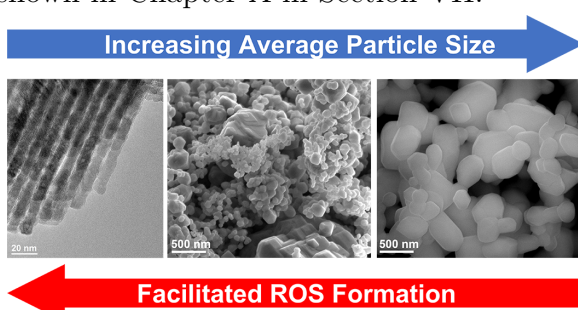
**DOI:**

10.3390/catal11111312

**Supporting Information:**

The Supporting Information can be accessed under [ht  
tps://www.mdpi.com/2073-4344/11/11/1312/s1](https://www.mdpi.com/2073-4344/11/11/1312/s1) and is shown in Chapter A in Section VII.

**Graphical Abstract:**



Maik Dreyer wrote the first manuscript draft and performed the gas phase CO oxidation measurements and their data analysis. Anna Rabe synthesized the P800 catalyst, performed the XRD measurements of spent catalysts, did the Rietveld refinement, and contributed in reading and editing of the original manuscript draft. Eko Budiyanto synthesized the SBA-15 templated catalysts and performed their characterization, and contributed in reading and editing of the original manuscript draft. Klaus Friedel Ortega developed the methodology together with Maik Dreyer and Sharif Najafishirtari. Furthermore, he contributed to the manuscript by reading and editing of the original manuscript draft. Sharif Najafishirtari developed the methodology together with Maik Dreyer and Klaus Friedel Ortega. Harun Tüysüz and Malte Behrens conceptualized the work, acquired the funding, administrated the project, read and edited the original manuscript draft.

The work was reprinted without changes under the CC BY 4.0 licence. © 2021 by the authors. Licensee MDPI, Basel, Switzerland.



Article

## Dynamics of Reactive Oxygen Species on Cobalt-Containing Spinel Oxides in Cyclic CO Oxidation

Maik Dreyer <sup>1</sup>, Anna Rabe <sup>1</sup>, Eko Budiyanto <sup>2</sup>, Klaus Friedel Ortega <sup>3</sup>, Sharif Najafishirtari <sup>1</sup>, Harun Tüysüz <sup>2</sup> and Malte Behrens <sup>1,3,4,\*</sup>

- <sup>1</sup> Faculty for Chemistry, Inorganic Chemistry, University of Duisburg-Essen, 45141 Essen, Germany; maik.dreyer@uni-due.de (M.D.); anna.rabe@uni-due.de (A.R.); sharif.najafishirtari@uni-due.de (S.N.)
  - <sup>2</sup> Max-Planck-Institut für Kohlenforschung, Kaiser-Wilhelm Platz 1, 45470 Mülheim an der Ruhr, Germany; budiyanto@kofo.mpg.de (E.B.); tueysuez@kofo.mpg.de (H.T.)
  - <sup>3</sup> Institute of Inorganic Chemistry, Christian-Albrechts-Universität zu Kiel, Max-Eyth-Straße 2, 24118 Kiel, Germany; kfriedel@ac.uni-kiel.de
  - <sup>4</sup> CENIDE, Center for Nanointegration, University of Duisburg-Essen, 47057 Duisburg, Germany
- \* Correspondence: mbehrrens@ac.uni-kiel.de



**Citation:** Dreyer, M.; Rabe, A.; Budiyanto, E.; Friedel Ortega, K.; Najafishirtari, S.; Tüysüz, H.; Behrens, M. Dynamics of Reactive Oxygen Species on Cobalt-Containing Spinel Oxides in Cyclic CO Oxidation. *Catalysts* **2021**, *11*, 1312. <https://doi.org/10.3390/catal11111312>

Academic Editor: Simone Mascotto

Received: 29 September 2021

Accepted: 25 October 2021

Published: 29 October 2021

**Abstract:** Reactive oxygen species (ROS) are considered to be responsible for the high catalytic activity of transition metal oxides like  $\text{Co}_{3-x}\text{Fe}_x\text{O}_4$  in oxidation reactions, but the detailed influences of catalyst composition and morphology on the formation of these reactive oxygen species are not fully understood. In the presented study,  $\text{Co}_3\text{O}_4$  spinels of different mesostructures, i.e., particle size, crystallinity, and specific surface area, are characterized by powder X-ray diffraction, scanning electron microscopy, and physisorption. The materials were tested in CO oxidation performed in consecutive runs and compared to a  $\text{Co}_{3-x}\text{Fe}_x\text{O}_4$  composition series with a similar mesostructure to study the effects of catalyst morphology and composition on ROS formation. In the first run, the CO conversion was observed to be dominated by the exposed surface area for the pure Co-spinels, while a negative effect of Fe content in the spinels was seen. In the following oxidation run, a U-shaped conversion curve was observed for materials with high surface area, which indicated the in situ formation of ROS on those materials that were responsible for the new activity at low temperature. This activation was not stable at the higher reaction temperature but was confirmed after temperature-programmed oxidation (TPO). However, no activation after the first run was observed for low-surface-area and highly crystalline materials, and the lowest surface-area material was not even activated after TPO. Among the catalyst series studied here, a correlation of small particle size and large surface area with the ability for ROS formation is presented, and the benefit of a nanoscaled catalyst is discussed. Despite the generally negative effect of Fe, the highest relative activation was observed at intermediate Fe contents suggesting that Fe may be involved in ROS formation.

**Keywords:** CO oxidation; spinel;  $\text{Co}_3\text{O}_4$ ;  $\text{Co}_{3-x}\text{Fe}_x\text{O}_4$ ; oxygen activation; reactive oxygen species

**Publisher's Note:** MDPI stays neutral with regard to jurisdictional claims in published maps and institutional affiliations.



**Copyright:** © 2021 by the authors. Licensee MDPI, Basel, Switzerland. This article is an open access article distributed under the terms and conditions of the Creative Commons Attribution (CC BY) license (<https://creativecommons.org/licenses/by/4.0/>).

### 1. Introduction

The oxidation of CO is an important model and probe reaction used to investigate oxidation catalysis, particularly for exhaust treatments. For this reaction, Co-based spinel catalysts like  $\text{Co}_3\text{O}_4$  and  $\text{CoFe}_2\text{O}_4$  have shown high activity even at temperatures as low as  $-80^\circ\text{C}$  [1–5]. The oxidation reaction on  $\text{Co}_3\text{O}_4$  catalysts has been extensively studied, and several possible reasons for the high activity of this specific spinel-based catalyst are mentioned in the literature.

There are reports on the importance of reactive oxygen species (ROS) and on an important role of vacancies on the surface of catalysts [3]. However, the generation and role of ROS are not fully understood yet, especially for mixed oxides containing more than one metal cation, such as Co and Fe. Several studies have been performed attempting to unravel the role of ROS in oxidation reactions on Co containing catalysts. In studies

from the 1990s, oxidized  $\text{Co}_3\text{O}_4$  is labeled as  $\text{Co}_3\text{O}_{4+x}$  containing excess oxygen as oxide species ( $\text{O}^{2-}$ ) and excluding adsorbed species such as dioxygen ( $\text{O}_2$ ), superoxo ( $\text{O}_2^-$ ), and peroxide ( $\text{O}_2^{2-}$ ) [6–9]. The activity was explained by nucleophilic lattice oxygen and activity loss over time by surface reduction from  $\text{Co}^{3+}$  to  $\text{Co}^{2+}$  [6–9]. Zasada et al. reported the reactivity of the diatomic superoxo and peroxy ROS on predominantly (100) terminated  $\text{Co}_3\text{O}_4$  below 160 °C and monoatomic  $\text{O}^-$  species between 160 °C and 300 °C by hydrogen oxidation on  $\text{Co}_3\text{O}_4$  [10]. In addition, the involvement of superoxo and peroxy species on the surface was proposed by density functional theory (DFT) for temperatures below 350 °C [10]. Further work by Zasada et al. showed higher activity of adsorbed suprafacial oxygen atoms than interfacial surface oxygen in methane oxidation [11]. Another study by Zasada et al. indicated CO being primarily oxidized by suprafacial diatomic oxygen adsorbed between threefold coordinated  $\text{Co}^{3+}$  and threefold coordinated  $\text{Co}^{2+}$  and/or monooxygen adsorbed on a threefold coordinated  $\text{Co}^{3+}$  center on  $\text{Co}_3\text{O}_4(111)$  [12]. A recent study by Liu et al. on  $\text{Co}_3\text{O}_4(100)$  thin films in the low-temperature CO oxidation revealed that the activated oxygen desorbs from oxidized surfaces below 120 K and below 270 K from pre-reduced surfaces, while superoxide/superoxide species do not re-oxidize the reduced surfaces [13]. In addition, the role of oxygen vacancies was critical, as the vacancies promote the formation of superoxo ( $\text{O}_2^-$ ) species that are highly active in CO oxidation [13].

Other possible reasons for the high activity of  $\text{Co}_3\text{O}_4$  in CO oxidation apart from the formation of ROS are presented in the literature, such as the exposed planes. In this regard, contradictory information is given for the active facets. For example, Xie et al. reported that (110) planes on nanorods, which are rich in  $\text{Co}^{3+}$  sites, are the active facets [2]. Teng et al. showed that the (111) termination, which is rich in  $\text{Co}^{2+}$  sites, is more active [14]. Octahedrally coordinated  $\text{Co}^{2+}$  can easily be oxidized to  $\text{Co}^{3+}$  on the surface, which is reported for several spinel oxides, and it is considered to be the reason for the catalytic activity of  $\text{Co}^{2+}$  containing materials like  $\text{CoFe}_2\text{O}_4$  [15]. For  $\text{Co}_3\text{O}_4$  in 2-propanol oxidation, a correlation of activity loss and reduction from  $\text{Co}^{3+}$  to  $\text{Co}^{2+}$  was shown by Anke et al., which can corroborate the higher activity of  $\text{Co}^{3+}$  in CO oxidation [16].

In terms of mechanisms in gas-phase catalysis, mainly the reaction of adsorbed species in the Langmuir-Hinshelwood (LH) and the Mars-van-Krevelen (MvK) mechanisms involving oxidation by lattice oxygen and subsequent filling of oxygen vacancies by gas-phase oxygen are discussed. A recent study by Lukashuk et al. indicated a complex reaction network consisting of several reaction pathways, including dissociation of CO followed by carbon oxidation to  $\text{CO}_2$  [17]. They indicated the presence of the MvK mechanism at temperatures above 100 °C and could not exclude LH at low temperatures [17].

Catalytic oxidation in several temperature cycles is frequently used in the literature to show catalyst stability [18,19]. However, some studies indicated further effects of either pretreatment or subsequently performed catalytic runs. After pre-treating  $\text{Co}_3\text{O}_4$  and CoO reductively with  $\text{H}_2$  prior to CO oxidation, an activity increase was found under oxidizing conditions (1% CO, 20%  $\text{O}_2$ ) for both types of oxides in consecutive runs up to 200 °C, which showed the restorability of  $\text{Co}^{3+}$  on the surface at temperatures even below 200 °C [15]. A study on  $\text{Co}_3\text{O}_4/\text{Al}_2\text{O}_3$  confirmed the results, a beneficial effect of a consecutive pretreatment with  $\text{H}_2$  at 300 °C and  $\text{O}_2$  at 250 °C has been observed and correlated to an increasing number of  $\text{Co}^{3+}$  on the surface and decreasing crystallite size. Additionally, an activation for the second of two consecutive runs has been reported [20]. Another paper reported improved catalyst recovery for regeneration in 10%  $\text{O}_2$  compared to Ar [21]. It seems likely that the activation behavior is related to ROS formation on the catalyst surface.

Not solely Co-containing transition metal oxides are interesting for catalytic oxidation reactions, also mixed Co and Fe transition metal oxides are used either within perovskites or spinel structures [22–32]. With increasing Fe content in spinels, the reducibility decreased steadily until inversion of the spinel materials was found experimentally. However, after inversion was observed, the reducibility behavior was unsteady and not clearly correlated

with the nominal Fe content anymore [33]. A mesoporous  $\text{Co}_{3-x}\text{Fe}_x\text{O}_4$  spinel series was synthesized via hard-templating using SBA-15 silica as a template, and the catalysts used for this specific study were previously used in different oxidation reactions. In the electrochemical oxygen evolution reaction (OER), a beneficial effect of Fe was observed [34]. In liquid-phase 2-propanol oxidation, however, no effect on the activity of the nominal Co:Fe ratio was detected [35]. Interestingly, if *tert*-butyl hydroperoxide was used as the oxidant, a beneficial effect of Fe was observed, which was related to different activation pathways [36]. The peroxidic oxidant has to be partially decomposed to be activated, whereas for oxygen activation, a spin transfer is needed [36].

In the presented study, these mesoporous  $\text{Co}_{3-x}\text{Fe}_x\text{O}_4$  spinels with high specific surface area were tested in CO oxidation and compared to two pristine  $\text{Co}_3\text{O}_4$  samples with lower specific surface area obtained commercially and from a template-free precipitation method. The samples differed in their mesostructure, namely interconnected nanowires, sintered previously hexagonal particles, and a non-homogeneous sample. Low-surface area  $\text{Co}_3\text{O}_4$  samples were characterized by powder X-ray diffraction (XRD), physisorption methods, and scanning electron microscopy (SEM) and compared to the SBA-15 templated materials, whose properties were already reported elsewhere [34–36]. All samples were tested in cyclic CO oxidation in 2% CO and 20% O<sub>2</sub> in three consecutive runs, while between the first and the second run no further pretreatment was performed, while between the second and the third run an oxidative pretreatment was performed. The goal was to study the dynamic behavior as a function of the catalyst's structure and composition and to discuss the results in the context of the different materials' ROS formation ability to help design future experiments to identify the ROS under *operando* conditions by means of dynamic experiments.

## 2. Results and Discussion

### 2.1. Characterization

Synthesis and characterization of SBA-15 templated Co:Fe nanowire oxides were reported in a previous publication [34] and the characterization is briefly summarized in the following paragraph. From XRD analysis, the crystalline spinel structure of all materials was verified after calcination at 500 °C. The materials are labelled by the nominal composition during the synthesis, which matched the experimental composition well and was confirmed by bulk energy-dispersive X-ray spectroscopy (EDX) for Co:Fe ratios of 32:1, 16:1, 7:1, 3:1, as well as pure  $\text{Co}_3\text{O}_4$  (labeled S500) and  $\text{CoFe}_2\text{O}_4$ . [34] Furthermore, X-ray photoelectron spectroscopy (XPS) analyses also confirmed the ratio between Co:Fe, which suggested a uniform cation distribution in the bulk and at the surface. The Fe species on the surface were found to be Fe<sup>3+</sup> for all catalysts, whereas the Co species were Co<sup>3+</sup> and Co<sup>2+</sup> despite only Co<sup>2+</sup> containing  $\text{CoFe}_2\text{O}_4$ , as expected from the stoichiometry [35].

In the transmission electron microscopy (TEM) micrographs, a decrease of the degree of the ordering of mesoporous structure and nanowire length was observed with the increasing of Fe content. Furthermore, upon incorporating Fe into the spinel structure, higher occupancy of Co<sup>2+</sup> in tetrahedral sites was reported and correlated with a distortion of the Co<sup>3+</sup>-O bonds [34,37]. In another study on the herein presented SBA-15 templated nanowires, indications for the presence of a  $\text{Co}_3\text{O}_4$  secondary phase were reported on  $\text{CoFe}_2\text{O}_4$  based on Rietveld refinements [35].

Nitrogen physisorption isotherms are presented in Figure S1a, and they show a typical type IV isotherm that is characteristic for mesoporous materials [38,39]. The hysteresis type of the  $\text{Co}_3\text{O}_4$  nanowires can be characterized as a H4 loop, whereas the other SBA-15 templated materials show a H3 loop [40]. Brunauer–Emmett–Teller (BET) surface areas of the SBA-15 templated samples are shown in Table 1. For the Co-rich samples, the BET surface areas scattered between 103 and 125 m<sup>2</sup> g<sup>-1</sup>, while  $\text{CoFe}_2\text{O}_4$  shows an increased BET surface area of 178 m<sup>2</sup> g<sup>-1</sup> due to the formation of small nanoparticles rather than nanowire arrays. From the Barrett–Joyner–Halenda (BJH) method, the pore size distributions were calculated and are shown in Figure S1b. The maximum in the pore-size

distribution for  $\text{Co}_3\text{O}_4$  was in the range of 3 nm, which indicates a perfect replication of the silica mesostructure since it corresponds to the SBA-15(100) silica wall thickness. Upon Fe incorporation into the spinel materials, additional pores in the range from 10–20 nm are observed due to the pores' alteration.

**Table 1.** BET surface areas of the catalysts used for catalytic testing.

Sample	$\text{S}_{\text{BET}}/\text{m}^2 \text{ g}^{-1}$
$\text{Co}_3\text{O}_4$ S500 (SBA-15 templated)	107
Co:Fe 32:1 (SBA-15 templated)	118
Co:Fe 16:1 (SBA-15 templated)	103
Co:Fe 7:1 (SBA-15 templated)	113
Co:Fe 3:1 (SBA-15 templated)	125
$\text{CoFe}_2\text{O}_4$ (SBA-15 templated)	178
$\text{Co}_3\text{O}_4$ C600 (commercial)	9
$\text{Co}_3\text{O}_4$ P800 (precipitated)	2

$\text{Co}_3\text{O}_4$  (labeled as P800) was synthesized by precipitation of a  $\text{Co}(\text{OH})_2$  precursor at constant temperature and pH, followed by its thermal decomposition at 800 °C. The synthesis and precursor properties were already reported in a previous study [41]. The BET surface area is very low with  $2 \text{ m}^2 \text{ g}^{-1}$  determined by Kr adsorption and might therefore be attributed with a notable error bar, and the material showed no measurable porosity with  $\text{N}_2$  adsorption–desorption experiments.  $\text{Co}_3\text{O}_4$  (labeled as C600) was purchased from Merck and recalcined in synthetic air in a rotating furnace at 600 °C and the surface area of C600 is  $9 \text{ m}^2 \text{ g}^{-1}$ . The corresponding  $\text{N}_2$  adsorption–desorption curve is shown in Figure S1a, the BJH pore size distribution in Figure S1b. The isotherms can be classified as type IV isotherms with a H3 loop [38–40], and the pore size distribution indicates a maximum in the range between 2 and 3 nm and another maximum in the range between 20 and 30 nm. The low values of the BET surface areas for P800 and C600 might be associated with a notable error bar, but we regard the difference between the two samples as reliable.

XRD patterns of C600, P800, and S500 are shown in Figure 1a. All patterns show the typical cubic spinel structure, as indicated by a literature  $\text{Co}_3\text{O}_4$  pattern (ICSD collection code 9362 [42]) and Rietveld refinement [43]. The refinement did not show any indication for secondary phases for all samples, and the refined patterns and the fit parameters are shown in Figure S2 and Table S1. The size of coherently scattering domains was found to be about 10 nm for S500, 45 nm for C600, and 53 nm for P800, as taken from Rietveld refinement. These findings agree with the expected increase of domain and particle size with calcination temperature due to sintering.

An exemplary SEM image of C600 is shown in Figure 1b, which shows a non-homogeneous particle size and shape distribution. As indicated by red arrows, large aggregates are present in the sample, which might be attributed to the sintering of smaller particles upon calcination. Another fraction of particles is exemplarily indicated by a light blue arrow and shows particles in the range of ~200 nm in diameter. In addition, there are two smaller particle fractions marked with a yellow and a dark blue arrow, whose particle sizes seem in a similar range as the average crystallite domain size.

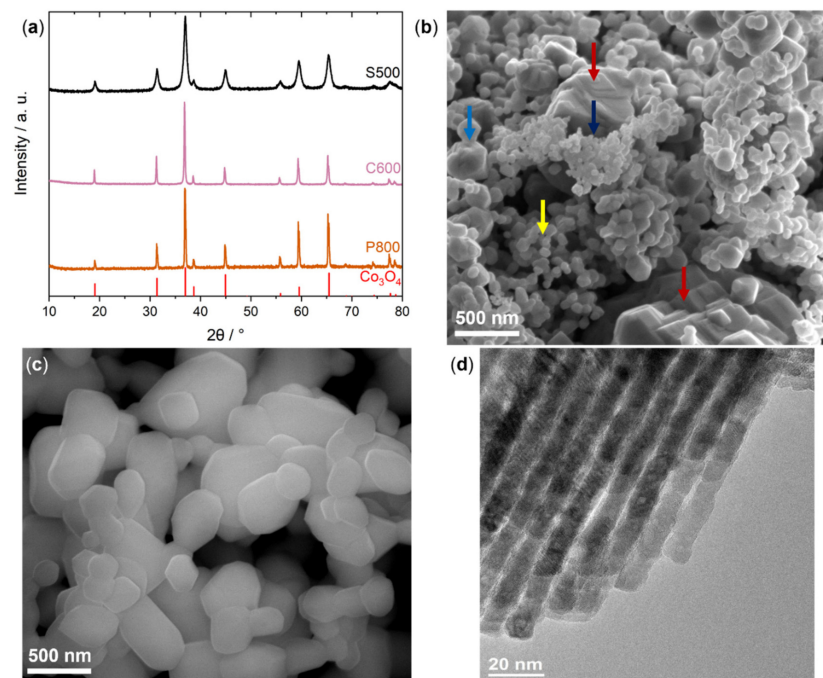


**Figure 1.** (a) XRD patterns of C600, P800, and S500. (b) SEM image of C600, different size particles are indicated exemplarily by the use of red (large particles), light blue (medium size), yellow (small), and dark blue (very small) arrows. (c) SEM image of P800. (d) TEM micrograph of S500.

An exemplary SEM image of the precipitated  $\text{Co}(\text{OH})_2$  precursor for P800 was shown in a previous study and revealed hexagonal platelets, which remained after calcination at  $400\text{ }^\circ\text{C}$  [41]. After calcination at  $800\text{ }^\circ\text{C}$ , the platelet structure in a SEM image of P800 in Figure 1c can hardly be seen. The platelets sintered together to more roundish particles with a nonuniform size distribution, which seems more uniform in comparison to C600. However, because of the high calcination temperature, no porosity is expected for C800. From an exemplary TEM image of S500 in Figure 1d, interconnected nanowires with the average diameter of 8 nm matching the silica template's pore size can be seen, which leads to mesoporosity [34]. Altogether, this study comprises three  $\text{Co}_3\text{O}_4$  catalysts of the same composition, but with different mesostructures, i.e., crystallinity, particle size and morphology, and specific surface area, ranging from a highly crystalline, sintered material with large particles and low specific surface area (P800), and crystalline particles of non-uniform size (C600), to a unique nanosized wire structure with high specific surface area (S500). In addition, the effect of the Fe incorporation into cobalt oxide was investigated by using a series of well-defined and crystalline cobalt iron oxide that was replicated from the SBA-15 silica template.

## 2.2. Catalysis

The results of the transient temperature-programmed CO oxidation of the Fe-incorporated SBA-templated catalysts are depicted in Figure 2a by showing the  $\text{CO}_2$  yield. Comparison of CO conversion and  $\text{CO}_2$  yield are shown in Figure S3, and both were found to follow the same trends as expected without indication for  $\text{CO}_2$  adsorption. It is evident that by increasing the Fe content incorporated into the spinel structure of the  $\text{Co}_3\text{O}_4$ , there

is a dampening effect on the activity. This can be attributed to the replacement of the highly reducible octahedral  $\text{Co}^{3+}$  with the less reducible  $\text{Fe}^{3+}$  resulting in a decrease of highly active sites on the surface [33]. DFT calculations on  $\text{Co}_3\text{O}_4(110)$ -B-surface show  $\text{Co}^{3+}$  are more active than  $\text{Co}^{2+}$  as it binds the CO molecule stronger and features the lower energy barrier. Furthermore, the reaction which is said to follow the Mars-van-Krevelen mechanism (MvK) [44], can be inversely affected by the presence of less reducible cations, in this case Fe. Indeed, the  $\text{Co}_3\text{O}_4$  S500 with no Fe content shows significant activity even close to room temperature, whereby cobalt ferrite spinel shows the lowest activity although it has the highest surface area among all samples. As already stated in the introduction, the incorporation of Fe has different effects on the activity for different oxidation reactions. In the herein investigated CO oxidation, Fe did not have a beneficial effect on the SBA-15 templated catalyst materials, similar to liquid-phase oxidation of 2-propanol with oxygen as the oxidant [35].

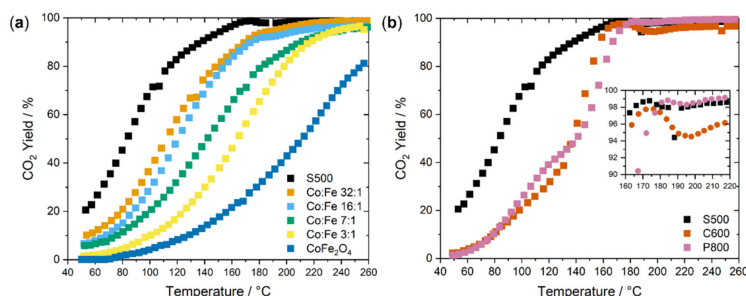


**Figure 2.** (a) Temperature-programmed CO oxidation activation of the SBA-15 templated pristine  $\text{Co}_3\text{O}_4$ ,  $\text{CoFe}_2\text{O}_4$ , and Fe incorporation series in the 1st run. (b) Temperature-programmed CO oxidation activity of the different Co oxide samples in the 1st run.

The effect of different synthesis routes resulting in different micro- and mesostructures for S500, C800, and P600 with the same nominal  $\text{Co}_3\text{O}_4$  composition is shown in Figure 2b. Comparison of CO conversion and CO<sub>2</sub> yield are shown in Figure S4. The conversion of S500 was higher, starting already below room temperature, where C600 and P800 hardly show activity in this temperature regime. This goes in line with our previous finding that high surface area ordered mesoporous  $\text{Co}_3\text{O}_4$  could catalyze CO oxidation even at room temperature [15,45]. While the onset of the transient activity for C600 and P800 is around 60 °C, whereas S500 already showed >20% conversion at this temperature. However, due to the immense differences in specific surface area, the activity differences cannot be directly concluded from the conversion curves, and a discussion of the reaction rates is presented below. Interestingly, the conversion curve shapes showed shoulders at low temperatures for C600 and P800. This shoulder was more pronounced for P800 leading to higher conversion at low temperatures, whereas at higher temperatures, the conversion of C600 was slightly higher. The temperature to reach 50% conversion ( $T_{50}$ ) was quite similar for both catalysts. These shoulders indicate changes of the catalyst during heating and may point to active sites, which are consumed rapidly and have a higher abundance on P800. Interestingly, all  $\text{Co}_3\text{O}_4$  catalysts reached full conversion in the same temperature range of ~180 °C despite their different mesostructure. In the range of full conversion, an intermediate drop for all catalysts was observed in the temperature range between 160 and 220 °C, that might be explained by reaction dynamics due to the high excess of oxygen in the feed.

Since the exposed BET surface areas of the samples covered a wide range as shown in Table 1 with two groups: high surface area SBA 15-templated and low surface-area materials, reaction rates normalized by the BET surface area were determined and are shown in Figure 3a. Clearly, P800 appeared superior to all catalysts after rate-normalization, followed by C600. The large extent of these rate differences is caused by the normalization

as these catalysts exhibit by far the lowest specific surface area and should be treated with care. Among the SBA-15 substitution series (Figure 3a, inset), the activity trend followed the amount of Fe incorporated in the samples, as already reported for the conversion curves. For a better comparison of the activities of the different samples,  $T_{50}$  and  $\text{CO}_2$  formation rates at 100 °C are shown in Figure 3b. Within the SBA-15 substitution series,  $T_{50}$  was increasing, indicating less activity, and the rate at 100 °C was decreasing accordingly with increasing Fe content in the samples.  $T_{50}$  values of P800 and C600 were similar and shifted to higher temperatures by ~60 °C compared to the high-surface-area catalyst S500. In Figure S5, a plot of the  $\text{CO}_2$  formation rate against the nominal Co content in the spinels is shown and indicates a nearly linear behavior for the SBA-15 templated catalysts with intermediate Fe content excluding the  $\text{Co}_3\text{O}_4$  and  $\text{CoFe}_2\text{O}_4$  catalysts. The deactivation with increasing Fe content was previously reported in liquid-phase 2-propanol oxidation, where ensembles of more than six coordinatively unsaturated  $\text{Co}^{3+}$  species were identified as the active site [35]. The observation is consistent with the proposal that the active sites of CO oxidation are also Co-centered (see below).

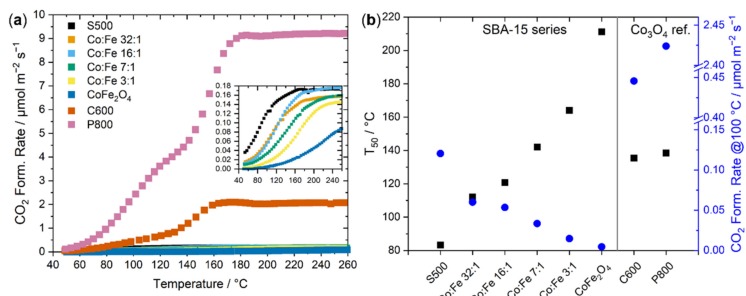


**Figure 3.** (a) Temperature-programmed CO oxidation rates of the investigated catalysts in the 1st run. SBA-15-templated Fe incorporation series is shown as a zoom-in insert for better visibility. (b) Temperature-programmed CO oxidation activity of the different Co oxide samples in the 1st run.

Directly after performing the first run and cooling down to room temperature, a second transient activity test was performed for all catalysts at the same heating rate and gas composition. The activities of the Fe-incorporation series SBA-15 catalysts during the second consecutive run are shown in Figure 4a. Comparisons between all three CO oxidation runs are shown in the Supplementary Material in Figures S6–S13 for each specific catalyst compared to the first run. All samples showed a significantly higher activity already in the lower temperature range. However, the conversion was initially decreasing with temperature for most catalysts before rising again in the high-temperature range of the experiment showing a U-shaped conversion curve. The first run has acted as an activating pretreatment for the second run on all SBA-15 templated catalysts, including the ones with a high Fe content, but the creation of the new activity at low temperature was not stable and could not be maintained during the heating experiment. The temperature to reach full conversion was similar to the first run indicating that the state after deactivation was similar to the first run. The general trend between composition and activity observed in the first run remains, with a slight deviation of the 16:1 and 32:1 samples at lower temperatures.

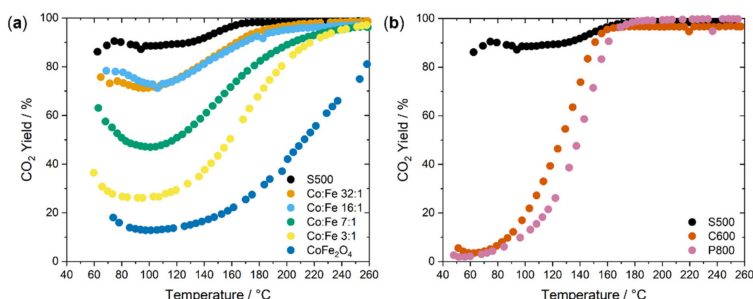


**Figure 4.** (a) Temperature-programmed CO oxidation activation of the SBA-15 templated Fe incorporation series in the 2nd run. (b) Temperature-programmed CO oxidation activity of the different Co oxide samples in the 2nd run.

Different effects of the pretreatment have been studied, for instance, Yu et al. reported a volcano-shaped curve between pretreatment temperature and conversion at  $-80^{\circ}\text{C}$  for the temperature range between  $25^{\circ}\text{C}$  and  $250^{\circ}\text{C}$  with a maximum for a pretreatment temperature at  $150^{\circ}\text{C}$ . The differences between treatments in  $\text{N}_2$  and dry air were minor [3]. For two consecutive runs on  $\text{Co}_3\text{O}_4$ , Hu et al. reported stable activity, but no activation of the samples in 2.5% CO and 20%  $\text{O}_2$ , which is in contradiction to our results but might be explained by lower BET surface area in the range of  $20\text{--}25 \text{ m}^2 \text{ g}^{-1}$  [19]. In another study on  $\text{Co}_3\text{O}_4/\text{Al}_2\text{O}_3$ , a beneficial effect of a consecutive pretreatment with  $\text{H}_2$  at  $300^{\circ}\text{C}$  and  $\text{O}_2$  at  $250^{\circ}\text{C}$  has been observed and correlated to an increasing number of  $\text{Co}^{3+}$  on the surface and decreasing crystallite size. Additionally, an activation for the second of two consecutive runs has been reported, which is in line with our results [20]. Since the catalysts in our study have been subjected to a rather oxidizing atmosphere of 2% CO and 20%  $\text{O}_2$  in the first reaction cycle and the very high initial activity was observed on all SBA-15 templated catalysts, a likely hypothesis for the activity increase at low temperatures is the formation of reactive oxygen species (ROS) upon performing the reaction at oxygen-rich conditions at high temperature and full conversion at the end of the first cycle. The conversion profile of the second cycle with the high initial conversion of CO followed by a rapid decrease until  $\sim 100^{\circ}\text{C}$  indicates consumption of these previously formed ROS in the low-temperature range. At higher temperatures, similar conversion profiles are observed again, as observed in the first run after ROS consumption. Likely, their re-formation requires higher temperature and/or dwell time at full conversion and cannot be detected in the reaction profiles. Based on literature reports from Zasada et. al., it is assumed that two fivefold coordinated  $\text{Co}^{3+}$  in octahedral sites ( $\text{Co}_{5c}^{\text{O}}$ ) are responsible for the oxygen activation by working as a tandem [46]. The nature of the ROS formed and active in the oxidation of CO at temperatures below  $450^{\circ}\text{C}$  was described as suprafacial  $\mu$ -superoxo  $\text{Co}_{3c}^{\text{O}}\text{-O}_2\text{-Co}_{3c}^{\text{T}}$  and metal-oxo  $\text{Co}_{3c}^{\text{O}}\text{-O}$  species [12]. In both cases, undercoordinated cobalt sites are active, as was also shown to be the case in gas- and liquid-phase 2-propanol oxidation on spinel catalysts, where (ensembles of) coordinatively unsaturated (surface)  $\text{Co}_{5c}^{\text{O}}$  species were described as the active site [16,35].

A similar U-shaped conversion curve in the second run was previously reported on a  $\text{Co}_3\text{O}_4\text{-SiO}_2$  catalyst in CO oxidation in a 3 ppm water-containing feed after air and nitrogen treatment with 100% conversion at sub-zero temperatures and a minimum in conversion around  $80^{\circ}\text{C}$ . The shape was attributed to negative apparent activation energies for certain temperature ranges, including two different oxygen species. However, when water was frozen out from the reaction mixture, no U-shaped curve was observed, and indications for the negative impact of water on the catalyst ability to provide active oxygen species were reported [47]. In another study, after pre-treating  $\text{Co}_3\text{O}_4$  and  $\text{CoO}$  before reaction with  $\text{H}_2$ , an increase in activity was found under similar reaction conditions (1%

CO, 20% O<sub>2</sub>) for both types of oxides in consecutive runs up to 200 °C, which showed the restorability of Co<sup>3+</sup> on the surface below 200 °C, which is in line with our results [15].

Zasada et al. reported the reactivity of diatomic ROS below 160 °C and monoatomic species between 160 °C and 300 °C by hydrogen oxidation on Co<sub>3</sub>O<sub>4</sub> [10]. In addition, below 350 °C superoxo and peroxy species on the surface were proposed by density functional theory (DFT) [10]. The temperature window fits the conditions of the end of the previously performed first reaction cycle. In a study on Co<sub>3</sub>O<sub>4</sub>(100) films, superoxide species on pre-oxidized surfaces were not active in CO oxidation, whereas superoxides on reduced surfaces catalyzed the reaction already at 120 K and up to 270 K, from which the need of a presence of vacancies and superoxide was concluded to be essential for low-temperature oxidation of CO [13].

Interestingly, in the case of Co<sub>3</sub>O<sub>4</sub> C600 and Co<sub>3</sub>O<sub>4</sub> P800, no significant activation was observed in contrast to SBA-15 templated Co<sub>3</sub>O<sub>4</sub> S500, as shown in Figure 4b. For C600 and P800, the low-temperature shoulders in the reaction profile of the first runs vanished, as shown in Figures S12 and S13. Still, the T<sub>50</sub> values are decreased, but the changes are much smaller than the high-surface-area nanowires. This indicates a lower ROS generation ability of C600 and P800 compared to S500 during the first run. This less pronounced formation of ROS is most likely related to the difference in particle size, specific surface area, and porosity, hence indicating that the higher surface energy of nanoscaled materials might facilitate effective ROS formation compared to the typically low-indexed and thermodynamically more stable surface terminations of larger or sintered particles. It thus seems that the sample preparation history has an effect not only on the starting surface area but also on intrinsic properties like dynamic ROS formation.

CO oxidation activities in the third run after temperature-programmed oxidation (TPO) up to 500 °C are shown in Figure 5a. The temperature of 500 °C was chosen to mimic the calcination protocol of the SBA-15 templated materials. During TPO between the second and third run, no CO<sub>2</sub> was detected by micro-GC in the outlet stream, which indicates no or only minor carbon laydown or carbonate formation during the reaction of the second run, supporting that the loss of ROS can explain the deactivation observed at medium temperatures. In the third run, the low-temperature activity of the SBA-15 substitution series samples was even more pronounced than during the second run, as well as the subsequent drop in activity upon further heating. This hints at the formation of more or more active ROS after TPO up to 500 °C compared to reaction up to 250 °C, and again to the consumption of these ROS on the surface during catalysis. Based on work from Zasada et al. in the higher temperature range, monoatomic metaloxo ROS are formed [10]. The before-mentioned higher activity of the 16:1 sample compared to the 32:1 sample in the second run is becoming evident over the whole temperature range up to 180 °C in the third run. This suggests that while Fe did not have a beneficial role for the CO oxidation in the first run, it may contribute to effective ROS formation at a higher temperature for specific compositions. For all other samples, the trend with respect to the Fe content was maintained.

As shown in Figure 5b, Co<sub>3</sub>O<sub>4</sub> C600 was activated in the third run like the catalysts of the SBA-15 series already in the second run, whereas Co<sub>3</sub>O<sub>4</sub> P800 remained inactive despite a specific surface area of the same order of magnitude, indicating again an effect of the mesostructure and domain size emerging from synthesis procedure and calcination temperature on the ROS formation ability and catalyst activity. C600 shows an inhomogeneous morphology containing a small fraction of nanoparticles, and P800 features mostly roundish sintered and exclusively larger particles evolved from hexagonal platelets of the Co(OH)<sub>2</sub> precursor. The decreased ROS formation capability of P800 might be related to its high calcination temperature and largest domain size in this study, suggesting again that ROS are preferably formed on small particles. Altogether, it strengthens the argument of ROS created on the highly reactive surface of the nanoscaled catalyst during reaction at 100% conversion at net oxidizing conditions or during TPO. In the case of low specific

surface area catalysts with large particles obtained at high calcination temperatures, the total number of ROS is lower, and their formation seems hindered.

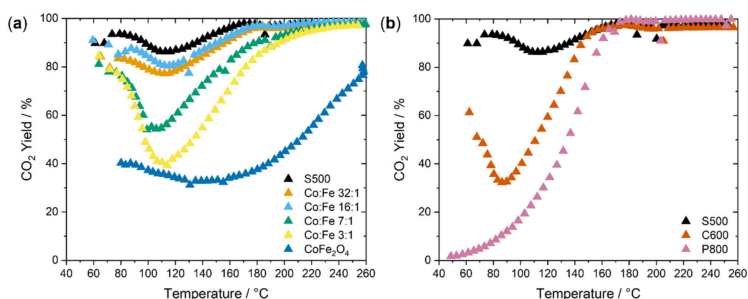


**Figure 5.** (a) Temperature-programmed CO oxidation activation of the SBA-15 templated Fe incorporation series in the 3rd run. (b) Temperature-programmed CO oxidation activity of the different  $\text{Co}_3\text{O}_4$  samples in the 3rd run.

The previous findings are supported by the extent of catalyst activation at 75 °C, which is assumed to be a measure of ROS formation. It was determined as the difference in conversion at 75 °C between first and second as well as first and third run,  $\Delta Y_{75^\circ\text{C}}$ , as shown in Figure 6a. A more negative value indicates a relatively more pronounced activation of the CO oxidation by ROS formation. As the maximum conversion at 75 °C during the second run was 82% for S500 and thus still below 100%, this evaluation between the first and second run is valid for all catalysts as their improvement is not limited by approaching full conversion. Looking at the composition dependency of the SBA-15 series, a volcano-like behavior with maximal activation at Co:Fe 16:1 was observed when comparing the first and second runs. This indicates that the ROS formation is favored at this specific composition and that Fe is involved in forming either a higher number or of intrinsically more active ROS. It also can be seen that activation by ROS formation for the Fe richer catalysts requires the more oxidizing conditions of TPO as the most substantial further activation in the third run was observed for these catalysts, as is also shown in Figure S14 as the difference between the second and the third run, where the peak of the volcano has shifted to a composition of Co:Fe 3:1. However, this trend has to be taken with care for the S500 sample since its conversion in the third run was already close to 100%, which limits the possibility of further improvement in comparison to the other catalysts. A correlation of  $Y_{75^\circ\text{C}}$  in the second run and the improvement in the third run in Figure S15 shows that higher starting conversions in the second run lead to lower relative improvements in the third run. It can be again seen for C600 and P800 that there was no activation during the first run, and only C600 was activated by the TPO.

Since C600 showed one of the clearest responses to the TPO, CO-TPR was performed before and after a TPO up to 500 °C to study the consumption of potential ROS from the surface. The results are shown in Figure S16. Before the TPO, i.e., in a non-oxygen treated state of the catalyst comparable to the initial 1st CO oxidation run, no direct CO<sub>2</sub> formation is evident at 40 °C temperature in the reactor after switching on the CO-containing atmosphere mixture. After starting to heat the reactor, only a slight increase in the concentration of CO<sub>2</sub> formed is observed at 79 °C. With rising temperature, the onset of catalyst bulk reduction was detected, and the catalyst was cooled down again. The CO<sub>2</sub> concentration decreased again, and no more CO<sub>2</sub> formation was detected from 154 °C onward during cooling. However, after the TPO and 15 min of purging in N<sub>2</sub>, directly after switching to the 2% CO containing feed gas, a strong formation of CO<sub>2</sub> is seen, which points out to the formation of ROS on the surface during the TPO, which are consumed over a period of 22 min already close to room temperature and finally in a small peak at 75 °C. The onset of bulk reduction was very similar to the untreated sample,

and  $\text{CO}_2$  formation decayed at a similar temperature, indicating that this protocol exerted no or only a very small effect on the bulk. After the oxidative treatment, the amount of  $\text{CO}_2$  formed increased from 0.298  $\mu\text{mol}$  to 0.393  $\mu\text{mol}$  over the whole period. After an integration starting from 70  $^\circ\text{C}$  to neglect the amount of highly active ROS in the beginning, the integral is 0.298  $\mu\text{mol}$  before TPO and 0.286  $\mu\text{mol}$  before TPO, which confirms the integrity of the bulk. These observations are well in line with the formation of ROS at the surface of this catalyst, causing the increase in catalytic activity.

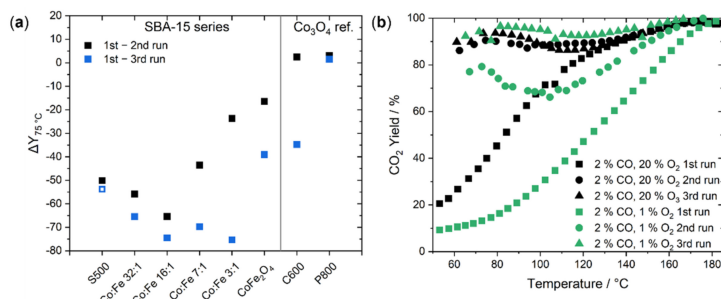


**Figure 6.** (a) Difference in conversion at 75  $^\circ\text{C}$  between the 1st and 2nd/3rd run ( $\Delta Y_{75^\circ\text{C}}$ ) of CO oxidation for all catalysts. Please note that the conversion of S500 is 90% during the 2nd run, which is why it cannot be excluded that the improvement of this sample is to some extent limited by approaching full conversion, and the data point is shown as a hollow symbol. (b) CO oxidation activity of S500 in all runs for feed compositions 2% CO and 20%  $\text{O}_2$  and 2% CO and 1%  $\text{O}_2$ .

As discussed above, the comparison between first run activity and second run activity suggests that the first run acts as an *in situ* TPO under reactive conditions leading to increased activity of the samples by creating ROS under the oxygen excess at full conversion. To support this hypothesis, another cyclic CO oxidation on a fresh batch of the templated nanowire catalyst S500 was performed with a stoichiometric feed containing 2% CO and only 1%  $\text{O}_2$ . The new runs with decreased oxygen concentration were compared to the initial runs with 20%  $\text{O}_2$  and are shown in Figure 6b. The initial activity in the first run was decreased for the lower oxygen content in the feed, which could indicate a Langmuir-Hinshelwood (LH) rather than a MvK mechanism due to the large effect of oxygen partial pressure on the activity. Again, the temperature to reach full conversion is comparable for both oxygen concentrations. According to Lukashuk et al., the MvK mechanism becomes dominant above 100  $^\circ\text{C}$ , which is in line with DFT studies that indicate a preferred MvK mechanism on  $\text{Co}_3\text{O}_4(110)$  B-terminated surfaces [17,44].

For the second run, there was still a substantial activity boost observed upon decreased oxygen concentration, but the magnitude of the activity boost was less pronounced than the measurement performed in 20%  $\text{O}_2$ . Jansson et al. reported the improved catalyst recovery for regeneration in 10%  $\text{O}_2$  compared to using Ar as the atmosphere for catalyst activity regeneration, so higher oxygen partial pressures are beneficial [21]. As a minimum temperature for catalyst regeneration, a temperature of 250  $^\circ\text{C}$  was reported, which indicates that the first run can act as an *in situ* regeneration of the sample and that the temperature treatment can be considered an important parameter for sample activation by ROS formation also in oxygen-leaner conditions at higher temperatures in a stoichiometric feed. The U-shaped curve of the second run in 1%  $\text{O}_2$  containing feed still indicates the consumption of ROS, but the degree of ROS formation seems to increase with oxygen content in the feed. However, after the TPO before the third run, the conversion of CO was slightly higher with 1%  $\text{O}_2$  in the reaction mixture compared to the 20%  $\text{O}_2$  containing reaction mixture, which might be explained by less competitive adsorption of CO and oxygen on the surface at lower total concentrations of reactive species in the feed gas stream.

To confirm the effect of the high concentration of  $\text{O}_2$  on the reactivity of the second run, a similar experiment as seen in Figure 6b on the catalyst S500 was also performed on the SBA-15 templated catalyst with a Co:Fe ratio 3:1 to check the effect of Fe. The mentioned experiment on 3:1 is shown in Figure S17 as an example for mixed Co:Fe catalysts. It confirmed the basically lower activity in the less oxidizing feed and shows even a decreased activity of the second run directly after the first run on an Fe-rich catalyst suggesting that these conditions are unable to cause ROS formation on the less active Fe-containing catalyst. However, the U-shaped curve and increased low-temperature activity were observed after TPO, as shown in Figure S17b. The  $\text{Co}_3\text{O}_4$  catalysts (S500, C600, and P800) were characterized by XRD, TEM (S500), and SEM (C600, P800) after the third run. The mesostructure remains unchanged, as is shown by electron microscopy images in Figure S18. The nanowire morphology of S500 remains intact as well as C600 shows particles in different shapes and sizes. In addition, the structure of P800 remains similar as well, but the particles appear more faceted, which might be a result of surface reconstruction but might also be explained by a better contrast of the image after catalysis. As seen from XRD after catalysis, also the bulk structure remains unchanged, as is shown in Figure S19. S500 shows broad reflections due to low domain size as already reported in the XRD of the as-prepared materials. The integrity of the bulk crystal structure and the particles support the claim that dynamic changes at the surface related to ROS are responsible for the observed dynamics in catalysis.

### 3. Materials and Methods

#### 3.1. Synthesis and Sample Preparation

S500 and further SBA-15 templated catalyst materials: SBA-15 templated  $\text{Co}_3\text{O}_4$  (labeled as S500 in this manuscript),  $\text{CoFe}_2\text{O}_4$ , and cobalt iron oxide series with controlled mesostructures via nanocasting have been prepared according to our previous report, the mentioned metal cation ratios have been used for synthesis as described in the previous work [34]. In brief, cobalt and iron precursors (Co:Fe atomic ratio of 1:0, 32:1, 16:1, 7:1, 3:1, and 1:2) were prepared by dissolving a stoichiometric amount of  $\text{Co}(\text{NO}_3)_2 \bullet 6\text{H}_2\text{O}$  and  $\text{Fe}(\text{NO}_3)_3 \bullet 9\text{H}_2\text{O}$  (Merck, Darmstadt, Germany, ACS reagent grade) in pure ethanol. The calculated concentration of precursor solution was 0.8 M. The precursor solutions were then impregnated into the pore system of SBA-15(100) template by the two-step wet impregnation method (15% total pore filling). For the first impregnation step, a mixture of precursor solution and template was stirred 2 h. Then the composites were dried in the oven at 50 °C overnight. The first calcination was carried out at 250 °C for 4 h (ramping rate 2 °C min<sup>-1</sup>). The same impregnation procedure was applied for the second impregnation step; however, the final calcination was carried out at 500 °C for 6 h with the intermediate dwell at 250 °C for 4 h (ramping rate 2 °C min<sup>-1</sup>). As an exception, a slower ramping rate (1 °C min<sup>-1</sup>) was applied for calcining  $\text{CoFe}_2\text{O}_4$ . SBA-15(100) template was then leached out with hot 2 M KOH solution. After four washing cycles and centrifugation in distilled water, the final product was then dried in the oven at 80 °C overnight.

P800: Precursor synthesis was conducted in an automatic lab reactor system (OptiMax 1001, Mettler Toledo), as reported before [41]. The precipitated  $\text{Co}(\text{OH})_2$  precursor was calcined at 800 °C for 3 h ( $\beta = 2 \text{ }^\circ\text{C min}^{-1}$ ) in stagnant air in a muffle furnace (B150, Nabertherm, Lilienthal, Germany) to achieve spinel formation.

C600:  $\text{Co}_3\text{O}_4$  was bought from Merck (Darmstadt, Germany). The material was recalcined in a rotary furnace GVA 12/450 (Carbolite Gero, Hope Valley, England) at 600 °C in synthetic air (99.999%, 20%  $\text{O}_2$  in  $\text{N}_2$ , 100 sccm) for 4 h.

For catalysis, all calcined samples were characterized as powders and pressed with a hydraulic press by PerkinElmer (5 t, 2 min, Überlingen, Germany), pestled, and sieved with stainless steel sieves from ATECHNIK (ISO 3310–1, Leinburg, Germany). A sieve fraction of 250–355  $\mu\text{m}$  was used for the kinetic analysis with a BELCAT-B (MicrotracBEL Corp., Haradanaka Toyonaka, Japan) catalyst analyzer.

### 3.2. Catalyst Characterization

$\text{N}_2$  adsorption-desorption experiment of C600 was performed with a NOVA3000e setup (Quantachrome Instruments, Boynton Beach, FL, USA) at  $-196^\circ\text{C}$  after degassing the samples at  $80^\circ\text{C}$  for 2 h in a vacuum. Kr adsorption-desorption experiment of P800 was performed with an ASiQwin setup (Quantachrome Instruments, Boynton Beach, FL, USA) at  $-196^\circ\text{C}$  after degassing the samples at  $150^\circ\text{C}$  for 24 h in a vacuum. BET (Brunauer–Emmett–Teller) surface areas were calculated from  $p/p_0$  data between 0.05 and 0.3. Total pore volumes were determined at  $p/p_0 = 0.99$ . Pore size distributions were determined using the Barrett–Joyner–Halenda (BJH) method during desorption. Kr adsorption experiment of P800 to determine the BET surface area was performed with a Belsorp-mini setup (MicrotracBEL Corp., Suminoe-ku, Osaka, Japan) after pretreatment in a vacuum at  $150^\circ\text{C}$  for 24 h.  $\text{N}_2$  adsorption–desorption experiments of the SBA-15 templated catalyst series were performed by using 3Flex Micromeritics at 77 K. The sample was degassed in a vacuum at  $120^\circ\text{C}$  for 10 h before the measurements. The Brunauer–Emmett–Teller (BET) surface area was calculated within the 0.06–0.3 relative pressure range ( $p/p_0$ ). The pore size distribution was calculated with the BJH method from the desorption branch.

Powder XRD patterns of C600 and P800 were recorded from  $5^\circ$  to  $90^\circ$  on a Bruker D8 Advance diffractometer (Bruker, Billerica, Massachusetts, USA) in Bragg–Brentano geometry with a position-sensitive LYNXEYE detector (Ni-filtered  $\text{CuK}_\alpha$  radiation Bruker, Billerica, Massachusetts, USA) applying a counting time of 0.3 s and step size of  $0.018^\circ$ . Samples were mounted by the use of dispersion in ethanol on a glass disc that was inserted in a round PMMA holder. The latter was subject to gentle rotation during scanning after removal of the ethanol by drying.

Scanning electron microscopy (SEM) of C600 and P800 was performed with an Apreo S LoVac (Thermo Fisher Scientific, Waltham, MA, United States). Before the measurements, the samples were sputtered with Pt/Au.

Transmission electron microscopy (TEM) of S500 were recorded with aberration (CS) corrected JEOL 2200FS (Tokyo, Japan) instrument equipped with a 200 kV Field Emission Gun (FEG). The samples were deposited on a Cu lacy carbon grid.

### 3.3. Catalytic CO Oxidation at Ambient Pressure

The catalytic experiments were performed in a BELCAT-B catalyst analyzer (MicrotracBEL Corp., Suminoe-ku, Osaka, Japan). To this aim, 60 mg (sieve fraction 250–355  $\mu\text{m}$ ) of each calcined catalyst sample diluted with 300 mg of silicon carbide ( $>355\ \mu\text{m}$ ) were placed inside a U-shaped quartz tube reactor (inner diameter = 8 mm). Each sample was pre-treated by heating at  $3\ ^\circ\text{C min}^{-1}$  in He (99.9999%, Air Liquide) from room temperature to  $100^\circ\text{C}$ , which was kept constant for 1 h. Thereafter, the sample was cooled down in He to  $45^\circ\text{C}$ .

Before starting the temperature-programmed catalytic experiments, the catalyst/SiC mixture was purged for 15 min with 2% CO and 20% O<sub>2</sub> in He to equilibrate the gas composition. Thereafter, the temperature was increased to  $250^\circ\text{C}$  at a heating rate of  $3\ ^\circ\text{C min}^{-1}$  for the first run. Then, the sample was cooled in 2% CO and 20% O<sub>2</sub> to  $45^\circ\text{C}$  with the maximum possible rate using a fan in the heating oven without data collection, the temperature was equilibrated for 5 min in He.

Afterward, the sample was purged with 2% CO and 20% O<sub>2</sub> for 15 min at  $45^\circ\text{C}$ , and a second consecutive run was performed by increasing the temperature to  $250^\circ\text{C}$  at a heating rate of  $3\ ^\circ\text{C min}^{-1}$  and 5 min dwell time at the maximum temperature.

For the preparation of the third run, the sample was again cooled down using the fan in the reactive atmosphere to  $100^\circ\text{C}$ , purged with He for 5 min and then temperature-programmed oxidation was performed in 20% O<sub>2</sub> in He to a maximum temperature of  $500^\circ\text{C}$  with a heating rate of  $10\ ^\circ\text{C min}^{-1}$ . The temperature of  $500^\circ\text{C}$  was chosen to mimic the calcination protocol of the SBA-15 templated materials. The maximum temperature was kept constant for 30 min after which the sample was cooled down with the maximum

rate using the fan to 45 °C in 20% O<sub>2</sub> balanced with He and kept constant for 15 min in He. Afterward, the sample was purged with 2% CO and 20% O<sub>2</sub> for 15 min at 45 °C. The third run was performed by increasing the temperature to 250 °C at a heating rate of 3 °C min<sup>-1</sup> and a 5 min dwell at the maximum temperature.

An additional experiment on SBA-15 templated Co<sub>3</sub>O<sub>4</sub> was performed under the same conditions regarding heating ramps and pretreatment with the only difference of changing the reactive gas mixture composition from 2% CO and 20% O<sub>2</sub> to 2% CO and 1% O<sub>2</sub>.

The total gas flow in all segments of the catalytic experiment was 80 mL min<sup>-1</sup>. The reactor outlet stream was analyzed using a MicroGC (Agilent Technologies 490, Santa Clara, CA, USA) equipped with a 5-Å molecular sieve and a Pora Plot Q column for the detection of CO, O<sub>2</sub>, and CO<sub>2</sub>.

#### 4. Conclusions

Co<sub>3-x</sub>Fe<sub>x</sub>O<sub>4</sub> spinel catalysts synthesized through nanocasting by using SBA-15 silica as template served as a model system to study the effect of composition in terms of Co:Fe ratio on cobalt spinel catalyst activity. A second comparison was made among the Co<sub>3</sub>O<sub>4</sub> catalysts from different synthesis procedures or sources (hard templating, precipitation, and commercial material) to investigate the role of mesostructure for their activity and formation of ROS during consecutive runs of CO oxidation in the oxidizing atmosphere up to 250 °C. A general negative correlation between increasing Fe content and initial activity in catalytic CO oxidation was found, suggesting that Fe was not involved directly in the active site. When comparing the first and the second run, the formation of ROS upon reaction in a highly oxidizing feed was observed. These ROS were not stable and vanished during further heating and were observed after TPO shown in an even increased activity. The relative activation was composition-dependent in a non-linear manner suggesting that Fe was involved in ROS formation. Comparison of pure Co<sub>3</sub>O<sub>4</sub> samples showed a higher conversion of the SBA-15 templated nanowire catalyst (S500) compared to materials from precipitation followed by calcination (P800) and a commercial material, which was recalcined (C600). P800 showed the lowest surface area, and larger but more uniform sintered particles with a roundish shape than C600, consisting of a mixture of morphologies and sizes. Only for S500, a strong activation in the second run was observed. After TPO, for C600, a clear activation was seen and ROS formation was confirmed by CO<sub>2</sub> formation observed in CO-TPR. However, for P800, again, no beneficial effect was observed. This indicates a correlation between particle size and exposed surface area with the capability of ROS formation induced by sample preparation history. The correlation can be explained by a hindered ROS formation on the large particle with low-indexed surface facets and low surface energy. After the three runs of the catalytic reaction, the mesostructure remained unchanged. The reactivity behavior of C600 and its strong dynamics upon TPO is currently studied in more detail to correlate surface structure and activity after different pretreatments to gain more insight into ROS nature and their formation and consumption.

**Supplementary Materials:** The following are available online at <https://www.mdpi.com/article/10.3390/catal1111312/s1>, Figure S1: Normalized N<sub>2</sub> adsorption-desorption isotherms (a) and normalized BJH pore size distribution (b). Figure S2: Rietveld refinement plots of C600 (a), P800 (b), and S500 (c). Table S1. Criteria of fit for the Rietveld Refinements of the x-ray diffraction patterns of the calcined samples. Figure S3: Comparison of CO conversion and CO<sub>2</sub> yield for the SBA-15 templated catalyst series. CO conversion in the 1st run (a). CO<sub>2</sub> yield in the 1st run (b). Figure S4: Comparison of CO conversion and CO<sub>2</sub> yield for the different Co<sub>3</sub>O<sub>4</sub> catalysts. CO conversion in the 1st run (a). CO<sub>2</sub> yield in the 1st run (b). CO conversion in the 2nd run (c). CO<sub>2</sub> yield in the 2nd run (d). CO conversion in the 3rd run (e). CO<sub>2</sub> yield in the 3rd run (f). Figure S5: Correlation between CO<sub>2</sub> formation rate at 100 °C and the cobalt content in the spinel materials. The red circle shows for clarity where a linear correlation between reaction rate and Co content can be observed. Figure S6: CO oxidation activity in the different runs for S500. Figure S7: CO oxidation activity in the different runs for SBA-15 templated Co:Fe 32:1. Figure S8: CO oxidation activity in the different runs for SBA-15 templated Co:Fe 16:1. Figure S9: CO oxidation activity in the different runs for SBA-15

templated Co:Fe 7:1. Figure S10: CO oxidation activity in the different runs for SBA-15 templated Co:Fe 3:1. Figure S11: CO oxidation activity in the different runs for SBA-15 templated  $\text{CoFe}_2\text{O}_4$ . Figure S12: CO oxidation activity in the different runs for  $\text{Co}_3\text{O}_4$  C600. Figure S13: CO oxidation activity in the different runs for  $\text{Co}_3\text{O}_4$  P800. Figure S14: Differences in conversion at 75 °C between the 2nd and the 3rd run of CO oxidation. Figure S15: Conversion at 75 °C in the 2nd run compared to the activation between 2nd and 3rd run for the SBA-15 templated materials. Figure S16: CO temperature programmed reduction of C600 without TPO and after TPO showing the evolved  $\text{CO}_2$  concentration (a) and the temperature in the reactor (b). Figure S17: (a) Initial measurement of 3:1 in the cyclic CO oxidation in 2% CO and 20%  $\text{O}_2$  in comparison to a new measurement in 2% CO and 1%  $\text{O}_2$  performed on another setup. Figure S18: (a) SEM image of C600 before catalysis. (b) SEM image of C600 after catalysis. (c) SEM image of C800 before catalysis. (d) TEM image of C800 after catalysis. (e) SEM image of S500 before catalysis. (f) TEM image of S500 after catalysis. Figure S19: XRD patterns of the spent catalysts.

**Author Contributions:** Conceptualization, H.T. and M.B.; Funding acquisition, H.T. and M.B.; Investigation, M.D., A.R., and E.B.; Methodology, M.D., A.R., and S.N.; Project administration, H.T. and M.B.; Resources, M.D., A.R., and E.B.; Supervision, H.T. and M.B.; Validation, M.D. and E.B.; Visualization, M.D., E.B. and A.R.; Writing—original draft, M.D.; Writing—review and editing, A.R., E.B., K.F.O., S.N., H.T., and M.B. All authors have read and agreed to the published version of the manuscript.

**Funding:** This work was funded by the Deutsche Forschungsgemeinschaft (DFG, German Research Foundation)—388390466—TRR 247 within the projects A1 and C1. We also acknowledge the financial support from the Mercator Research Center Ruhr (MERCUR, Pe-2018-0034). H.T. thanks Max Planck Society for the basic funding. We acknowledge support by the Open Access Publication Fund of the University of Duisburg-Essen.

**Acknowledgments:** The authors also acknowledge Kateryna Loza for SEM measurements, Markus Heidelmann, and Thai Binh Nguyen for TEM, and Dietrich Tönnes for XRD measurements. Furthermore, we acknowledge Benjamin Mockenhaupt, Jil Gieser, Noushin Arshadi, and Michael Thelen for BET measurements. Additionally, we thank Sven Anke for calcination of the C600 material.

**Conflicts of Interest:** The authors declare no conflict of interest.

## References

- Freund, H.J.; Meijer, G.; Scheffler, M.; Schlögl, R.; Wolf, M. CO oxidation as a prototypical reaction for heterogeneous processes. *Angew. Chem. Int. Ed. Engl.* **2011**, *50*, 10064–10094. [[CrossRef](#)]
- Xie, X.; Li, Y.; Liu, Z.Q.; Haruta, M.; Shen, W. Low-temperature oxidation of CO catalysed by  $\text{Co}(3)\text{O}(4)$  nanorods. *Nature* **2009**, *458*, 746–749. [[CrossRef](#)]
- Yu, Y.B.; Takei, T.; Ohashi, H.; He, H.; Zhang, X.L.; Haruta, M. Pretreatments of  $\text{Co}_3\text{O}_4$  at moderate temperature for CO oxidation at –80 °C. *J. Catal.* **2009**, *267*, 121–128. [[CrossRef](#)]
- Royer, S.; Duprez, D. Catalytic Oxidation of Carbon Monoxide over Transition Metal Oxides. *ChemCatChem* **2011**, *3*, 24–65. [[CrossRef](#)]
- Thomas, J.; Thomas, N.; Girgisdies, F.; Behrens, M.; Huang, X.; Sudheesh, V.D.; Sebastian, V. Synthesis of cobalt ferrite nanoparticles by constant pH co-precipitation and their high catalytic activity in CO oxidation. *N. J. Chem.* **2017**, *41*, 7356–7363. [[CrossRef](#)]
- Busca, G.; Guidetti, R.; Lorenzelli, V. Fourier-transform infrared study of the surface properties of cobalt oxides. *J. Chem. Soc. Faraday Trans.* **1990**, *86*. [[CrossRef](#)]
- Finocchio, E.; Willey, R.J.; Busca, G.; Lorenzelli, V. FTIR studies on the selective oxidation and combustion of light hydrocarbons at metal oxide surfaces Part 3.—Comparison of the oxidation of C3 organic compounds over  $\text{Co}_3\text{O}_4$ ,  $\text{MgCr}_2\text{O}_4$  and  $\text{CuO}$ . *J. Chem. Soc. Faraday Trans.* **1997**, *93*, 175–180. [[CrossRef](#)]
- Finocchio, E.; Busca, G.; Lorenzelli, V.; Escribano, V.S. FTIR studies on the selective oxidation and combustion of light hydrocarbons at metal oxide surfaces. Part 2.—Propane and propene oxidation on  $\text{Co}_3\text{O}_4$ . *J. Chem. Soc. Faraday Trans.* **1996**, *92*, 1587–1593. [[CrossRef](#)]
- Busca, G.; Daturi, M.; Finocchio, E.; Lorenzelli, V.; Ramis, G.; Willey, R.J. Transition metal mixed oxides as combustion catalysts: Preparation, characterization and activity mechanisms. *Catal. Today* **1997**, *33*, 239–249. [[CrossRef](#)]
- Zasada, F.; Janas, J.; Piskorz, W.; Sojka, Z. Surface oxygen dynamics and H2 oxidation on cobalt spinel surface probed by  $^{18}\text{O}/^{16}\text{O}$  isotopic exchange and accounted for by DFT molecular modeling: Facile interfacial oxygen atoms flipping through transient peroxy intermediate. *Res. Chem. Intermed.* **2016**, *43*, 2865–2880. [[CrossRef](#)]

11. Zasada, F.; Janas, J.; Piskorz, W.; Gorczynska, M.; Sojka, Z. Total Oxidation of Lean Methane over Cobalt Spinel Nanocubes Controlled by the Self-Adjusted Redox State of the Catalyst: Experimental and Theoretical Account for Interplay between the Langmuir–Hinshelwood and Mars–Van Krevelen Mechanisms. *ACS Catal.* **2017**, *7*, 2853–2867. [[CrossRef](#)]
12. Zasada, F.; Grybos, J.; Budiyanto, E.; Janas, J.; Sojka, Z. Oxygen species stabilized on the cobalt spinel nano-octahedra at various reaction conditions and their role in catalytic CO and CH<sub>4</sub> oxidation, N<sub>2</sub>O decomposition and oxygen isotopic exchange. *J. Catal.* **2019**, *371*, 224–235. [[CrossRef](#)]
13. Liu, Y.; Peng, Y.; Naschitzki, M.; Gewinner, S.; Schollkopf, W.; Kuhlenbeck, H.; Pentcheva, R.; Roldan Cuenya, B. Surface oxygen Vacancies on Reduced Co<sub>3</sub>O<sub>4</sub> (100): Superoxide Formation and Ultra-Low-Temperature CO Oxidation. *Angew. Chem. Int. Ed.* **2021**, *60*, 16514–16520. [[CrossRef](#)] [[PubMed](#)]
14. Teng, Y.; Kusano, Y.; Azuma, M.; Haruta, M.; Shimakawa, Y. Morphology effects of Co<sub>3</sub>O<sub>4</sub> nanocrystals catalyzing CO oxidation in a dry reactant gas stream. *Catal. Sci. Technol.* **2011**, *1*, 920–922. [[CrossRef](#)]
15. Gu, D.; Jia, C.J.; Weidenthaler, C.; Bongard, H.J.; Spliethoff, B.; Schmidt, W.; Schüth, F. Highly Ordered Mesoporous Cobalt-Containing Oxides: Structure, Catalytic Properties, and Active Sites in Oxidation of Carbon Monoxide. *J. Am. Chem. Soc.* **2015**, *137*, 11407–11418. [[CrossRef](#)]
16. Anke, S.; Bendt, G.; Sinev, I.; Hajiyani, H.; Antoni, H.; Zegkinoglou, I.; Jeon, H.; Pentcheva, R.; Roldan Cuenya, B.; Schulz, S.; et al. Selective 2-Propanol Oxidation over Unsupported Co<sub>3</sub>O<sub>4</sub> Spinel Nanoparticles: Mechanistic Insights into Aerobic Oxidation of Alcohols. *ACS Catal.* **2019**, *9*, 5974–5985. [[CrossRef](#)]
17. Lukashuk, L.; Yigit, N.; Rameshan, R.; Kolar, E.; Teschner, D.; Havecker, M.; Knop-Gericke, A.; Schlögl, R.; Föttinger, K.; Rupprechter, G. Operando Insights into CO Oxidation on Cobalt Oxide Catalysts by NAP-XPS, FTIR, and XRD. *ACS Catal.* **2018**, *8*, 8630–8641. [[CrossRef](#)]
18. Dreyer, M.; Krebs, M.; Najafishirtari, S.; Rabe, A.; Friedel Ortega, K.; Behrens, M. The Effect of Co Incorporation on the CO Oxidation Activity of LaFe<sub>1-x</sub>CoxO<sub>3</sub> Perovskites. *Catalysts* **2021**, *11*, 550. [[CrossRef](#)]
19. Hu, L.H.; Sun, K.Q.; Peng, Q.; Xu, B.Q.; Li, Y.D. Surface Active Sites on Co<sub>3</sub>O<sub>4</sub> Nanobelt and Nanocube Model Catalysts for CO Oxidation. *Nano Res.* **2010**, *3*, 363–368. [[CrossRef](#)]
20. Yang, J.; Guo, J.; Wang, Y.B.; Wang, T.; Gu, J.; Peng, L.M.; Xue, N.H.; Zhu, Y.; Guo, X.F.; Ding, W.P. Reduction-oxidation pretreatment enhanced catalytic performance of Co<sub>3</sub>O<sub>4</sub>/Al<sub>2</sub>O<sub>3</sub> over CO oxidation. *Appl. Surf. Sci.* **2018**, *453*, 330–335. [[CrossRef](#)]
21. Jansson, J.; Palmqvist, A.E.C.; Fridell, E.; Skoglundh, M.; Osterlund, L.; Thormahlen, P.; Langer, V. On the catalytic activity of Co<sub>3</sub>O<sub>4</sub> in low-temperature CO oxidation. *J. Catal.* **2002**, *211*, 387–397. [[CrossRef](#)]
22. Chakrapani, K.; Bendt, G.; Hajiyani, H.; Lunkenbein, T.; Greiner, M.T.; Masliuk, L.; Salamon, S.; Landers, J.; Schlögl, R.; Wende, H.; et al. The Role of Composition of Uniform and Highly Dispersed Cobalt Vanadium Iron Spinel Nanocrystals for Oxygen Electrocatalysis. *ACS Catal.* **2018**, *8*, 1259–1267. [[CrossRef](#)]
23. Büker, J.; Alkan, B.; Fu, Q.; Xia, W.; Schulwitz, J.; Waffel, D.; Falk, T.; Schulz, C.; Wiggers, H.; Muhler, M.; et al. Selective cyclohexene oxidation with O<sub>2</sub>, H<sub>2</sub>O<sub>2</sub> and tert-butyl hydroperoxide over spray-flame synthesized LaCo<sub>1-x</sub>FexO<sub>3</sub> nanoparticles. *Catal. Sci. Technol.* **2020**, *10*, 5196–5206. [[CrossRef](#)]
24. Waffel, D.; Alkan, B.; Fu, Q.; Chen, Y.T.; Schmidt, S.; Schulz, C.; Wiggers, H.; Muhler, M.; Peng, B. Towards Mechanistic Understanding of Liquid-Phase Cinnamyl Alcohol Oxidation with tert-Butyl Hydroperoxide over Noble-Metal-Free LaCo<sub>1-x</sub>FexO<sub>3</sub> Perovskites. *ChemPlusChem* **2019**, *84*, 1155–1163. [[CrossRef](#)] [[PubMed](#)]
25. Waag, F.; Gökce, B.; Kalapu, C.; Bendt, G.; Salamon, S.; Landers, J.; Hagemann, U.; Heidelmann, M.; Schulz, S.; Wende, H.; et al. Adjusting the catalytic properties of cobalt ferrite nanoparticles by pulsed laser fragmentation in water with defined energy dose. *Sci. Rep.* **2017**, *7*, 13161. [[CrossRef](#)] [[PubMed](#)]
26. Chakrapani, K.; Bendt, G.; Hajiyani, H.; Schwarzkopf, I.; Lunkenbein, T.; Salamon, S.; Landers, J.; Wende, H.; Schlögl, R.; Pentcheva, R.; et al. Role of Composition and Size of Cobalt Ferrite Nanocrystals in the Oxygen Evolution Reaction. *ChemCatChem* **2017**, *9*, 2988–2995. [[CrossRef](#)]
27. Anke, S.; Falk, T.; Bendt, G.; Sinev, I.; Havecker, M.; Antoni, H.; Zegkinoglou, I.; Jeon, H.; Knop-Gericke, A.; Schlögl, R.; et al. On the reversible deactivation of cobalt ferrite spinel nanoparticles applied in selective 2-propanol oxidation. *J. Catal.* **2020**, *382*, 57–68. [[CrossRef](#)]
28. Friedel Ortega, K.; Anke, S.; Salamon, S.; Özcan, F.; Heese, J.; Andronescu, C.; Landers, J.; Wende, H.; Schuhmann, W.; Muhler, M.; et al. Topotactic Synthesis of Porous Cobalt Ferrite Platelets from a Layered Double Hydroxide Precursor and Their Application in Oxidation Catalysis. *Chemistry* **2017**, *23*, 12443–12449. [[CrossRef](#)]
29. Budiyanto, E.; Zerebecki, S.; Weidenthaler, C.; Kox, T.; Kenmoe, S.; Spohr, E.; DeBeer, S.; Rüdiger, O.; Reichenberger, S.; Barcikowski, S.; et al. Impact of Single-Pulse, Low-Intensity Laser Post-Processing on Structure and Activity of Mesostructured Cobalt Oxide for the Oxygen Evolution Reaction. *ACS Appl. Mater. Interfaces* **2021**. [[CrossRef](#)]
30. Alkan, B.; Medina, D.; Landers, J.; Heidelmann, M.; Hagemann, U.; Salamon, S.; Andronescu, C.; Wende, H.; Schulz, C.; Schuhmann, W.; et al. Spray-Flame-Prepared LaCo<sub>1-x</sub>FexO<sub>3</sub> Perovskite Nanoparticles as Active OER Catalysts: Influence of Fe Content and Low-Temperature Heating. *ChemElectroChem* **2020**, *7*, 2564–2574. [[CrossRef](#)]
31. Alkan, B.; Cychy, S.; Varhade, S.; Muhler, M.; Schulz, C.; Schuhmann, W.; Wiggers, H.; Andronescu, C. Spray-Flame-Synthesized LaCo<sub>1-x</sub>FexO<sub>3</sub> Perovskite Nanoparticles as Electrocatalysts for Water and Ethanol Oxidation. *ChemElectroChem* **2019**, *6*, 4266–4274. [[CrossRef](#)]

32. Angel, S.; Neises, J.; Dreyer, M.; Friedel Ortega, K.; Behrens, M.; Wang, Y.; Arandiyan, H.; Schulz, C.; Wiggers, H. Spray-flame synthesis of  $\text{La}(\text{Fe}, \text{Co})\text{O}_3$  nano-perovskites from metal nitrates. *AIChE J.* **2019**, *66*, 441. [[CrossRef](#)]
33. Bahlawane, N.; Ngamou, P.H.; Vannier, V.; Kottke, T.; Heberle, J.; Kohse-Hoinghaus, K. Tailoring the properties and the reactivity of the spinel cobalt oxide. *Phys. Chem. Chem. Phys.* **2009**, *11*, 9224–9232. [[CrossRef](#)] [[PubMed](#)]
34. Budiyanto, E.; Yu, M.Q.; Chen, M.M.; DeBeer, S.; Rudiger, O.; Tüysüz, H. Tailoring Morphology and Electronic Structure of Cobalt Iron Oxide Nanowires for Electrochemical Oxygen Evolution Reaction. *ACS Appl. Energy Mater.* **2020**, *3*, 8583–8594. [[CrossRef](#)]
35. Falk, T.; Budiyanto, E.; Dreyer, M.; Pfleiger, C.; Waffel, D.; Büker, J.; Weidenthaler, C.; Ortega, K.F.; Behrens, M.; Tüysüz, H.; et al. Identification of Active Sites in the Catalytic Oxidation of 2-Propanol over  $\text{Co}_{1+x}\text{Fe}_{2-x}\text{O}_4$  Spinel Oxides at Solid/Liquid and Solid/Gas Interfaces. *ChemCatChem* **2021**, *13*, 2942–2951. [[CrossRef](#)]
36. Waffel, D.; Budiyanto, E.; Porske, T.; Büker, J.; Falk, T.; Fu, Q.; Schmidt, S.; Tüysüz, H.; Muhler, M.; Peng, B.X. Investigation of Synergistic Effects between Co and Fe in  $\text{Co}_3\text{-xFexO}_4$  Spinel Catalysts for the Liquid-Phase Oxidation of Aromatic Alcohols and Styrene. *Mol. Catal.* **2020**, *498*, 111251. [[CrossRef](#)]
37. Wang, X.T.; Ouyang, T.; Wang, L.; Zhong, J.H.; Ma, T.; Liu, Z.Q. Redox-Inert  $\text{Fe}^{(3+)}$  Ions in Octahedral Sites of Co-Fe Spinel Oxides with Enhanced Oxygen Catalytic Activity for Rechargeable Zinc-Air Batteries. *Angew. Chem. Int. Ed.* **2019**, *58*, 13291–13296. [[CrossRef](#)] [[PubMed](#)]
38. Thommes, M. Physical Adsorption Characterization of Nanoporous Materials. *Chem. Ing. Tech.* **2010**, *82*, 1059–1073. [[CrossRef](#)]
39. Thommes, M.; Kaneko, K.; Neimark, A.V.; Olivier, J.P.; Rodriguez-Reinoso, F.; Rouquerol, J.; Sing, K.S.W. Physisorption of gases, with special reference to the evaluation of surface area and pore size distribution (IUPAC Technical Report). *Pure Appl. Chem.* **2015**, *87*, 1051–1069. [[CrossRef](#)]
40. Neimark, A.V.; Sing, K.S.W.; Thommes, M. Surface Area and Porosity. In *Handbook of Heterogeneous Catalysis*; Wiley-VCH Verlag GmbH & Co. KGaA: Weinheim, Germany, 2008; pp. 721–738.
41. Rabe, A.; Büker, J.; Salamon, S.; Koul, A.; Hagemann, U.; Landers, J.; Ortega, K.F.; Peng, B.; Muhler, M.; Wende, H.; et al. The Roles of Composition and Mesosstructure of Cobalt-based Spinel Catalysts in Oxygen Evolution Reactions. *Chem. Eur. J.* **2021**. [[CrossRef](#)]
42. Kotousova, I.; Polyakov, S. Electron-diffraction study of  $\text{Co}_3\text{O}_4$ . *Kristallografiya* **1972**, *17*, 661–663.
43. Rietveld, H.M. Line Profiles of Neutron Powder-Diffraction Peaks for Structure Refinement. *Acta Crystallogr.* **1967**, *22*, 151. [[CrossRef](#)]
44. Wang, H.F.; Kavanagh, R.; Guo, Y.L.; Guo, Y.; Lu, G.Z.; Hu, P. Origin of extraordinarily high catalytic activity of  $\text{Co}_3\text{O}_4$  and its morphological chemistry for CO oxidation at low temperature. *J. Catal.* **2012**, *296*, 110–119. [[CrossRef](#)]
45. Tüysüz, H.; Comotti, M.; Schüth, F. Ordered mesoporous  $\text{Co}_3\text{O}_4$  as highly active catalyst for low temperature CO-oxidation. *Chem. Commun.* **2008**, *34*, 4022–4024. [[CrossRef](#)] [[PubMed](#)]
46. Zasada, F.; Piskorz, W.; Janas, J.; Budiyanto, E.; Sojka, Z. Dioxygen Activation Pathways over Cobalt Spinel Nanocubes—From Molecular Mechanism into Ab Initio Thermodynamics and  $16\text{O}_2/18\text{O}_2$  Exchange Microkinetics. *J. Phys. Chem. C* **2017**, *121*, 24128–24143. [[CrossRef](#)]
47. Jia, C.J.; Schwickardi, M.; Weidenthaler, C.; Schmidt, W.; Korhonen, S.; Weckhuysen, B.M.; Schüth, F.  $\text{Co}_3\text{O}_4\text{-SiO}_2$  nanocomposite: A very active catalyst for CO oxidation with unusual catalytic behavior. *J. Am. Chem. Soc.* **2011**, *133*, 11279–11288. [[CrossRef](#)]

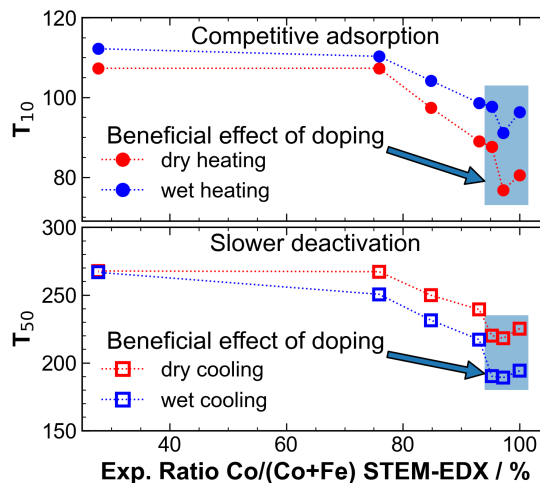
## 8. Beneficial Effects of Low Iron Contents on Cobalt-Containing Spinel Catalysts in the Gas Phase 2-Propanol Oxidation

**Title:** “Beneficial Effects of Low Iron Contents on Cobalt-Containing Spinel Catalysts in the Gas Phase 2-Propanol Oxidation”

**Authors:** Maik Dreyer, Ulrich Hagemann, Markus Heidelmann, Eko Budiyanto, Nicolas Cosanne, Klaus Friedel Ortega, Sharif Najafishirtari, Harun Tüysüz, Nils Hartmann, Malte Behrens

**Supporting Information:** The Supporting Information is shown in Chapter A in Section VIII.

**Graphical Abstract:**



This manuscript is currently under review at ChemCatChem (manuscript number: 10.1002/cctc.202200472).

Maik Dreyer wrote the manuscript draft and performed the gas phase 2-propanol oxidation experiments. Furthermore, he organized the distribution of materials to deeper characterization and performed the evaluation despite the XPS analysis. Ulrich Hagemann was responsible for XPS and its evaluation. Markus Heidelmann operated the TEM and TEM-EDX. Eko Budiyanto synthesized the materials and organized the basic characterization. Nicolas Cosanne measured the gas phase 2-propanol oxidation of one catalyst during a practical course. Klaus Friedel Ortega supervised the work and conceptualized

parts of it. Sharif Najafishirtari took responsibility in supervision and conceptualization. Harun Tüysüz, Nils Hartmann, and Malte Behrens acquired the funding, supervised the work, and administrated the project. All authors contributed to review and editing of the original draft.

## RESEARCH ARTICLE

**Beneficial Effects of Low Iron Contents on Cobalt-Containing Spinel Catalysts in the Gas Phase 2-Propanol Oxidation**

Maik Dreyer<sup>a</sup>, Ulrich Hagemann<sup>b</sup>, Markus Heidelmann<sup>b</sup>, Eko Budiyanto<sup>c</sup>, Nicolas Cosanne<sup>d</sup>, Klaus Friedel Ortega<sup>d</sup>, Sharif Najafishirtari<sup>d</sup>, Nils Hartmann<sup>b</sup>, Harun Tüysüz<sup>c</sup>, Malte Behrens<sup>a,d\*</sup>

[a] Maik Dreyer, Prof. Dr. Malte Behrens  
Faculty for Chemistry and Center for Nanointegration Duisburg-Essen (CENIDE)  
University of Duisburg-Essen  
Universitätstr. 7, D-45141 Essen, Germany  
E-mail: mbbehrens@ac.uni-kiel.de

[b] Dr. Ulrich Hagemann, Dr. Markus Heidelmann, Prof. Dr. Nils Hartmann  
Interdisciplinary Center for Analytics on the Nanoscale (ICAN) and Center for Nanointegration Duisburg-Essen (CENIDE)  
NanoEnergieTechnikZentrum at University of Duisburg-Essen  
Carl-Benz-Str. 199, D-47057 Duisburg

[c] Eko Budiyanto, PD Dr. Harun Tüysüz  
Heterogeneous Catalysis and Sustainable Energy  
Kaiser-Wilhelm-Platz 1, D-45740 Mülheim an der Ruhr

[d] Nicolas Cosanne, Dr. Klaus Friedel Ortega, Dr. Sharif Najafishirtari, Prof. Dr. Malte Behrens  
Institute of Inorganic Chemistry  
Christian-Albrechts-Universität zu Kiel  
Max-Eyth-Straße 2, D-24118 Kiel

Supporting information for this article is given via a link at the end of the document.

**Abstract:** Oxidation reactions are highly relevant transformation reactions in the industry. Mixed Co and Fe containing oxides are promising substitutes for noble-metal-based catalysts due to lower cost and higher thermal stability. Performing oxidation catalysis in the liquid phase is desired to prevent total oxidation. An approach toward liquid phase reactions is water vapor added to the gas stream, which can help to build an experimental bridge between both phases. Here, nanocasted  $Co_{3-x}Fe_xO_4$  spinels are studied in the gas phase oxidation of 2-propanol as a probe for selective oxidation without and with the addition of water into the reaction feed. In both cases, low amounts of Fe ( $\leq 4\%$ ) were found to be beneficial for the activity. Under wet conditions, there is a negative effect on the activity below 150 °C during heating due to competitive adsorption. However, at higher temperatures during cooling, the activity is higher due to a slower deactivation.

**Introduction**

Cobalt-containing spinel oxides are among the most promising materials studied in recent years to replace noble-metal-based catalysts in oxidation catalysis for the formation of value-added products or in total oxidation processes.<sup>[1]</sup> Thus, the oxidation reactions of several reactants were extensively studied on cobalt-based spinel catalysts, such as CO oxidation,<sup>[2]</sup> methane combustion,<sup>[3]</sup> longer-chain alkane combustion,<sup>[4]</sup> as well as gas phase and liquid phase 2-propanol oxidation.<sup>[5]</sup> From the mechanistic point of view, the O<sub>2</sub> activation and the formation of reactive oxygen species (ROS) at the surface of these cobalt oxide catalysts play an important role in CO and methane oxidation.<sup>[6]</sup> Zasada et al. reported that two fivefold coordinated Co<sup>3+</sup> centers in octahedral sites of the spinel activate the oxygen as a cooperative tandem.<sup>[7]</sup> In the temperature range below 450 °C, they reported  $\mu$ -superoxo and metal-oxo species.<sup>[3b]</sup> Another study by Liu et al. showed that oxygen

vacancies could activate O<sub>2</sub> and form superoxo species on the surface.<sup>[8]</sup> In general, cobalt oxide spinel with a predominantly exposed (110) surface shows higher activity than that of materials with other low-indexed surface terminations as seen in CO oxidation,<sup>[2e]</sup> gas-phase 2-propanol oxidation,<sup>[5a]</sup> methane,<sup>[9]</sup> and toluene oxidation.<sup>[10]</sup> CO oxidation is considered to take place by different mechanisms. The mechanisms mentioned by Lukashuk et al. are namely Langmuir-Hinshelwood at low temperature, Mars-van-Krevelen at high temperature, and the additional mechanisms CO dissociation, carbon oxidation, and formation of carbonate spectators.<sup>[11]</sup>

2-Propanol oxidation on  $Co_3O_4$  spinel catalysts was mainly studied as a probe reaction for selective oxidations relevant to the chemical industry. It was proposed that coordinatively unsaturated Co<sup>3+</sup> is the active site in the liquid- and gas-phase oxidation.<sup>[5c, 5e]</sup> In terms of 2-propanol oxidation on the (100) surface, a preferential Langmuir-Hinshelwood mechanism was reported,<sup>[5c]</sup> while on the (110) surface, the Mars-van-Krevelen mechanism was proposed based on DFT+U calculations.<sup>[5a]</sup>

On spinel oxides, the addition of water to the reaction feed typically dampens the activity in oxidation catalysis,<sup>[12]</sup> which was observed on  $Co_3O_4$ -based spinel catalysts in several reactions under wet conditions, e.g., total propane oxidation,<sup>[4a]</sup> hydrocarbon oxidation,<sup>[12]</sup> and CO oxidation.<sup>[13]</sup> The lower CO oxidation activity was related to water adsorption on Co<sup>3+</sup> sites. Consequently, the sites are not available for the adsorption of reactant molecules.<sup>[13]</sup> Another possible reason is surface coverage with OH groups instead of H<sub>2</sub>O<sup>[13]</sup> which possibly hinders the oxygen transfer.<sup>[13-14]</sup> However, a different reaction mechanism occurs on the (110) surface; a CO molecule can additionally be adsorbed on a Co<sup>3+</sup> with a pre-adsorbed OH group and still form CO<sub>2</sub>.<sup>[13]</sup> Our previous work showed a lower deactivation rate in a wet feed than a dry feed on cobalt iron mixed perovskites,<sup>[15]</sup> which shows that also positive effects of water addition are possible, that need further studies.

## RESEARCH ARTICLE

A general synergistic effect of different cations was reported in the literature for several reactions regarding the catalyst composition. For example, the highest selectivity to lower olefins in CO hydrogenation was found for an intermediate Mn content in  $\text{Mn}_x\text{Fe}_{3-x}\text{O}_4$  spinels.<sup>[16]</sup> The same was observed for the activity of  $\text{Mn}_{1-x}\text{Zn}_x\text{Fe}_2\text{O}_4$  materials in the gas-phase oxidation of benzyl alcohol.<sup>[17]</sup> In  $\text{N}_2\text{O}$  decomposition, Wójcik et al. showed the effects of doping with various cations, where surface promoters like Na, K, and Cs had a beneficial effect on the catalytic activity with content of <1.5 wt.%, whereas positive effects of bulk substituents Ni and Zn were achieved with contents of 17 and 11 wt.%, respectively.<sup>[18]</sup> Also, a beneficial effect of Fe was reported previously in the literature when doping  $\text{Mn}_3\text{O}_4$  spinel catalysts in the reduction of NO with ammonia, attributed to a  $\text{Fe}_{\text{oct}}-\text{O}-\text{Mn}_{\text{tet}}$  site.<sup>[19]</sup> Also, in the electrocatalytic oxygen evolution reaction (OER), the doping effects of Fe on  $\text{Co}_3\text{O}_4$  are extensively reported in the literature.<sup>[20]</sup> As a result of DFT+U calculations, a beneficial effect of Fe doping at an octahedral site on a  $\text{Co}_3\text{O}_4(001)$  A-layer with exposed tetrahedrally coordinated Co was found to lower the overpotential of the reaction.<sup>[21]</sup>

Iron substitution in the  $\text{Co}_3\text{O}_4$  spinel catalyst was studied on mesoporous materials synthesized via the nanocasting method using SBA-15 silica as a hard-template. An increase of catalytic activity in cinnamyl alcohol oxidation in the liquid phase catalyzed by these catalysts was observed when *tert*-butyl hydroperoxide (TPHP) was used as the oxidant. In contrast, no beneficial effect was seen in cinnamyl alcohol oxidation with  $\text{O}_2$  as the oxidant.<sup>[22]</sup> A similar catalytic enhancement promoted by iron substitution could also be observed in cinnamyl alcohol oxidation reaction with TBHP oxidant and  $\text{LaCo}_{1-x}\text{CoFe}_x\text{O}_3$  perovskite catalysts.<sup>[23]</sup> In the electrochemical OER catalyzed by the aforementioned SBA-15 templated spinels, iron substitution could facilitate a faster reaction kinetics due to the higher spin state of  $\text{Co}^{3+}$  ions in octahedral positions,<sup>[5c, 24]</sup> and alteration in the  $\text{Co}^{3+}-\text{O}$  bonds.<sup>[20a]</sup> In this study, effects of water addition and iron doping/incorporation are investigated for 2-propanol oxidation using empirical composition-activity correlations in dry and wet feeds. The catalysts are mixed mesoporous  $\text{Co}_{3-x}\text{Fe}_x\text{O}_4$  spinel catalysts, synthesized using SBA-15 silica hard template via the nanocasting route as described in the literature.<sup>[5e, 20a, 22]</sup> The composition of the samples was varied in a range from a few percent of Fe substitution in  $\text{Co}_3\text{O}_4$  to  $\text{CoFe}_2\text{O}_4$  and they were characterized by powder X-ray diffraction (XRD), X-ray photoelectron spectroscopy (XPS), high-resolution scanning transmission electron microscopy (STEM), electron energy loss spectroscopy (EELS) and energy-dispersive X-ray spectroscopy (EDX). After thorough characterization, the materials were tested in the gas phase oxidation of 2-propanol in three consecutive runs. Before each run, temperature-programmed oxidation (TPO) was performed to restore the catalysts' initial conditions. The first two runs were performed without a co-feed of water into the gas stream. A tenfold amount of water was added to the feed for the 3<sup>rd</sup> run. In both cases, a non-stable but highly active low-temperature (LT) activity channel and a less active but stable high-temperature (HT) activity channel were observed. Under both dry and wet conditions, a beneficial effect of small contents of Fe ( $\leq 4\%$ ) was seen. On the LT activity, the effect of water is always detrimental. However, when cooling down, water has a beneficial effect that coincides with higher stability during an isothermal dwell at 300 °C. Post-mortem characterization reveals morphologic stability of the hard templated catalysts and no clear

connection between Co content and surface-near Co oxidation state changes.

## Results and Discussion

## Characterization

The synthesis and characterization of SBA-15 templated cobalt iron oxide ( $\text{Co}_{3-x}\text{Fe}_x\text{O}_4$ ) sample series with the Co:Fe atomic ratios of 100:0 ( $\text{Co}_3\text{O}_4$ ), 64:1, 32:1, 16:1, 7:1, 3:1, and 1:2 ( $\text{CoFe}_2\text{O}_4$ ) were reported in detail in previous publications and are summarized in the following paragraph.<sup>[5e, 20a, 22]</sup> The above-mentioned ratios refer to the nominal stoichiometric ratio of Co:Fe used in the synthesis, and the composition was verified by scanning transmission electron microscopy (STEM) energy-dispersive X-ray spectroscopy (EDX) and X-ray photoelectron spectroscopy (XPS). XRD analysis revealed a pure single spinel phase on  $\text{Co}_3\text{O}_4$  and  $\text{Co}_{3-x}\text{Fe}_x\text{O}_4$  with Co:Fe atomic ratios of 64:1, 32:1, 16:1. For mixed samples with Co:Fe ratios of 7:1, 3:1 and 1:2 the two miscible phases of  $\text{Co}_3\text{O}_4$  and  $\text{CoFe}_2\text{O}_4$  could be assigned.<sup>[5e]</sup> With increasing Fe content in the catalysts, transmission electron microscopy (TEM) revealed less ordering of the mesoporous structure and nanowire length, as also visible from TEM images before catalysis in this study (see Figure S1). Another effect of incorporating Fe was seen on the increase of occupancy of  $\text{Co}^{2+}$  species in tetrahedral sites and distorted  $\text{Co}^{3+}-\text{O}$  bonds.<sup>[20a]</sup> A bulk elemental analysis by STEM-EDX and near-surface elemental quantification by X-ray photoelectron spectroscopy (XPS) showed a good agreement of the experimental Co:Fe content compared to its nominal or theoretical value, as shown in Figure 1a.<sup>[5e, 22]</sup> The Co 2p XPS spectra of the as-prepared materials are shown in Figure S2. The results for the STEM-EDX and XPS analysis are given in Table S1. Comparing STEM-EDX and XPS, a considerable difference in Co content on the surface compared to the bulk was seen only for the  $\text{CoFe}_2\text{O}_4$  catalyst. A greater extent of Co in the near-surface regions was also reported before for the SBA-15 templated  $\text{CoFe}_2\text{O}_4$  catalyst, which might be in line with the confirmation of a surface-segregated  $\text{Co}_3\text{O}_4$  secondary phase in this sample, as shown by Rietveld refinement.<sup>[5e, 22]</sup> The evaluation of Co species was then performed with XPS spectra. In general, fitting the Co 2p region is prone to errors in mixed Co and Fe containing oxides.<sup>[25]</sup> Since  $\text{Co}^{2+}/\text{Co}^{3+}$  oxidation states were desired to be investigated, and not  $\text{CoO}$  and  $\text{Co}_3\text{O}_4$  phase contributions, a model using the reference fits of  $\text{Co}^{2+}$  in  $\text{CoO}$  from the literature<sup>[25a]</sup> and  $\text{Co}^{3+}$  from a measurement on a  $\text{MgCo}_2\text{O}_4$  catalyst synthesized by Rabe et al.<sup>[26]</sup> was further constructed. For the three samples with the highest Fe contents, the Fe-LMM Auger peak overlapping with the Co 2p peak cannot be neglected. As the Fe is present as  $\text{Fe}^{3+}$  in our samples, we used the reference spectra from a  $\text{Fe}_2\text{O}_3$  sample to model the size, shape, and position of the Fe Auger signal. Especially for the  $\text{CoFe}_2\text{O}_4$  sample, this leads to an increase in the precision for the Co species determination. The results are shown in Figure 1b, and only minor changes between the different samples are observed. Two different reference composition curves are given per species. The horizontal curves show the ratio from a normal  $\text{Co}_3\text{O}_4$  spinel consisting of 2/3  $\text{Co}^{3+}$  in octahedral positions and 1/3  $\text{Co}^{2+}$  in tetrahedral positions. The hyperbolas show the composition upon substitution of Co by Fe under the assumption that Fe is always present as  $\text{Fe}^{3+}$ , as indicated from the Fe 2p

## RESEARCH ARTICLE

signals. A comparison between data and references reveals that the data mimics the behavior well with the hyperbolic curve shape despite for 3:1, which shows the composition of a normal spinel. For 32:1 and 64:1, the values determined by XPS are slightly higher than expected by both methods. For  $\text{CoFe}_2\text{O}_4$ , expected as an inverse spinel with only  $\text{Co}^{2+}$  contributions, minor contributions of a  $\text{Co}^{3+}$  species are possible, which is in line with phase segregation reported in the literature.<sup>[5e]</sup>

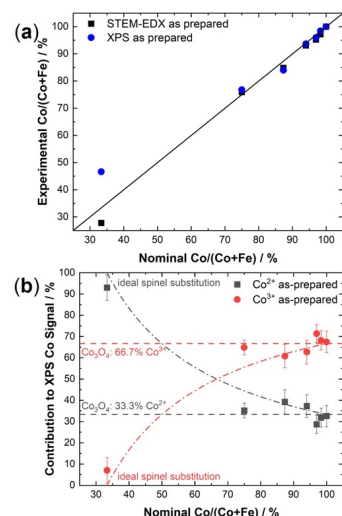


**Figure 1.** (a) Parity plot of experimental  $\text{Co}/(\text{Co}+\text{Fe})$  ratio derived from STEM-EDX and XPS in the as-prepared state. (b) Contribution of  $\text{Co}^{2+}$  and  $\text{Co}^{3+}$  to the Co XPS signal in the as-prepared state. The dashed horizontal lines indicate the Co oxidation state composition of a normal  $\text{Co}_3\text{O}_4$  spinel with 33.3%  $\text{Co}^{2+}$  and 66.7%  $\text{Co}^{3+}$ . The hyperbole curves show the Co oxidation states when substituting Co by Fe in  $\text{Co}_3\text{O}_4$  under the assumption that Fe exclusively is present as  $\text{Fe}^{3+}$ .

In electron energy loss spectroscopy (EELS), the Co L<sub>3</sub>/L<sub>2</sub> intensity ratio was determined from spectra shown in Figure S3a and the calculated ratio is shown in Figure S3b for all catalysts. A higher value of this ratio indicates a lower oxidation state of the Co cations.<sup>[27]</sup> This local spectroscopy technique confirmed that all catalysts despite  $\text{CoFe}_2\text{O}_4$  show comparable Co oxidation states and that  $\text{CoFe}_2\text{O}_4$  has a lower overall Co oxidation state. Furthermore, it is confirmed that the catalyst 3:1 differs from the expected hyperbole curve (Figure 1b) assuming a static  $\text{Fe}^{3+}$  oxidation state.

Specific BET surface areas of the catalysts are reproduced from the previous work<sup>[6]</sup> with the exception of Co:Fe 64:1 and are shown in Table S1. For Co-rich samples, the exposed surface areas ranged between 103 and 128  $\text{m}^2 \text{g}^{-1}$ . For  $\text{CoFe}_2\text{O}_4$ , the surface area increased to 178  $\text{m}^2 \text{g}^{-1}$  due to the formation of small nanoparticles instead of elongated nanowires arrays.<sup>[20a]</sup>

## Catalysis Data Evaluation Procedure

As previously applied in a study of  $\text{LaFe}_{1-x}\text{Co}_x\text{O}_3$  perovskites,<sup>[15]</sup> a consecutive three-run catalytic procedure was used to determine the activity of the catalyst materials in the gas phase oxidation of 2-propanol as a function of Co content in the catalyst as well as of the water content in the reaction mixture. Each run consisted of heating and cooling segments separated by an isothermal dwell period of 1 h at 300 °C. The two first runs were performed in a 1:1 mixture of O<sub>2</sub> and 2-propanol under identical conditions to check for stability and performance restorability. The 3<sup>rd</sup> run was performed with the 10-fold co-dosing of water compared to 2-propanol and O<sub>2</sub> into the feed to study its effect compared to the dry runs. Before each catalytic run, an oxidative treatment was performed to burn off surface-blocking carbonaceous species and regenerate the catalyst's surface. This oxidative activation step could fully restore the conversion profile for all catalysts. For the  $\text{Co}_3\text{O}_4$  catalyst, the steady-state conversion was comparable to that observed during cooling in the transient experiment.<sup>[5e]</sup> Such comparable conversions during cooling and under steady-state conditions were also observed in the gas-phase 2-propanol oxidation on perovskites.<sup>[11g]</sup>

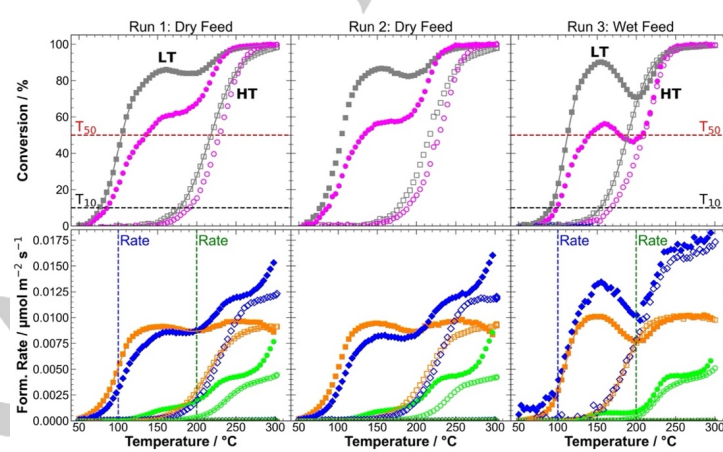


**Figure 2.** Exemplary dataset of Co:Fe 64:1 obtained from gas phase 2-propanol oxidation consisting of conversions of 2-propanol (■) and oxygen (●, top row) and product formation rates for acetone (■), water (▲) and  $\text{CO}_2$  (●, bottom row) during three consecutive runs. Filled symbols show data points during heating. Empty

## RESEARCH ARTICLE

characters show the behavior during cooling. Solid lines indicate the fit of the curve. Parameters  $T_{10}$ ,  $T_{50}$ , and the reaction rates at 100 °C and 200 °C are shown where they were extracted with dashed lines.

In Figure 2, an exemplary dataset is shown for Co:Fe 64:1. In the 1<sup>st</sup> and 2<sup>nd</sup> runs, the typical pattern of spinel catalysts was observed with a low-temperature (LT) conversion maximum during heating, which disappeared during cooling. Still, it can be restored after temperature-programmed oxidation between the 1<sup>st</sup> and 2<sup>nd</sup> run.<sup>[5a-d]</sup> Until the temperature reached 130 °C, the only products are acetone coupled with water, indicating an oxidative dehydrogenation pathway.  $\text{CO}_2$  evolution from total oxidation is observed at higher temperatures, accompanied by a decrease in acetone yield in the high-temperature (HT) channel. The restorability of the conversion curves in the 1<sup>st</sup> and 2<sup>nd</sup> run is shown for all catalysts in Figure S4 with very similar profiles. Therefore, further detailed evaluations in the following discussion are based only on the 1<sup>st</sup> run. When co-feeding water in the 3<sup>rd</sup> run, the conversion curves show the same general features of LT and HT reaction channels, but changes in the catalytic profiles are observed and discussed in detail below. Therefore, the activity of the catalysts was compared based on reactivity parameters,<sup>[15]</sup> which are graphically shown in Figure 2 with the example of Co:Fe 64:1. Furthermore, the LT reaction channel is characterized by two factors: the temperature needed to reach 10% conversion ( $T_{10}$ ) during heating and the surface-area normalized 2-propanol consumption rate at 100 °C. On the other hand, the HT channel is characterized by  $T_{10}$  and  $T_{50}$  during cooling and the reaction rate at 200 °C during cooling. In terms of product formation, oxidative dehydrogenation to acetone remains the main reaction pathway in the wet feed. At the same time, the onset of the  $\text{CO}_2$  formation shifts to higher temperatures, and the drop in acetone formation at high temperatures is less pronounced than in the dry feed indicating an additional effect of water on the selectivity.

#### Effect of Fe Doping and Substitution on Gas Phase 2-Propanol Oxidation Activity

2-Propanol conversion curves are shown in Figure 3a for all catalysts. The typical features like the unstable LT activity channel are present in the conversion curves of all different catalyst materials during heating, which is discussed in more detail in the Supporting Information (SI) pages S7 and S8. Corresponding  $\text{O}_2$  conversions with similar trends as 2-propanol are shown in Figure S5g and the product distributions are depicted in Figure S6. A comparative discussion of the catalytic data is conducted here using the conversion-based reactivity parameters  $T_x$  and rates in Figure 3b-f as a function of the experimental cobalt content Co/(Co+Fe) determined by STEM-EDX. The  $T_{10}$  values during heating as an indicator for LT channel activity indicate a general decrease of activity with increasing Fe content seen by a higher  $T_{10}$  value until the Co:Fe ratio of 3:1 (Figure 3b). After further increasing the Fe content, no further negative effect on this activity parameter was observed. However, there is a small promotion by the smallest amount of Fe incorporated into the catalyst seen by a slightly decreased  $T_{10}$  value for Co:Fe 64:1 compared to the pristine  $\text{Co}_3\text{O}_4$ . This coincides with an increase

in the specific surface area of Co:Fe 64:1 compared to the pristine  $\text{Co}_3\text{O}_4$ . In the HT channel, represented by  $T_{10}$  and  $T_{50}$  during cooling, similar trends for both parameters are observed (Figure 3b). Both parameters show a promoting effect of Co:Fe 64:1 and Co:Fe 32:1 with a minimum in the required temperature. The general negative impact of high Fe contents remains present, even though the  $T_{10}$  value for Co:Fe 3:1 during cooling indicates less activity than for  $\text{CoFe}_2\text{O}_4$ .

After all, variation of the Co content below a Co:Fe ratio of 3:1 in the material was not found to have an apparent effect on catalytic conversion. In contrast, a trend of increasing activity with a maximum at the Fe doping level was observed for higher Co content. In the liquid phase oxidation of 2-propanol with  $\text{O}_2$  as the oxidant and in the CO oxidation, no beneficial effect of doping with small amounts of Fe was found on the similar catalysts presented in this study.<sup>[5e, 6]</sup> In contrast, for CO oxidation, Baidya et al. reported activation of  $\text{Co}_3\text{O}_4$  catalysts with Fe doping synthesized via solution combustion. This was discussed as an effect of the  $\text{Fe}^{2+}/\text{Fe}^{3+}$  redox couple since TPR showed that the  $\text{Co}^{3+}-\text{O}$  bonding strength is only slightly higher than  $\text{Fe}^{3+}-\text{O}$ .<sup>[28]</sup> Since coordinatively unsaturated  $\text{Co}^{3+}$  in octahedral sites is considered as the active site in 2-propanol oxidation,<sup>[5e]</sup> especially on 110-oriented spinel surfaces,<sup>[5a]</sup> a positive effect of the increasing ratio of tetrahedrally to octahedrally coordinated Co species seems no reasonable explanation for the activity increase observed for low Fe contents.<sup>[20a]</sup> A beneficial effect of Fe was reported previously in the literature when doping  $\text{Mn}_3\text{O}_4$  spinel catalysts in the reduction of NO with ammonia, attributed to a  $\text{Fe}_{\text{oct}}-\text{O}-\text{Mn}_{\text{tet}}$  site.<sup>[19]</sup> In the OER, the doping effects of Fe on  $\text{Co}_3\text{O}_4$  are extensively reported in the literature.<sup>[20]</sup> From DFT+U calculations, a beneficial effect of Fe doping at an octahedral site on a 001 terminated  $\text{Co}_3\text{O}_4$  spinel A-layer with exposed tetrahedrally coordinated Co was found to lower the overpotential on the electrochemical OER.<sup>[21]</sup> Co:Fe 64:1 is more active than  $\text{Co}_3\text{O}_4$  in terms of  $T_x$  but also has a higher specific surface area and much larger pore volume. Furthermore, the  $\text{CoFe}_2\text{O}_4$  catalyst features a higher BET surface area by a factor of 1.7 than the lowest surface area material. Therefore, rates were calculated and normalized based on the exposed surface area. The weight-normalized 2-propanol consumption rates and the specific surface-area normalized rates are shown in Figure S5c and Figure S5e, respectively. Regarding the rate at 100 °C during heating shown in Figure 3c and representing the LT channel, the beneficial effect of doping  $\text{Co}_3\text{O}_4$  with a low amount of Fe to Co:Fe 64:1 remains valid, and the maximum rate was detected for this catalyst. From the 2-propanol consumption rates at 200 °C during cooling, i.e., the kinetic parameter for the HT channel, the beneficial effect of Fe doping was confirmed for Co:Fe 64:1 and Co:Fe 32:1 as well as the detrimental impact of further increasing the Fe content in the catalyst as shown in Figure 3d.

## RESEARCH ARTICLE

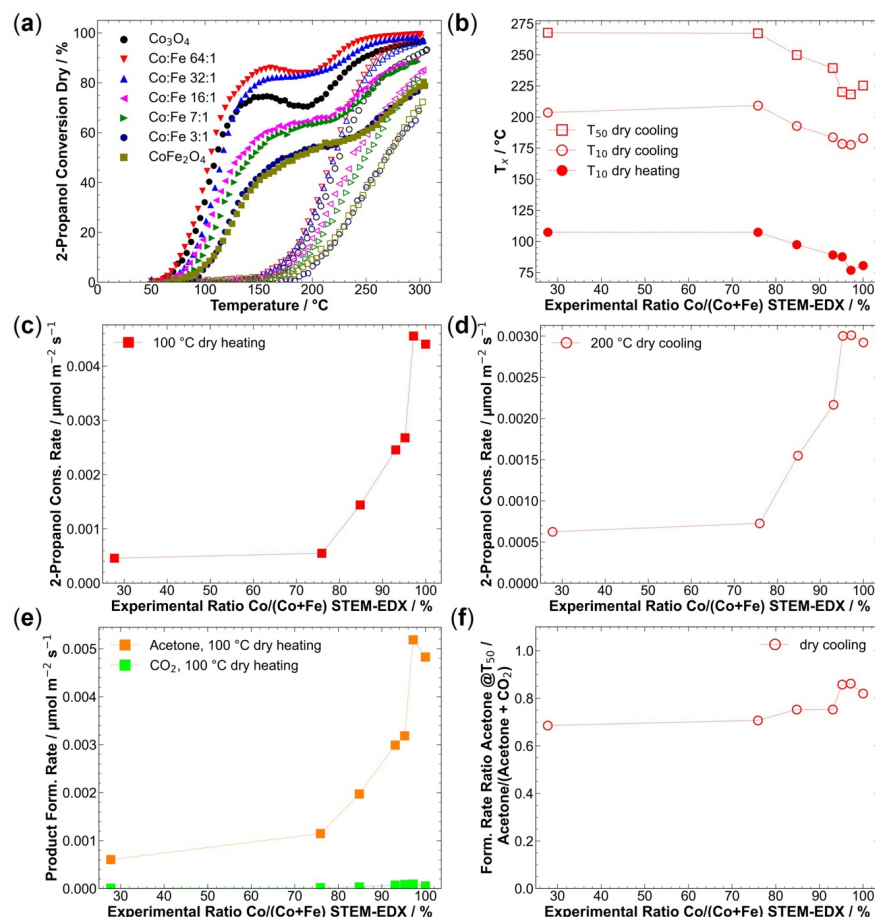


**Figure 3.** (a) 2-Propanol conversions in dry feed. Solid and hollow symbols show data points during heating and cooling, respectively. (b)  $T_{10}$  values during heating and cooling and  $T_{50}$  during cooling in dry feed plotted against the experimental  $\text{Co}/(\text{Co}+\text{Fe})$  derived from STEM-EDX. (c) Surface-area normalized 2-propanol consumption rates at 100 °C during dry feed heating. (d) Surface-area normalized 2-propanol consumption rates at 200 °C during dry feed cooling. (e) Surface-area normalized acetone and  $\text{CO}_2$  formation rates at 200 °C during cooling. (f) Surface-normalized formation ratio of acetone/(acetone+ $\text{CO}_2$ ) at  $T_{50}$  during cooling.

In terms of product formation at 200 °C during cooling, the main products, acetone, and  $\text{CO}_2$  are considered for further comparison to investigate the effect of Co content on the product distribution, as shown in Figure 3e. For  $\text{CoFe}_2\text{O}_4$  and  $\text{Co:Fe 3:1}$ , only minor contents of  $\text{CO}_2$  were detected, while for the other catalysts, a notable amount of  $\text{CO}_2$  formed and increased with increasing Co content in the spinel materials. The acetone formation rate increased with Co content but showed a maximum at  $\text{Co:Fe 32:1}$  and decreased slightly for  $\text{Co:Fe 64:1}$  and  $\text{Co}_3\text{O}_4$ . The formation rate ratio acetone/(acetone+ $\text{CO}_2$ ) at  $T_{50}$  during cooling (HT channel) is shown in Figure 3f and offers a relatively constant ratio in the range of 70-80% selective oxidation. However, interestingly,  $\text{Co:Fe 64:1}$  and  $\text{Co:Fe 32:1}$  show a higher ratio of acetone to  $\text{CO}_2$  and not only a higher conversion. This

indicates that low amounts of Fe promote acetone formation, but not the further total oxidation to  $\text{CO}_2$ .

In summary, all catalyst materials show a more active but non-stable LT activity channel that disappears after the heating cycle with lower catalytic activity on the Fe-rich catalysts. However, the activity does not increase linearly with the Co content. In the LT channel, the presence of a tiny amount of Fe improves the activity compared to the pure  $\text{Co}_3\text{O}_4$ , while in the HT channel, a similar effect is observed on the samples with 1.6 - 4% of Fe content. In addition, the selectivity towards selective oxidation is increased in these doped catalysts compared to the other samples studied in this substitution series.

## RESEARCH ARTICLE

## Effect of Water on the Gas Phase 2-Propanol Oxidation Activity

Wet feed conversion curves for 2-propanol are shown in Figure 4a and corresponding  $\text{O}_2$  conversions in Figure S5h. As discussed in the SI, several more minor differences can be observed in comparing dry and wet feed conversion curves. The

product distribution for all catalysts is shown in Figure S6. These and several more minor differences observed in comparing dry and wet feed conversion are discussed in the SI on pages S7 and S8 in more detail and compared to the recent study on perovskites.<sup>[15]</sup>

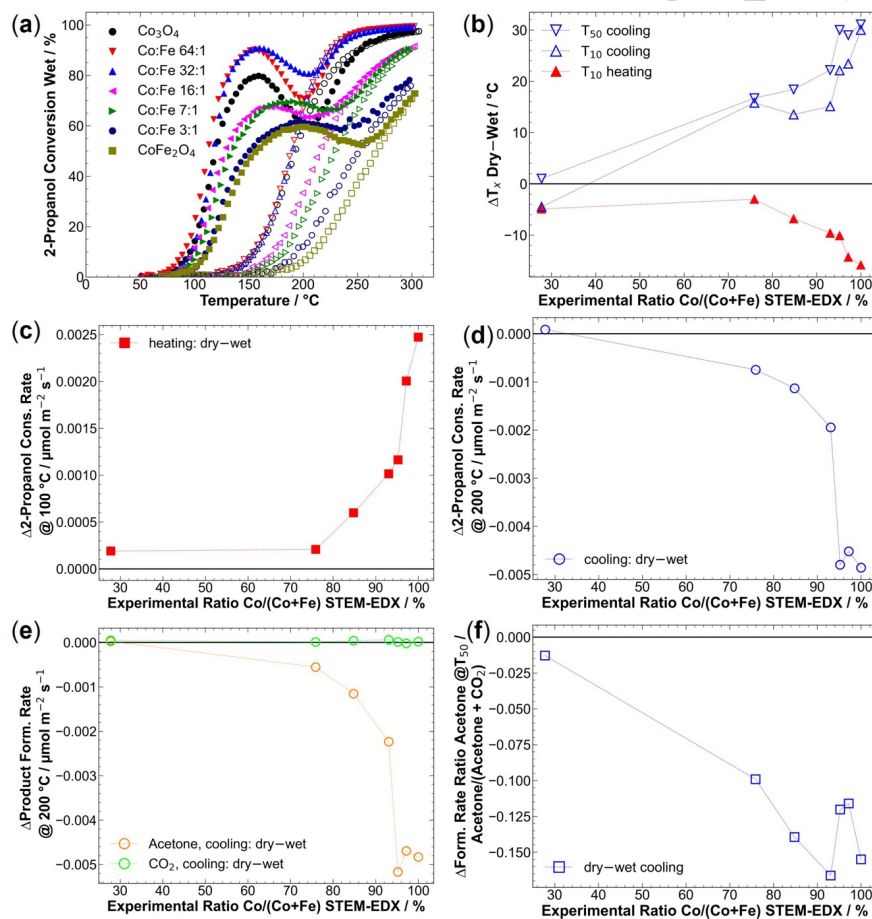


**Figure 4.** (a) 2-Propanol conversions in wet feed. Solid and hollow symbols show data points during heating and cooling, respectively. (b) Differences between  $T_{10}$  during heating cooling and  $T_{50}$  during cooling for  $T_x$  dry, and  $T_x$  wet differences ( $\Delta$ =dry-wet) plotted against the experimental  $\text{Co}/(\text{Co}+\text{Fe})$  derived from STEM-EDX. (c) Differences between surface-area normalized 2-propanol consumption rate at 150 °C during heating. (d) Surface-area normalized 2-propanol consumption rate differences at 200 °C during cooling. (e) Differences in surface-area normalized acetone and  $\text{CO}_2$  formation rates at 200 °C during cooling. (f) The difference in the acetone/(acetone+ $\text{CO}_2$ ) ratio at  $T_{50}$  during cooling.

The differences between dry and wet feed are discussed here based on the aforementioned kinetic parameters and are now newly introduced as the difference between dry and wet feed ( $\Delta$ ) in Figure 4b-f. The  $\Delta T_x$  values in Figure 4b describe the effect of water in the feed. In this regard, a negative  $\Delta T_x$  value indicates lower activity in the wet feed, while a positive value indicates a promoting effect of water on the activity. The absolute values for

dry and wet are shown in Figure S7a. From the  $\Delta T_{10}$  value during heating, a clear negative impact of water on the LT activity is seen, as reported previously for perovskites.<sup>[15]</sup> This shift of the onset of the reaction to higher temperatures can be explained by the competitive adsorption of water on the catalyst surface.<sup>[15, 29]</sup> Consequently, the LT activity observed in the dry feed for increasing Co contents was quenched by the presence of water,

## RESEARCH ARTICLE

and the negative effect became more pronounced. This effect is supported by steady-state data at 160 °C close to the temperature of the LT maximum on  $Co_3O_4$  from a previous study (reproduced and depicted in Figure S8).<sup>[5e]</sup> where a fast deactivation of the LT channel was observed under dry and wet conditions.

In the HT channel based on  $\Delta T_x$  during cooling in Figure 4b, except  $CoFe_2O_4$ , all catalysts are positively affected by the addition of water into the feed gas stream. This beneficial effect increases with increasing Co content in the spinel, although from Co:Fe 32:1 upwards, the effect remains nearly unchanged in  $\Delta T_{50}$ . Inspection of the absolute values in Figure S7 shows that the promoting effect of low amounts of Fe observed in the dry feed is also present in the wet feed for  $T_{50}$ . This observation is also in line with the previous perovskite-based study. The conversion curves during wet cooling were found to shift to lower temperatures for high Co contents compared to the dry feed on the same catalyst. This was interpreted as a boosted activity of the HT channel or a slower deactivation of the Co-rich catalysts under wet conditions.<sup>[15]</sup>

In a liquid phase 2-propanol oxidation study by Falk et al. on the same catalyst materials, no beneficial effect of Fe doping on the spinel catalysts was seen, indicating differences between wet feed gas phase and liquid phase catalysis attributed to different active oxygen species in gas- and liquid phase oxidation.<sup>[5e]</sup> A beneficial effect of Mn doping in  $Co_3O_4$  cubes is reported in the simultaneous oxidations of CO,  $C_3H_6$ , and  $C_3H_8$  in a wet atmosphere.<sup>[12]</sup> It might result from a weakened adsorption strength on the  $Co_3O_4$  surface leading to an improved transfer of surface oxygen species and an improved amount of surface-adsorbed oxygen.<sup>[12]</sup> A similar catalyst activation might be occurring here when introducing Fe into the catalyst. However, water decreases the activity in CO oxidation,<sup>[12]</sup> most probably because of the formation of hydroxyl groups that hinder the oxygen transfer.<sup>[13-14]</sup> This is in line with the evaluation of the conversion profiles in the HT channel during the isothermal dwell period at 300 °C between heating and cooling in Figure S9 under dry conditions (Figure S9a), activity decrease with time is observed for all catalysts. However, under wet conditions (Figure S9b) the activity remains constant over the whole period even though the conversions for the catalysts  $Co_3O_4$ , Co:Fe 64:1, and Co:Fe 32:1 are close to 100%, and conclusions on stability in this regime are not recommended. However, in a comparison between dry and wet in Figure S9c, it becomes obvious that there is a clear difference starting from similar conversions. These results hint at a stabilizing effect of water acting against the catalyst deactivation by most probably preventing the formation of carbonaceous adsorbates. Altogether, this indicates a lower deactivation rate in the wet feed than the dry feed, as also concluded for perovskites.<sup>[15]</sup>

In the gas phase 2-propanol oxidation, Dissanayake et al. report a high tolerance to water vapor on  $Co_3O_4$ , the  $T_{50}$  shifts to higher temperatures by 9 °C.<sup>[30]</sup> In general, lower activity is observed in  $Co_3O_4$ -based spinel catalysts in several reactions under wet conditions, e.g., total propane oxidation,<sup>[4a]</sup> hydrocarbon oxidation,<sup>[12]</sup> and CO oxidation.<sup>[13]</sup> The lowered activity in CO oxidation was related to the adsorption of water on  $Co^{3+}$  sites, which would be consequently not available for the adsorption of other molecules.<sup>[13]</sup> Another possible reason is surface coverage with OH groups.<sup>[13]</sup> Interestingly, on the 110 facet, a CO molecule can additionally be adsorbed on a  $Co^{3+}$  with a preadsorbed OH group and still form  $CO_2$ .<sup>[13]</sup>

Based on rate differences at 100 °C, an increase of water's negative effect on the LT channel's activity becomes apparent with Co content in the spinel as seen in Figure 4c, where positive values refer to a detrimental effect of steam addition. There is a continuous increase of the negative impact of water in the feed on the activity with the Co content. A similar pattern is observed from individual rates at 100 °C in dry and wet feed (Figure S7b), including the promotional effect of Fe in the Co:Fe 64:1 catalyst. However, an increasingly beneficial effect with Co content in the HT reaction channel is observed during cooling at 200 °C, as shown by the negative values in Figure 4d and the difference in Figure S7c. Higher 2-propanol consumption rates were found for all catalysts under wet conditions except for  $CoFe_2O_4$ .

In terms of  $\Delta$  product formation rates shown in Figure 4e, no effect of adding water is observed on the  $CO_2$  formation rate. However, the curve shape of acetone formation is analogous to the 2-propanol consumption, which shows that the higher activity under wet conditions originates from the 2-propanol oxidative dehydration and not from the promotion of the total oxidation. Thus, the yields of acetone as the selective oxidation product are higher in the wet feed. When looking at the difference between dry and wet in the product formation rate ratio at  $T_{50}$  during cooling (Figure 4f), this positive effect of the co-feeding of water is observed for all catalysts, and the beneficial effect rises with the Co content. However, two catalysts affected by the Fe promotion showing the highest acetone formation ratio under dry conditions, Co:Fe 64:1 and Co:Fe 32:1, are not as positively affected in the  $\Delta$  plots as expected from their Co content. The absolute numbers can explain this in Figure S7e showing that by a combination of the two promoting effects of Fe and water, the 100% selectivity is already obtained and cannot be further increased to reveal the full potential.

In summary, the co-feeding of water has diverse impacts on the selective gas phase oxidation of the studied cobalt based spinel catalysts. For all catalysts, the LT activity is negatively affected by the presence of water due to competitive adsorption. However, the promotional effect of low amounts of Fe observed under dry conditions was confirmed when comparing dry and wet feed values. Under wet conditions, the cooling curves are additionally shifted to lower temperatures than at dry conditions, indicating another promoting effect on conversion and selectivity of water in the HT reaction channel or slower catalyst deactivation. This effect was found to scale with the cobalt content at the surface of the catalysts. A likely reason is that the HT channel is more stable under wet conditions, while under isothermal conditions, the LT channel deactivates similarly fast under dry and wet conditions.

**Analysis of Spent Catalysts**

The spent catalysts were investigated via TEM, TEM-EDX, XPS, and EELS after the three-run catalytic cycle protocol after storage in air, and the characterization results are shown in Figure 5a for the ratio of Co/(Co+Fe) post-catalysis. There is still a good agreement between XPS and STEM-EDX with the nominal values in the cation's ratio. However, like the as-prepared state, the experimental ratio for  $CoFe_2O_4$  differs in the near-surface region compared to the bulk counterpart (obtained from STEM-EDX). No clear change in Co/(Co+Fe) ratio was found both in STEM-EDX and XPS for the as-prepared (ap) and post-catalysis (pc) samples.

## RESEARCH ARTICLE

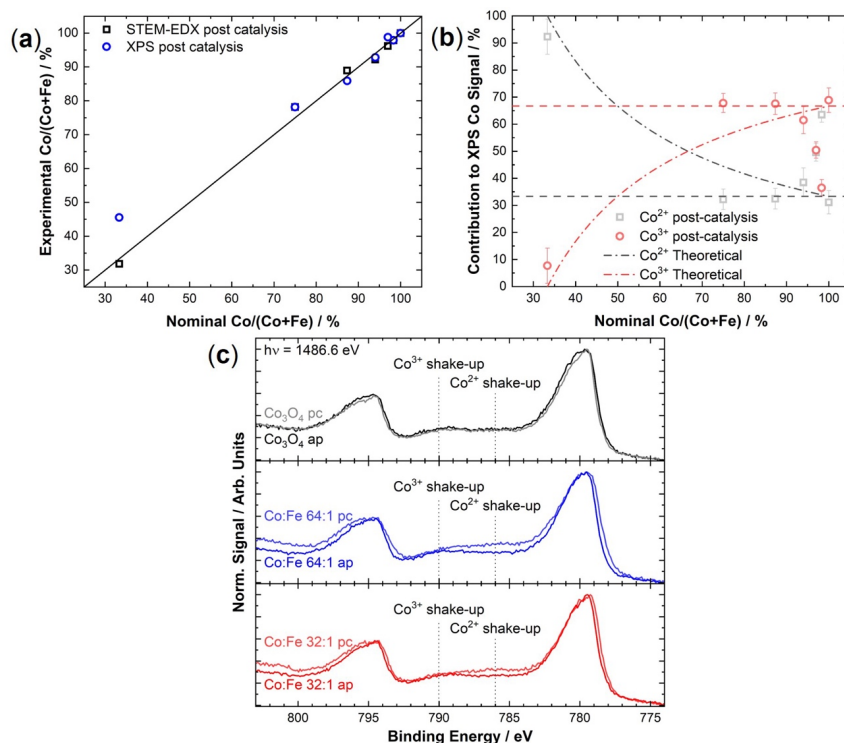


**Figure 5.** (a) Parity plot of experimental Co/(Co+Fe) ratio derived from STEM-EDX and XPS after catalysis. (b) Differences  $\Delta$  as-prepared–post catalysis in the experimental Co/(Co+Fe) ratio derived from STEM-EDX and XPS. The dashed horizontal lines indicate the composition of a normal  $\text{Co}_3\text{O}_4$  spinel with 33.3%  $\text{Co}^{2+}$  and 66.7%  $\text{Co}^{3+}$ . The hyperbole curves show the Co oxidation states under the assumption that Fe exclusively is present as  $\text{Fe}^{3+}$ . (c) Co 2p XP spectra of  $\text{Co}_3\text{O}_4$ , Co:Fe 64:1, and Co:Fe 32:1 in the as-prepared (ap) and post-catalysis (pc) state.

However, a notable effect was observed in the contributions of different cobalt oxide species to the overall Co signal in XPS, as seen in the Co signal contributions post-catalysis in Figure 5c. The individual Co 2p spectra after catalysis are shown in Figure S2. For  $\text{CoFe}_2\text{O}_4$ , no change is observed in the Co oxidation state distribution, it remains mainly  $\text{Co}^{2+}$  as expected for an inverse spinel. With increasing Co content, Co:Fe 3:1 and Co:Fe 7:1 still show the normal spinel composition of oxidation states as in  $\text{Co}_3\text{O}_4$  and therewith no change. However, for Co:Fe 16:1, Co:Fe 32:1, and Co:Fe 64:1, which have 2–7% experimental Fe content, a clear increase of the  $\text{Co}^{2+}$  content at the near-surface regions after catalysis is observed (Figure 5c). In the post-catalysis spectrum, there is a visible  $\text{Co}^{2+}$  shake-up peak whereas there is no change in the  $\text{Co}_3\text{O}_4$  catalyst.<sup>[25]</sup> The higher content of  $\text{Co}^{2+}$  species indicates a higher degree of Co reduction during catalysis if Fe is present in low concentrations which might explain the unexpectedly high activity of Co:Fe 32:1 and Co:Fe 64:1 associated with surface  $\text{Co}^{3+}$  reducibility. From previous work on  $\text{Co}_3\text{O}_4$ , a reduction of the surface to  $\text{CoO}$  was expected since a reduction was seen in comparing XPS before and after reaction and X-ray absorption spectroscopy.<sup>[5c]</sup> The prominent change of the Co:Fe 64:1 catalyst after catalysis is also confirmed by local EELS spectroscopy where it is the only catalyst that shows a

significant change on Co L<sub>3</sub>/L<sub>2</sub> intensity ratio between the as-prepared and post-catalysis state (Figure S3b). In CO oxidation, Baidya et al. reported activation of  $\text{Co}_3\text{O}_4$  catalysts with Fe doping synthesized due to an effect of the  $\text{Fe}^{2+}/\text{Fe}^{3+}$  redox couple since TPR showed that the  $\text{Co}^{3+}$ –O bonding strength is only slightly higher than  $\text{Fe}^{3+}$ –O, which is in line with our results.<sup>[28]</sup> This post-process characterization aligns only partially with the previously reported catalyst reduction as the reason for the LT activity loss in the studied particles.<sup>[5a–d]</sup> Therefore, also the formation of adsorbates on the surface must play an essential role in the deactivation mechanism of the LT channel. TEM images of  $\text{Co}_3\text{O}_4$  as prepared are shown in Figure 6a and Figure 6b, images post catalysis in Figure 6c and Figure 6d. As seen from comparing the images with lower magnification, the nanowire structure remains intact even after catalysis. The images with higher magnification support this conclusion where indications for surface roughening can be observed as well, which might be due to amorphization and surface reduction, as seen from XPS for catalysts with low Fe contents. These indications are marked with arrows in Figure 6d. The same conclusions are valid for the other catalyst materials, as seen from a comparison of as prepared and post catalysis TEM images for all catalysts in Figure S1.

## RESEARCH ARTICLE

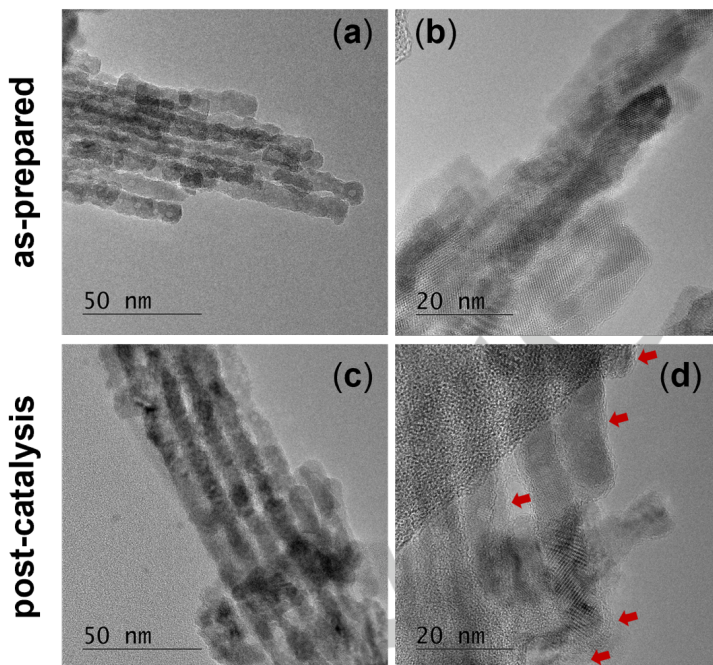


**Figure 6.** TEM micrographs of  $\text{Co}_3\text{O}_4$  before catalysis in different magnifications (a) and (b) and after catalysis in different magnifications (c) and (d).

Altogether, a comparison of XPS and STEM(-EDX) before and after catalysis revealed no significant change in the  $\text{Co}/(\text{Co}+\text{Fe})$  ratio neither in the near-surface region nor in the bulk. However, a reduction of  $\text{Co}^{3+}$  species to  $\text{Co}^{2+}$  species is seen from XPS analysis for catalysts with low Fe amounts. The reduction might be accompanied by surface roughening seen in TEM images after catalysis. However, the overall nanowire morphology of the SBA-15 templated catalyst remains undamaged during catalysis. These conclusions need to be taken with care as the ex-situ analysis cannot account for reversible changes. In addition, the change of surface properties due to the contact of the spent catalyst with air during the transfer from the reactor to analytical instruments (TEM and XPS) cannot be excluded. Irrespective of these uncertainties, the comprehensive ex-situ materials analysis suggests that the bulk composition, particle morphology, and structure of the catalysts remain largely unchanged throughout catalysis even under wet conditions. This is considered an important prerequisite for the knowledge-based synthesis of  $\text{Co}_{3-x}\text{Fe}_x\text{O}_4$  spinels for low-temperature liquid phase oxidation catalysis.

### Conclusion

A series of  $\text{Co}_{3-x}\text{Fe}_x\text{O}_4$  spinel catalysts was synthesized via the nanocasting route and tested in the gas phase 2-propanol oxidation in dry and wet conditions, i.e., without and with water vapor in the gas feed stream, respectively. The typical spinel

catalyst activity behavior of a highly active but non-stable low-temperature and a less active but stable high-temperature channel was found. A beneficial effect of Fe substitution ( $\leq 4\%$ ) was found under dry and wet conditions. Water always affects the activity negatively on the low-temperature channel but has a promoting effect on the high-temperature channel. This promoting effect can be correlated with a lower speed of activity decay during an isothermal experiment. Furthermore, water addition favors the selective oxidation of 2-propanol. Transmission electron microscopy and energy-dispersive X-ray spectroscopy reveal the structural and chemical stability of the bulk of the nanocasted catalysts throughout catalysis, even under wet conditions. Also, using X-ray photoelectron spectroscopy and electron energy loss spectroscopy, no compositional change during catalysis and no clear correlation between the  $\text{Co}^{2+}/\text{Co}^{3+}$  ratio and Co content in the spinels was found neither before nor after the reaction, except for very low Fe contents. Fe substitution at the doping level, i.e.,  $\leq 4\%$  showed beneficial effect in the reducibility of the near-surface Co species which correlated with the enhanced catalytic activities compared to the  $\text{Co}_3\text{O}_4$ . The comparative characterization and catalytic study on the whole sample series have shown an empirical composition-activity correlation that reliably revealed two promoting effects of Fe substitution at the doping level and water co-feeding. On this basis, forthcoming work can be designed to investigate and understand these phenomena.

## RESEARCH ARTICLE

## Experimental Section

## Synthesis and Sample Preparation

Catalyst materials with controlled mesostructure were prepared by the nanocasting route according to the previous report.<sup>[26]</sup> In brief, cobalt and iron precursors (Co:Fe atomic ratio of 100:0, 64:1, 32:1, 16:1, 7:1, 3:1, and 1:2) were prepared by dissolving a stoichiometric amount of  $\text{Co}(\text{NO}_3)_2 \cdot 6\text{H}_2\text{O}$  and  $\text{Fe}(\text{NO}_3)_3 \cdot 9\text{H}_2\text{O}$  (Sigma Aldrich, ACS reagent grade, 99.5% purity) in pure ethanol. The calculated concentration of precursor solution was 0.8 M. The precursor solutions were then impregnated into the pore system of the SBA-15 (that was aged at 100 °C) template by the two-step wet impregnation method (15% total pore filling). For the first impregnation step, a mixture of precursor solution and template was stirred for 2 h. Then the composites were dried in the oven at 50 °C overnight. The first calcination was at 250 °C for 4 h (ramping rate 2 °C min<sup>-1</sup>). The same impregnation procedure was applied for the second step; however, the final calcination was carried out at 500 °C for 6 h with the intermediate dwell at 250 °C for 4 h (ramping rate 2 °C min<sup>-1</sup>). As an exception, a slower ramping rate (1 °C min<sup>-1</sup>) was applied for calcining  $\text{CoFe}_2\text{O}_4$  to avoid the formation of hematite phase ( $\alpha\text{-Fe}_2\text{O}_3$ ) in the final product. SBA-15 template was then leached out with a 2 M KOH solution at 70 °C. After four washing cycles and centrifugation in distilled water, the final product was dried in the oven at 80 °C overnight. The materials were pressed and sieved into a sieve fraction of 250 – 355 µm for catalytic tests and the smaller sieve fraction <250 µm was used for the analytics.

## Catalyst Characterization

X-ray photoelectron spectroscopy (XPS) measurements were performed using a VersaProbe II (ULVAC-Phi, Chanhassen, USA). All the XPS spectra were referenced to the C 1s peak. Casa XPS was used to analyze the spectra. A dual-beam charge neutralization scheme using an electron flood gun with slow-moving  $\text{Ar}^+$  ions was employed to counter any charging effects. To identify the  $\text{Co}^{2+}$  and  $\text{Co}^{3+}$  ratios, we fitted the Al K<sub>α</sub> spectra of the Co 2p by using the peak shapes from a  $\text{Co}^{2+}$  (CoO) reference from the literature<sup>[25]</sup> and a  $\text{Co}^{3+}$  reference from  $\text{MgCo}_2\text{O}_4$  material, whose synthesis is published elsewhere.<sup>[26]</sup> For the set of samples with a non-negligible Fe Auger peak – samples CoFe 7:1, 3:1 and  $\text{CoFe}_2\text{O}_4$  – this peak's position, shape, and intensity were modeled from reference  $\text{Fe}_2\text{O}_3$  spectra and included in the fitting of the Co 2p spectra. The key fit parameters were the intensities of the reference peaks. To calculate the Co:Fe ratios, we measured the Co and Fe 2p with Mg K<sub>α</sub> light to circumvent the Auger-XPS overlapping problem of these two elements occurring with Al K<sub>α</sub> radiation.

High-resolution scanning transmission electron microscopy (STEM) studies were carried out on a Jeol JEM 2200 fs microscope (Akishima, Japan) equipped with a probe-side Cs-corrector operated at 200 kV acceleration voltage. Micrographs were taken in conventional bright field mode. In addition, EDX elemental mappings were acquired with an X-Max 100 detector (Oxford Instruments, Abingdon, United Kingdom). EELS spectra have been acquired using the JEOL omega filter and a Gatan Ultrascan 1000 camera. The FWHM of the zero-loss peak was 1.4 eV. To improve signal-to-noise ratio ten consecutive spectra with 2 s acquisition time have been acquired and summed. The Co L<sub>3</sub>/L<sub>2</sub> intensity ratio was determined after power-law background correction and normalization by integration in the respective peak areas using HyperSpy.<sup>[31]</sup>

## Catalytic Gas Phase 2-Propanol Oxidation

The measurements were performed in a home-built apparatus consisting of a gas dosing unit (HovaGAS N G6 VOC-S, IAS GmbH, Germany) and a Tube Furnace MTF 10/25/130 (Carbolite Gero, Neuhausen, Germany), which is placed in a heating cabinet Thermocenter TC100 (SalvisLab, Rotkreuz, Switzerland). The reaction mixture, either going through or bypassing the reactor, was analyzed on a downstream dual-carrier gas

Fusion Micro GC (Inficon GmbH, Bad Ragaz, Switzerland) equipped with four separation modules (2x Rt-Molsieve 5A, 1x Stabilwax DB, 1x Rt-Q-Bond). 100 mg of the catalyst (sieve fraction of 250 – 355 µm) was placed in a quartz reactor with an inner diameter of 8 mm.

The test protocol consisted of three runs performed under the same temperature program. Only the reactive gas mixture was changed between the runs. Before each run, temperature-programmed oxidation (TPO) up to 300 °C was performed at a flow rate of 50 mL min<sup>-1</sup> with an O<sub>2</sub> concentration of 10% (balanced in N<sub>2</sub>), the heating rate was set to 3 °C min<sup>-1</sup>. The maximum temperature was kept constant for 2 h. Afterward, the temperature was cooled down to 50 °C with a heating rate of 3 °C min<sup>-1</sup>. The temperature was kept constant for 65 min. During the first 20 min, the remaining O<sub>2</sub> was purged out by N<sub>2</sub> (100 mL min<sup>-1</sup>). In the last 45 min, the reaction mixture was purged to stabilize the MFC flows. Afterward, the temperature was increased to 300 °C in the reaction mixture with a heating rate of 1 K min<sup>-1</sup> up and held constant for 1 h. After the isothermal dwell, the temperature was cooled down to 50 °C with a heating rate of 1 K min<sup>-1</sup> in the reaction mixture. Before starting the next TPO, the temperature was maintained for 10 min under a flow of 100 mL min<sup>-1</sup> N<sub>2</sub>. The reaction mixture consisted of 0.168% 2-propanol and 0.195% O<sub>2</sub> balanced in N<sub>2</sub> (dry mixture) for the first two runs and 0.175% 2-propanol, 0.195% O<sub>2</sub>, and 1.86% H<sub>2</sub>O in N<sub>2</sub> for the third run (wet mixture). The flow rate was kept constant at 100 mL min<sup>-1</sup>.

## Acknowledgements

This work was funded by the Deutsche Forschungsgemeinschaft (DFG, German Research Foundation) – 388390466 – TRR 247 within the projects A1 and C1. MB and SN gratefully acknowledge the financial support from the Mercator Research Center Ruhr (MERCUR, Pe-2018-0034). HT thanks Max Planck Society for the basic funding. We acknowledge support from the Open Access Publication Fund of the University of Duisburg-Essen. Open Access funding was enabled and organized by Projekt DEAL.

**Keywords:** 2-Propanol • Cobalt Iron Oxide • Gas Phase • Oxidation • Spinel Phases

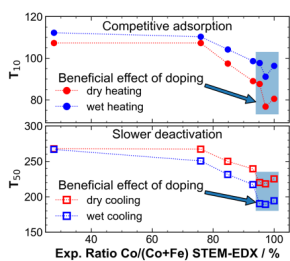
- [1] a) M. S. Kamal, S. A. Razzak, M. M. Hossain, *Atmos. Environ.* **2016**, *140*, 117-124; b) Z. Zhang, Z. Jiang, W. Shangguan, *Catal. Today* **2016**, *264*, 270-278.
- [2] a) G. A. El-Shobaky, M. M. Selim, I. F. Hewaidy, *Surf. Technol.* **1980**, *10*, 55-63; b) S. A. Singh, G. Madras, *Appl. Catal., A* **2015**, *504*, 463-475; c) D. Gu, C. J. Jia, C. Weidenthaler, H. J. Bongard, B. Spliethoff, W. Schmidt, F. Schüth, *J. Am. Chem. Soc.* **2015**, *137*, 11407-11418; d) H. Tuysuz, M. Comotti, F. Schüth, *Chem. Commun. (Cambridge, U. K.)* **2008**, 4022-4024; e) Y. B. Yu, T. Takei, H. Ohashi, H. He, X. L. Zhang, M. Haruta, *J. Catal.* **2009**, *267*, 121-128.
- [3] a) W. Hu, J. Lan, Y. Guo, X.-M. Cao, P. Hu, *ACS Catal.* **2016**, *6*, 5508-5519; b) F. Zasada, J. Grybos, E. Budiyanto, J. Janas, Z. Sojka, *J. Catal.* **2019**, *371*, 224-235; c) F. Zasada, J. Janas, W. Piskorz, M. Gorczyńska, Z. Sojka, *ACS Catal.* **2017**, *7*, 2853-2867.
- [4] a) W. Zhang, P. Anguita, J. Díez-Ramírez, C. Descorme, J. L. Valverde, A. Giroir-Fendler, *Catalysts* **2020**, *10*; b) G. Chai, W. Zhang, L. F. Liotta, M. Li, Y. Guo, A. Giroir-Fendler, *Appl. Catal., B* **2021**, 298.
- [5] a) T. Falk, S. Anke, H. Hajiyani, S. Saddeler, S. Schulz, R. Pentcheva, B. X. Peng, M. Muhler, *Catal. Sci. Technol.* **2021**, *11*, 7552-7562; b) S. Anke, T. Falk, G. Bendt, I. Sinev, M. Havecker, H. Antoni, I. Zegkinoglou, H. Jeon, A. Knop-Gericke, R. Schlögl, B. Roldan Cuanya, S. Schulz, M. Muhler, *J. Catal.* **2020**, *382*, 57-68; c) S. Anke, G. Bendt, I. Sinev, H. Hajiyani, H. Antoni, I. Zegkinoglou, H. Jeon, R. Pentcheva, B. Roldan Cuanya, S. Schulz, M. Muhler, *ACS Catal.* **2019**, *9*, 5974-5985; d) K. Friedel Ortega, S. Anke, S. Salamon, F. Özcan, J. Heese, C. Andronescu, J. Landers, H. Wende, W. Schuhmann, M. Muhler, T. Lunkenbein, M.

## RESEARCH ARTICLE

- Behrens, *Chem. Eur. J.* **2017**, *23*, 12443-12449; e) T. Falk, E. Budiyanto, M. Dreyer, C. Pflieger, D. Waffel, J. Büker, C. Weidenthaler, K. F. Ortega, M. Behrens, H. Tüysüz, M. Muhler, B. Peng, *ChemCatChem* **2021**, *13*, 2942-2951.
- [6] M. Dreyer, A. Rabe, E. Budiyanto, K. Friedel Ortega, S. Najafishirtari, H. Tüysüz, M. Behrens, *Catalysts* **2021**, *11*, 1312.
- [7] F. Zasada, W. Piskorz, J. Janas, E. Budiyanto, Z. Sojka, *J. Phys. Chem. C* **2017**, *121*, 24128-24143.
- [8] Y. Liu, Y. Peng, M. Naschitzki, S. Gewinner, W. Schollkopf, H. Kuhlenbeck, R. Pentcheva, B. Roldan Cuanya, *Angew. Chem. Int. Ed.* **2021**, *60*, 16514-16520.
- [9] L. Hu, Q. Peng, Y. Li, *J. Am. Chem. Soc.* **2008**, *130*, 16136-16137.
- [10] Q. Ren, S. Mo, R. Peng, Z. Feng, M. Zhang, L. Chen, M. Fu, J. Wu, D. Ye, *J. Mater. Chem. A* **2018**, *6*, 498-509.
- [11] L. Lukashuk, N. Yigit, R. Rameshan, E. Kolar, D. Teschner, M. Havecker, A. Knop-Gericke, R. Schlögl, K. Föttinger, G. Rupprechter, *ACS Catal.* **2018**, *8*, 8630-8641.
- [12] J. Bae, D. Shin, H. Jeong, C. Choe, Y. Choi, J. W. Han, H. Lee, *ACS Catal.* **2021**, *11*, 11066-11074.
- [13] H. F. Wang, R. Kavanagh, Y. L. Guo, Y. Guo, G. Z. Lu, P. Hu, *Angew. Chem. Int. Ed.* **2012**, *51*, 6657-6661.
- [14] J. Bae, D. Shin, H. Jeong, B.-S. Kim, J. W. Han, H. Lee, *ACS Catal.* **2019**, *9*, 10093-10100.
- [15] M. Dreyer, D. Cruz, U. Hagemann, P. Zeller, M. Heidelmann, S. Salamon, J. Landers, A. Rabe, K. F. Ortega, S. Najafishirtari, H. Wende, N. Hartmann, A. Knop-Gericke, R. Schlögl, M. Behrens, *Chem. Eur. J.* **2021**, *27*, 17127-17144.
- [16] B. Shi, Z. Zhang, Y. Liu, J. Su, X. Liu, X. Li, J. Wang, M. Zhu, Z. Yang, J. Xu, Y.-F. Han, *J. Catal.* **2020**, *381*, 150-162.
- [17] E. Hema, A. Manikandan, M. Gayathri, M. Durka, S. A. Antony, B. R. Venkatraman, *J. Nanosci. Nanotechnol.* **2016**, *16*, 5929-5943.
- [18] S. Wójcik, G. Grzybek, P. Stelmachowski, Z. Sojka, A. Kotarba, *Catalysis* **2019**, *10*.
- [19] Z. Liu, G. Sun, C. Chen, K. Sun, L. Zeng, L. Yang, Y. Chen, W. Wang, B. Liu, Y. Lu, Y. Pan, Y. Liu, C. Liu, *ACS Catal.* **2020**, *10*, 6803-6809.
- [20] a) E. Budiyanto, M. Q. Yu, M. M. Chen, S. DeBeer, O. Rüdiger, H. Tüysüz, *ACS Appl. Energy Mater.* **2020**, *3*, 8583-8594; b) T. Grewe, X. Deng, H. Tüysüz, *Chem. Mater.* **2014**, *26*, 3162-3168; c) K. Min, M. Hwang, S. E. Shim, D. Lim, S.-H. Baeck, *Chem. Eng. J.* **2021**, *424*.
- [21] Y. Peng, H. Hajipani, R. Pentcheva, *ACS Catal.* **2021**, *11*, 5601-5613.
- [22] D. Waffel, E. Budiyanto, T. Porske, J. Büker, T. Falk, Q. Fu, S. Schmidt, H. Tüysüz, M. Muhler, B. X. Peng, *Mol. Catal.* **2020**, *498*, 111251.
- [23] D. Waffel, B. Alkan, Q. Fu, Y. T. Chen, S. Schmidt, C. Schulz, H. Wiggers, M. Muhler, B. Peng, *ChemPlusChem* **2019**, *84*, 1155-1163.
- [24] X. T. Wang, T. Ouyang, L. Wang, J. H. Zhong, T. Ma, Z. Q. Liu, *Angew. Chem. Int. Ed.* **2019**, *58*, 13291-13296.
- [25] a) M. C. Blesinger, B. P. Payne, A. P. Grosvenor, L. W. M. Lau, A. R. Gerson, R. S. C. Smart, *Appl. Surf. Sci.* **2011**, *257*, 2717-2730; b) T. Mathew, N. R. Shiju, K. Sreekumar, B. S. Rao, C. S. Gopinath, *J. Catal.* **2002**, *210*, 405-417; c) J. Yang, H. Liu, W. N. Martens, R. L. Frost, *J. Phys. Chem. C* **2010**, *114*, 111-119; d) P. N. Anantharamaiah, P. A. Joy, *Phys. Chem. Chem. Phys.* **2016**, *18*, 10516-10527.
- [26] A. Rabe, J. Büker, S. Salamon, A. Koul, U. Hagemann, J. Landers, K. Friedel Ortega, B. Peng, M. Muhler, H. Wende, W. Schuhmann, M. Behrens, *Chem. Eur. J.* **2021**, *27*, 17038-17048.
- [27] a) Z. L. Wang, J. S. Yin, Y. D. Jiang, *Micron* **2000**, *31*, 571-580; b) Y. Zhao, T. E. Feltes, J. R. Regalbuto, R. J. Meyer, R. F. Klie, *J. Appl. Phys.* **2010**, *108*; c) H. Tan, J. Verbeeck, A. Abakumov, G. Van Tendeloo, *Ultramicroscopy* **2012**, *116*, 24-33; d) Z. Zhang, *Ultramicroscopy* **2007**, *107*, 598-603.
- [28] T. Baidya, T. Murayama, P. Bera, O. V. Safonova, P. Steiger, N. K. Katiyar, K. Biswas, M. Haruta, *J. Phys. Chem. C* **2017**, *121*, 15256-15265.
- [29] R. Zhang, H. Almandari, S. Kalaignanme, *Appl. Catal. B* **2007**, *72*, 331-341.
- [30] S. Dissanayake, N. Wasalathanthri, A. Shirazi Amin, J. He, S. Poges, D. Rathnayake, S. L. Suib, *Appl. Catal. A* **2020**, *590*.
- [31] F. de la Peña, E. Prestat, V. T. Fauske, P. Burdet, J. Lähnemann, T. Furnival, P. Jokubauskas, M. Nord, T. Ostasevicius, K. E. MacArthur, D. N. Johnstone, M. Sarahan, T. Aarholt, J. Taillon, pquinn-dls, V. Migunov, A. Eljarrat, J. Caron, T. Poon, S. Mazzucco, C. Francis, B. Martineau,

RESEARCH ARTICLE

Entry for the Table of Contents



Mixed Co and Fe spinel catalysts were tested in the gas phase oxidation of 2-propanol and a beneficial effect of doping on the activity was found. When adding water to the gas stream, the activity at low temperatures during heating decreases due to competitive adsorption, while also the deactivation speed decreases which leads to a higher activity during cooling.

ORCID:

Maik Dreyer [0000-0001-8158-3946](#)  
Ulrich Hagemann [0000-0002-1880-6550](#)  
Markus Heidelmann [0000-0002-6153-6103](#)  
Eko Budiyanto [0000-0001-6184-8863](#)  
Nicolas Cosanne  
Klaus Friedel Ortega  
Sharif Najafishirvari [0000-0003-2121-7439](#)  
Nils Hartmann [0000-0001-6804-514X](#)  
Harun Tüysüz  
Malte Behrens [0000-0003-3407-5011](#)

## 9. Summary and Outlook

In this thesis, the determination of composition-activity correlations is a unifying concept on perovskite and spinel catalysts in oxidation catalysis in all chapters. The first focus was the synthesis of perovskite materials via co-precipitation and thermal decomposition of precursor materials. The materials were only synthesized phase-pure as an orthorhombic perovskite up to a nominal Co content of 30%. A three-phase mixture of orthorhombic perovskite, rhombohedral perovskite, and cubic spinel formed at higher Co content. As another pillar, spinel materials were synthesized either by Anna Rabe from the group of Prof. Dr. Malte Behrens at the University of Duisburg-Essen or by Eko Budiyanto in the group of PD Dr. Harun Tüysüz at the Max Planck Institute for Coal Research in Mülheim/Ruhr, and both material families have been tested in the gas phase oxidation of CO and 2-propanol. The phase-pure perovskite materials were tested in addition to the electrochemical OER. Depending on the specific research question, the materials were characterized by selected methods out of AAS, XRD, N<sub>2</sub> physisorption followed by BET and BJH analysis, FTIR, XPS, NAP XPS, (*operando*) DRIFTS, magnetometry, Mössbauer spectroscopy, TEM, STEM, energy dispersive X-ray spectroscopy (EDX), SEM and TPR.

In the phase-pure perovskites, a distortion of the MO<sub>6</sub> octahedrons with increasing Co content was observed, which affects the strength of the M–O bond. If only 5% Co is incorporated into the structure, there is a pronounced increase in CO oxidation activity. However, the activity increase does not continue linearly with increasing the Co content further. Instead, a strong correlation between the LT reduction peak in TPR and the CO oxidation activity was found. Perovskite reducibility is therefore more decisive for the activity than the nominal composition. *Operando* DRIFTS revealed the formation of surface carbonates during the surface exposition to the reaction mixture consisting of CO and O<sub>2</sub>. The number of carbonates formed decreased with increasing Co content, while the CO<sub>2</sub> formation increased. From this, we conclude that more stable carbonates are formed on Fe rich materials. In the cyclic CO oxidation on spinel catalysts, a strong effect of the (meso)structure on the activity of Co<sub>3</sub>O<sub>4</sub> catalysts was found. Especially, the formation of ROS is dependent on the morphology and decreases with increasing particle size and decreasing BET surface area, which shows a negative effect of the exposure of high-indexed surface facets on ROS formation. A steady activity decay was found with increasing Fe content in the materials in terms of composition. However, the activity increase compared to different runs was the most pronounced for Fe containing catalysts which means that Fe might contribute to ROS formation during pretreatment.

The application of phase-pure perovskites in the electrochemical OER confirmed an activity boost with the incorporation of a small amount of Co into the materials. However,

the LaFeO<sub>3</sub> material exposes the highest double-layer capacitance. This hints towards an intrinsic activity increase with Co present in the spinels. The activity increase with Co content was nonmonotonic, as observed in CO oxidation. The positive effect and nonmonotonic behavior were also confirmed by DFT+U calculations on BO<sub>2</sub>-terminated materials. The theoretically used termination was also found in the catalyst powder, as resolved in TEM(-EDX). Furthermore, the calculations reveal that deprotonation of the \*OH species is the potential limiting step and that in the studied materials also surrounding sites are active in the catalytic cycle. Therefore, a cooperative effect of Co and Fe in OER catalysis is assumed with a contribution of sub-surface layers.

In the gas phase 2-propanol oxidation, the effects of composition and water were investigated on perovskite and spinel catalysts. In the case of the perovskites, DRIFTS analysis revealed that the formation of acetone might be dependent on the surface coverage with 2-propanol and disappears at high coverages. The 2-propanol consumption, acetone formation, and CO<sub>2</sub> formation curves were fitted to generate parametrized data like temperatures to reach 10% and 50% conversion ( $T_{10}$  and  $T_{50}$ ) for the comparison of the different catalyst materials. By this means, also in the third reaction, a pronounced activity increase was found when Co is present in comparison to LaFeO<sub>3</sub>. Co was therefore proven to be catalytically more active than Fe. Again, no monotonic trend of the activity with Co content was observed even though the addition of Co has a positive effect on the activity. However, the behavior of LT and HT activity channels reported before by Anke et al. and Falk et al. on spinels was also found in the perovskite catalysts.<sup>22,23,28,32,33,120</sup> Water in the feed has a negative impact on the LT activity channel due to competitive adsorption but a positive effect on the HT activity channel parameters for catalysts with more than 15% Co in the perovskite structure. However, steady-state experiments showed that the Co-containing catalysts deactivate slower in wet feed than dry feed. From *operando* NAP-XPS a reduction of Co<sup>3+</sup> to Co<sup>2+</sup> was observed at 200 °C in dry and wet conditions. However, more hydroxide and carbonate species are observed under wet conditions in the O 1s spectra. In the C 1s spectra, a high amount of adsorbed carbon was observed, which explains the catalyst deactivation. In post-mortem analysis of the catalytic measurements, a diffusion of the A-cations to the catalyst surface is observed, which might be another reason for catalyst deactivation apart from Co reduction and carbonaceous species formation.

In spinel 2-propanol oxidation, a positive effect of doping with Fe in the low content range ( $\leq 4\%$ ) was found in the HT and LT activity channel, which also remains present during wet feed experimentation. In wet feed, again, an adverse effect was found on the LT track due to competitive adsorption, while except for CoFe<sub>2</sub>O<sub>4</sub>, there was a positive impact of the water admixture in the feed. In contrast to the perovskites, close to the maximum of the LT channel, the steady-state on Co<sub>3</sub>O<sub>4</sub> is reached in similar time in dry and wet conditions. However, during 1 h isothermal holding time at 300 °C in the HT

channel, the activity decreases in dry feed while there is no activity decrease in wet feed. This indicates a slower deactivation rate in the wet feed. In the post-mortem analysis, a  $\text{Co}^{3+}$  surface reduction to  $\text{Co}^{2+}$  was especially observed for the catalysts that show a beneficial effect of low amounts of Fe present, which indicates that reducibility plays a major role with the presence of Fe. In terms of morphology, the mesostructure remained intact.

A comparison of spinels and perovskites based on six reactivity parameters is shown in Figure 9.1 with the joint x-axis of surface-near Co/(Co+Fe) determined by XPS. In Figure 9.1a the  $T_{10}$  value is shown during dry heating, in Figure 9.1b  $T_{10}$  is shown during wet heating, in Figure 9.1c  $T_{50}$  during dry cooling, in Figure 9.1d  $T_{50}$  during wet cooling, in Figure 9.1e the difference dry–wet ( $\Delta$ )  $\Delta T_{10}$  during heating, and in Figure 9.1f  $\Delta T_{50}$  during cooling. One main conclusion becomes immediately obvious: The phase-pure perovskites and the spinels together span the whole composition range from Fe rich to Co rich materials. The perovskites are Fe rich, the spinels Co rich.

However, in the  $T_{10}$  values, there is a clear trend of the values in dry and wet feed with the surface near Co content, as seen in Figure 9.1a and Figure 9.1b, respectively, where the structure type changes from perovskite to spinel. In terms of  $T_{50}$  during heating and cooling, shown in Figure 9.1c and Figure 9.1d, still a general trend shows: the more Co, the better the activity. Even though there are some inconsistencies and deviations from a potentially linear trend, the surface-near Co content seems to be the more decisive factor for the catalytic properties than the structure type.

The  $\Delta$  values in Figure 9.1e show a generally negative effect of water on the low temperature activity as seen in  $\Delta T_{10}$  during heating. However, the  $\Delta T_{50}$  during cooling in Figure 9.1f indicates that high amounts of the surface near Co lead to a higher activity during wet cooling compared to dry cooling. For Fe rich materials, the effect is negative on the HT activity. Furthermore, it seems like there might be two decoupled individual trends for spinels and perovskites, which could be explained with the higher relative  $\text{Co}^{3+}$  content in perovskites than in spinels.

In general, Co is the more active transition metal than Fe in perovskite and spinel catalysts due to its better redox properties. However, there are beneficial effects if the two metals are present. In gas phase catalysis, both deactivate due to formation of carbonaceous species, and surface reduction. The activity can be restored upon oxidative treatment. The effect of water on the surface chemistry is complex, but leads to slower deactivation due to more hydroxides and carbonates on the surface.

This thesis is embedded in the research consortium CRC/TRR 247 “Heterogeneous Oxidation Catalysis in the Liquid Phase”. In the framework of the CRC, a comparative study was performed, where gas phase 2-propanol oxidation was used as a screening reaction for many different spinel and perovskite catalysts. The previously discussed individual sample series for spinels and perovskites were subseries of the whole dataset,

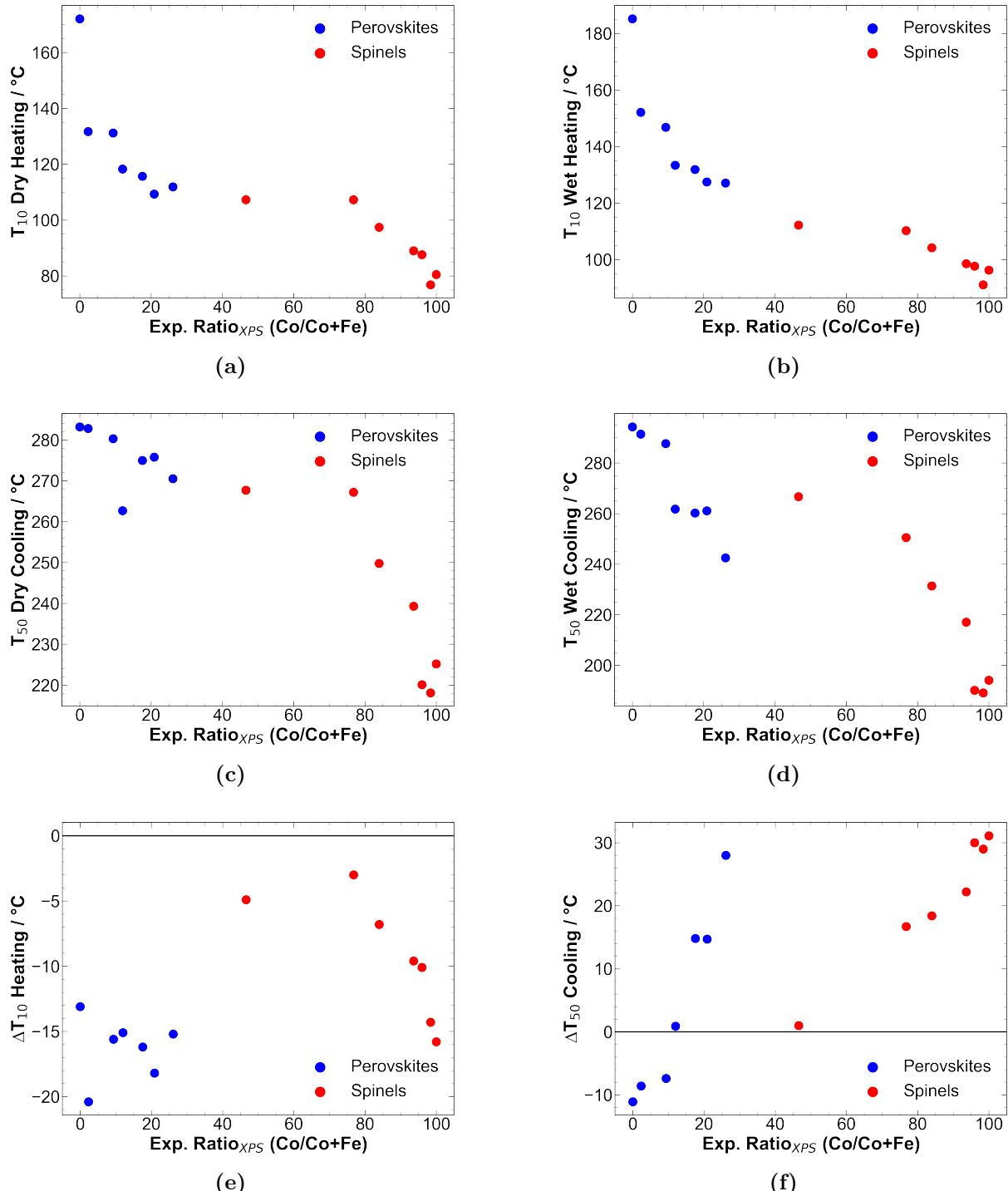


**Figure 9.1:** Comparison of phase-pure perovskites and spinels on different reaction parameters: (a) T<sub>10</sub> dry heating, (b) T<sub>10</sub> wet heating, (c) T<sub>50</sub> dry cooling, (d) T<sub>50</sub> wet cooling, (e)  $\Delta T_{10}$  heating, (f)  $\Delta T_{50}$  cooling

even though a complete evaluation of potential structural parameters such as composition is still in progress. The perovskite materials mentioned above were synthesized by me, the majority of the materials was synthesized by Anna Rabe, Eko Budiyanto, Nicolas Cosanne, Steven Angel, Swen Zerebecki, Sascha Saddeler, and Carsten Placke-Yan.

The current state of the results of the comparative study dataset is shown in Figure 9.2 with the common y-axis of nominal  $\text{Co}^{3+}$  content  $\text{Co}^{3+}/(\text{Co}+\text{Fe})$  derived from the sum formula of the materials and assuming that Fe is always in the oxidation state  $\text{Fe}^{3+}$ . At  $\text{Co}^{3+}/(\text{Co}+\text{Fe})=0$  there are  $\text{LaFeO}_3$  perovskites and many  $\text{CoFe}_2\text{O}_4$  spinels, and at  $\text{Co}^{3+}/(\text{Co}+\text{Fe})=0.67$  there are many different  $\text{Co}_3\text{O}_4$  spinels. These families of the same composition that span another vector of the comparative study: a mesostructure vector like presented in the CO oxidation in Chapter 7 for only three catalysts. However, the structural analysis to resolve the two major non-compositional vectors of the comparative study are not available yet.

The trends discussed before are from the broad comparative study view on the gas phase 2-propanol oxidation in dry and wet feed. As seen in Figure 9.2a, a general decrease of  $T_{10}$  during dry heating is observed, as well as in wet heating, as shown in Figure 9.2b. Interestingly, the  $\text{CoFe}_2\text{O}_4$  and  $\text{Co}_3\text{O}_4$  materials span an extensive range of activity parameters.

At  $T_{50}$  during cooling, there is still a general trend that high amounts of  $\text{Co}^{3+}$  are beneficial for the catalytic activity in dry feed as shown in Figure 9.2c and in wet feed (Figure 9.2c). The negative influence of water on the  $T_{10}$  parameter during heating is confirmed as well throughout nearly the whole dataset with three outlying datapoints, as seen in Figure 9.2e. In Figure 9.2f, the influence of water on the  $T_{50}$  parameter during cooling is shown. In this Figure, the positive effect of water after surpassing a certain amount of Co in the materials becomes evident even though there are three samples without nominal  $\text{Co}^{3+}$  that show an activation. Among the  $\text{Co}_3\text{O}_4$  materials, there is also a material with no positive effect of water on  $T_{50}$  during cooling, which highlights the importance of the catalysts' mesostructure. Comparing Figure 9.1f and Figure 9.2f, it can be seen that the interruption between perovskites and spinels seems to be vanished if the nominal  $\text{Co}^{3+}$  content is used as the x-axis. This supports the hypothesis that not the total Co content but rather the  $\text{Co}^{3+}$  content is responsible for the observed positive effect of water.

In the future, the investigation of catalyst mesostructures should play a significant role in catalysis research since it was shown that mesostructure has an influence on the ROS formation ability and also that the catalysts with different mesostructure but the same nominal composition span a wide width in activity parameters. Therefore, selected catalysts with the same nominal composition should be characterized in-depth, and a detailed kinetic study should be performed that includes dry gas phase 2-propanol oxidation, wet gas phase 2-propanol oxidation, and liquid phase 2-propanol oxidation. In comparing these experiments, there is a lot to learn about the effect of the mesostructure on the reaction kinetics, and several parameters like surface termination, nanoparticle size, or oxidation states on the surface will influence the activity. Furthermore, it is essential to study the selected catalysts by *operando* methods to find changes during the reaction and

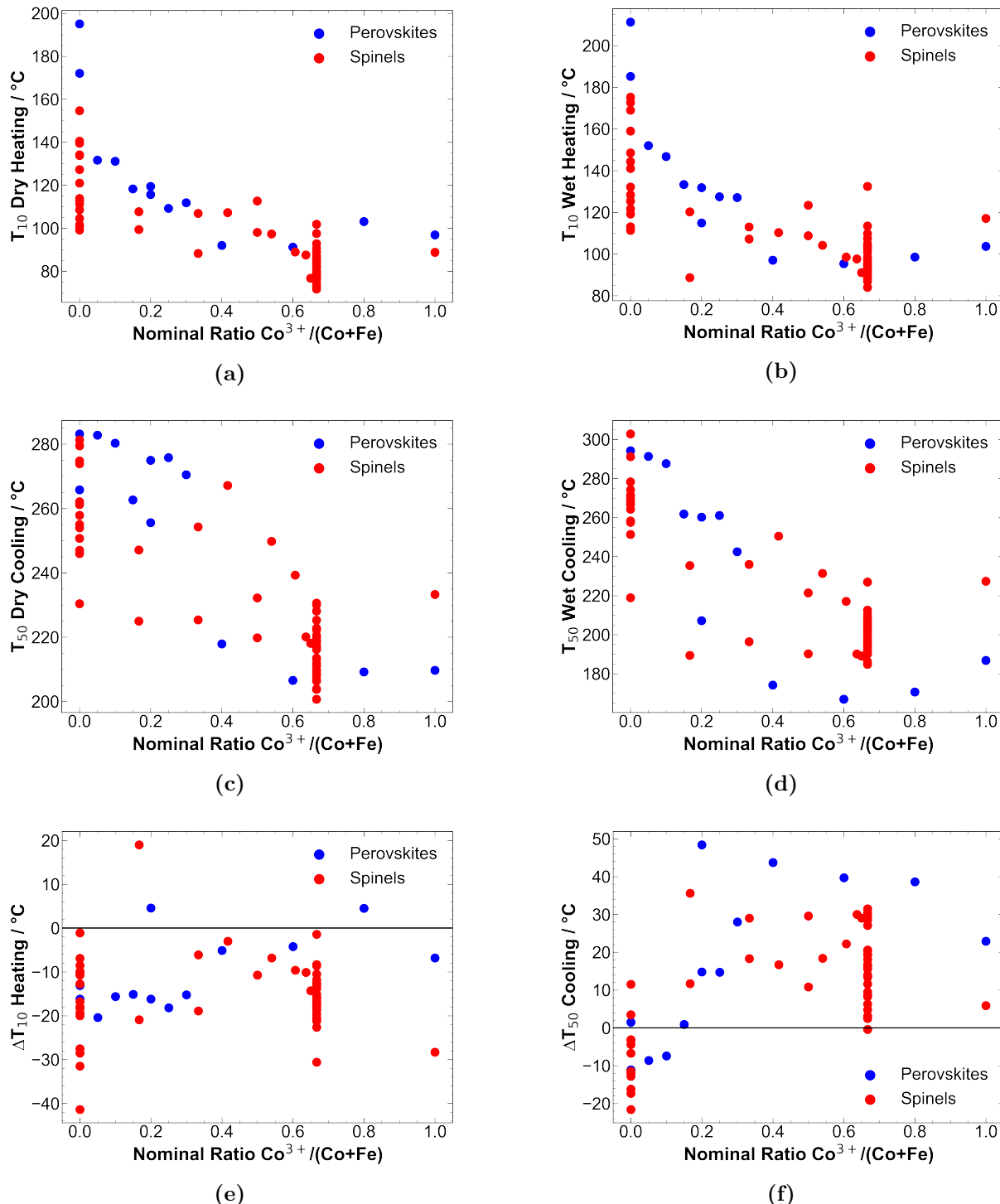


**Figure 9.2:** Comparison of the comparative study dataset on reaction parameters: (a)  $T_{10}$  dry heating, (b)  $T_{10}$  wet heating, (c)  $T_{50}$  dry cooling, (d)  $T_{50}$  wet cooling, (e)  $\Delta T_{10}$  heating, (f)  $\Delta T_{50}$  cooling

the influence of those changes on activity and selectivity patterns. Of course, automated data evaluation and artificial intelligence can and should play a role in evaluating the measurement results and the comparative study dataset. The help of theoretical work will be of great importance within the mechanistic evaluation and the determination of the significance of different mesostructures that come with varying surface terminations. In

addition, a step towards larger and more complex probe molecules than CO and 2-propanol should be made when a deeper mechanistic understanding of the reaction mechanisms on well-characterized catalyst materials is derived. These studies are planned for the second funding period of the CRC/TRR 247 and will be based on the results presented in this thesis.



# 10. Bibliography

- (1) Védrine, J. C.; Fechete, I. *C. R. Chim.* **2016**, *19*, 1203–1225, DOI: 10.1016/j.crci.2015.09.021.
- (2) Najafishirtari, S.; Friedel Ortega, K.; Douthwaite, M.; Pattisson, S.; Hutchings, G. J.; Bondu, C. J.; Tschulik, K.; Waffel, D.; Peng, B.; Deitermann, M.; Busser, G. W.; Muhler, M.; Behrens, M. *Chem. Eur. J.* **2021**, *27*, 16809–16833, DOI: 10.1002/chem.202102868.
- (3) Mehlo makulu, B.; Nguyen, T. T. N.; Delichere, P.; van Steen, E.; Millet, J. M. M. *J. Catal.* **2012**, *289*, 1–10, DOI: 10.1016/j.jcat.2012.01.001.
- (4) Yeo, B. R.; Pudge, G. J. F.; Bugler, K. G.; Rushby, A. V.; Kondrat, S.; Bartley, J.; Golunski, S.; Taylor, S. H.; Gibson, E.; Wells, P. P.; Brookes, C.; Bowker, M.; Hutchings, G. J. *Surf. Sci.* **2016**, *648*, 163–169, DOI: 10.1016/j.susc.2015.11.010.
- (5) Zhang, S.; Li, J. P. H.; Zhao, J.; Wu, D.; Yuan, B.; Hernández, W. Y.; Zhou, W.-J.; He, T.; Yu, Y.; Yang, Y.; Ordomsky, V.; Li, T. *Nano Res.* **2020**, *14*, 479–485, DOI: 10.1007/s12274-020-2651-x.
- (6) Zhang, L.-L.; Hao, K.; Wang, R.-K.; Ma, X.-Q.; Liu, T.; Song, L.; Yu, Q.; Wang, Z.-W.; Zeng, J.-M.; Zeng, R.-C. *Front. Mater. Sci.* **2020**, *14*, 52–61, DOI: 10.1007/s11706-020-0494-8.
- (7) Katryniok, B.; Paul, S.; Dumeignil, F. *ACS Catal.* **2013**, *3*, 1819–1834, DOI: 10.1021/cs400354p.
- (8) Murayama, T.; Katryniok, B.; Heyte, S.; Araque, M.; Ishikawa, S.; Dumeignil, F.; Paul, S.; Ueda, W. *ChemCatChem* **2016**, *8*, 2415–2420, DOI: 10.1002/cctc.201600430.
- (9) Oyama, S. T.; Desikan, A. N.; Hightower, J. W. In *Catalytic Selective Oxidation*; ACS Symposium Series, Vol. 523; American Chemical Society: 1993; Chapter 1, pp 1–14, DOI: 10.1021/bk-1993-0523.ch001.
- (10) Warren, B. K.; Oyama, S. T., *Heterogeneous hydrocarbon oxidation*; ACS Publications: 1996.
- (11) Schlägl, R. *Top. Catal.* **2016**, *59*, 1461–1476, DOI: 10.1007/s11244-016-0684-x.
- (12) Schlägl, R. *Angew. Chem. Int. Ed.* **2015**, *54*, 3465–520, DOI: 10.1002/anie.201410738.
- (13) Gavriilidis, A.; Constantinou, A.; Hellgardt, K.; Hii, K. K.; Hutchings, G. J.; Brett, G. L.; Kuhn, S.; Marsden, S. P. *React. Chem. Eng.* **2016**, *1*, 595–612, DOI: 10.1039/c6re00155f.

- (14) Jagadeesh, R. V.; Junge, H.; Pohl, M. M.; Radnik, J.; Brückner, A.; Beller, M. *J. Am. Chem. Soc.* **2013**, *135*, 10776–82, DOI: 10.1021/ja403615c.
- (15) Jagadeesh, R. V.; Stemmler, T.; Surkus, A. E.; Bauer, M.; Pohl, M. M.; Radnik, J.; Junge, K.; Junge, H.; Brückner, A.; Beller, M. *Nat. Protoc.* **2015**, *10*, 916–26, DOI: 10.1038/nprot.2015.049.
- (16) Chee, S. W.; Lunkenbein, T.; Schlögl, R.; Roldan Cuenya, B. *J. Phys.: Condens. Matter* **2021**, *33*, 153001, DOI: 10.1088/1361-648X/abddfd.
- (17) Rabieah, J.; Briois, V.; Adomeit, S.; La Fontaine, C.; Bentrup, U.; Brückner, A. *Chemistry* **2020**, *26*, 7395–7404, DOI: 10.1002/chem.202000436.
- (18) Negahdar, L.; Parlett, C. M. A.; Isaacs, M. A.; Beale, A. M.; Wilson, K.; Lee, A. F. *Catal. Sci. Technol.* **2020**, *10*, 5362–5385, DOI: 10.1039/d0cy0055j.
- (19) Zaera, F. *J. Catal.* **2021**, *10.1016/j.jcat.2021.08.013*, DOI: 10.1016/j.jcat.2021.08.013.
- (20) Royer, S.; Duprez, D.; Can, F.; Courtois, X.; Batiot-Dupeyrat, C.; Laassiri, S.; Alamdari, H. *Chem. Rev.* **2014**, *114*, 10292–368, DOI: 10.1021/cr500032a.
- (21) Zhao, Q.; Yan, Z.; Chen, C.; Chen, J. *Chem. Rev.* **2017**, *117*, 10121–10211, DOI: 10.1021/acs.chemrev.7b00051.
- (22) Anke, S.; Bendt, G.; Sinev, I.; Hajiyani, H.; Antoni, H.; Zegkinoglou, I.; Jeon, H.; Pentcheva, R.; Roldan Cuenya, B.; Schulz, S.; Muhler, M. *ACS Catal.* **2019**, *9*, 5974–5985, DOI: 10.1021/acscatal.9b01048.
- (23) Falk, T.; Budiyanto, E.; Dreyer, M.; Pflieger, C.; Waffel, D.; Büker, J.; Weidenthaler, C.; Ortega, K. F.; Behrens, M.; Tüysüz, H.; Muhler, M.; Peng, B. *ChemCatChem* **2021**, *13*, 2942–2951, DOI: 10.1002/cctc.202100352.
- (24) Angel, S.; Neises, J.; Dreyer, M.; Friedel Ortega, K.; Behrens, M.; Wang, Y.; Arandiyan, H.; Schulz, C.; Wiggers, H. *AIChE J.* **2019**, *66*, 441, DOI: 10.1002/aic.16748.
- (25) Jansson, J.; Palmqvist, A. E. C.; Fridell, E.; Skoglundh, M.; Osterlund, L.; Thormahlen, P.; Langer, V. *J. Catal.* **2002**, *211*, 387–397, DOI: 10.1006/jcat.2002.3738.
- (26) Wang, X. Y.; Liu, Y.; Zhang, T. H.; Luo, Y. J.; Lan, Z. X.; Zhang, K.; Zuo, J. C.; Jiang, L. L.; Wang, R. H. *ACS Catal.* **2017**, *7*, 1626–1636, DOI: 10.1021/acscatal.6b03547.
- (27) Blasin-Aubé, V.; Belkouch, J.; Monceaux, L. *Appl. Catal., B* **2003**, *43*, 175–186, DOI: 10.1016/s0926-3373(02)00302-8.

- (28) Friedel Ortega, K.; Anke, S.; Salamon, S.; Özcan, F.; Heese, J.; Andronescu, C.; Landers, J.; Wende, H.; Schuhmann, W.; Muhler, M.; Lunkenbein, T.; Behrens, M. *Chem. Eur. J.* **2017**, *23*, 12443–12449, DOI: 10.1002/chem.201702248.
- (29) Büker, J.; Alkan, B.; Chabbra, S.; Kochetov, N.; Falk, T.; Schnegg, A.; Schulz, C.; Wiggers, H.; Muhler, M.; Peng, B. *Chem. Eur. J.* **2021**, *27*, 16912–16923, DOI: 10.1002/chem.202103381.
- (30) Waffel, D.; Alkan, B.; Fu, Q.; Chen, Y. T.; Schmidt, S.; Schulz, C.; Wiggers, H.; Muhler, M.; Peng, B. *ChemPlusChem* **2019**, *84*, 1155–1163, DOI: 10.1002/cplu.201900429.
- (31) Waffel, D.; Budiyanto, E.; Porske, T.; Büker, J.; Falk, T.; Fu, Q.; Schmidt, S.; Tüysüz, H.; Muhler, M.; Peng, B. *X. Mol. Catal.* **2020**, *498*, 111251, DOI: 10.1016/j.mcat.2020.111251.
- (32) Anke, S.; Falk, T.; Bendt, G.; Sinev, I.; Havecker, M.; Antoni, H.; Zegkinoglou, I.; Jeon, H.; Knop-Gericke, A.; Schlögl, R.; Roldan Cuenya, B.; Schulz, S.; Muhler, M. *J. Catal.* **2020**, *382*, 57–68, DOI: 10.1016/j.jcat.2019.12.007.
- (33) Anke, S. Catalytic Activity and Selectivity Patterns of Cobalt-Based Mixed Metal Oxides applied in Selective 2-Propanol Oxidation, Thesis, 2020.
- (34) Védrine, J. C. In *Metal Oxides in Heterogeneous Catalysis*, Védrine, J. C., Ed.; Elsevier: 2018, pp 1–41, DOI: 10.1016/b978-0-12-811631-9.00001-6.
- (35) Védrine, J. C. *ChemSusChem* **2019**, *12*, 577–588, DOI: 10.1002/cssc.201802248.
- (36) Gawande, M. B.; Pandey, R. K.; Jayaram, R. V. *Catal. Sci. Technol.* **2012**, *2*, DOI: 10.1039/c2cy00490a.
- (37) Védrine, J. *Catalysts* **2017**, *7*, DOI: 10.3390/catal7110341.
- (38) Bera, A.; Bullert, D.; Linke, M.; Hasselbrink, E. *J. Phys. Chem. C* **2021**, *125*, 7721–7727, DOI: 10.1021/acs.jpcc.1c01603.
- (39) Granger, P.; Kaliaguine, S.; Pârvulescu, V. I.; Prellier, W., *Perovskites and related mixed oxides: Concepts and applications*; Wiley-VCH Verlag GmbH & Co: Weinheim, Germany, 2016.
- (40) Mitchell, R. H.; Welch, M. D.; Chakhmouradian, A. R. *Mineral. Mag.* **2018**, *81*, 411–461, DOI: 10.1180/minmag.2016.080.156.
- (41) Sangaletti, L.; Depero, L. E.; Allieri, B.; Nunziante, P.; Traversa, E. *J. Eur. Ceram. Soc.* **2001**, *21*, 719–726, DOI: 10.1016/S0955-2219(00)00267-3.
- (42) Haas, O.; Struis, R. P. W. J.; McBreen, J. M. *J. Solid State Chem.* **2004**, *177*, 1000–1010, DOI: 10.1016/j.jssc.2003.10.004.

- (43) Momma, K.; Izumi, F. *J. Appl. Crystallogr.* **2011**, *44*, 1272–1276, DOI: 10.1107/s0021889811038970.
- (44) Nakamura, T.; Misono, M.; Yoneda, Y. *Bull. Chem. Soc. Jpn.* **1982**, *55*, 394–399, DOI: 10.1246/bcsj.55.394.
- (45) Pena, M. A.; Fierro, J. L. *Chem. Rev.* **2001**, *101*, 1981–2017, DOI: 10.1021/cr980129f.
- (46) Manhas, A.; Singh, M.; Hussain, M. I.; Javed, Y.; Sharma, S. K. In *Spinel Nanoferrites*; Topics in Mining, Metallurgy and Materials Engineering, Vol. 1; Springer, Cham: 2021; Chapter Chapter 1, pp 1–40, DOI: 10.1007/978-3-030-79960-1\_1.
- (47) Holleman, A. F.; Wiberg, N.; Wiberg, E., *Lehrbuch der Anorganischen Chemie*; de Gruyter: Berlin, 2007; Vol. 102, DOI: 10.1515/9783110206845.
- (48) Janiak, C.; Meyer, H.-J.; Gudat, D.; Kurz, P., *Riedel Moderne Anorganische Chemie*; Riedel Moderne Anorganische Chemie, Vol. 3; De Gruyter: Berlin, 2018, DOI: 10.1515/9783110441635.
- (49) Kotousova, I.; Polyakov, S. *Kristallografiya* **1972**, *17*, 661–663.
- (50) Tang, G. D.; Ji, D. H.; Yao, Y. X.; Liu, S. P.; Li, Z. Z.; Qi, W. H.; Han, Q. J.; Hou, X.; Hou, D. L. *Appl. Phys. Lett.* **2011**, *98*, DOI: 10.1063/1.3553774.
- (51) Han, Q. J.; Ji, D. H.; Tang, G. D.; Li, Z. Z.; Hou, X.; Qi, W. H.; Liu, S. R.; Bian, R. R. *J. Magn. Magn. Mater.* **2012**, *324*, 1975–1981, DOI: 10.1016/j.jmmm.2012.01.039.
- (52) Hajiyani, H.; Pentcheva, R. *ACS Catal.* **2018**, *8*, 11773–11782, DOI: 10.1021/acscatal.8b00574.
- (53) Peng, Y.; Hajiyani, H.; Pentcheva, R. *ACS Catal.* **2021**, *11*, 5601–5613, DOI: 10.1021/acscatal.1c00214.
- (54) Grasselli, R. K. *Top. Catal.* **2002**, *21*, 79–88, DOI: 10.1023/a:1020556131984.
- (55) Haber, J. In *Handbook of Heterogeneous Catalysis*; Wiley-VCH: Weinheim, Germany, pp 3359–3384, DOI: <https://doi.org/10.1002/9783527610044.hetcat0170>.
- (56) Bielański, A.; Haber, J. *Catal. Rev.* **1979**, *19*, 1–41, DOI: 10.1080/03602457908065099.
- (57) Mars, P.; van Krevelen, D. W. *Chem. Eng. Sci.* **1954**, *3*, 41–59, DOI: 10.1016/s0009-2509(54)80005-4.
- (58) Langmuir, I. *Trans. Faraday Society* **1922**, *17*, DOI: 10.1039/tf9221700621.
- (59) Hinshelwood, C. N. *J. Phys. Chem. A* **1934**, *38*, 855, DOI: 10.1021/j150357a019.
- (60) Eley, D. D.; Rideal, E. K. *Nature* **1940**, *146*, 401–402, DOI: 10.1038/146401d0.
- (61) Rideal, E. K. *Math. Proc. Camb. Philos. Soc.* **1939**, *35*, 130–132, DOI: 10.1017/s030500410002082x.

- (62) Celayasanfiz, A.; Hansen, T.; Sakthivel, A.; Trunschke, A.; Schlögl, R.; Knoester, A.; Brongersma, H.; Looi, M.; Hamid, S. *J. Catal.* **2008**, *258*, 35–43, DOI: 10.1016/j.jcat.2008.05.028.
- (63) Védrine, J. C. *Res. Chem. Intermed.* **2015**, *41*, 9387–9423, DOI: 10.1007/s11164-015-1982-9.
- (64) Polo-Garzon, F.; Wu, Z. *J. Mater. Chem. A* **2018**, *6*, 2877–2894, DOI: 10.1039/c7ta10591f.
- (65) Hattori, H.; Ono, Y. In *Metal Oxides in Heterogeneous Catalysis*, 2018, pp 133–209, DOI: 10.1016/b978-0-12-811631-9.00004-1.
- (66) Dai, W.; Ren, L. In *Handbook of Heterogeneous Catalysis*, Ertl, G., Knözinger, H., Schüth, F., Weitkamp, J., Eds.; Wiley-VCH Verlag GmbH & Co. KGaA: Weinheim, Germany, 2008, p 2159, DOI: 10.1002/9783527610044.hetcat0165.
- (67) Zhang, Y.; Mullins, D. R.; Savara, A. *J. Phys. Chem. C* **2020**, *124*, 3650–3663, DOI: 10.1021/acs.jpcc.9b10797.
- (68) Busca, G. *Ind. Eng. Chem. Res.* **2009**, *48*, 6486–6511, DOI: 10.1021/ie801878d.
- (69) Tanabe, K.; Hölderich, W. F. *Appl. Catal., A* **1999**, *181*, 399–434, DOI: 10.1016/S0926-860X(98)00397-4.
- (70) Bion, N.; Can, F.; Courtois, X.; Duprez, D. In *Metal Oxides in Heterogeneous Catalysis*, 2018, pp 287–353, DOI: 10.1016/b978-0-12-811631-9.00006-5.
- (71) Najjar, H.; Batis, H. *Catal. Rev.* **2016**, *58*, 371–438, DOI: 10.1080/01614940.2016.1198203.
- (72) Hu, L.; Peng, Q.; Li, Y. *J. Am. Chem. Soc.* **2008**, *130*, 16136–16137, DOI: 10.1021/ja806400e.
- (73) Liu, X.; Qiu, G.; Li, X. *Nanotechnology* **2005**, *16*, 3035–3040, DOI: 10.1088/0957-4484/16/12/051.
- (74) Zasada, F.; Gryboś, J.; Indyka, P.; Piskorz, W.; Kaczmarczyk, J.; Sojka, Z. *J. Phys. Chem. C* **2014**, *118*, 19085–19097, DOI: 10.1021/jp503737p.
- (75) Kapteijn, F.; Rodriguez-Mirasol, J.; Moulijn, J. A. *Appl. Catal., B* **1996**, *9*, 25–64, DOI: 10.1016/0926-3373(96)90072-7.
- (76) Zasada, F.; Piskorz, W.; Janas, J.; Gryboś, J.; Indyka, P.; Sojka, Z. *ACS Catal.* **2015**, *5*, 6879–6892, DOI: 10.1021/acscatal.5b01900.
- (77) Zasada, F.; Grybos, J.; Budiyanto, E.; Janas, J.; Sojka, Z. *J. Catal.* **2019**, *371*, 224–235, DOI: 10.1016/j.jcat.2019.02.010.
- (78) Zasada, F.; Gryboś, J.; Hudy, C.; Janas, J.; Sojka, Z. *Catal. Today* **2020**, *354*, 183–195, DOI: 10.1016/j.cattod.2019.03.061.

- (79) Hu, W.; Lan, J.; Guo, Y.; Cao, X.-M.; Hu, P. *ACS Catal.* **2016**, *6*, 5508–5519, DOI: 10.1021/acscatal.6b01080.
- (80) Wang, H.; Sapi, A.; Thompson, C. M.; Liu, F.; Zhrebetsky, D.; Krier, J. M.; Carl, L. M.; Cai, X.; Wang, L. W.; Somorjai, G. A. *J. Am. Chem. Soc.* **2014**, *136*, 10515–20, DOI: 10.1021/ja505641r.
- (81) Royer, S.; Duprez, D.; Kaliaguine, S. *J. Catal.* **2005**, *234*, 364–375, DOI: 10.1016/j.jcat.2004.11.041.
- (82) Freund, H. J.; Meijer, G.; Scheffler, M.; Schlögl, R.; Wolf, M. *Angew. Chem. Int. Ed. Engl.* **2011**, *50*, 10064–94, DOI: 10.1002/anie.201101378.
- (83) Royer, S.; Duprez, D. *ChemCatChem* **2011**, *3*, 24–65, DOI: 10.1002/cctc.201000378.
- (84) Engel, T.; Ertl, G. *J. Chem. Phys.* **1978**, *69*, DOI: 10.1063/1.436666.
- (85) Engel, T.; Ertl, G. In *Adv. Catal.* Eley, D. D., Pines, H., Weez, P. B., Eds.; Academic Press: 1979, pp 1–78, DOI: 10.1016/S0360-0564(08)60133-9.
- (86) Cunningham, D. A. H.; Kobayashi, T.; Kamijo, N.; Haruta, M. *Catal. Lett.* **1994**, *25*, 257–264, DOI: 10.1007/Bf00816305.
- (87) Xie, X.; Li, Y.; Liu, Z. Q.; Haruta, M.; Shen, W. *Nature* **2009**, *458*, 746–9, DOI: 10.1038/nature07877.
- (88) Yu, Y. B.; Takei, T.; Ohashi, H.; He, H.; Zhang, X. L.; Haruta, M. *J. Catal.* **2009**, *267*, 121–128, DOI: 10.1016/j.jcat.2009.08.003.
- (89) Hu, L. H.; Sun, K. Q.; Peng, Q.; Xu, B. Q.; Li, Y. D. *Nano Res.* **2010**, *3*, 363–368, DOI: 10.1007/s12274-010-1040-2.
- (90) Iablokov, V.; Barbosa, R.; Pollefeyt, G.; Van Driessche, I.; Chenakin, S.; Kruse, N. *ACS Catal.* **2015**, *5*, 5714–5718, DOI: 10.1021/acscatal.5b01452.
- (91) Ding, K.; Wang, D.; Yang, P.; Hou, P.; Cheng, X. *RSC Adv.* **2016**, *6*, 16208–16214, DOI: 10.1039/c6ra01092j.
- (92) Singh, S. A.; Madras, G. *Appl. Catal., A* **2015**, *504*, 463–475, DOI: 10.1016/j.apcata.2014.10.024.
- (93) Luo, J.; Meng, M.; Li, X.; Li, X.; Zha, Y.; Hu, T.; Xie, Y.; Zhang, J. *J. J. Catal.* **2008**, *254*, 310–324, DOI: 10.1016/j.jcat.2008.01.007.
- (94) Lukashuk, L.; Föttinger, K.; Kolar, E.; Rameshan, C.; Teschner, D.; Havecker, M.; Knop-Gericke, A.; Yigit, N.; Li, H.; McDermott, E.; Stöger-Pollach, M.; Rupprechter, G. *J. Catal.* **2016**, *344*, 1–15, DOI: 10.1016/j.jcat.2016.09.002.
- (95) Lukashuk, L.; Yigit, N.; Rameshan, R.; Kolar, E.; Teschner, D.; Havecker, M.; Knop-Gericke, A.; Schlögl, R.; Föttinger, K.; Rupprechter, G. *ACS Catal.* **2018**, *8*, 8630–8641, DOI: 10.1021/acscatal.8b01237.

- (96) Lukashuk, L.; Yigit, N.; Li, H.; Bernardi, J.; Föttinger, K.; Rupprechter, G. *Catal. Today* **2019**, *336*, 139–147, DOI: 10.1016/j.cattod.2018.12.052.
- (97) Liu, Y.; Peng, Y.; Naschitzki, M.; Gewinner, S.; Schollkopf, W.; Kuhlenbeck, H.; Pentcheva, R.; Roldan Cuenya, B. *Angew. Chem. Int. Ed.* **2021**, *60*, 16514–16520, DOI: 10.1002/anie.202103359.
- (98) Voorhoeve, R. J.; Johnson D. W., J.; Remeika, J. P.; Gallagher, P. K. *Science* **1977**, *195*, 827–33, DOI: 10.1126/science.195.4281.827.
- (99) Tascón, J. M. D.; Tejuca, L. G. *J. Chem. Soc., Faraday Trans. 1* **1981**, *77*, DOI: 10.1039/f19817700591.
- (100) Tascón, J. M. D.; Fierro, J. L. G.; Tejuca, L. G. *Z. Phys. Chem.* **1981**, *124*, 249–257, DOI: 10.1524/zpch.1981.124.2.249.
- (101) Chan, K. S.; Ma, J.; Jaenicke, S.; Chuah, G. K.; Lee, J. Y. *Appl. Catal., A* **1994**, *107*, 201–227, DOI: 10.1016/0926-860x(94)85156-5.
- (102) Zhang-Steenwinkel, Y.; van der Zande, L. M.; Castricum, H. L.; Bliek, A. *Appl. Catal., B* **2004**, *54*, 93–103, DOI: 10.1016/j.apcatb.2004.02.008.
- (103) Petrolekas, P. D.; Metcalfe, I. S. *J. Catal.* **1995**, *152*, 147–163, DOI: 10.1006/jcat.1995.1069.
- (104) Petrolekas, P. D.; Metcalfe, I. S. *J. Catal.* **1995**, *157*, 545–549, DOI: 10.1006/jcat.1995.1318.
- (105) Pinto, D.; Glisenti, A. *Catal. Sci. Technol.* **2019**, *9*, 2749–2757, DOI: 10.1039/c9cy00210c.
- (106) Gong, J.; Flaherty, D. W.; Yan, T.; Mullins, C. B. *ChemPhysChem* **2008**, *9*, 2461–6, DOI: 10.1002/cphc.200800680.
- (107) Xu, X.; Friend, C. M. *Surf. Sci.* **1992**, *260*, 14–22, DOI: 10.1016/0039-6028(92)90013-v.
- (108) Bürgi, T.; Bieri, M. *J. Phys. Chem. B* **2004**, *108*, 13364–13369, DOI: 10.1021/jp048187u.
- (109) Uvdal, P.; Wiegand, B. C.; Serafin, J. G.; Friend, C. M. *J. Chem. Phys.* **1992**, *97*, 8727–8735, DOI: 10.1063/1.463392.
- (110) Davis, J. L.; Barreau, M. A. *Surf. Sci.* **1988**, *197*, 123–152, DOI: 10.1016/0039-6028(88)90577-8.
- (111) Nondek, L.; Sedláček, J. *J. Catal.* **1975**, *40*, 34–39, DOI: 10.1016/0021-9517(75)90223-7.
- (112) Nondek, L.; Kraus, M. *J. Catal.* **1975**, *40*, 40–45, DOI: 10.1016/0021-9517(75)90224-9.

- (113) Schwab, G. M.; Wandinger, L. Z. *Elektrochem., Ber. Bunsenges. Physikal. Chem.* **1956**, *60*, 929–938, DOI: 10.1002/bbpc.19560600827.
- (114) Sedlacek, J. *J. Catal.* **1976**, *44*.
- (115) Sedláček, J.; Kraus, M. *React. Kinet. Catal. Lett.* **1975**, *2*, 57–63.
- (116) Lokras, S. S.; Deshpande, P. K.; Kuloor, N. R. *Ind. Eng. Chem. Process. Des. Dev.* **1970**, *9*, 293–297, DOI: 10.1021/i260034a022.
- (117) Centeno, M. A.; Paulis, M.; Montes, M.; Odriozola, J. A. *Appl. Catal., A* **2002**, *234*, 65–78, DOI: 10.1016/s0926-860x(02)00214-4.
- (118) Liu, S. Y.; Yang, S. M. *Appl. Catal., A* **2008**, *334*, 92–99, DOI: 10.1016/j.apcata.2007.09.037.
- (119) Dissanayake, S.; Wasalathanthri, N.; Shirazi Amin, A.; He, J.; Poges, S.; Rathnayake, D.; Suib, S. L. *Appl. Catal., A* **2020**, *590*, DOI: 10.1016/j.apcata.2019.117366.
- (120) Falk, T.; Anke, S.; Hajiyani, H.; Saddeler, S.; Schulz, S.; Pentcheva, R.; Peng, B. X.; Muhler, M. *Catal. Sci. Technol.* **2021**, *11*, 7552–7562, DOI: 10.1039/d1cy00944c.
- (121) Jira, R. *Angew. Chem. Int. Ed. Engl.* **2009**, *48*, 9034–7, DOI: 10.1002/anie.200903992.
- (122) Luyben, W. L. *Ind. Eng. Chem. Res.* **2010**, *50*, 1206–1218, DOI: 10.1021/ie901923a.
- (123) Gervasini, A.; Auroux, A. *J. Catal.* **1991**, *131*, 190–198, DOI: 10.1016/0021-9517(91)90335-2.
- (124) Ouqour, A.; Coudurier, G.; Vedrine, J. C. *J. Chem. Soc., Faraday Trans.* **1993**, *89*, 3151–3155, DOI: 10.1039/ft9938903151.
- (125) Lahousse, C.; Bachelier, J.; Lavalle, J.-C.; Lauron-Pernot, H.; Le Govic, A.-M. *J. Mol. Catal.* **1994**, *87*, 329–332, DOI: 10.1016/0304-5102(93)e0232-6.
- (126) Thomasson, P.; Tyagi, O. S.; Knözinger, H. *Appl. Catal., A* **1999**, *181*, 181–188, DOI: 10.1016/s0926-860x(98)00435-9.
- (127) Noller, H.; Thomke, K. *J. Mol. Catal.* **1979**, *6*, 375–392, DOI: 10.1016/0304-5102(79)85013-0.
- (128) Käßner, P.; Baerns, M. *Appl. Catal., A* **1996**, *139*, 107–129, DOI: 10.1016/0926-860x(95)00335-5.
- (129) Weiss, J.; Hoffmann, V. *J. Mol. Struct.* **1990**, *218*, 441–446, DOI: 10.1016/0022-2860(90)80307-6.
- (130) Fiorenza, R.; Bellardita, M.; Palmisano, L.; Scirè, S. *J. Mol. Catal. A: Chem.* **2016**, *415*, 56–64, DOI: 10.1016/j.molcata.2016.01.025.
- (131) Finocchio, E.; Busca, G.; Lorenzelli, V.; Escribano, V. S. *J. Chem. Soc., Faraday Trans.* **1996**, *92*, 1587–1593, DOI: 10.1039/ft9969201587.

- (132) Busca, G.; Daturi, M.; Finocchio, E.; Lorenzelli, V.; Ramis, G.; Willey, R. J. *Catal. Today* **1997**, *33*, 239–249, DOI: 10.1016/s0920-5861(96)00112-5.
- (133) Finocchio, E.; Willey, R. J.; Busca, G.; Lorenzelli, V. *J. Chem. Soc., Faraday Trans.* **1997**, *93*, 175–180, DOI: 10.1039/a605341f.
- (134) Busca, G.; Finocchio, E.; Lorenzelli, V.; Ramis, G.; Baldi, M. *Catal. Today* **1999**, *49*, 453–465, DOI: 10.1016/s0920-5861(98)00441-6.
- (135) Hosseini, S. A.; Niaezi, A.; Salari, D.; Nabavi, S. R. *Ceram. Int.* **2012**, *38*, 1655–1661, DOI: 10.1016/j.ceramint.2011.09.057.
- (136) Hosseini, S. A.; Alvarez-Galvan, M. C.; Fierro, J. L. G.; Niaezi, A.; Salari, D. *Ceram. Int.* **2013**, *39*, 9253–9261, DOI: 10.1016/j.ceramint.2013.05.033.
- (137) Hohner, C.; Ronovský, M.; Brummel, O.; Skála, T.; Šmíd, B.; Tsud, N.; Vorokhta, M.; Prince, K. C.; Mysliveček, J.; Johánek, V.; Lykhach, Y.; Libuda, J. *J. Catal.* **2021**, *398*, 171–184, DOI: 10.1016/j.jcat.2021.04.005.
- (138) Radha, R.; Swamy, C. S. *Surf. Technol.* **1985**, *24*, 157–163, DOI: 10.1016/0376-4583(85)90132-3.
- (139) Kubo, J.; Ueda, W. *Mater. Res. Bull.* **2009**, *44*, 906–912, DOI: 10.1016/j.materresbull.2008.08.013.
- (140) Hosseini, S. A.; Niaezi, A.; Salari, D.; Nabavi, S. R. *J. Taiwan. Inst. Chem. Eng.* **2014**, *45*, 85–91, DOI: 10.1016/j.jtice.2013.04.010.
- (141) Foo, G. S.; Polo-Garzon, F.; Fung, V.; Jiang, D.-e.; Overbury, S. H.; Wu, Z. *ACS Catal.* **2017**, *7*, 4423–4434, DOI: 10.1021/acscatal.7b00783.
- (142) Bao, Z.; Fung, V.; Polo-Garzon, F.; Hood, Z. D.; Cao, S.; Chi, M.; Bai, L.; Jiang, D.-e.; Wu, Z. *J. Catal.* **2020**, *384*, 49–60, DOI: 10.1016/j.jcat.2020.02.014.
- (143) Tan, S.; Gray, M. B.; Kidder, M. K.; Cheng, Y.; Daemen, L. L.; Lee, D.; Lee, H. N.; Ma, Y.-Z.; Doughty, B.; Lutterman, D. A. *ACS Catal.* **2017**, *7*, 8118–8129, DOI: 10.1021/acscatal.7b02417.
- (144) Sapi, A.; Liu, F.; Cai, X.; Thompson, C. M.; Wang, H.; An, K.; Krier, J. M.; Somorjai, G. A. *Nano Lett.* **2014**, *14*, 6727–30, DOI: 10.1021/nl5035545.
- (145) Liu, F. D.; Han, H. L.; Carl, L. M.; Zhrebetskyy, D.; An, K.; Wang, L. W.; Somorjai, G. A. *J. Phys. Chem. C* **2019**, *123*, 7577–7583, DOI: 10.1021/acs.jpcc.8b00405.
- (146) Liu, Y.; Dai, H.; Deng, J.; Li, X.; Wang, Y.; Arandiyan, H.; Xie, S.; Yang, H.; Guo, G. *J. Catal.* **2013**, *305*, 146–153, DOI: 10.1016/j.jcat.2013.04.025.
- (147) Wang, C. B.; Lin, H. K.; Tang, C. W. *Catal. Lett.* **2004**, *94*, 69–74, DOI: 10.1023/B:CATL.0000019333.73968.c6.

- (148) Contractor, R. M.; Horowitz, H. S.; Sisler, G. M.; Bordes, E. *Catal. Today* **1997**, *37*, 51–57, DOI: 10.1016/s0920-5861(96)00257-x.
- (149) Zhang, R.; Alamdari, H.; Kaliaguine, S. *Appl. Catal., B* **2007**, *72*, 331–341, DOI: 10.1016/j.apcatb.2006.10.025.
- (150) Wang, H. F.; Kavanagh, R.; Guo, Y. L.; Guo, Y.; Lu, G. Z.; Hu, P. *Angew. Chem. Int. Ed.* **2012**, *51*, 6657–61, DOI: 10.1002/anie.201108981.
- (151) Bae, J.; Shin, D.; Jeong, H.; Choe, C.; Choi, Y.; Han, J. W.; Lee, H. *ACS Catal.* **2021**, *11*, 11066–11074, DOI: 10.1021/acscatal.1c01666.
- (152) Bae, J.; Shin, D.; Jeong, H.; Kim, B.-S.; Han, J. W.; Lee, H. *ACS Catal.* **2019**, *9*, 10093–10100, DOI: 10.1021/acscatal.9b02920.
- (153) Zhang, W.; Anguita, P.; Díez-Ramírez, J.; Descorme, C.; Valverde, J. L.; Giroir-Fendler, A. *Catalysts* **2020**, *10*, DOI: 10.3390/catal10080865.
- (154) Liu, G.; Dastafkan, K.; Zhao, C. In *Heterogeneous Catalysts*, 2021, pp 533–555, DOI: 10.1002/9783527813599.ch30.
- (155) Crabtree, G. W.; Dresselhaus, M. S.; Buchanan, M. V. *Phys. Today* **2004**, *57*, 39–44, DOI: 10.1063/1.1878333.
- (156) Li, X.; Hao, X.; Abudula, A.; Guan, G. *J. Mater. Chem. A* **2016**, *4*, 11973–12000, DOI: 10.1039/c6ta02334g.
- (157) McCrory, C. C.; Jung, S.; Ferrer, I. M.; Chatman, S. M.; Peters, J. C.; Jaramillo, T. F. *J. Am. Chem. Soc.* **2015**, *137*, 4347–57, DOI: 10.1021/ja510442p.
- (158) Wang, J.; Yue, X.; Yang, Y.; Sirisomboonchai, S.; Wang, P.; Ma, X.; Abudula, A.; Guan, G. *J. Alloys Compd.* **2020**, *819*, DOI: 10.1016/j.jallcom.2019.153346.
- (159) Liang, Q.; Brocks, G.; Bieberle-Hütter, A. *J. Phys. Energy* **2021**, *3*, DOI: 10.1088/2515-7655/abdc85.
- (160) Rossmeisl, J.; Qu, Z. W.; Zhu, H.; Kroes, G. J.; Nørskov, J. K. *J. Electroanal. Chem.* **2007**, *607*, 83–89, DOI: 10.1016/j.jelechem.2006.11.008.
- (161) Seh, Z. W.; Kibsgaard, J.; Dickens, C. F.; Chorkendorff, I.; Norskov, J. K.; Jaramillo, T. F. *Science* **2017**, *355*, DOI: 10.1126/science.aad4998.
- (162) Burstein, G. T. *Corros. Sci.* **2005**, *47*, 2858–2870, DOI: 10.1016/j.corsci.2005.07.002.
- (163) Roger, I.; Shipman, M. A.; Symes, M. D. *Nature Reviews Chemistry* **2017**, *1*, DOI: 10.1038/s41570-016-0003.
- (164) Suntivich, J.; Gasteiger, H. A.; Yabuuchi, N.; Nakanishi, H.; Goodenough, J. B.; Shao-Horn, Y. *Nat. Chem.* **2011**, *3*, 546–50, DOI: 10.1038/nchem.1069.

- (165) Alkan, B.; Cychy, S.; Varhade, S.; Muhler, M.; Schulz, C.; Schuhmann, W.; Wiggers, H.; Andronescu, C. *ChemElectroChem* **2019**, *6*, 4266–4274, DOI: 10.1002/celc.201900168.
- (166) Budiyanto, E.; Yu, M. Q.; Chen, M. M.; DeBeer, S.; Rüdiger, O.; Tüysüz, H. *ACS Appl. Energy Mater.* **2020**, *3*, 8583–8594, DOI: 10.1021/acsaem.0c01201.
- (167) Alkan, B.; Medina, D.; Landers, J.; Heidelmann, M.; Hagemann, U.; Salamon, S.; Andronescu, C.; Wende, H.; Schulz, C.; Schuhmann, W.; Wiggers, H. *ChemElectroChem* **2020**, *7*, 2564–2574, DOI: 10.1002/celc.201902051.
- (168) Rabe, A.; Büker, J.; Salamon, S.; Koul, A.; Hagemann, U.; Landers, J.; Friedel Ortega, K.; Peng, B.; Muhler, M.; Wende, H.; Schuhmann, W.; Behrens, M. *Chem. Eur. J.* **2021**, *27*, 17038–17048, DOI: 10.1002/chem.202102400.
- (169) Seo, M. H.; Park, H. W.; Lee, D. U.; Park, M. G.; Chen, Z. W. *ACS Catal.* **2015**, *5*, 4337–4344, DOI: 10.1021/acscatal.5b00114.
- (170) Monteverde Videla, A. H. A.; Stelmachowski, P.; Ercolino, G.; Specchia, S. *J. Appl. Electrochem.* **2017**, *47*, 295–304, DOI: 10.1007/s10800-016-1040-3.
- (171) Saddeler, S.; Hagemann, U.; Schulz, S. *Inorg. Chem.* **2020**, *59*, 10013–10024, DOI: 10.1021/acs.inorgchem.0c01180.
- (172) Saddeler, S.; Bendt, G.; Salamon, S.; Haase, F. T.; Landers, J.; Timoshenko, J.; Rettenmaier, C.; Jeon, H. S.; Bergmann, A.; Wende, H.; Roldan Cuenya, B.; Schulz, S. *J. Mater. Chem. A* **2021**, *9*, 25381–25390, DOI: 10.1039/d1ta06568h.
- (173) Bergmann, A.; Jones, T. E.; Martinez Moreno, E.; Teschner, D.; Chernev, P.; Gliech, M.; Reier, T.; Dau, H.; Strasser, P. *Nat. Catal.* **2018**, *1*, 711–719, DOI: 10.1038/s41929-018-0141-2.
- (174) Chen, Z.; Kronawitter, C. X.; Yeh, Y.-W.; Yang, X.; Zhao, P.; Yao, N.; Koel, B. E. *J. Mater. Chem. A* **2017**, *5*, 842–850, DOI: 10.1039/c6ta07482k.
- (175) Vojvodic, A.; Norskov, J. K. *Science* **2011**, *334*, 1355–6, DOI: 10.1126/science.1215081.
- (176) Yoo, J. S.; Rong, X.; Liu, Y.; Kolpak, A. M. *ACS Catal.* **2018**, *8*, 4628–4636, DOI: 10.1021/acscatal.8b00612.
- (177) Man, I. C.; Su, H.-Y.; Calle-Vallejo, F.; Hansen, H. A.; Martínez, J. I.; Inoglu, N. G.; Kitchin, J.; Jaramillo, T. F.; Nørskov, J. K.; Rossmeisl, J. *ChemCatChem* **2011**, *3*, 1159–1165, DOI: 10.1002/cctc.201000397.
- (178) Lee, Y. L.; Gadre, M. J.; Shao-Horn, Y.; Morgan, D. *Phys. Chem. Chem. Phys.* **2015**, *17*, 21643–63, DOI: 10.1039/c5cp02834e.
- (179) Rong, X.; Parolin, J.; Kolpak, A. M. *ACS Catal.* **2016**, *6*, 1153–1158, DOI: 10.1021/acscatal.5b02432.

- (180) Tripkovic, V.; Hansen, H. A.; Garcia-Lastra, J. M.; Vegge, T. *J. Phys. Chem. C* **2018**, *122*, 1135–1147, DOI: 10.1021/acs.jpcc.7b07660.
- (181) Mefford, J. T.; Rong, X.; Abakumov, A. M.; Hardin, W. G.; Dai, S.; Kolpak, A. M.; Johnston, K. P.; Stevenson, K. J. *Nature Communications* **2016**, *7*, 11053, DOI: 10.1038/ncomms11053.
- (182) Hwang, J.; Rao, R. R.; Giordano, L.; Katayama, Y.; Yu, Y.; Shao-Horn, Y. *Science* **2017**, *358*, 751–756, DOI: 10.1126/science.aam7092.
- (183) Grimaud, A.; Diaz-Morales, O.; Han, B.; Hong, W. T.; Lee, Y. L.; Giordano, L.; Stoerzinger, K. A.; Koper, M. T. M.; Shao-Horn, Y. *Nat. Chem.* **2017**, *9*, 457–465, DOI: 10.1038/nchem.2695.
- (184) Zhu, Y.; Zhou, W.; Yu, J.; Chen, Y.; Liu, M.; Shao, Z. *Chem. Mater.* **2016**, *28*, 1691–1697, DOI: 10.1021/acs.chemmater.5b04457.
- (185) Duan, Y.; Sun, S.; Xi, S.; Ren, X.; Zhou, Y.; Zhang, G.; Yang, H.; Du, Y.; Xu, Z. J. *Chem. Mater.* **2017**, *29*, 10534–10541, DOI: 10.1021/acs.chemmater.7b04534.
- (186) Dreyer, M.; Krebs, M.; Najafishirtari, S.; Rabe, A.; Friedel Ortega, K.; Behrens, M. *Catalysts* **2021**, *11*, 550, DOI: 10.3390/catal11050550.
- (187) Füngerlings, A.; Koul, A.; Dreyer, M.; Rabe, A.; Morales, D. M.; Schuhmann, W.; Behrens, M.; Pentcheva, R. *Chem. Eur. J.* **2021**, *27*, 17145–17158, DOI: 10.1002/chem.202102829.
- (188) Dreyer, M.; Cruz, D.; Hagemann, U.; Zeller, P.; Heidelmann, M.; Salamon, S.; Landers, J.; Rabe, A.; Ortega, K. F.; Najafishirtari, S.; Wende, H.; Hartmann, N.; Knop-Gericke, A.; Schlögl, R.; Behrens, M. *Chem. Eur. J.* **2021**, *27*, 17127–17144, DOI: 10.1002/chem.202102791.
- (189) Dreyer, M.; Rabe, A.; Budiyanto, E.; Friedel Ortega, K.; Najafishirtari, S.; Tüysüz, H.; Behrens, M. *Catalysts* **2021**, *11*, 1312, DOI: 10.3390/catal11111312.

# A. Appendix

## I. List of Figures

2.1. Projection of the crystal structure of the orthorhombic LaFeO <sub>3</sub> perovskite along the [110] viewing direction, reproduced from ICSD collection code 93611 (a). <sup>41</sup> Projection of the crystal structure of the rhombohedral LaCoO <sub>3</sub> perovskite along the [110] viewing direction, reproduced from ICSD collection code 93611 (b). <sup>42</sup> La ions are shown in blue, Fe ions and their hexagonal oxygen coordination polyhedra are shown in yellow, Co ions and their hexagonal oxygen coordination polyhedra are shown in orange. O ions are shown in red. The images were created with VESTA. <sup>43</sup>	4
2.2. (a) Projection of the crystal structure of the cubic Co <sub>3</sub> O <sub>4</sub> normal spinel along the [024] viewing direction, reproduced from ICSD collection code 9362. <sup>49</sup> (b) Projection of the crystal structure of the cubic Co <sub>3</sub> O <sub>4</sub> normal spinel along the [024] viewing direction and its tetrahedral sites. (c) Projection of the crystal structure of the cubic Co <sub>3</sub> O <sub>4</sub> normal spinel along the [024] viewing direction and its octahedral sites. Co <sup>2+</sup> ions and their tetrahedral oxygen coordination polyhedra are shown in magenta, Co <sup>3+</sup> ions and their octahedral oxygen coordination polyhedra are shown in orange. O ions are shown in red. The image was created with VESTA. <sup>43</sup>	5
2.3. Molecular orbital diagram for di-oxygen O <sub>2</sub> (a), atom orbital diagram for the metal-oxo ion O <sup>-</sup> (b), and for the oxide anion O <sup>2-</sup> (c).	7
2.4. Molecular orbital diagrams for (a) the superoxide anion O <sub>2</sub> <sup>-</sup> and (b) the peroxide anion O <sub>2</sub> <sup>2-</sup> .	8
3.1. Screenshot of the user interface of the BELCAT-B system.	23
3.2. Piping and Instrumentation Diagram of the MultiCat system.	24
9.1. Comparison of phase-pure perovskites and spinels on different reaction parameters: (a) T <sub>10</sub> dry heating, (b) T <sub>10</sub> wet heating, (c) T <sub>50</sub> dry cooling, (d) T <sub>50</sub> wet cooling, (e) ΔT <sub>10</sub> heating, (f) ΔT <sub>50</sub> cooling	118
9.2. Comparison of the comparative study dataset on reaction parameters: (a) T <sub>10</sub> dry heating, (b) T <sub>10</sub> wet heating, (c) T <sub>50</sub> dry cooling, (d) T <sub>50</sub> wet cooling, (e) ΔT <sub>10</sub> heating, (f) ΔT <sub>50</sub> cooling	120

## **II. List of Schemes**

### III. List of Reactions

Reaction (R2.1): Oxygen activation steps . . . . .	8
Reaction (R2.2): CO oxidation . . . . .	11
Reaction (R2.3): CO adsorption . . . . .	12
Reaction (R2.4): Oxygen adsorption . . . . .	12
Reaction (R2.5): Carbon dioxide formation . . . . .	12
Reaction (R2.6): Oxygen adsorption and dissociation . . . . .	13
Reaction (R2.7): CO adsorption . . . . .	13
Reaction (R2.8): Carbonate formation . . . . .	13
Reaction (R2.9): Carbonate decomposition . . . . .	13
Reaction (R2.10): Carbon dioxide desorption . . . . .	13
Reaction (R2.11): Dehydrogenation . . . . .	14
Reaction (R2.12): Oxidative dehydrogenation . . . . .	14
Reaction (R2.13): Dehydration . . . . .	14
Reaction (R2.14): Total Oxidation . . . . .	14
Reaction (R2.15): Oxygen evolution reaction . . . . .	19
Reaction (R2.16): Hydrogen evolution reaction . . . . .	19
Reaction (R2.17): Overall water splitting reaction . . . . .	19
Reaction (R2.18): Hydroxide adsorption . . . . .	20
Reaction (R2.19): Hydrogen abstraction . . . . .	20
Reaction (R2.20): First hydroxide addition . . . . .	20
Reaction (R2.21): Second hydroxide addition and decomposition . . . . .	20

## **IV. SI: The Effect of Co Incorporation on the CO Oxidation Activity of $\text{LaFe}_{1-x}\text{Co}_x\text{O}_3$**

The main text to this Supporting Information is shown in Chapter 4.

**The effect of Co incorporation on the CO oxidation activity of  
 $\text{LaFe}_{1-x}\text{Co}_x\text{O}_3$  perovskites**

**Supplementary Materials**

Maik Dreyer<sup>1</sup>, Moritz Krebs<sup>1,2</sup>, Sharif Najafishirtari<sup>1</sup>, Anna Rabe<sup>1</sup>, Klaus Friedel Ortega<sup>2</sup>,  
Malte Behrens<sup>1,2,3\*</sup>

<sup>1</sup> Faculty for Chemistry, Inorganic Chemistry, University of Duisburg-Essen, 45141 Essen,  
Germany

<sup>2</sup> Institute for Inorganic Chemistry, Christian-Albrechts-Universität zu Kiel, 24118 Kiel,  
Germany

<sup>3</sup> CENIDE, Center for Nanointegration, University of Duisburg-Essen, 47057 Duisburg,  
Germany

\*Corresponding author: [mbehrens@ac.uni-kiel.de](mailto:mbehrens@ac.uni-kiel.de)

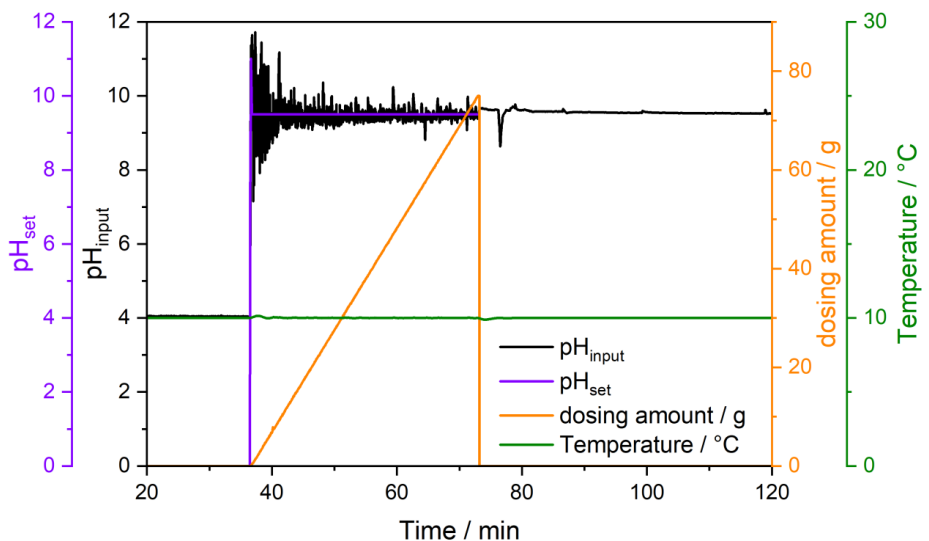


Figure S1: Synthesis protocol of sample  $x = 0.00$ .

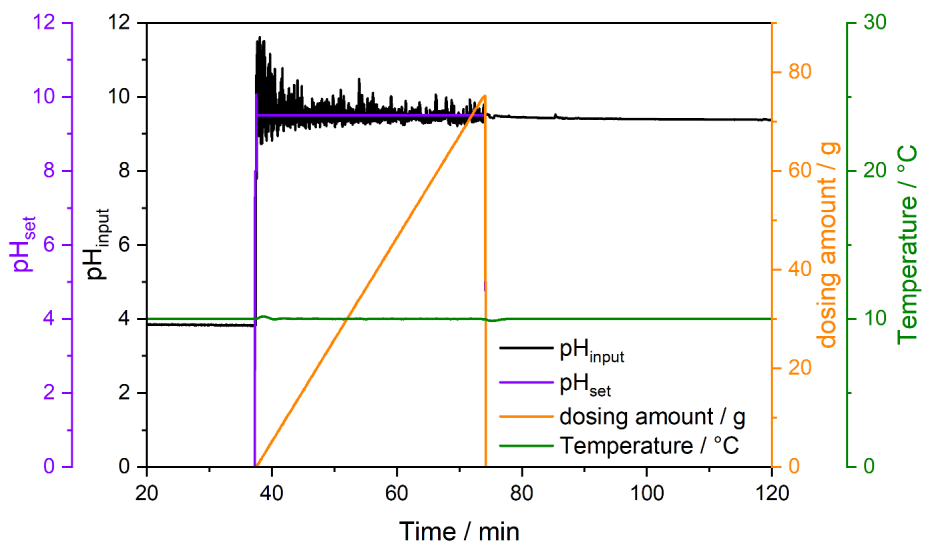
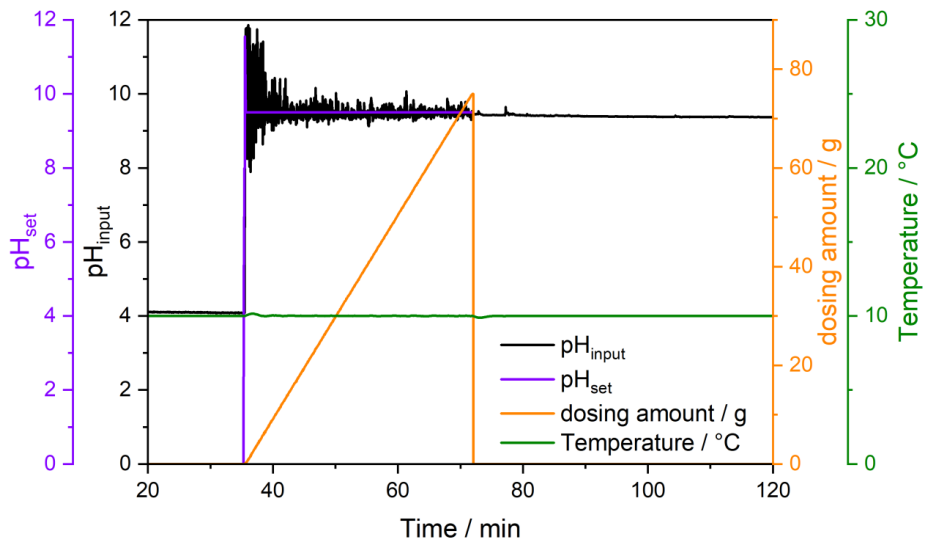
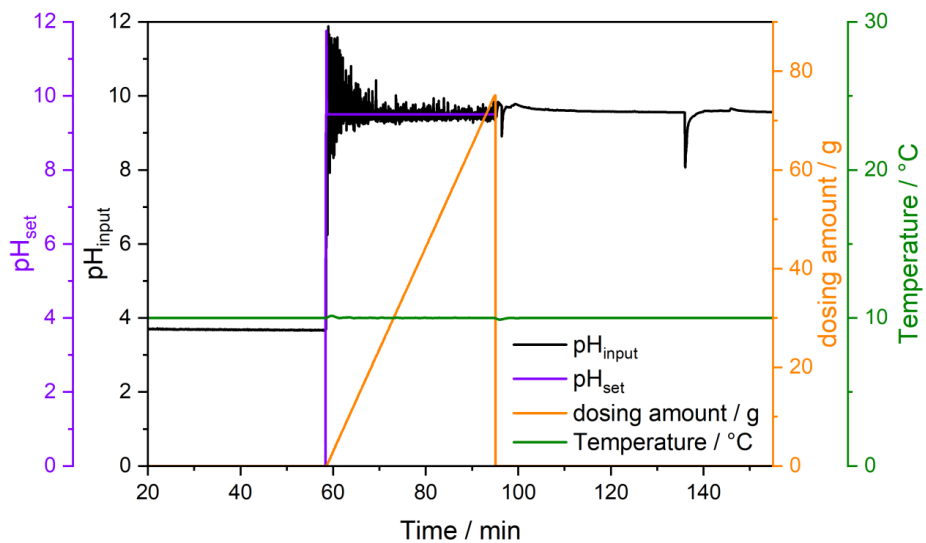


Figure S2. Synthesis protocol of sample  $x = 0.05$ .

Figure S3. Synthesis protocol of sample  $x = 0.10$ .Figure S4. Synthesis protocol of sample  $x = 0.15$ .

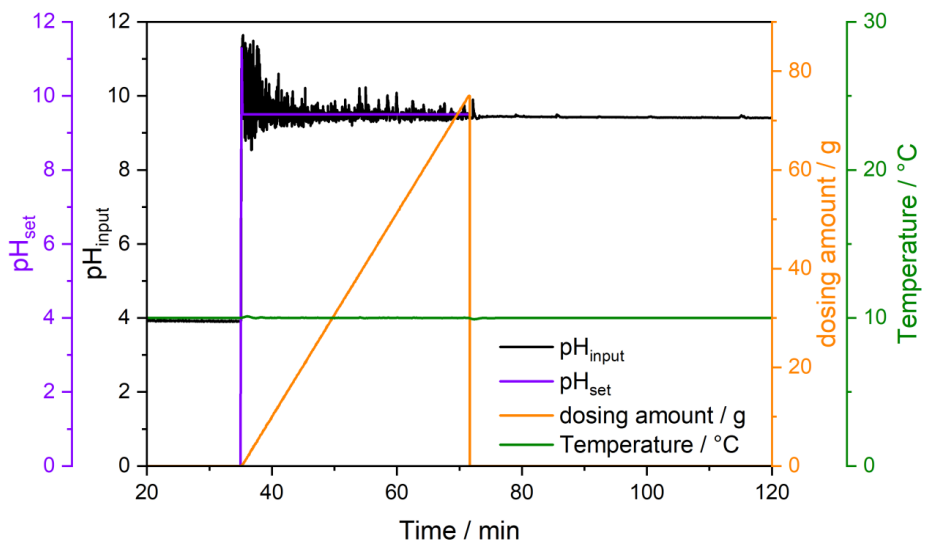


Figure S5. Synthesis protocol of sample  $x = 0.20$ .

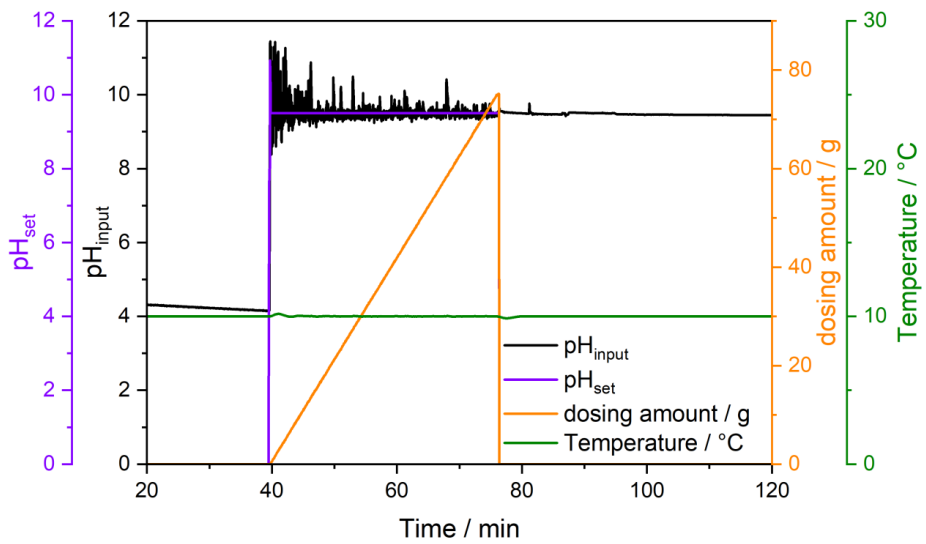


Figure S6. Synthesis protocol of sample  $x = 0.25$ .

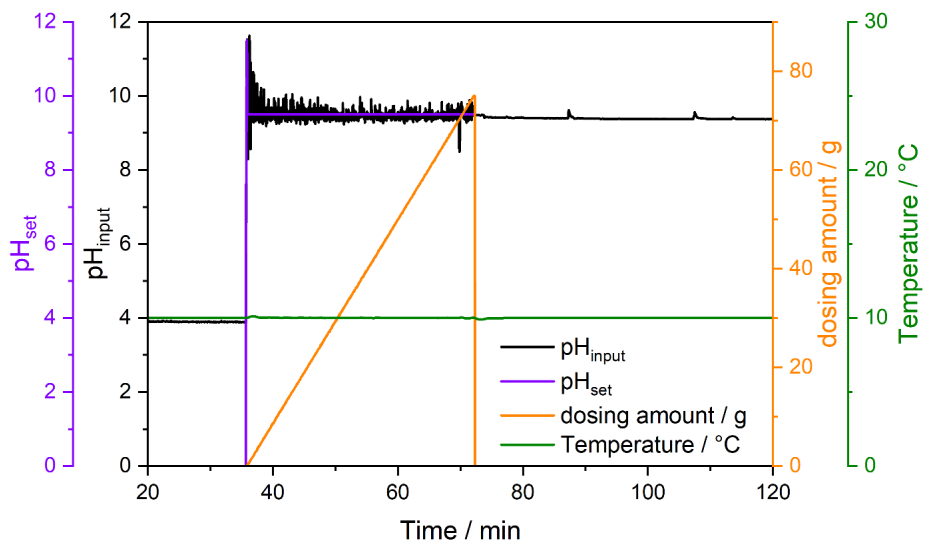


Figure S7. Synthesis protocol of sample  $x = 0.30$ .

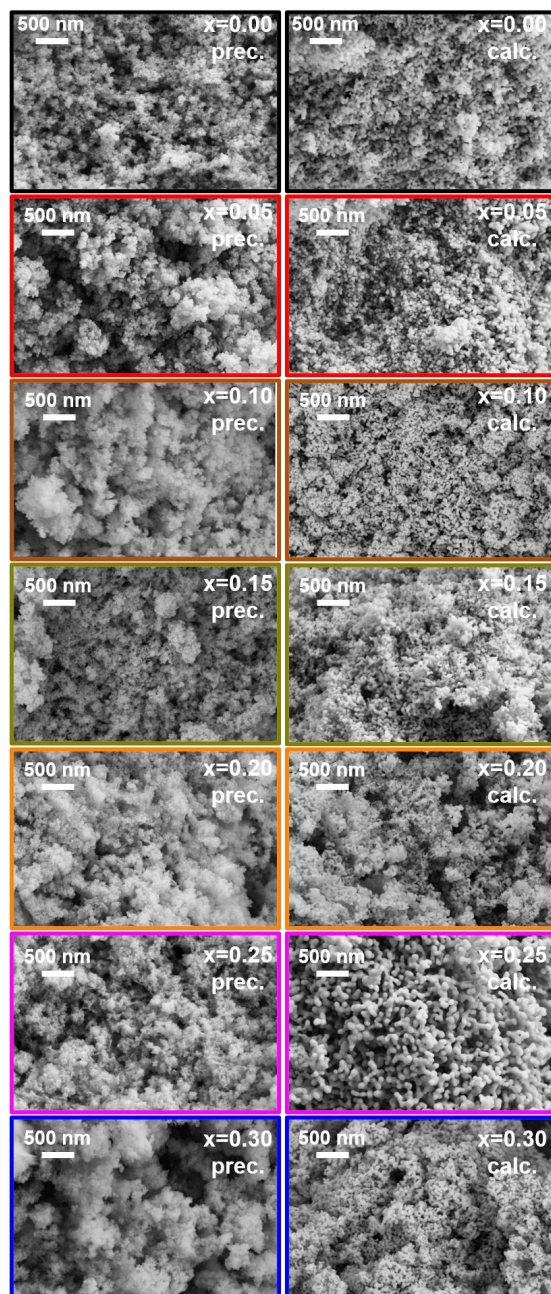


Figure S8. SEM images of the precursors (left column) and the calcined materials (right column).

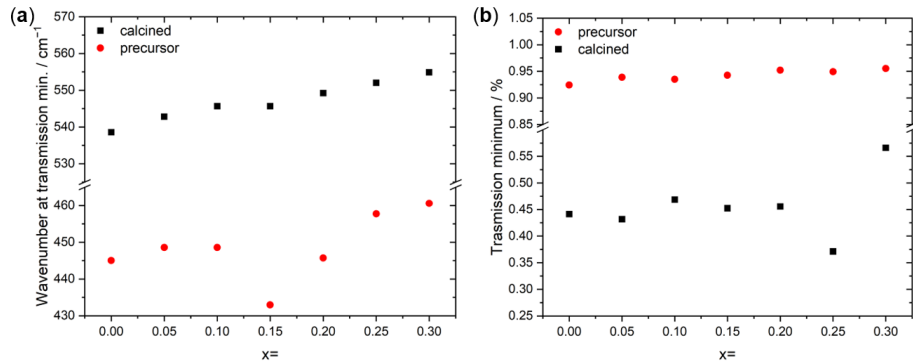


Figure S9. (a) Positions of the transmission minimum in the M-O and M-OH region (< 580 cm⁻¹) in the IR spectra. (b) Transmission minimum in IR spectra in the M-O and M-OH region (< 580 cm⁻¹) corresponding to the minimum positions shown in (a).

Table 1. Criteria of fit for the Rietveld Refinements of the X-ray diffraction patterns of the calcined samples.

Sample	R <sub>exp</sub>	R <sub>wp</sub>	R <sub>exp'</sub>	R <sub>wp'</sub>	R <sub>p'</sub>	GOF	R <sub>Bragg</sub>
x=0.00	7.88	10.10	4.68	6.00	4.73	1.28	2.572
x=0.05	9.20	11.29	4.79	5.87	4.68	1.23	2.933
x=0.10	7.79	11.49	4.54	6.69	5.24	1.47	3.904
x=0.15	10.02	12.52	5.70	7.12	5.41	1.25	3.582
x=0.20	8.24	12.48	4.71	7.14	5.38	1.52	4.586
x=0.25	7.84	13.08	4.41	7.36	5.81	1.67	5.205
x=0.30	7.59	13.50	4.47	7.95	5.98	1.78	5.230

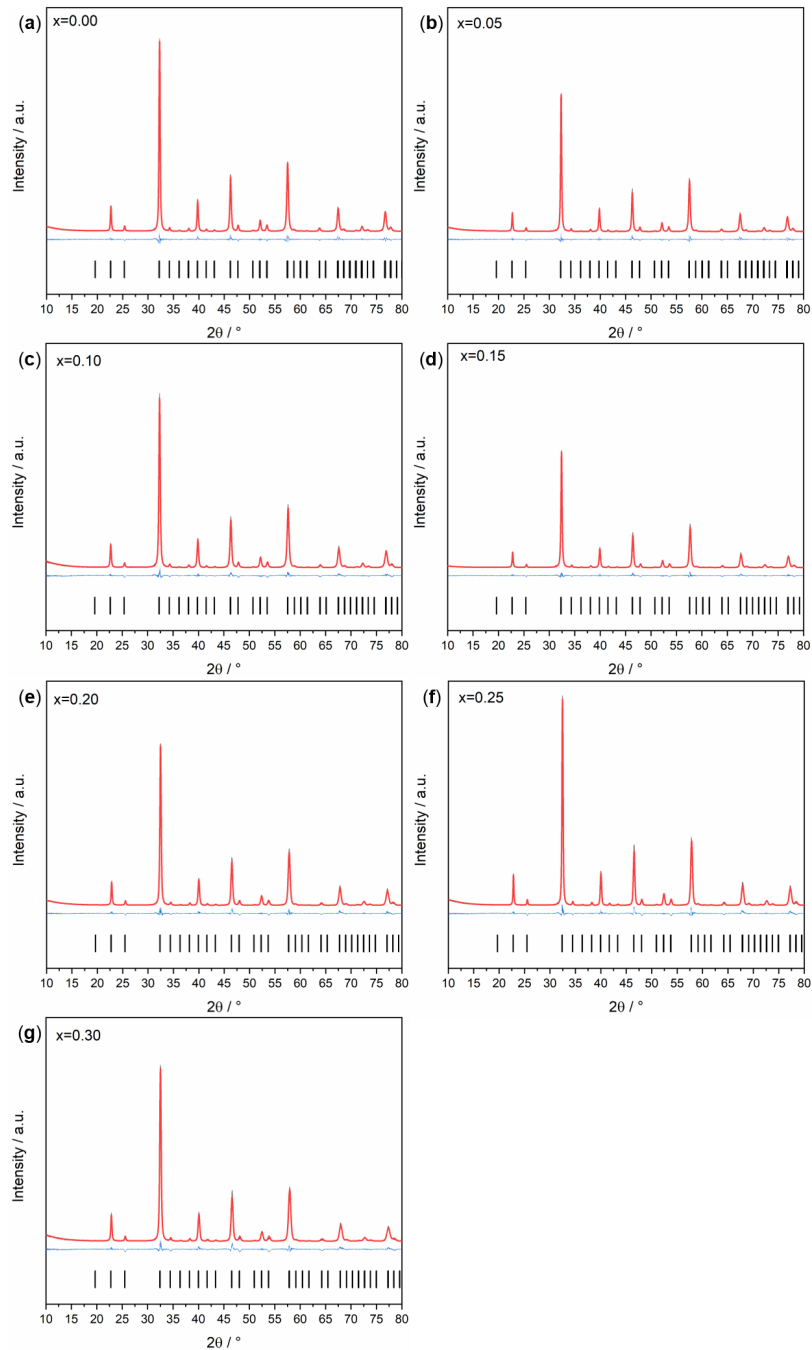


Figure S10. (a) Rietveld plots of  $x=0.00$ . (b) Rietveld plots of  $x=0.05$ . (c) Rietveld plots of  $x=0.10$ . (d) Rietveld plots of  $x=0.15$ . (e) Rietveld plots of  $x=0.20$ . (f) Rietveld plots of  $x=0.25$ . (g) Rietveld plots of  $x=0.30$ . Grey: experimental pattern; red: calculated pattern; blue: difference plot; black: Bragg peak position

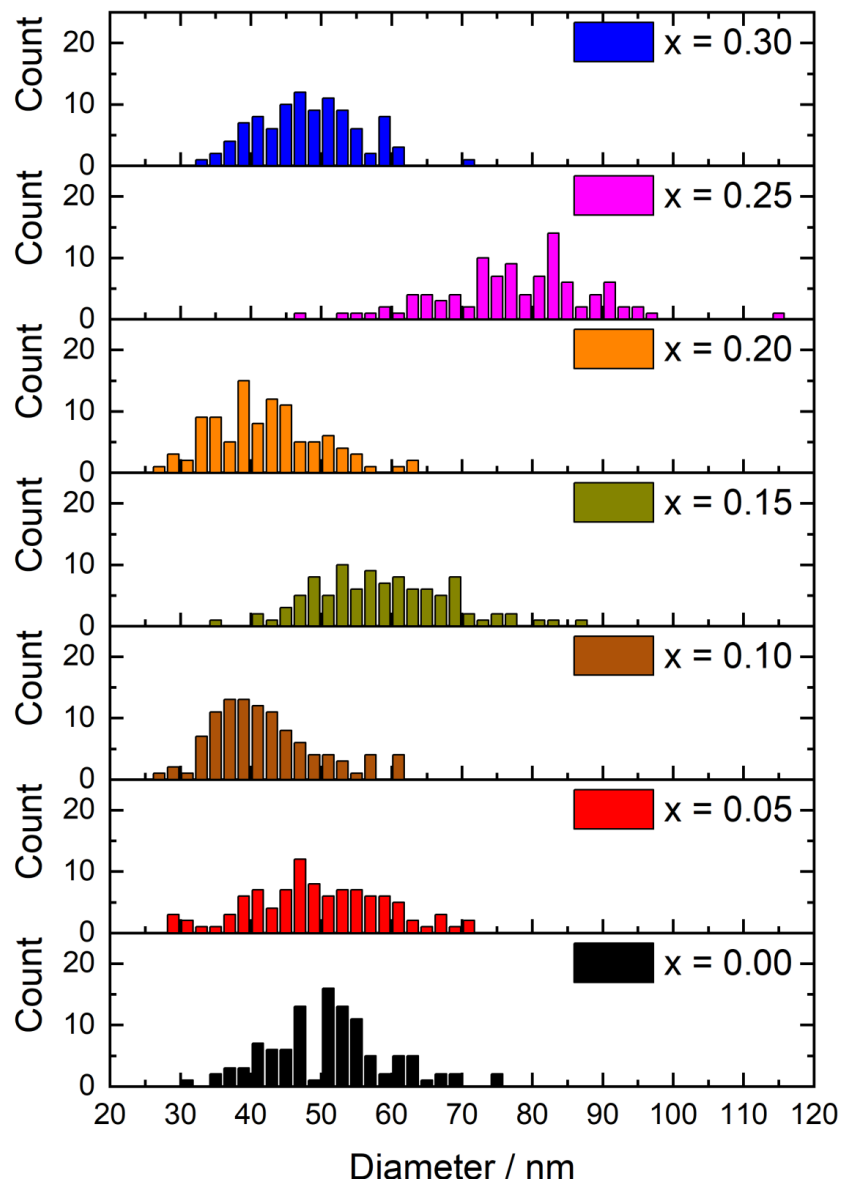


Figure S11. SEM particle size counts of all samples after calcination from 100 particles per sample.

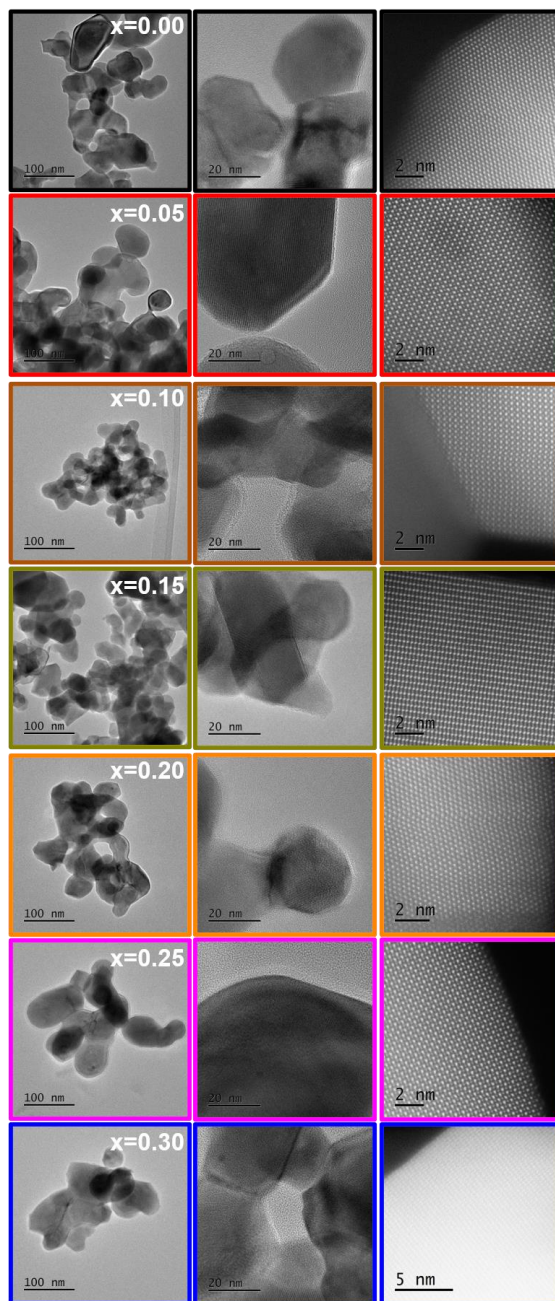


Figure S12. TEM images in the magnifications 60 k (left column), 300 k (middle column), and 10 M (right column).

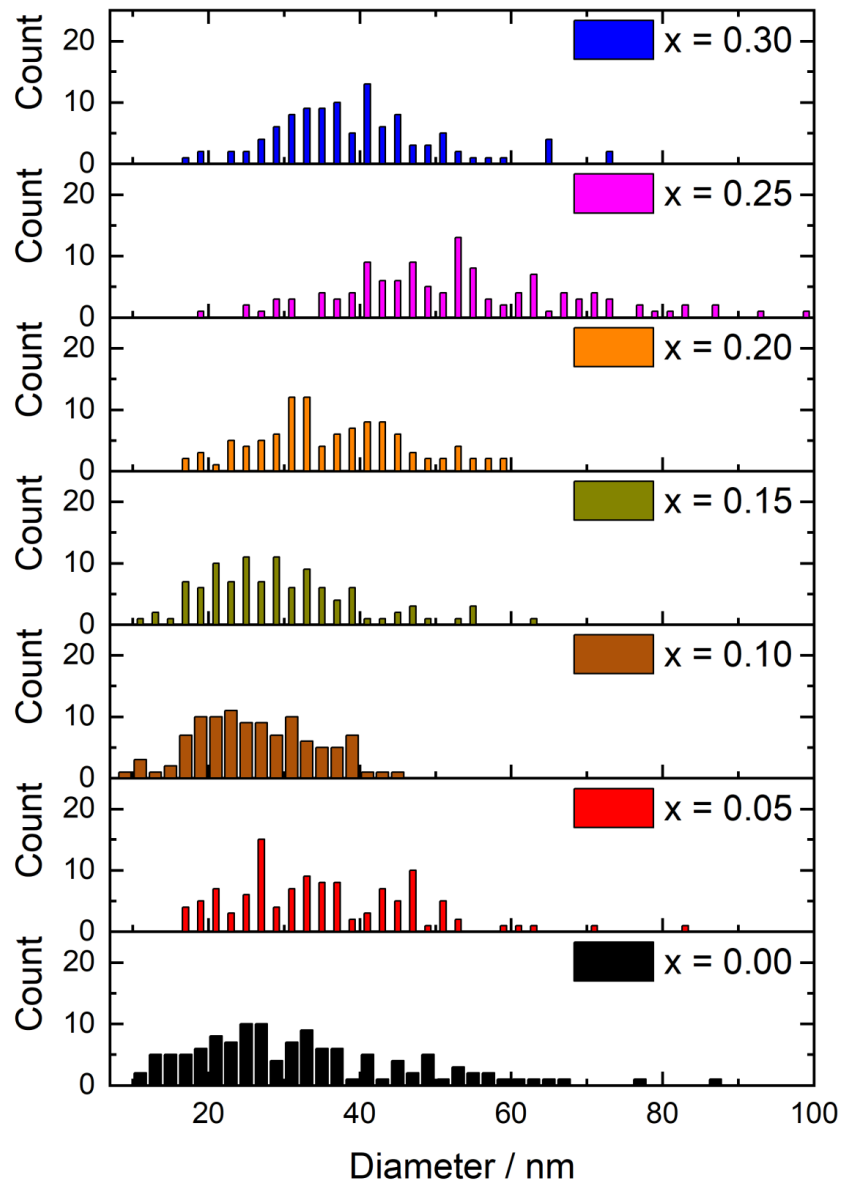


Figure S13. TEM particle size counts of all samples after calcination from 100 particles per sample.

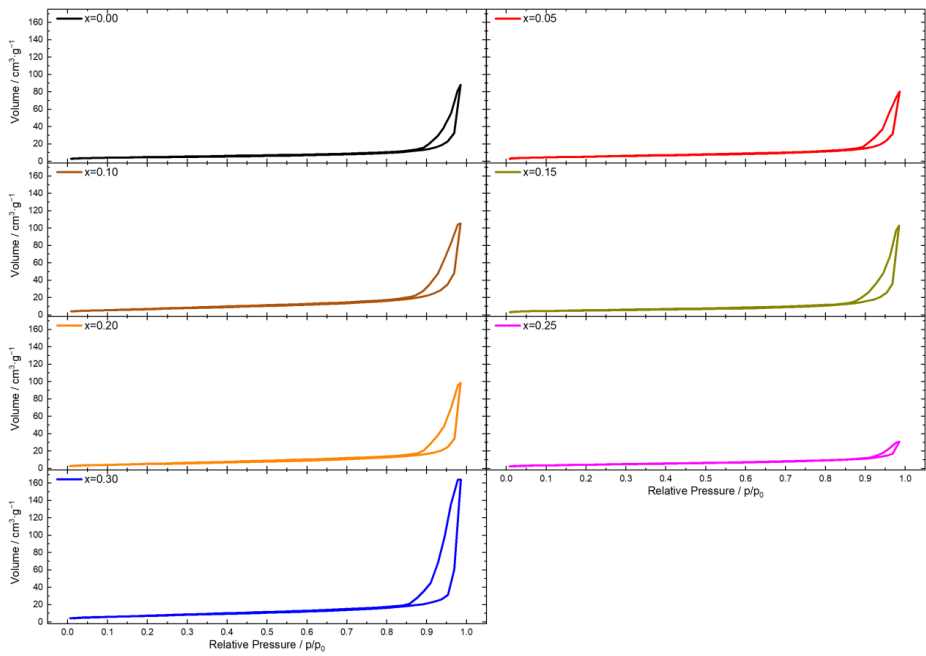


Figure S14. BET isotherms of all samples.

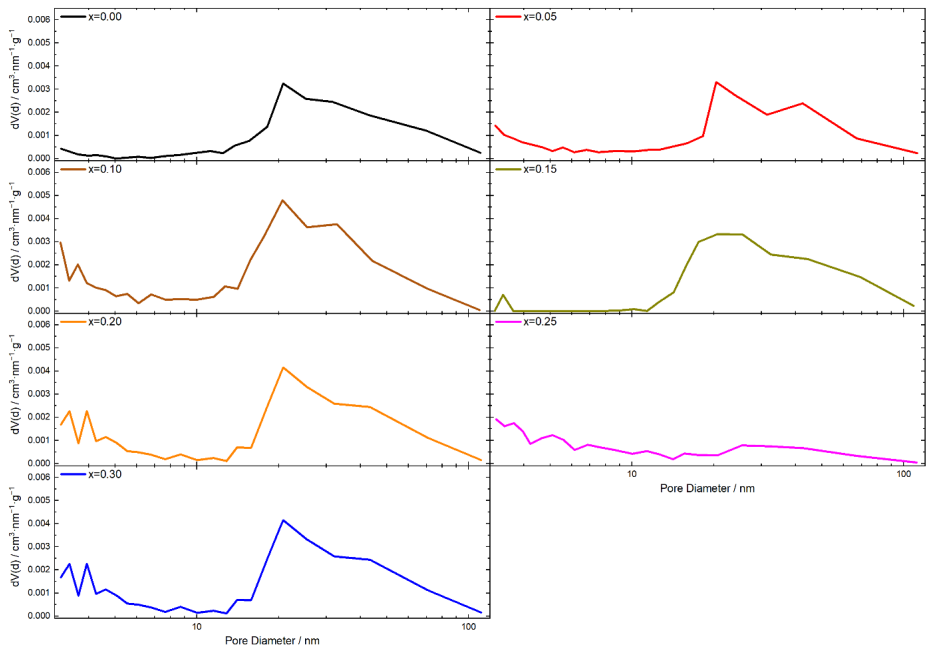


Figure S15. Pore size distribution of all samples.

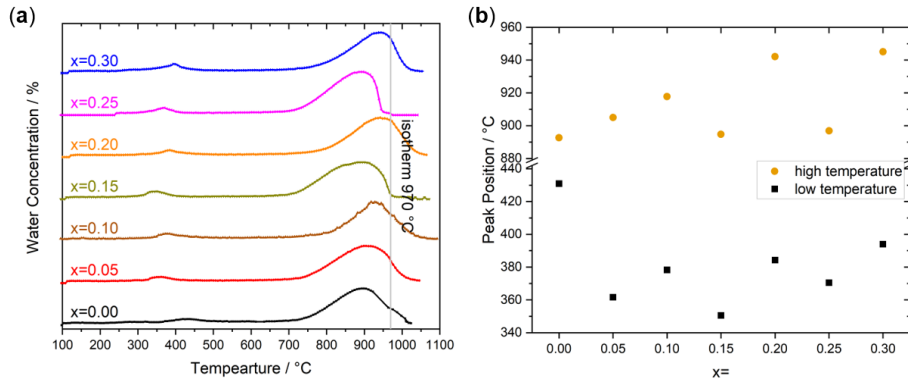
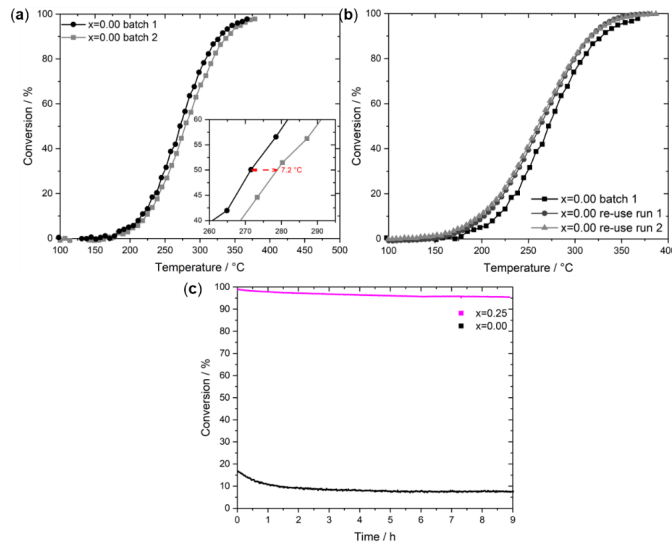


Figure S16. (a) H<sub>2</sub>-TPR profiles of the sample series. (b) Positions of the maxima below 500 °C (labelled low temperature) and above 500 °C (labelled high temperature) derived from the TPR curves in (a).

In Figure S16a, temperature-programmed reduction in hydrogen curves (H<sub>2</sub>-TPR) are shown.

The measurements were performed in a home-built apparatus consisting of a gas dosing unit (HovaGAS N G6 VOC-S, IAS GmbH, Germany) and a Tube Furnace MTF 10/25/130 (Carbolite Gero, Neuhausen, Germany) which is placed in a heating cabinet Thermocenter TC100 (SalvisLab, Rotkreuz, Switzerland). The reaction mixture, either going through or bypassing the reactor, was analyzed on a downstream dual-carrier gas Fusion Micro GC (Inficon GmbH, Bad Ragaz, Switzerland) equipped with four separation modules (2x Rt-Molsieve 5A, 1x Stabilwax DB, 1x Rt-Q-Bond). The catalyst mixture was placed in a quartz reactor (inner diameter = 8 mm).

For H<sub>2</sub>-TPR, 20 mg (sieve fraction 250–355 µm) of each calcined catalyst was placed inside a U-shaped quartz tube reactor. Each sample was pre-treated by heating at 3 °C min<sup>-1</sup> in N<sub>2</sub> from room temperature to 100 °C, kept constant for 1 hr. After that, the sample was cooled down in N<sub>2</sub> to 50 °C. Afterwards, a mixture of 7 % H<sub>2</sub> in Ar with a flow rate of 80 mL min<sup>-1</sup> was used for H<sub>2</sub>-TPR with a linear heating rate of 6 K min<sup>-1</sup> up to 1000 °C. The latter was held for 15 min. The reduction profile were obtained from the H<sub>2</sub>O concentrations derived from GC measurements.



*Figure S17. (a) Transient CO oxidation conversion curves of  $x=0.00$  derived from two different synthesis batches in the reaction mixture of 2% CO+20% O<sub>2</sub> balanced in He. (b) Transient CO oxidation conversion curves of sample  $x=0.00$  batch 1 in the reaction mixture of 2% CO+20% O<sub>2</sub> balanced in He and reusability test and reproducibility test after storage in air in the reaction mixture of 2% CO+20% O<sub>2</sub> balanced in N<sub>2</sub>. (c) Stability test of the re-used  $x=0.00$  after temperature-programmed oxidation and a fresh batch  $x=0.25$  after temperature-programmed oxidation at 200 °C in the reaction mixture of 2% CO+20% O<sub>2</sub> balanced in N<sub>2</sub>.*

In Figure S17a and S17b, transient CO oxidation curves are shown that derived from another instrument compared to transient oxidation curves in Figure S17a. The measurements were performed in a home-built apparatus consisting of a gas dosing unit (HovaGAS N G6 VOC-S, IAS GmbH, Germany) and a Tube Furnace MTF 10/25/130 (Carbolite Gero, Neuhausen, Germany) which is placed in a heating cabinet Thermocenter TC100 (SalvisLab, Rotkreuz, Switzerland). The reaction mixture, either going through or by-passing the reactor, was analyzed on a downstream dual-carrier gas Fusion Micro GC (Inficon GmbH, Bad Ragaz, Switzerland) equipped with four separation modules (2x Rt-Molsieve 5A, 1x Stabilwax DB, 1x Rt-Q-Bond). The catalyst mixture was placed in a quartz reactor (inner diameter = 8 mm).

The protocol of the re-use of  $x=0.00$  from batch 1 (mixture was unloaded from the reactor after the initial measurement and stored in air) consisted of three different exposures to a reaction mixture of 2% CO and 20% O<sub>2</sub> (balanced in N<sub>2</sub>). Prior to each run, a temperature-programmed oxidation (TPO) was performed in 20% O<sub>2</sub> in N<sub>2</sub> with a heating rate of 3 °C min<sup>-1</sup> up to 300 °C and a dwell time of 1 h. After cooling down to 50 °C, the catalyst was purged with N<sub>2</sub>, afterwards equilibrated in the reaction mixture for 15 min. For the transient CO oxidation, the temperature was increased linearly with a heating rate of 3 °C min<sup>-1</sup> up to 500 °C and dwelled for 15 min. Afterwards, the reactor was cooled to 50 °C and purged with N<sub>2</sub> for 90 min. After TPO, a second exactly same transient reaction was performed to investigate restorability of the activity. The third step contained a similar TPO was performed with the deviation of cooling only being performed to 200 °C, again purged with the reaction mixture for 15 min and afterwards, 9 h of reaction have been investigated on the catalyst at 200 °C to judge on the stability. The results are shown in Figure S17c.

For the stability test of x=0.25, 100 mg of a fresh batch were diluted with 500 mg of SiC. Afterwards, the stability test was performed at 200 °C for 10 h in 2% CO and 20% O<sub>2</sub> balanced in N<sub>2</sub> as specified above.

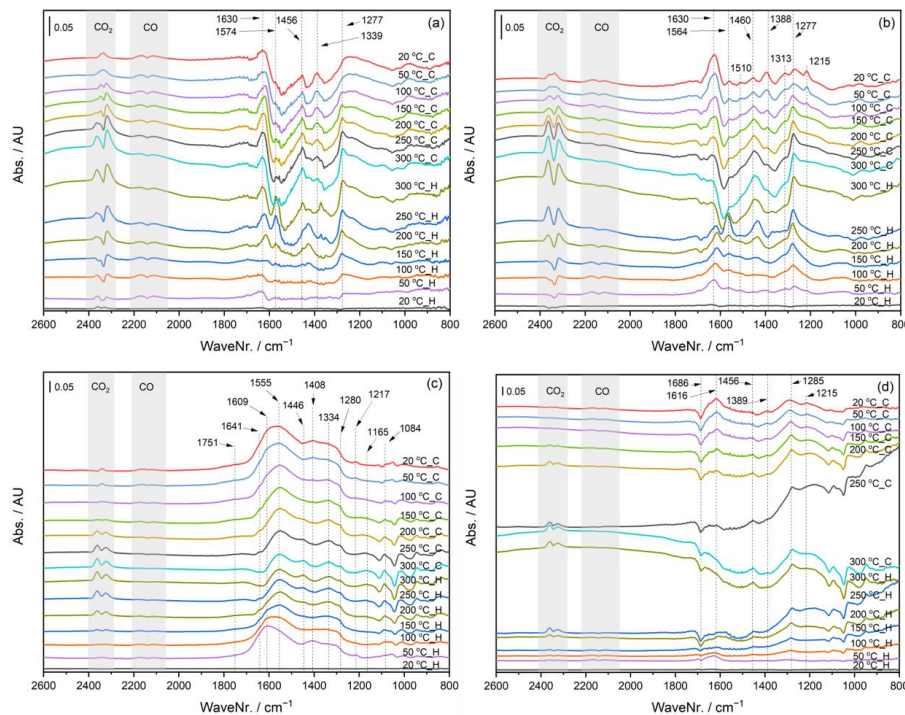


*Figure S18. DRIFTS spectra of the selected catalysts exposed to the reaction mixture of 0.2% CO+2% O<sub>2</sub> balanced in He, after a He-treatment at 150 °C during a transient experiment; (a) x=0.00, (b) x=0.05, (c) x=0.20 and (d) x=0.30 Co incorporation. In the legends, H and C designate the heating and cooling segments, respectively.*

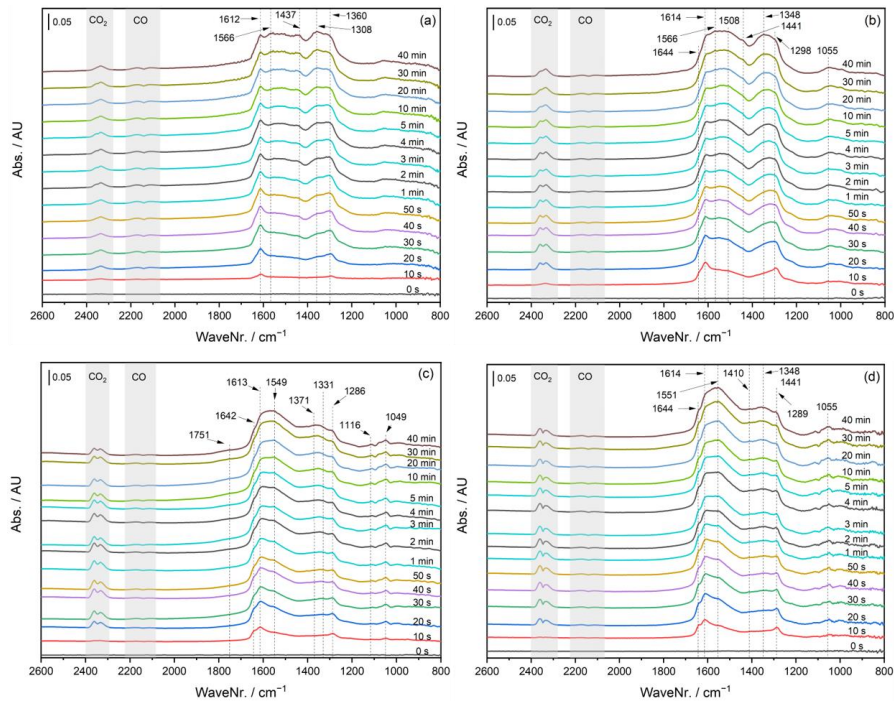


Figure S19. DRIFTS spectra of the selected catalysts exposed to the reaction mixture of 0.2% CO+2% O<sub>2</sub> balanced in He, after an oxidative treatment during 40 min of steady-state condition at 200 °C; (a)  $x=0.00$ , (b)  $x=0.05$ , (c)  $x=0.20$  and (d)  $x=0.30$  Co incorporation.

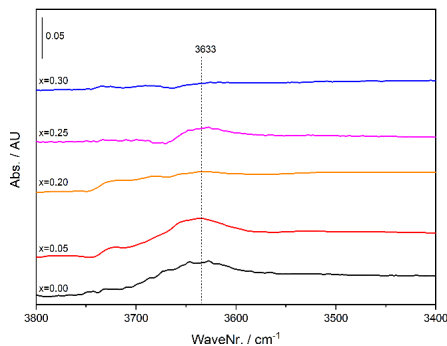


Figure S20. OH-region DRIFTS spectra of the selected catalysts exposed to the reaction mixture of 0.2% CO+2% O<sub>2</sub> balanced in He, after an oxidative treatment during 40 min of steady-state condition at 200 °C.

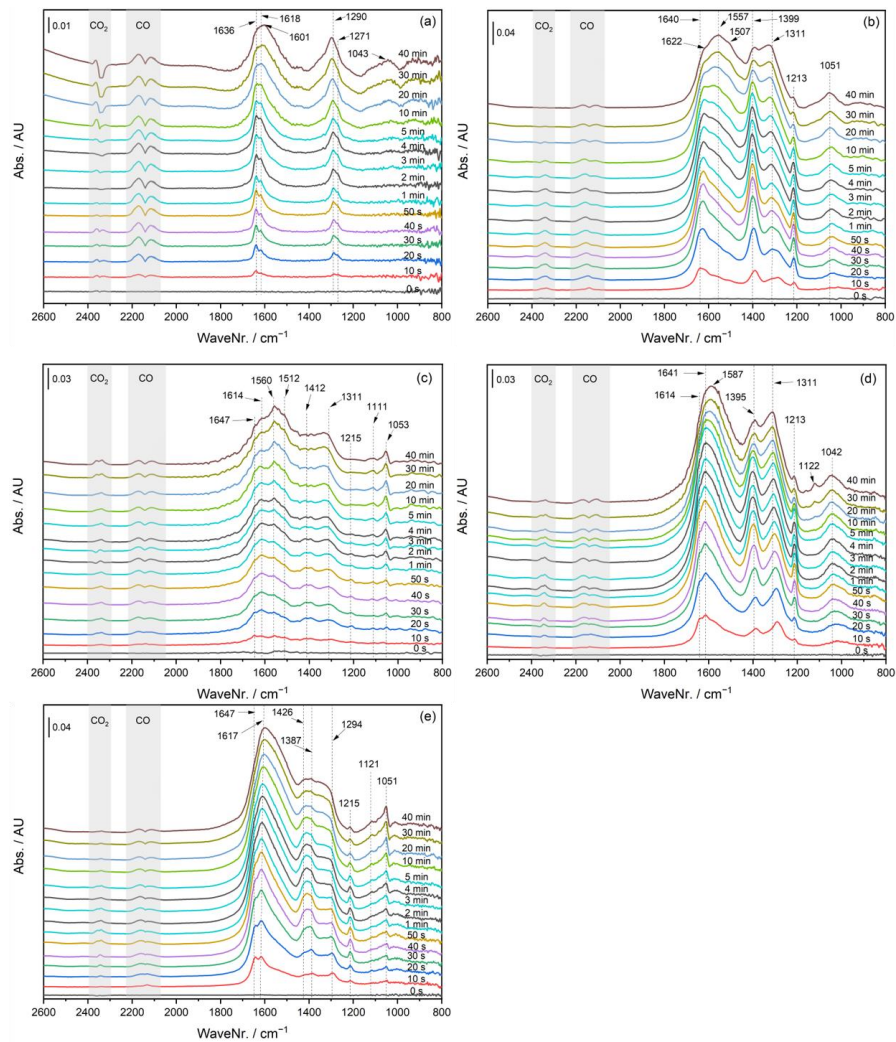


Figure S21. DRIFTS spectra of the selected catalysts exposed to the probe gas of 0.2% CO in He, after an oxidative treatment during 40 min of steady-state condition at 10 °C; (a)  $x=0.00$ , (b)  $x=0.05$ , (c)  $x=0.20$ , (d)  $x=0.25$  and (e)  $x=0.30$  Co incorporation.

## **V. SI: Synergistic Effects of Co and Fe on the Oxygen Evolution Reaction Activity of $\text{LaCo}_x\text{Fe}_{1-x}\text{O}_3$**

The main text to this Supporting Information is shown in Chapter 5.

# **Chemistry—A European Journal**

Supporting Information

**Synergistic Effects of Co and Fe on the Oxygen Evolution Reaction Activity of  $\text{LaCo}_x\text{Fe}_{1-x}\text{O}_3$**

# **Chemistry—A European Journal**

Supporting Information

**Synergistic Effects of Co and Fe on the Oxygen Evolution Reaction Activity of  $\text{LaCo}_x\text{Fe}_{1-x}\text{O}_3$**

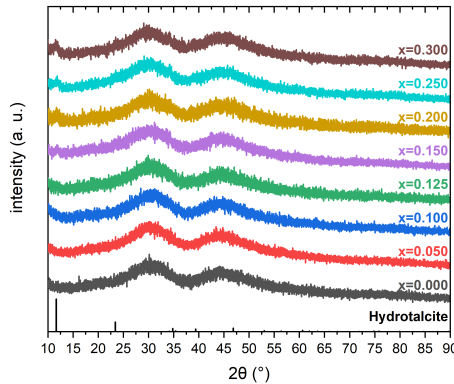


Figure S1: PXRD patterns of the co-precipitated precursor materials.

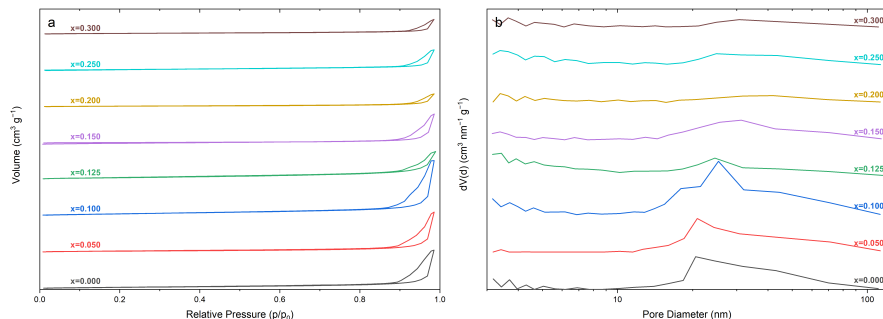


Figure S2: (a)  $N_2$  adsorption and desorption isotherms of the calcined perovskite materials.  
(b) Pore size distributions determined by the BJH-method.

Table S1: Structural characterization data of the samples. Co/(Co+Fe) ratios ( $x_{\text{exp}}$ ) derived from atomic absorption spectroscopy of the precursor materials, BET surface area derived by  $N_2$  physisorption calculated from  $p/p_0$  data between 0.05 and 0.3, pore volumes determined at  $p/p_0$ .

$x$	$x_{\text{exp}}$ (%)	BET Surface Area ( $\text{m}^2 \text{ g}^{-1}$ )	Pore volume ( $\text{m}^3 \text{ g}^{-1}$ )
0.000	0.000	20.0	0.1671
0.050	0.044	17.3	0.1738
0.100	0.085	28.9	0.2375
0.125	0.101	24.7	0.1214
0.150	0.129	11.7	0.1265
0.200	0.171	11.0	0.0570
0.250	0.230	14.4	0.0893
0.300	0.282	10.6	0.0643

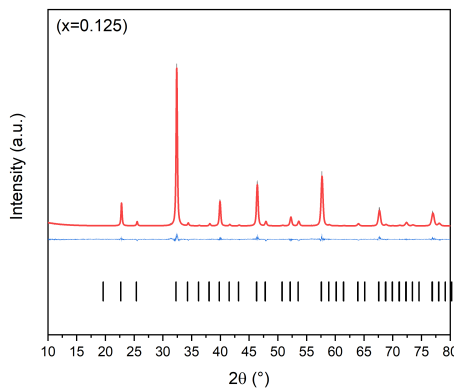
Figure S3: Rietveld difference plots of  $x = 0.125$ .

Table S2: Criteria of fit for the Rietveld refinements of the XRD patterns of the calcined samples.

$x$	$R_{\text{exp}}$	$R_{\text{wp}}$	$R_p$	$R_{\text{exp}'}$	$R_{\text{wp}'}$	$R_p'$	GOF	$R_{\text{Bragg}}$
0.000 <sup>S1</sup>	7.88	10.10	7.05	4.68	6.00	4.73	1.28	2.57
0.125	12.14	15.25	9.95	5.01	6.30	5.14	1.26	3.90
0.250 <sup>S1</sup>	7.84	13.08	8.88	4.41	7.36	5.81	1.67	5.21

Table S3: Potentials  $E_{j=10}$  required to reach a current density of 10 mA/cm<sup>2</sup> and current densities  $J_{1.8}$  measured at a potential of 1.8 V vs RHE for perovskite samples with different Co content  $x$ .

$x$	$E_{j=10}$ (V vs. RHE)	$J_{1.8}$ (mA/cm <sup>2</sup> )
0.000	1.760	19
0.050	1.702	34
0.100	1.682	45
0.125	1.696	43
0.150	1.690	45
0.200	1.693	36
0.250	1.689	38
0.300	1.698	29

Table S4: Double layer capacitance  $C_{DL}$ , coefficient of determination  $R^2$  and exponent  $\alpha$  obtained from the allometric regression of charging current vs. scan rate plots.

$x$	Cathodic scan			Anodic scan			Average $C_{DL}$ ( $\mu\text{F}$ )
	$C_{DL}$ ( $\mu\text{F}$ )	$R^2$	$\alpha$	$C_{DL}$ ( $\mu\text{F}$ )	$R^2$	$\alpha$	
0	11.10	0.998	0.63	12.12	0.999	0.65	11.37
0.05	8.42	0.987	0.56	8.09	0.995	0.53	8.30
0.1	8.04	0.985	0.45	8.35	0.986	0.46	8.45
0.125	8.37	0.961	0.53	8.30	0.998	0.52	8.23
0.15	9.34	0.940	0.47	9.39	0.955	0.49	9.01
0.2	8.65	0.990	0.50	8.84	0.991	0.51	8.78
0.25	8.53	0.993	0.57	8.67	0.996	0.58	8.45
0.3	8.00	0.988	0.49	7.88	0.990	0.51	8.04

Table S5: Potential windows used for the determination of double layer capacitance of perovskite samples with different Co content. Potentials are indicated vs. Ag/AgCl/KCl.

$x$	Lower vertex potential (V)	Open circuit potential (V)	Upper vertex potential (V)
0	-0.325	-0.074	0.177
0.05	-0.204	-0.053	0.098
0.1	-0.271	-0.071	0.128
0.125	-0.236	-0.036	0.164
0.15	-0.273	-0.073	0.127
0.2	-0.283	-0.083	0.116
0.25	-0.247	-0.096	0.055
0.3	-0.233	-0.082	0.069

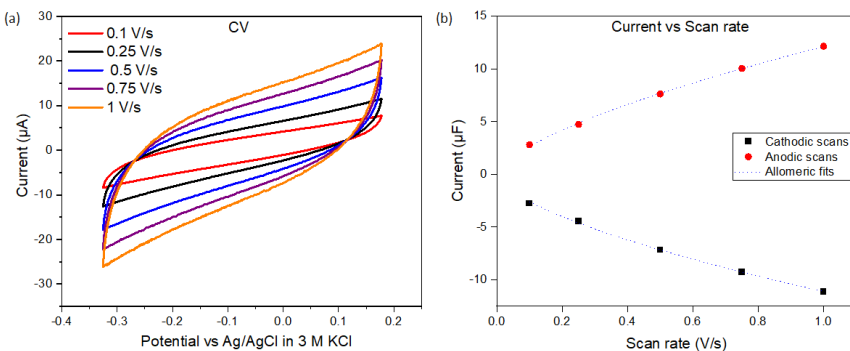


Figure S4: Example of determination of double layer capacitance of a perovskite sample ( $x = 0$ ). (a) CVs centered at OCP, recorded at scan rates 0.1, 0.25, 0.5, 0.75 and 1 V/s in Ar-saturated 1 M KOH as electrolyte, and the corresponding (b) anodic and cathodic currents measured at the potential corresponding to OCP as a function of the scan rate, showing their respective allometric fits as dotted lines.

Table S6: Energy differences (in eV/f.u.) for bulk  $\text{LaCo}_x\text{Fe}_{1-x}\text{O}_3$  with different B-cation and magnetic arrangements and spin states, calculated using pseudocubic  $2 \times 2 \times 2$  cells. Concerning the cation arrangement we have considered configuration A (all Co atoms in the same layer, alternating with layers containing only Fe B-cations), C (each Co atom having two Co nearest neighbors, i.e. Co arranged in "columns") and G (Co atoms having only Fe nearest neighbors). We note that for  $x = 0.500$  not all combinations are possible. Moreover, we have taken into account different magnetic configurations: ferro- and antiferromagnetic (A, C, G-type), as well as configurations with high spin for Fe and low spin for Co (but also intermediate and high spin for Co was explored), as well as low spin for both cations. The corresponding magnetic moments are  $M_{\text{Fe}}^{\text{HS}} \sim 4.1 - 4.3 \mu_B$ ,  $M_{\text{Fe}}^{\text{LS}} \sim 1.1 \mu_B$  and  $M_{\text{Co}}^{\text{LS}} \sim 0.1 - 0.3 \mu_B$ ,  $M_{\text{Co}}^{\text{IS}} \sim 1.8 - 2.3 \mu_B$  and  $M_{\text{Co}}^{\text{HS}} \sim 3.0 \mu_B$ . Cases where Co is in IS are marked by <sup>IS</sup>, while mixed HS/IS is denoted by <sup>HS/IS</sup>. In some cases an initial Fe (HS)/Co (HS) configuration relaxed to Fe (HS)/Co (LS). With the exception of  $x = 0.000$ , Fe (LS) could only be obtained in a ferromagnetic configuration. For  $x = 0.250$ , all antiferromagnetic G-type configurations are nearly degenerate, as is the case for  $x = 0.500$  in a G-type ion arrangement for Fe (HS)/Co (LS) AFM and FM. Since the energy differences in those cases are of the order of the numerical error, we have selected for consistency the G-type ion arrangement in combination with G-type AFM order for all concentrations.

	$\Delta E$ (eV/f.u.)									
	Spin Configuration									
B-site order	Fe (LS)/ Co (LS)	Fe (HS)/Co (LS)				Fe (HS)/Co (HS/IS)				
		A-AF	C-AF	G-AF	FM	A-AF	C-AF	G-AF	FM	
$x = 0.000$										
	1.476	0.162	0.083	<b>0.000</b>	0.253					
$x = 0.125$										
	-	0.126	0.058	<b>0.000</b>	0.191	-	-	-	-	-
$x = 0.250$										
A	-	0.079	0.037	-0.006	0.121	-	<sup>IS</sup> 0.087	0.008	-	
C	1.088	0.089	0.049	0.008	0.158	<sup>IS</sup> 0.142	<sup>IS</sup> 0.084	0.007	-	
G	-	0.090	0.045	<b>0.000</b>	0.129	<sup>IS</sup> 0.136	<sup>IS</sup> 0.093	0.009	-	
$x = 0.500$										
A	0.772		0.101	0.059	0.148	<sup>IS</sup> 0.144	0.117	0.034	<sup>IS</sup> 0.144	
C	0.761		0.072	0.025	0.069	<sup>HS/IS</sup> 0.156	0.127	0.038	<sup>IS</sup> 0.179	
G	0.758			<b>0.000</b>	-0.009	<sup>IS</sup> 0.123	0.119	0.038	<sup>IS</sup> 0.186	

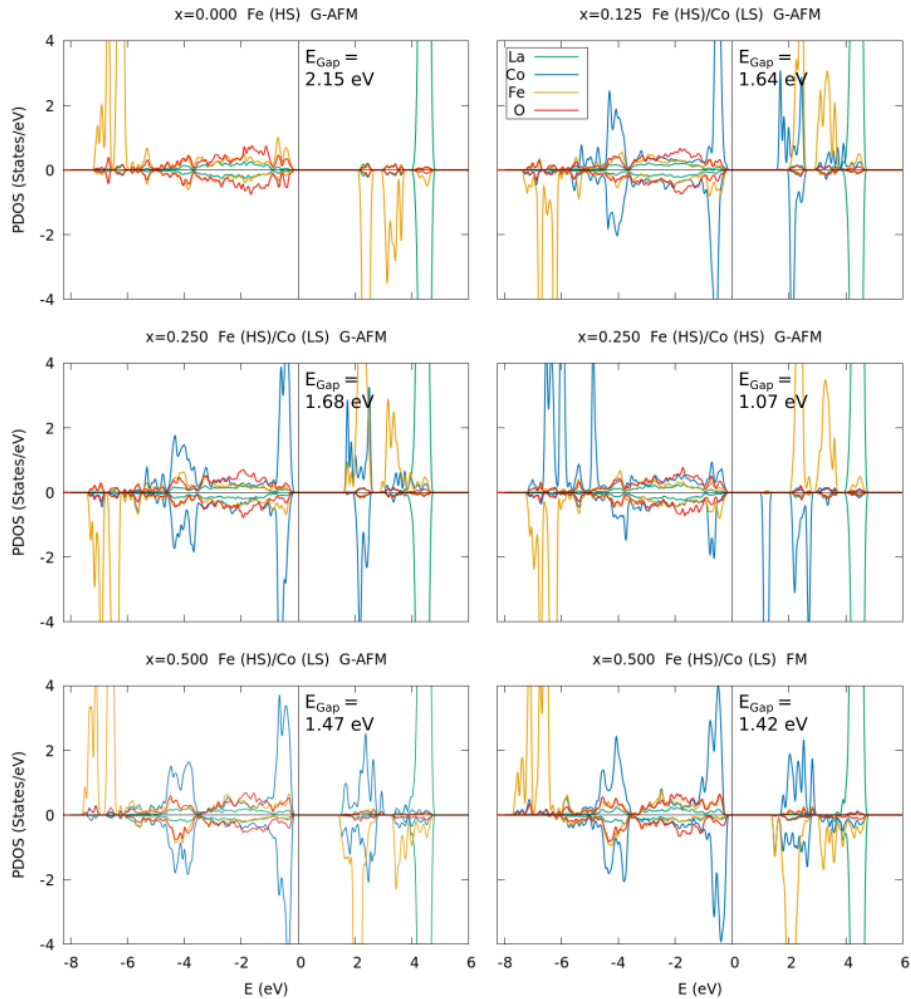


Figure S5: Projected density of states of the different species for bulk LCFO with G-type Fe/Co arrangement and G-AF order. In addition, for  $x=0.250$ , one of the competing states, Fe (HS)/Co (HS) is shown. For  $x=0.500$  the competing ferromagnetic state is shown.

## References

- (S1) Dreyer, M.; Krebs, M.; Najafishirtari, S.; Rabe, A.; Friedel Ortega, K.; Behrens, M. The Effect of Co Incorporation on the CO Oxidation Activity of  $\text{LaFe}_{1-x}\text{Co}_x\text{O}_3$  Perovskites. *Catalysts* **2021**, *11*, 550.

## **VI. SI: The Effect of Water on the 2-Propanol Oxidation Activity of Co-Substituted LaFe<sub>1-x</sub>Co<sub>x</sub>O<sub>3</sub> Perovskites**

The main text to this Supporting Information is shown in Chapter 6.

# **Chemistry—A European Journal**

Supporting Information

**The Effect of Water on the 2-Propanol Oxidation Activity of Co-Substituted  $\text{LaFe}_{1-\text{x}}\text{Co}_\text{x}\text{O}_3$  Perovskites**

# **Chemistry—A European Journal**

Supporting Information

**The Effect of Water on the 2-Propanol Oxidation Activity of Co-Substituted  $\text{LaFe}_{1-\text{x}}\text{Co}_\text{x}\text{O}_3$  Perovskites**

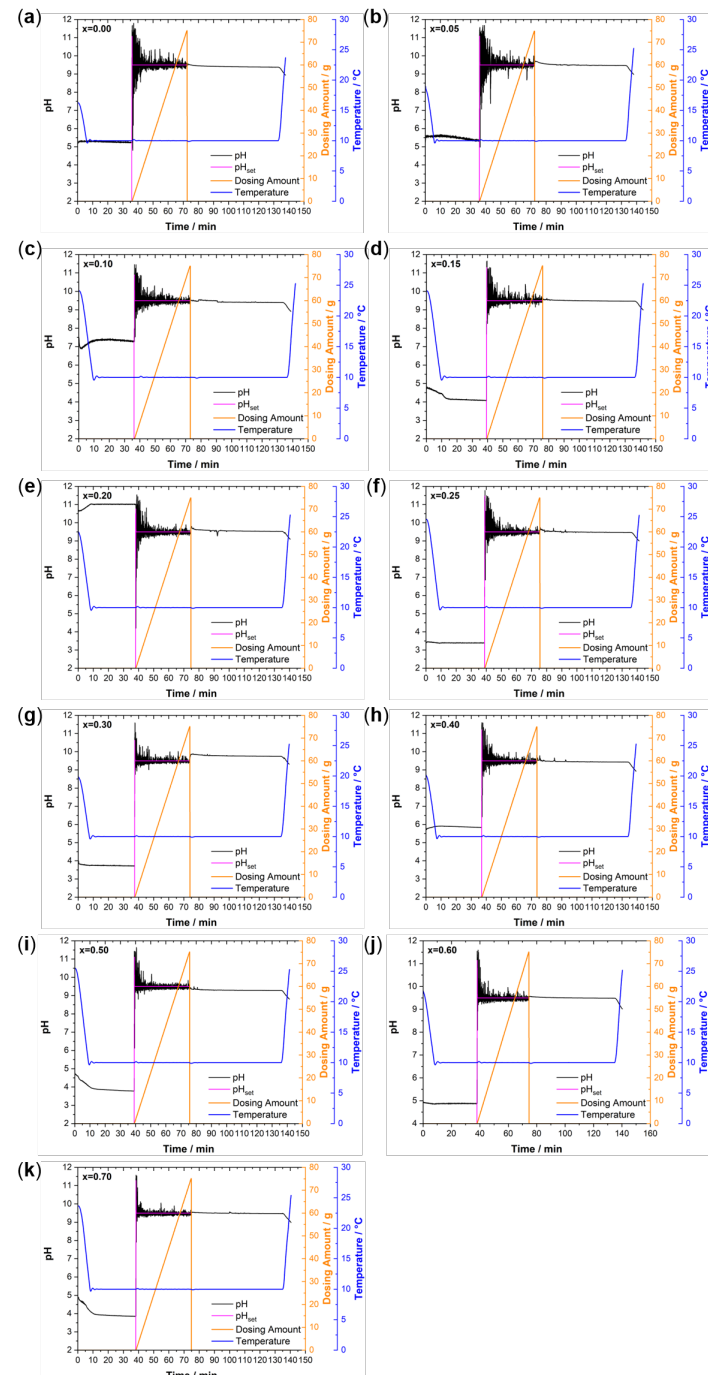


Figure S1: Synthesis protocols of (a)  $x=0.00$ , (b)  $x=0.05$ , (c)  $x=0.10$ , (d)  $x=0.15$ , (e)  $x=0.20$ , (f)  $x=0.25$ , (g)  $x=0.30$ , (h)  $x=0.40$ , (i)  $x=0.50$ , (j)  $x=0.60$  and (k)  $x=0.70$ .

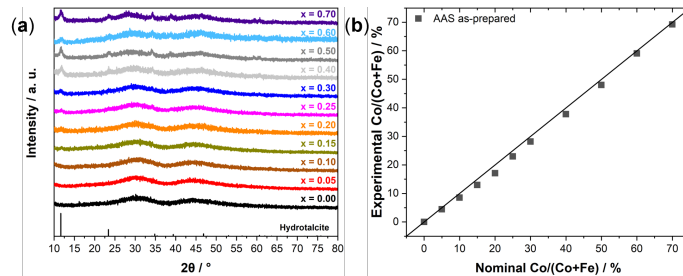


Figure S2: (a) XRD patterns of the co-precipitated precursor materials. (b) Experimental ratio  $\text{Co}/(\text{Co}+\text{Fe})$  derived from AAS of the precursors.

Table S1. Criteria of fit for the Rietveld refinements of the X-ray diffraction patterns of the calcined samples. In case of the  $R_{\text{Bragg}}$  values, the indicator O is the abbreviation for the orthorhombic perovskite, R for the rhombohedral perovskite and S for the spinel phase.

x=	$R_{\text{exp}}$	$R_{\text{wp}}$	$R_p$	$R_{\text{exp}'}$	$R_{\text{wp}'}$	$R_p'$	GOF	$R_{\text{Bragg,O}}$	$R_{\text{Bragg,R}}$	$R_{\text{Bragg,S}}$
0.00	10.98	12.54	8.61	5.65	6.45	5.09	1.14	2.051	—	—
0.05	9.55	12.16	8.1	5	6.37	5.09	1.27	2.966	—	—
0.10	10.55	13.09	8.62	5.19	6.44	5.08	1.24	3.368	—	—
0.15	9.2	13.01	8.89	4.75	6.72	5.5	1.41	4.1	—	—
0.20	9.17	13.33	9.17	4.81	7	5.7	1.45	4.625	—	—
0.25	9.76	14.68	10.05	4.87	7.33	5.99	1.5	5.301	—	—
0.30	8.66	14.99	10.27	4.75	8.23	6.57	1.73	5.898	—	—
0.40	10.71	15.11	10.73	5.03	7.1	6.08	1.41	4.202	4.084	5.196
0.50	10.05	15.75	11.46	4.91	7.69	6.68	1.57	4.34	5.829	4.202
0.60	9.52	14.54	10.64	5.03	7.68	6.59	1.53	2.703	3.172	4.429
0.70	9.98	13.75	10.31	5.62	7.74	6.61	1.38	3.531	3.362	3.229

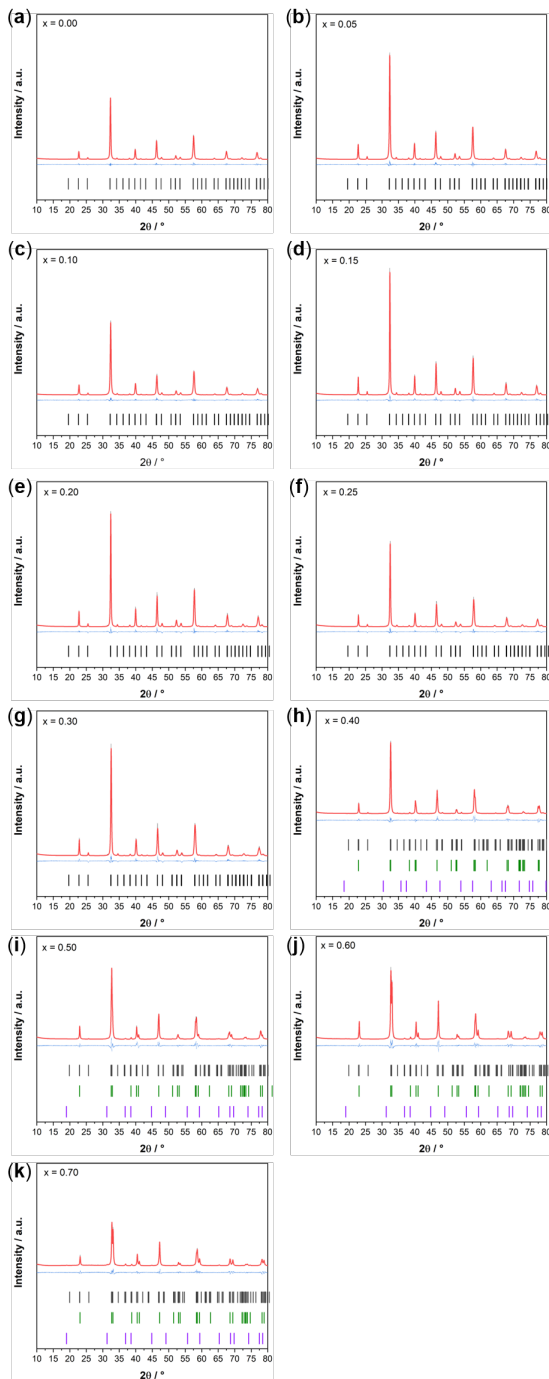


Figure S3: Rietveld refinement plots of (a)  $x=0.00$ , (b)  $x=0.05$ , (c)  $x=0.10$ , (d)  $x=0.15$ , (e)  $x=0.20$ , (f)  $x=0.25$ , (g)  $x=0.30$ , (h)  $x=0.40$ , (i)  $x=0.50$ , (j)  $x=0.60$  and (k)  $x=0.70$ .

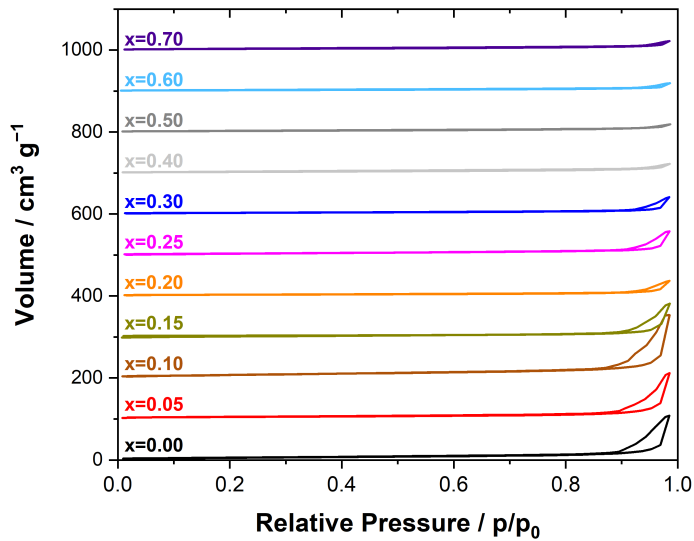
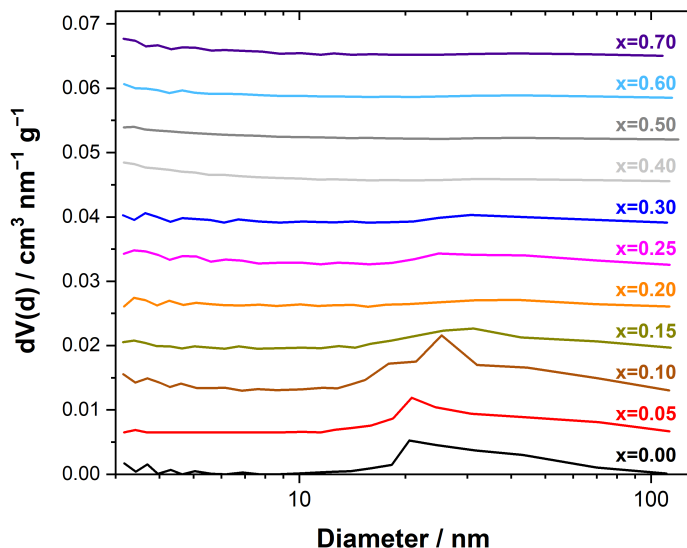
Figure S4:  $N_2$  adsorption isotherms.

Figure S5: Pore size distributions determined by the BJH method during desorption.

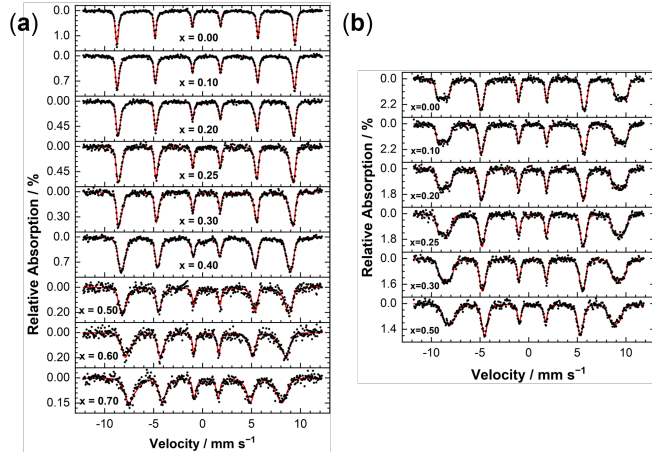


Figure S6: Mössbauer spectra (black dots) and fits (red lines) for 5 K zero field (a) and 4.3 K 5 T (b) measurements. Zero field spectra were reproduced via narrow distributions of the hyperfine field  $B_{HF}$ , while in-field spectra were fitted using distributions of the canting angle between the applied magnetic field and spin direction. Spectral structure and line intensities are indicative of a canted antiferromagnetic (weakly FM) structure.

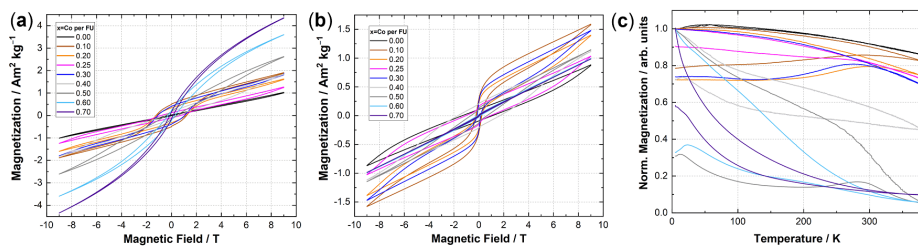


Figure S7: (a) 9 T  $M(H)$  magnetization curves recorded at 4.3 K. (b) 9 T  $M(H)$  magnetization curves recorded at 300 K. (c) Temperature dependent magnetization curves recorded between 5 K and 380 K at 0.1 T using the standard zero field cooled - field cooled (ZFC-FC) protocol.

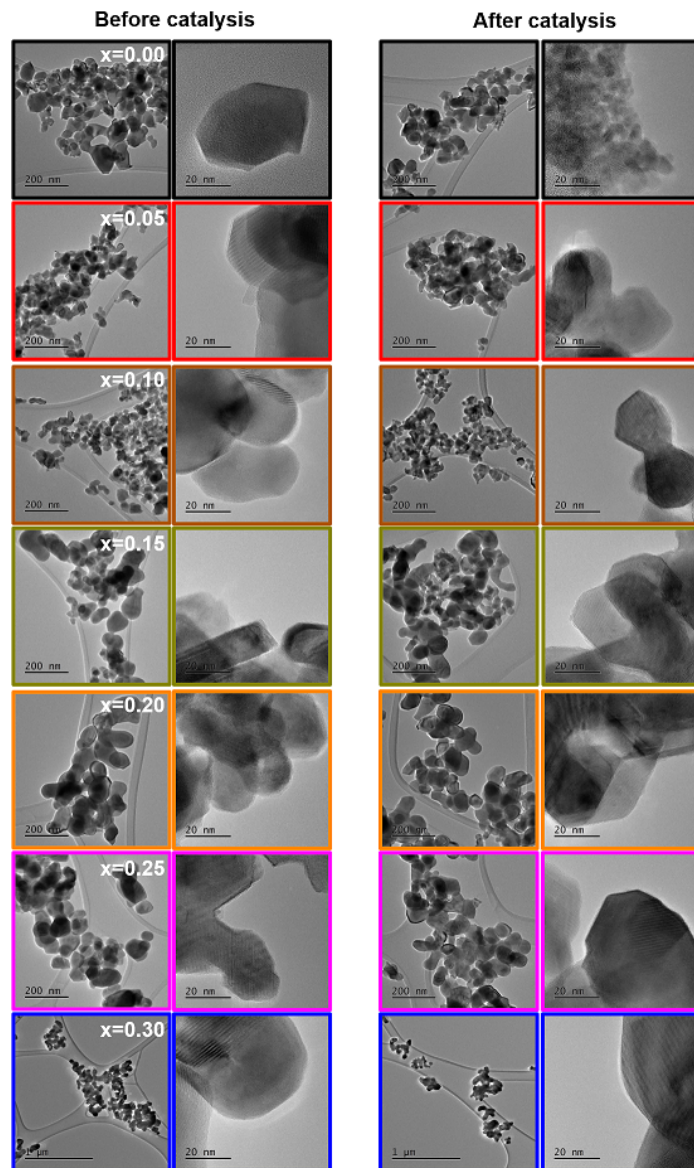


Figure S8: TEM micrographs before and after catalysis for  $0.00 \leq x \leq 0.30$ .

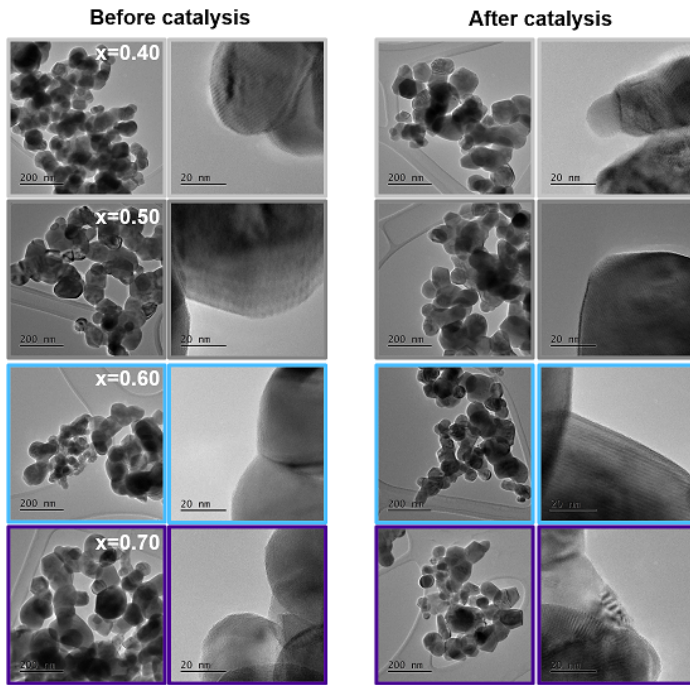


Figure S9: TEM micrographs before and after catalysis for  $0.40 \leq x \leq 0.70$ .

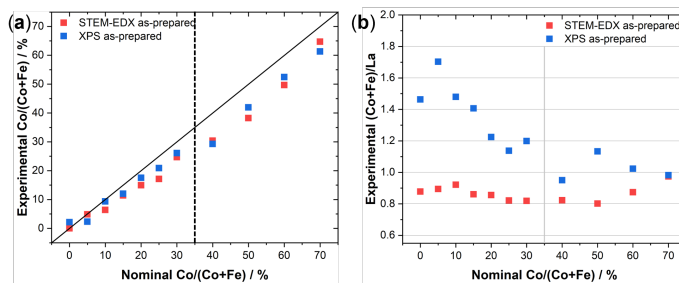


Figure S10: (a) Experimental ratio  $\text{Co}/(\text{Co}+\text{Fe})$  derived from STEM-EDX and XPS. (b) Experimental ratio  $(\text{Co}+\text{Fe})/\text{La}$  derived from STEM-EDX and XPS. The term *as-prepared* refers to the calcined material prior to any catalytic experiment.

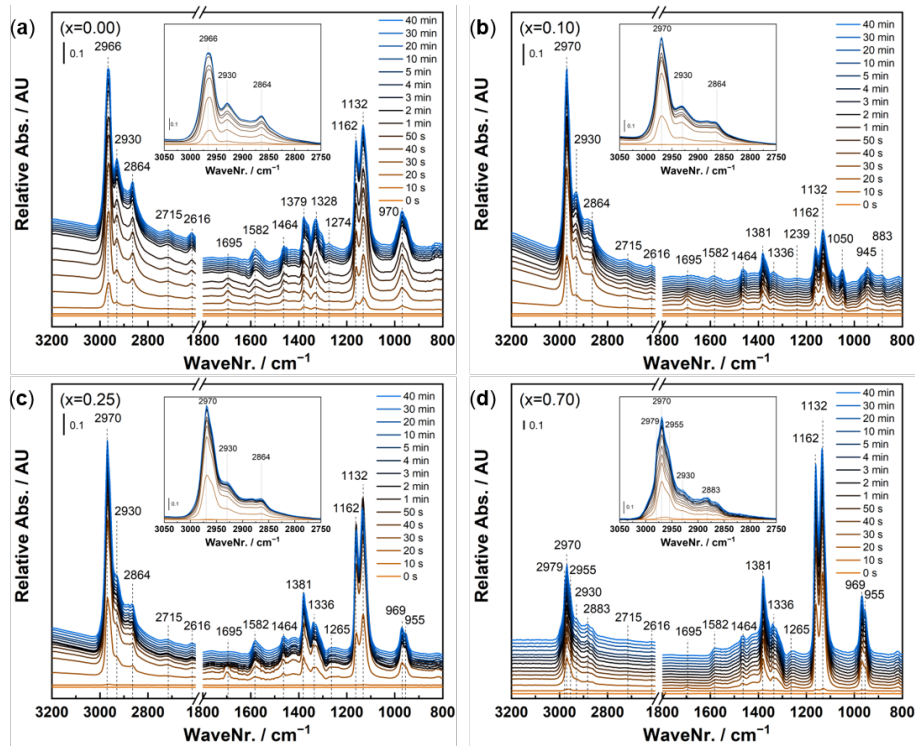


Figure S11: Stacked time-dependent DRIFTS spectra during 2-propanol adsorption for (a)  $x=0.00$ , (b)  $x=0.10$ , (c)  $x=0.25$ , and (d)  $x=0.70$ . The insets show the non-stacked spectra for the wavenumber range corresponding to the  $\text{CH}_3$  and  $\text{CH}$  stretching vibrations.

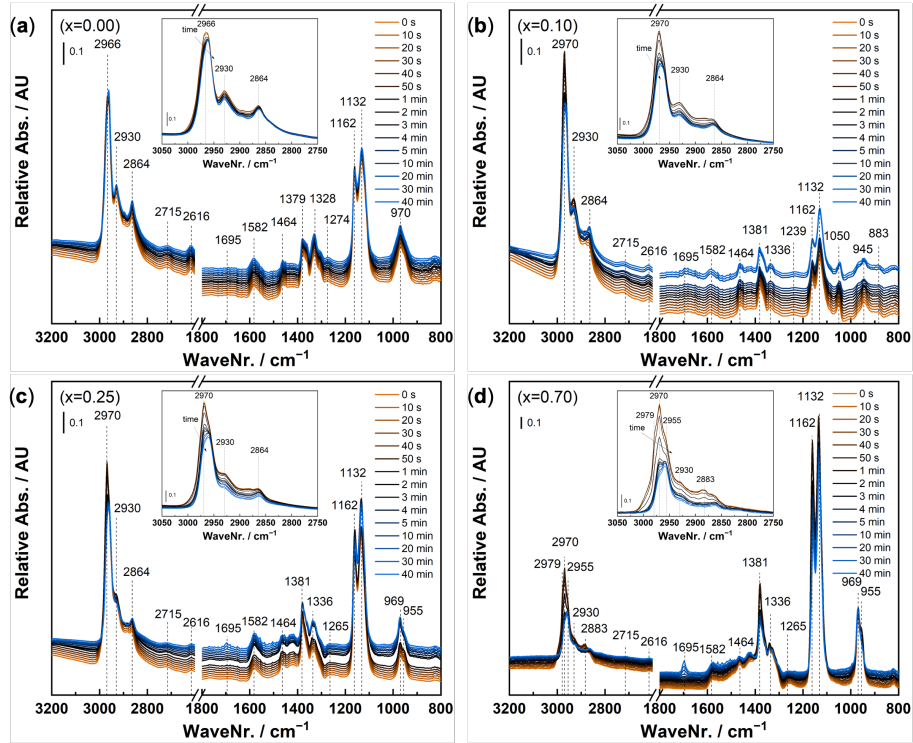


Figure S12: Stacked time-dependent DRIFTS spectra during 2-propanol desorption for (a)  $x=0.00$ , (b)  $x=0.10$ , (c)  $x=0.25$ , and (d)  $x=0.70$ . The insets show the non-stacked spectra for the wavenumber range corresponding to the  $\text{CH}_3$  and  $\text{CH}$  stretching vibrations

Table S2: Summary of the FTIR bands and their assignments ( $\nu$ : stretching,  $\delta$ : scissoring,  $\rho$ : rocking modes of vibrations with "as" and "s" denoting the asymmetric and symmetric respectively).

Band position / cm <sup>-1</sup>	Assignment
2967	$\nu (\text{C} - \text{H}_3)\text{as}$
2931	$\nu (\text{C} - \text{H}_3)\text{s}$
2865	$\nu (\text{C} - \text{H})$
1693	$\nu (\text{C} = \text{O})$
1590	$\nu (\text{C} = \text{C})$
1464	$\delta (\text{C} - \text{H}_3)\text{as}$
1381	$\delta (\text{C} - \text{H}_3)\text{s}$
1333	$\delta (\text{C} - \text{H})$
1242	$\delta (\text{O} - \text{H})$
1163	$\nu (\text{C} - \text{C})$
1130	$\rho (\text{C} - \text{H}_3)$ and $\nu (\text{C} - \text{O})$

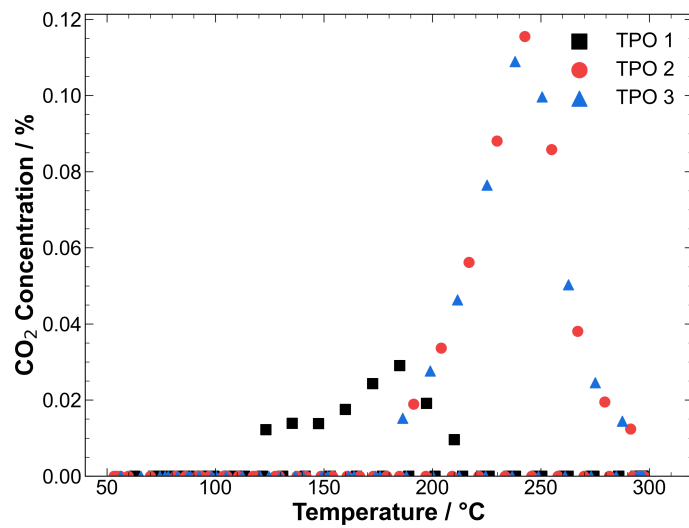


Figure S13: CO<sub>2</sub> concentrations during TPO experiments for  $x=0.25$ .

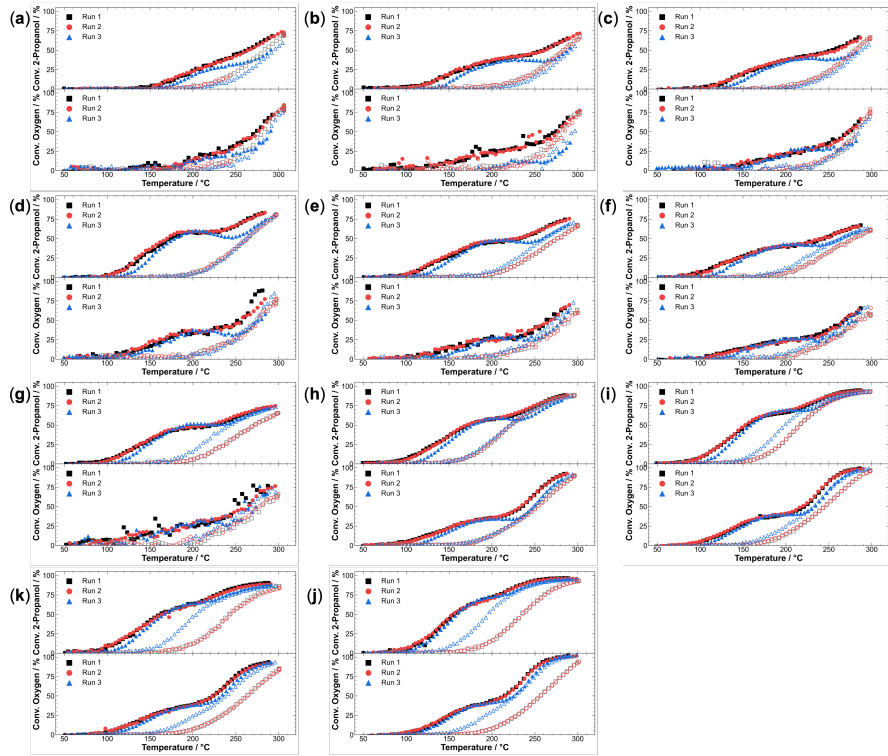


Figure S14: 2-Propanol and oxygen conversion during the dry (Run 1 and Run 2) and wet feed (Run 3) runs for (a)  $x=0.00$ , (b)  $x=0.05$ , (c)  $x=0.10$ , (d)  $x=0.15$ , (e)  $x=0.20$ , (f)  $x=0.25$ , (g)  $x=0.30$ , (h)  $x=0.40$ , (i)  $x=0.50$ , (j)  $x=0.60$  and (k)  $x=0.70$ . Filled symbols show data points during heating, empty characters show the behavior during cooling.

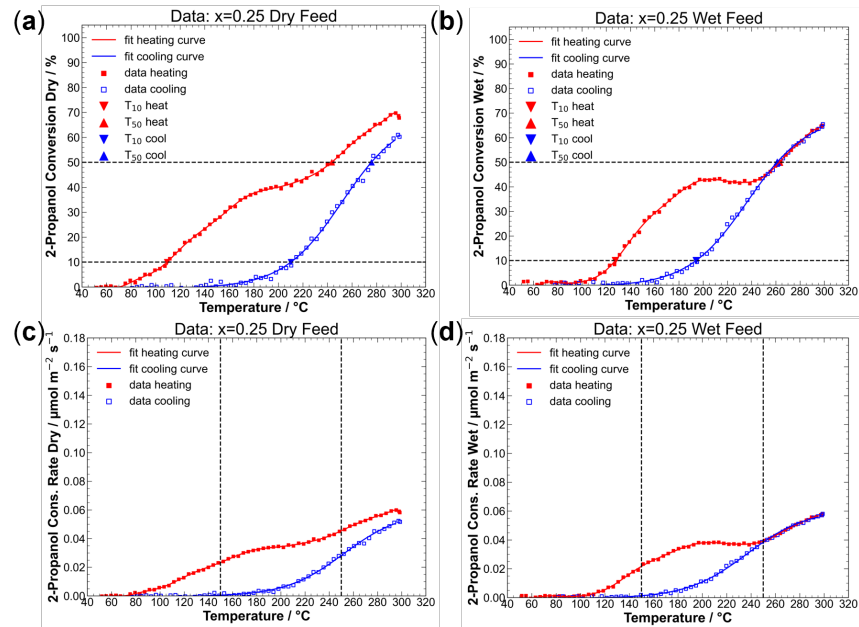


Figure S15: 2-Propanol conversions during heating and cooling and corresponding fits for  $x=0.25$  in (a) dry feed and (b) wet feed. 2-Propanol consumption rate fits for  $x=0.25$  in (c) dry feed and (d) wet feed.

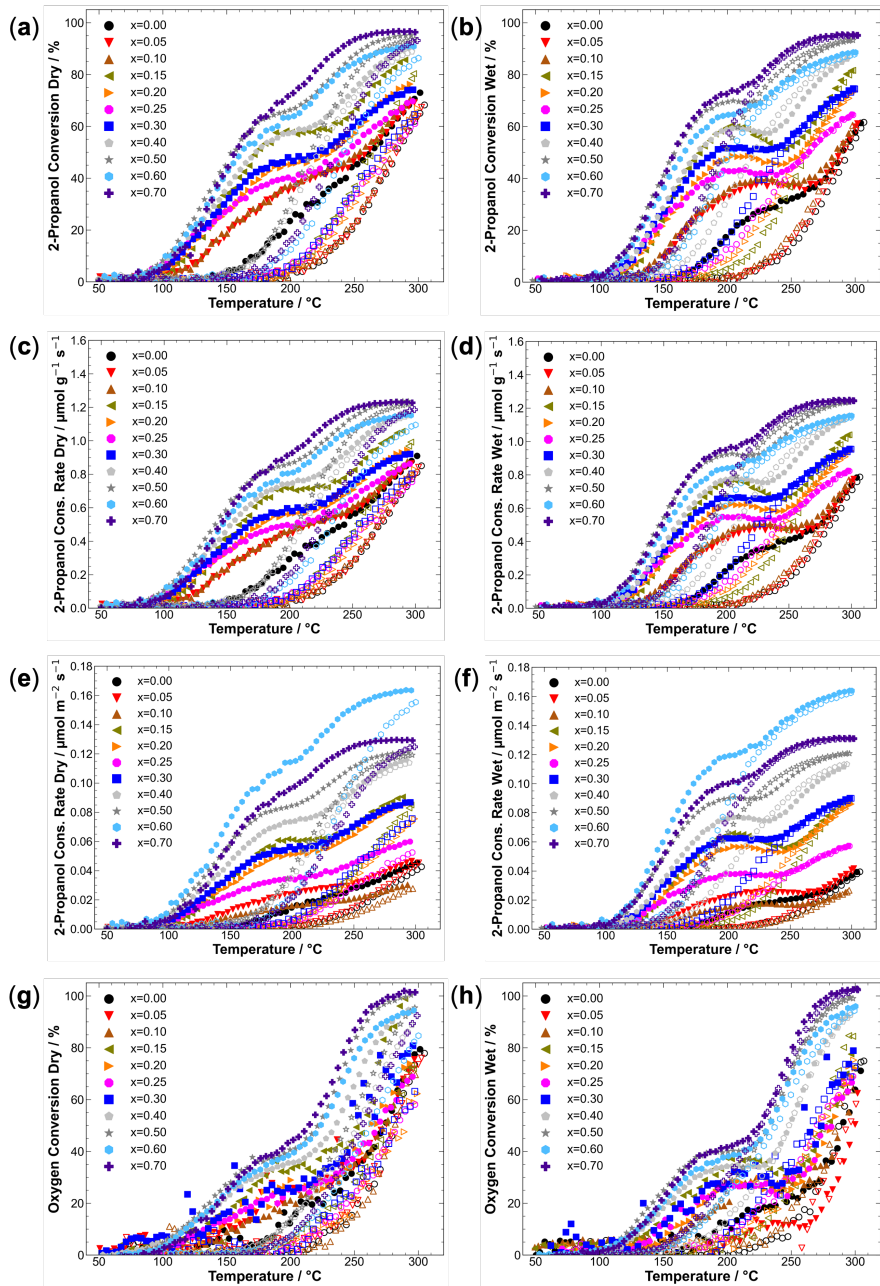


Figure S16: (a) 2-Propanol conversions in dry feed. (b) 2-Propanol conversions in wet feed. (c) Weight normalized 2-propanol consumption rates in dry feed. (d) Weight normalized 2-propanol consumption rates in wet feed. (e) Surface area normalized 2-propanol consumption rates in dry feed. (f) Surface area normalized 2-propanol consumption rates in wet feed. (g) Oxygen conversions in dry feed. (h) Oxygen conversions in wet feed. Filled symbols show data points during heating, empty characters show the behavior during cooling.

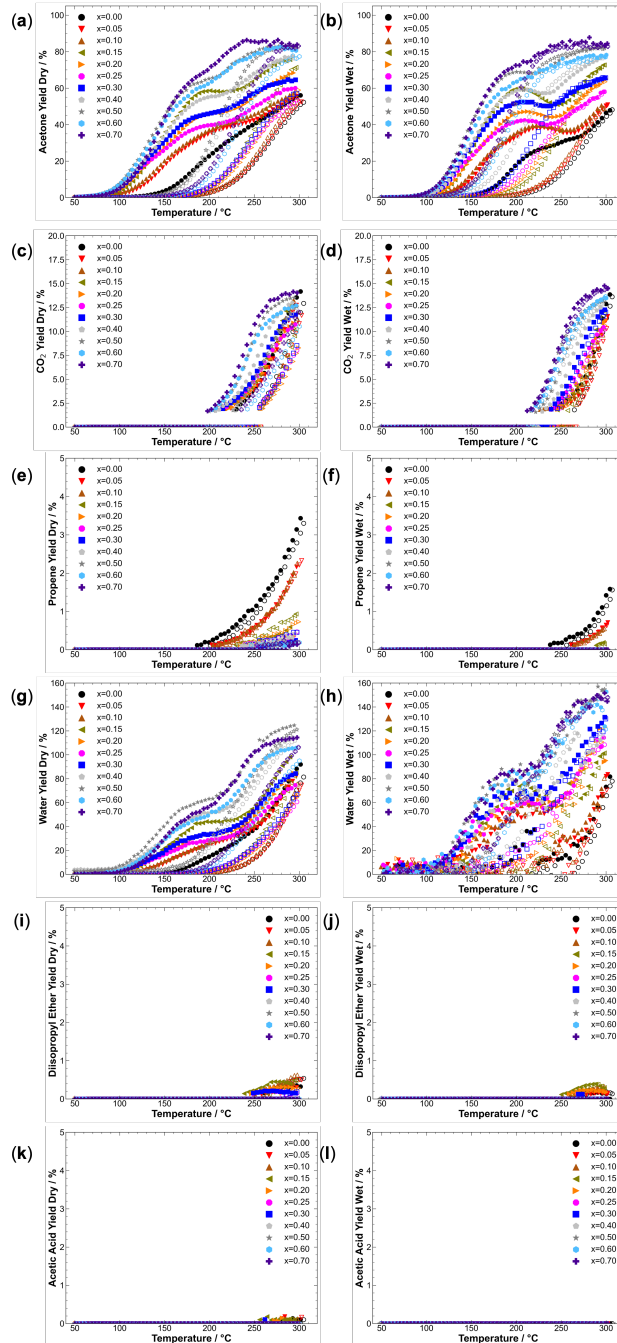


Figure S17: (a) Acetone yields in dry feed. (b) Acetone yields in wet feed. (c)  $\text{CO}_2$  yields in dry feed. (d)  $\text{CO}_2$  yields in wet feed. (e) Propene yields in dry feed. (f) Propene yields in wet feed. (g) Water yields in dry feed. (h) Water yields in wet feed. (i) Diisopropylether yields in dry feed. (j) Diisopropylether yields in wet feed. (k) Acetic acid yields in dry feed. (l) Acetic acid yields in wet feed. Filled symbols show data points during heating, empty characters show the behavior during cooling.

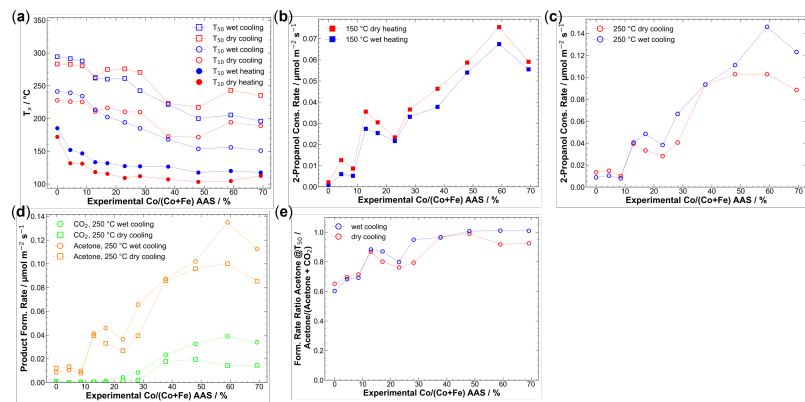


Figure S18: (a)  $T_{10}$  values during heating and cooling and  $T_{50}$  during cooling in dry and wet feed plotted against the experimental Co content derived from AAS. (b) Surface-area normalized 2-propanol consumption rates at 150 °C during dry and wet feed heating plotted against the experimental Co content derived from AAS. (c) Surface-area normalized 2-propanol consumption rates at 250 °C during dry and wet feed cooling plotted against the experimental Co content derived from AAS.

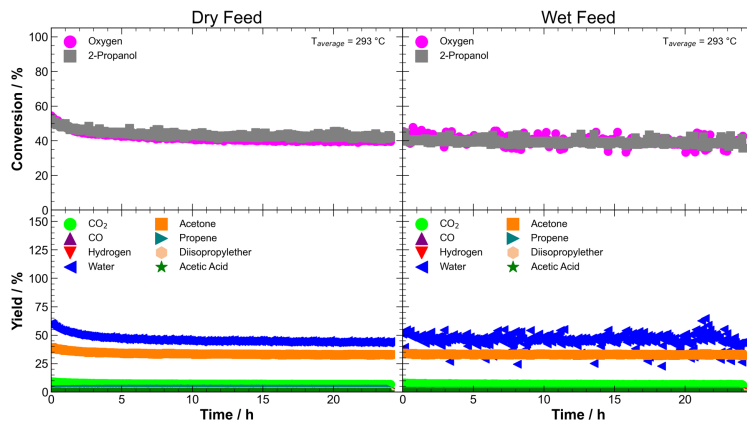


Figure S19: Stability dataset for  $x=0.00$ ; conversions of 2-propanol and oxygen (top row) and product yields (bottom row) during dry and wet runs.

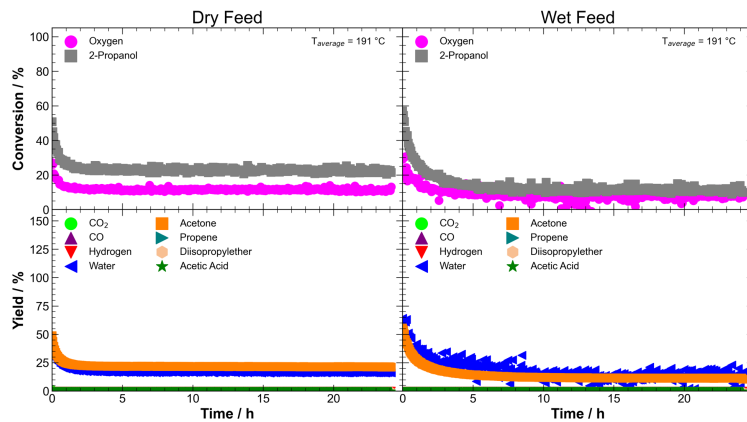


Figure S20: Stability dataset for  $x=0.25$ ; conversions of 2-propanol and oxygen (top row) and product yields (bottom row) during dry and wet runs.

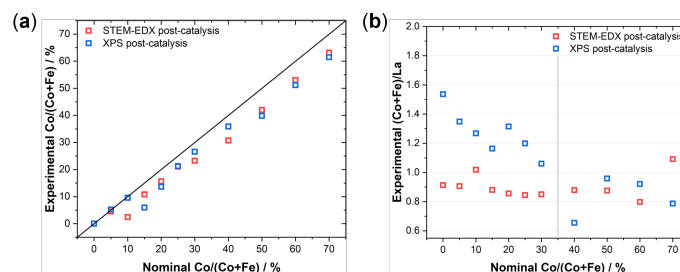


Figure S21: (a) Comparison of nominal and experimental Co content derived from (S)TEM-EDX and XPS after catalysis. (b) Ratio of B-cations to A-cations derived from (S)TEM-EDX and XPS after catalysis.

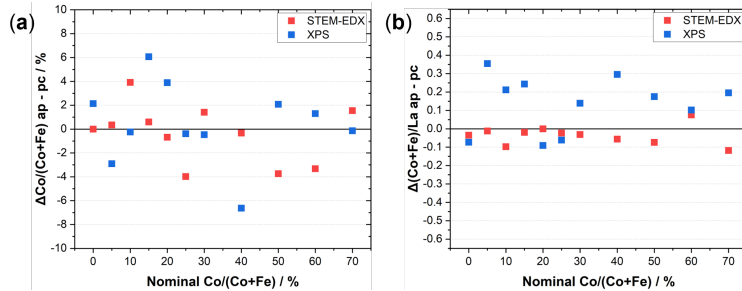


Figure S22: (a) Differences in experimental Co content between the cases of as-prepared (ap) and post-catalysis (pc). (b) Differences in ratio of B-cations to A-cations between as-prepared (ap) and post-catalysis (pc).

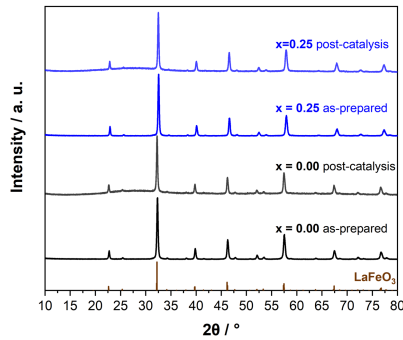


Figure S23: XRD patterns of  $x=0.00$  and  $x=0.25$  in the as-prepared state and in the post-catalysis state after the steady-state measurements shown in Figure S19 and Figure S20.

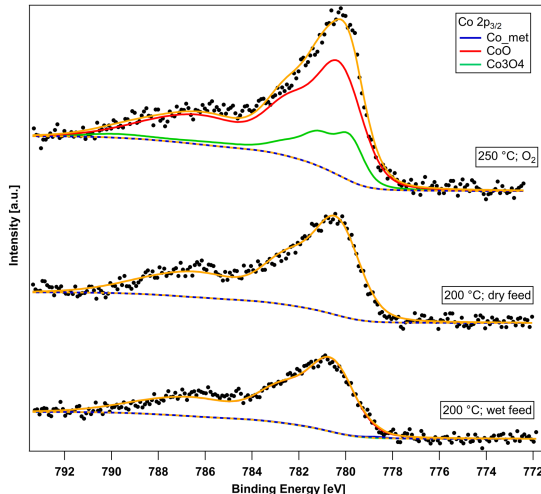


Figure S24: Linear combination fits (see main text) to determine the occupancy of different Co oxidation states during dry feed and wet feed as well as during the pre-treatment step at  $250 {}^\circ\text{C}$  in  $0.25 \text{ mbar O}_2$ . For the wet and dry feed, the Co is purely  $\text{CoO}$ , seen by an overlap of the red line of the  $\text{CoO}$  components with the overall fitting curve (orange).

## **VII. SI: Dynamics of Reactive Oxygen Species on Cobalt-Containing Spinel Oxides in Cyclic CO Oxidation**

The main text to this Supporting Information is shown in Chapter 7.

Dynamics of Reactive Oxygen Species on Cobalt-Containing Spinel Oxides in Cyclic CO  
Oxidation

Maik Dreyer<sup>1</sup>, Anna Rabe<sup>1</sup>, Eko Budiyanto<sup>2</sup>, Klaus Friedel Ortega<sup>3</sup>, Sharif Najafishirtari<sup>1</sup>,  
Harun Tüysüz<sup>2</sup>, Malte Behrens<sup>1,3,4\*</sup>

<sup>1</sup> Faculty for Chemistry, Inorganic Chemistry, University of Duisburg-Essen, 45141 Essen,  
Germany

<sup>2</sup> Max-Planck-Institut für Kohlenforschung, Kaiser-Wilhelm Platz 1, 45470 Mülheim an der  
Ruhr, Germany

<sup>3</sup> Institute of Inorganic Chemistry, Christian-Albrechts-Universität zu Kiel, 24118 Kiel,  
Germany

<sup>4</sup> CENIDE, Center for Nanointegration, University of Duisburg-Essen, 47057 Duisburg,  
Germany

\*Corresponding author: [mbehrens@ac.uni-kiel.de](mailto:mbehrens@ac.uni-kiel.de)

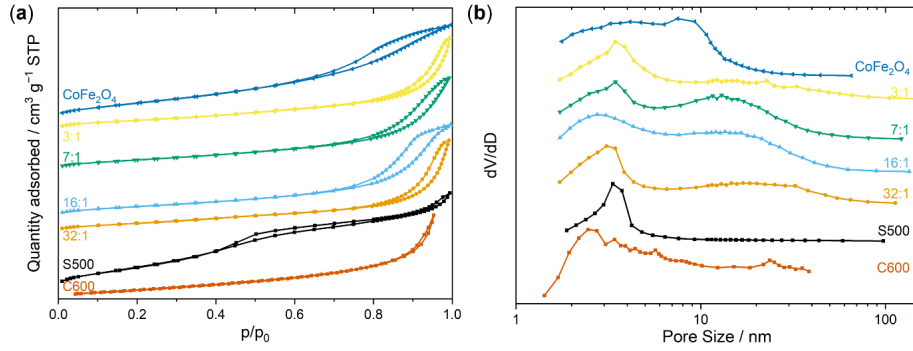


Figure S1: Normalized  $N_2$  adsorption-desorption isotherms (a) and normalized BJH pore size distribution (b).

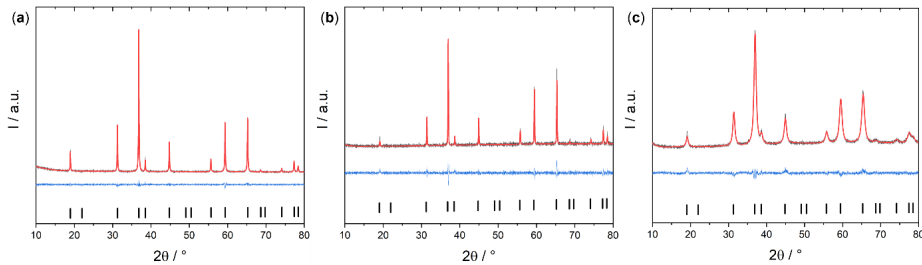


Figure S2: Rietveld refinement plots of C600 (a), P800 (b) and S500 (c).

Table S1. Criteria of fit for the Rietveld Refinements of the X-ray diffraction patterns of the calcined samples.

Sample	R <sub>exp</sub>	R <sub>wp</sub>	R <sub>p</sub>	R <sub>exp'</sub>	R <sub>wp'</sub>	R <sub>p'</sub>	GOF	R <sub>Bragg</sub>
C600	5.67	8.20	6.35	9.10	13.17	11.22	1.45	1.527
P800	9.59	13.85	10.83	15.18	21.94	21.05	1.45	2.175
C500	3.57	4.09	3.23	6.34	7.27	6.60	1.15	1.262

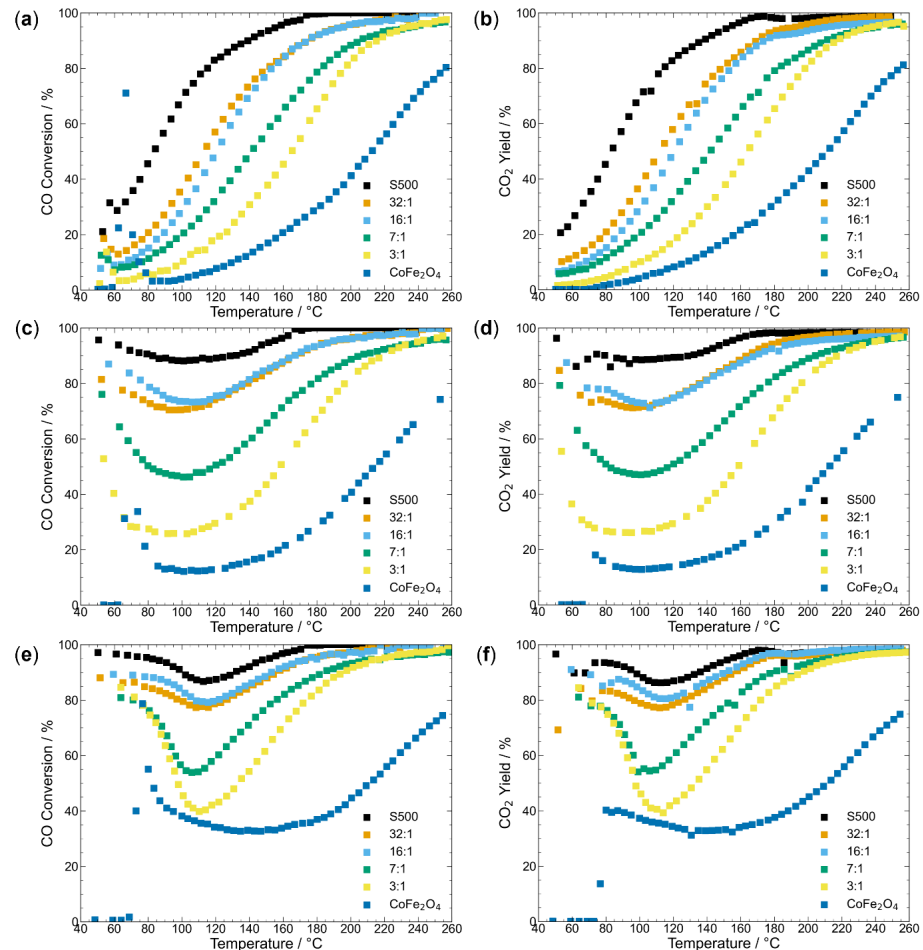


Figure S3: Comparison of CO conversion and CO<sub>2</sub> yield for the SBA-15 templated catalyst series. CO conversion in the 1st run (a). CO<sub>2</sub> yield in the 1st run (b). CO conversion in the 2nd run (c). CO<sub>2</sub> yield in the 2nd run (d). CO conversion in the 3rd run (e). CO<sub>2</sub> yield in the 3rd run (f).

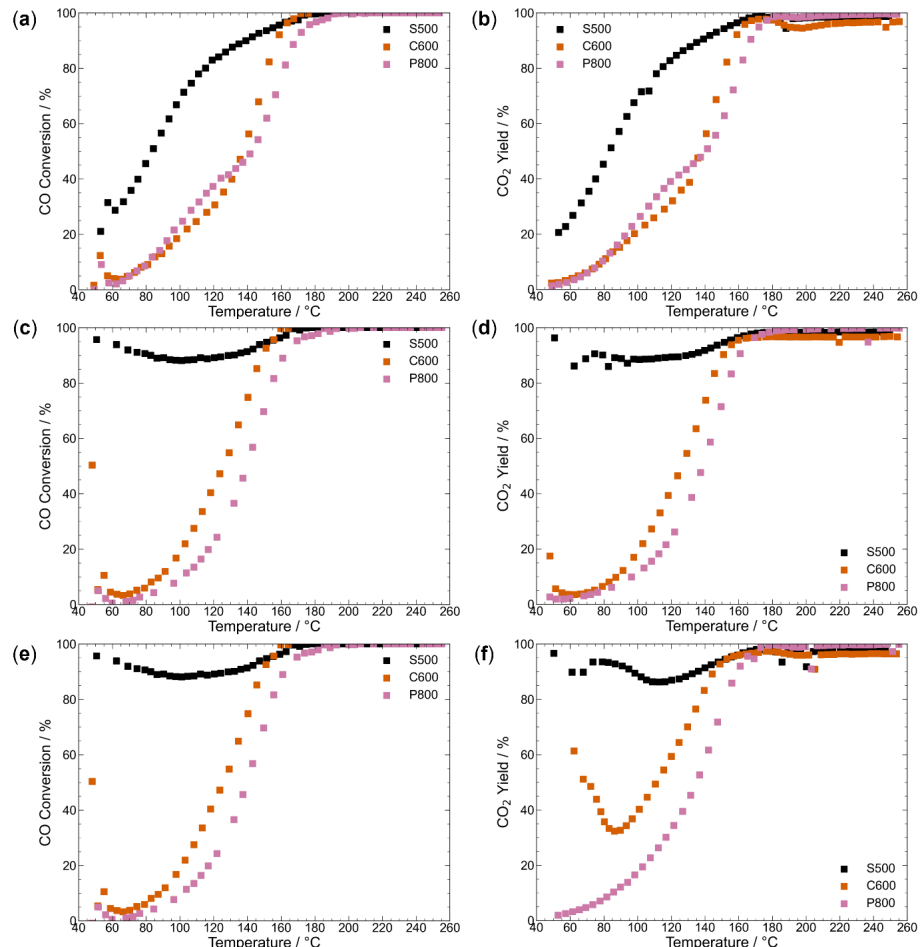


Figure S4: Comparison of CO conversion and CO<sub>2</sub> yield for the different Co<sub>3</sub>O<sub>4</sub> catalysts. CO conversion in the 1st run (a). CO<sub>2</sub> yield in the 1st run (b). CO conversion in the 2nd run (c). CO<sub>2</sub> yield in the 2nd run (d). CO conversion in the 3rd run (e). CO<sub>2</sub> yield in the 3rd run (f).

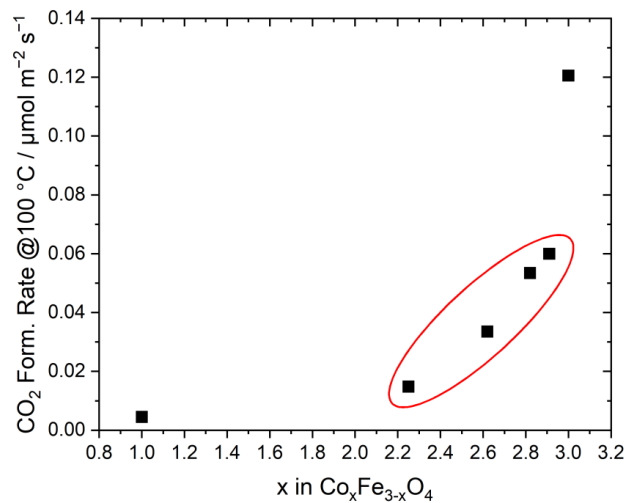


Figure S5: Correlation between  $\text{CO}_2$  formation rate at  $100^\circ\text{C}$  and the cobalt content in the spinel materials. The red circle shows for clarity where a linear correlation between reaction rate and Co content can be observed.

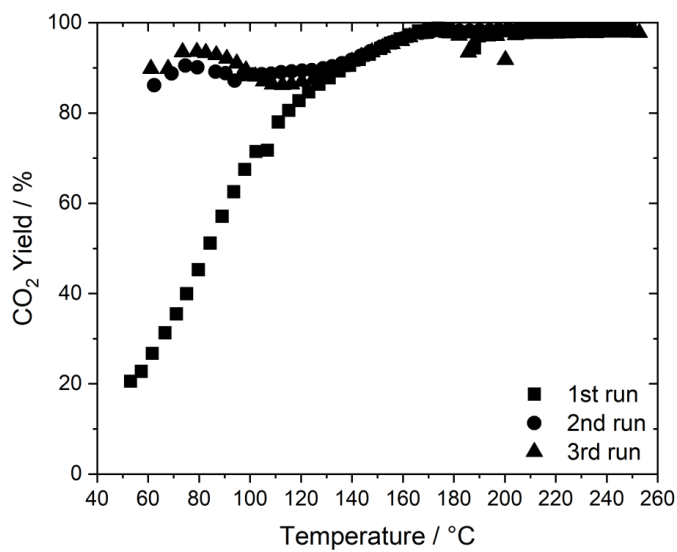


Figure S6:  $\text{CO}$  oxidation activity in the different runs for S500.

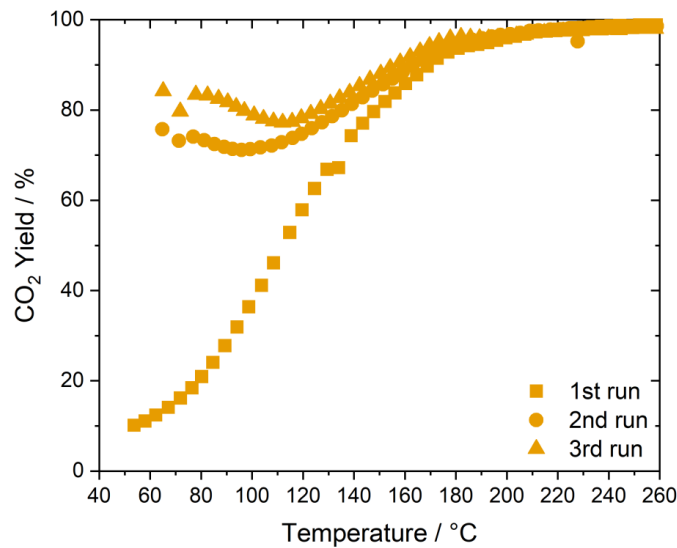


Figure S7: CO oxidation activity in the different runs for SBA-15 templated Co:Fe 32:1.

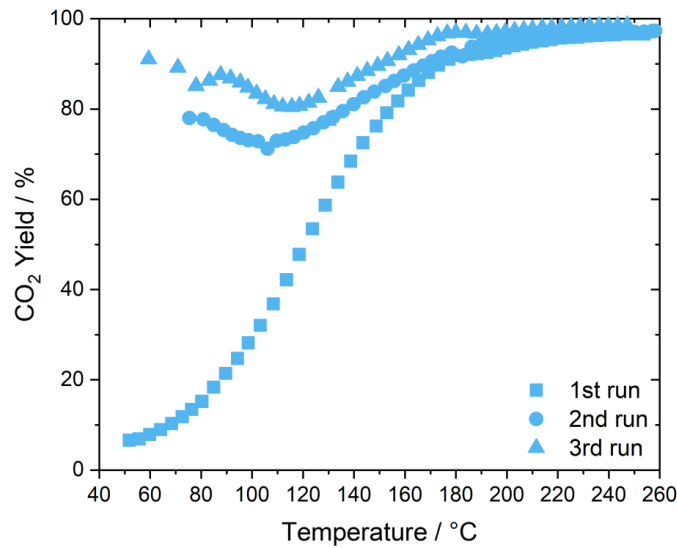


Figure S8: CO oxidation activity in the different runs for SBA-15 templated Co:Fe 16:1.

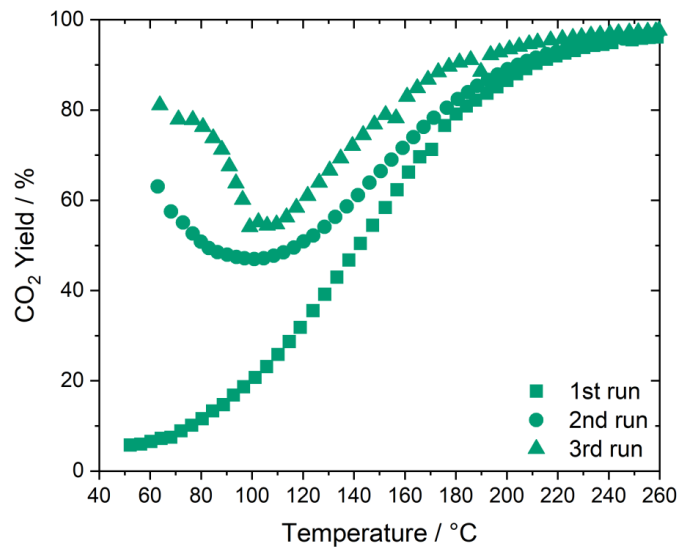


Figure S9: CO oxidation activity in the different runs for SBA-15 templated Co:Fe 7:1.

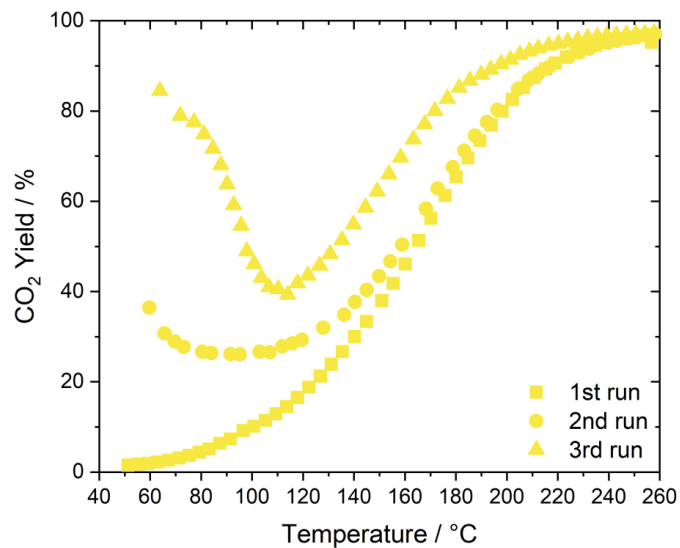


Figure S10: CO oxidation activity in the different runs for SBA-15 templated Co:Fe 3:1.

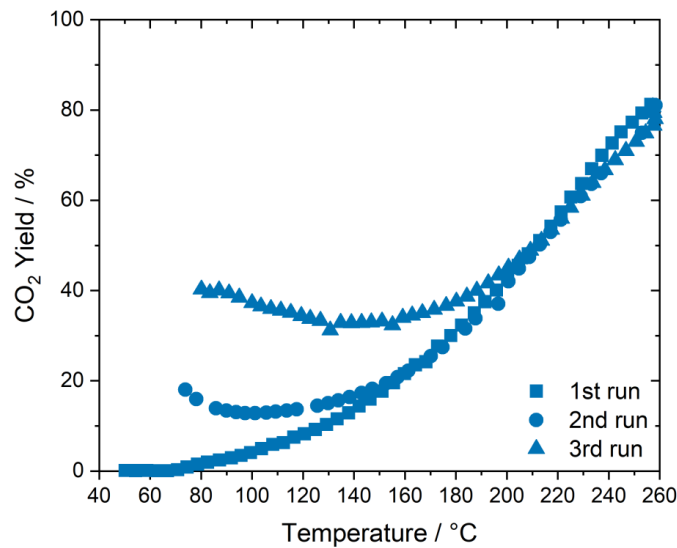


Figure S11: CO oxidation activity in the different runs for SBA-15 templated CoFe<sub>2</sub>O<sub>4</sub>.

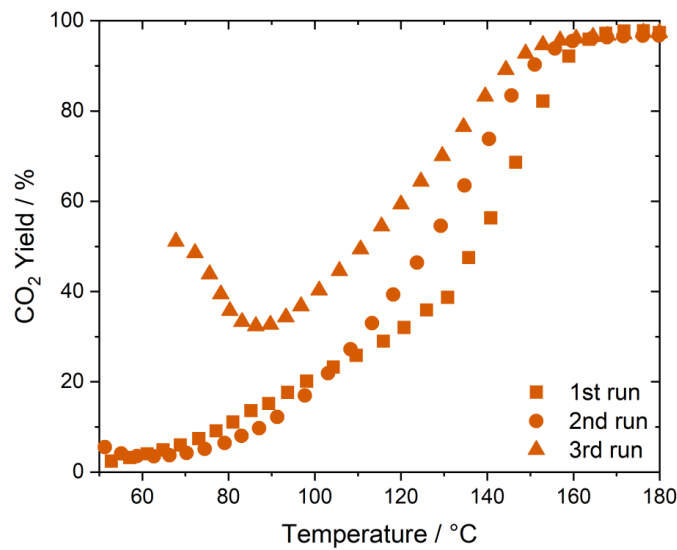


Figure S12: CO oxidation activity in the different runs for Co<sub>3</sub>O<sub>4</sub> C600.

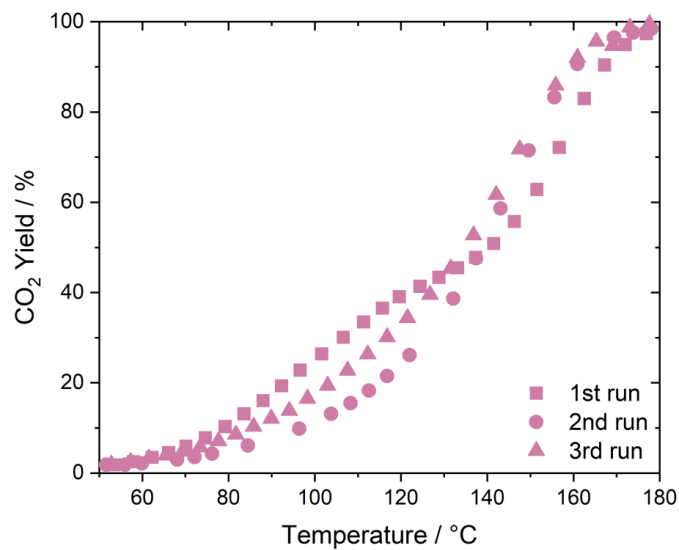


Figure S13: CO oxidation activity in the different runs for Co<sub>3</sub>O<sub>4</sub> P800.

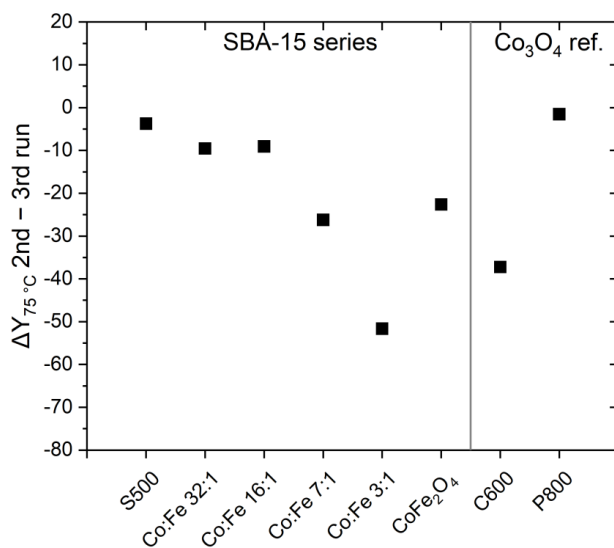


Figure S14: Differences in conversion at 75 °C between the 2nd and the 3rd run of CO oxidation.

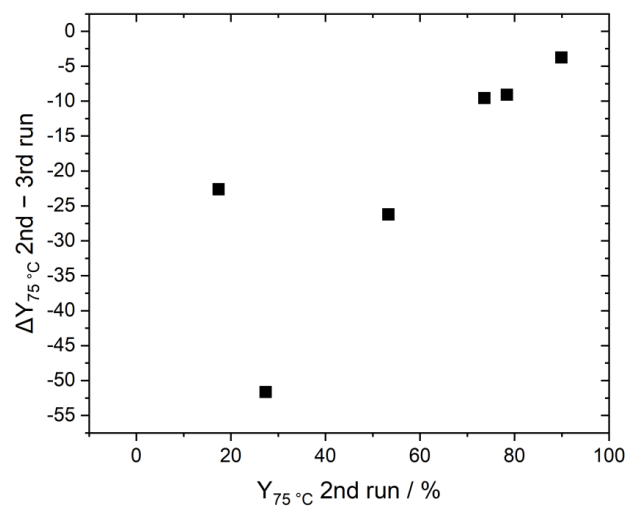
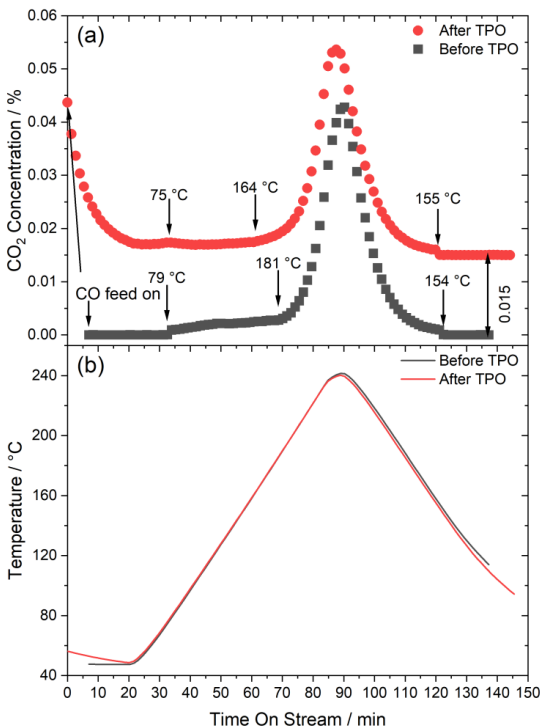


Figure S15: Conversion at 75 °C in the 2nd run compared to the activation between 2nd and 3rd run for the SBA-15 templated materials.



*Figure S16: CO temperature programmed reduction of C600 without TPO and after TPO showing the evolved CO<sub>2</sub> concentration (a) and the temperature in the reactor (b). The time on stream was calibrated based on the time when the maximum temperature was reached.*

The CO-TPR experiments shown in Figure S16 were performed in a self-constructed apparatus consisting of a gas dosing unit (HovaGAS N G6 VOC-S, IAS GmbH, Germany) and a Tube Furnace MTF 10/25/130 (Carbolite Gero, Neuhausen, Germany) which is placed in a heating cabinet Thermocenter TC100 (SalvisLab, Rotkreuz, Switzerland). The reaction mixture, either going through or by-passing the reactor, was analyzed on a downstream dual-carrier gas Fusion Micro GC (Inficon GmbH, Bad Ragaz, Switzerland) equipped with four separation modules (2x Rt-Molsieve 5A, 1x Stabilwax DB, 1x Rt-Q-Bond). The catalyst mixture consisted of 60 mg (sieve fraction 250–355 µm) calcined catalyst C600 sample diluted with 300 mg of silicon carbide (>355 µm) and was placed in a quartz reactor (inner diameter = 8 mm) on a quartz wool support. The total gas flow in all segments of the catalytic experiment was 80 mL<sub>n</sub> min<sup>-1</sup>.

The protocol consisted of two different exposures to a reaction mixture of 2% CO balanced in N<sub>2</sub>. Prior to the 1st TPR, the catalyst/SiC mixture was pre-treated by heating at 3 °C min<sup>-1</sup> in N<sub>2</sub> from room temperature to 100 °C, which was kept constant for 1 h. Thereafter, the sample was cooled down in N<sub>2</sub> to 50 °C. The temperature was stabilized in a N<sub>2</sub> flow and afterward the

reaction mixture was purged for 15 min to equilibrate the gas composition. Thereafter, the temperature was increased to 250 °C at a heating rate of 3 °C min<sup>-1</sup> for the 1st run. Then, the sample was cooled in the reaction mixture to 50 °C with at a heating rate of 3 °C min<sup>-1</sup> the temperature was equilibrated in N<sub>2</sub>.

For the preparation of the 2nd run, the sample was cooled down at a heating rate of 3 °C min<sup>-1</sup> in the reactive atmosphere to 100 °C, purged with N<sub>2</sub> for 5 min and then temperature-programmed oxidation was performed in 20% O<sub>2</sub> in N<sub>2</sub> to a maximum temperature of 500 °C with a heating rate of 10 °C min<sup>-1</sup>. The temperature of 500 °C was chosen to mimic the calcination protocol of the SBA-15 templated materials. The maximum temperature was kept constant for 30 min after which the sample was cooled down with a heating rate of 10 °C min<sup>-1</sup> to 50 °C in 20% O<sub>2</sub> balanced with N<sub>2</sub> and temperature was equilibrated in N<sub>2</sub>. Afterward, the sample was purged with the reaction mixture for 15 min at 50 °C. The 3rd run was performed by increasing the temperature to 250 °C at a heating rate of 3 °C min<sup>-1</sup> and a 5 min dwell at the maximum temperature. Afterward, the sample was again cooled down at a heating rate of 3 °C min<sup>-1</sup> in the reactive atmosphere to 50 °C.

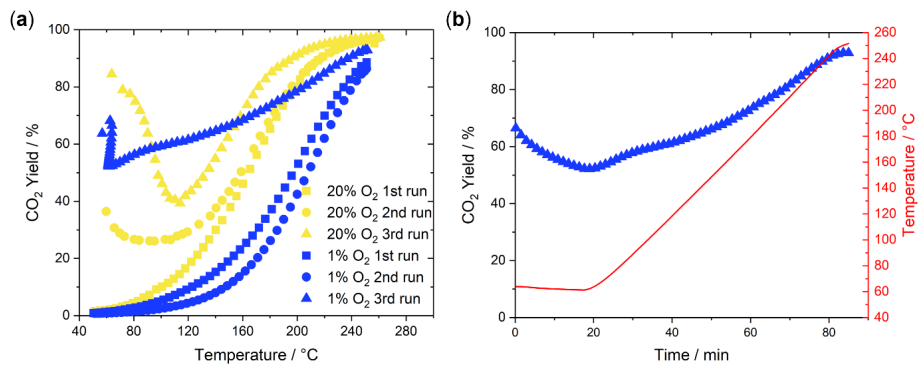


Figure S17: (a) Initial measurement of 3:1 in the cyclic CO oxidation in 2% CO and 20% O<sub>2</sub> in comparison to a new measurement in 2% CO and 1% O<sub>2</sub> performed on another setup. (b) Representation of Run 3 in 1% O<sub>2</sub> versus time.

The data shown in Figure S17 for 1% O<sub>2</sub> are derived from another instrument compared to transient oxidation curves in Figures 2-6 and S6 to S13 and 20% O<sub>2</sub> in the same Figure as the originally used instrument was not available. Due to its unfavorable gas switching properties, the U-shaped curve is clearly seen only if the conversion is plotted versus time as the conversion changes already during the isothermal period at the beginning of the experiment. The measurements were performed in a home-built apparatus consisting of a gas dosing unit (HovaGAS N G6 VOC-S, IAS GmbH, Germany) and a Tube Furnace MTF 10/25/130 (Carbolite Gero, Neuhausen, Germany) which is placed in a heating cabinet Thermocenter TC100 (SalvisLab, Rotkreuz, Switzerland). The reaction mixture, either going through or bypassing the reactor, was analyzed on a downstream dual-carrier gas Fusion Micro GC (Inficon GmbH, Bad Ragaz, Switzerland) equipped with four separation modules (2x Rt-Molsieve 5A, 1x Stabilwax DB, 1x Rt-Q-Bond). The catalyst mixture consisted of 60 mg (sieve fraction 250–355 µm) calcined catalyst C600 sample diluted with 300 mg of silicon carbide (>355 µm) and was placed in a quartz reactor (inner diameter = 8 mm) on a quartz wool support. The total gas flow in all segments of the catalytic experiment was 80 mL min<sup>-1</sup>.

The protocol consisted of three different exposures to a reaction mixture of (2% CO and 1% O<sub>2</sub> balanced in N<sub>2</sub>). Prior to the 1st run, the catalyst/SiC mixture was pre-treated by heating at 3 °C min<sup>-1</sup> in N<sub>2</sub> from room temperature to 100 °C, which was kept constant for 1 h. Thereafter, the sample was cooled down in N<sub>2</sub> to 50 °C. The temperature was stabilized in a N<sub>2</sub> flow and afterward the reaction mixture was purged for 15 min to equilibrate the gas composition. Thereafter, the temperature was increased to 250 °C at a heating rate of 3 °C min<sup>-1</sup> for the 1st run. Then, the sample was cooled in the reaction mixture to 50 °C with a heating rate of 3 °C min<sup>-1</sup> the temperature was equilibrated in N<sub>2</sub>.

Afterward, the sample was purged with the reaction mixture for 15 min at 45 °C and a 2nd consecutive run was performed by increasing the temperature to 250 °C at a heating rate of 3 °C min<sup>-1</sup> and 5 min dwell time at the maximum temperature.

For the preparation of the 3rd run, the sample was again cooled down at a heating rate of 3 °C min<sup>-1</sup> in the reactive atmosphere to 100 °C, purged with N<sub>2</sub> for 5 min and then temperature-programmed oxidation was performed in 20% O<sub>2</sub> in N<sub>2</sub> to a maximum temperature of 500 °C with a heating rate of 10 °C min<sup>-1</sup>. The temperature of 500 °C was chosen to mimic the calcination protocol of the SBA-15 templated materials. The maximum temperature was kept constant for 30 min after which the sample was cooled down with a heating rate of 10 °C min<sup>-1</sup> to 50 °C in 20% O<sub>2</sub> balanced with N<sub>2</sub> and temperature was equilibrated in N<sub>2</sub>. Afterward, the sample was purged with the reaction mixture for 15 min at 50 °C. The 3rd run was performed by increasing the temperature to 250 °C at a heating rate of 3 °C min<sup>-1</sup> and a 5 min dwell at the maximum temperature. Afterward, the sample was again cooled down at a heating rate of 3 °C min<sup>-1</sup> in the reactive atmosphere to 50 °C.

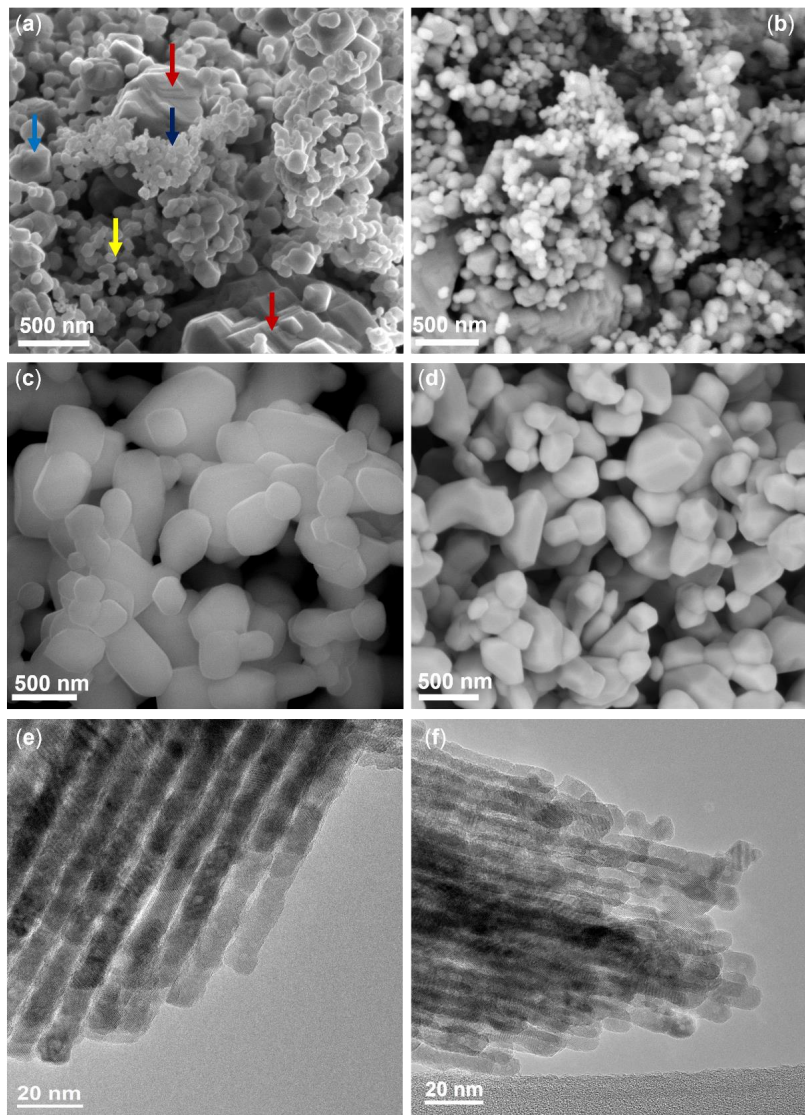


Figure S18: (a) SEM image of C600 before catalysis. (b) SEM image of C600 after catalysis. (c) SEM image of C800 before catalysis. (d) TEM image of C800 after catalysis. (e) SEM image of S500 before catalysis. (f) TEM image of S500 after catalysis. Figures (a), (c) and (e) are shown in the main text as Figures 1b, 1c and 1d.

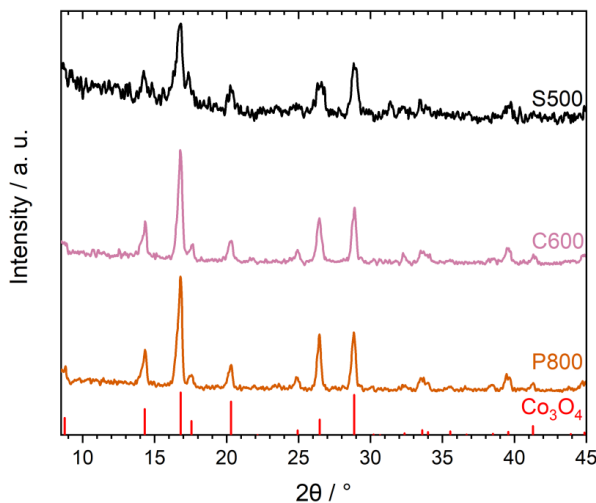


Figure S19: XRD patterns of the spent catalysts.

XRD patterns of the spent catalysts shown in Figure S19 were recorded on a STOE transmission diffractometer STADI P in Debye-Scherrer geometry at room temperature using a curved image-plate position sensitive detector ( $R = 150$  mm, Ge crystal monochromator filtered MoK $\alpha$ 1 radiation). A  $2\theta$  range of  $2 \times 70^\circ$  (only positive values were shown in the range between  $8.5$  and  $45^\circ$ ) and a step width of  $0.0015^\circ$  were applied with an overall counting time of 1800 s.

## **VIII. SI: Beneficial Effects of Low Iron Contents on Cobalt-Containing Spinel Catalysts in the Gas Phase 2-Propanol Oxidation**

The main text to this Supporting Information is shown in Chapter 8.

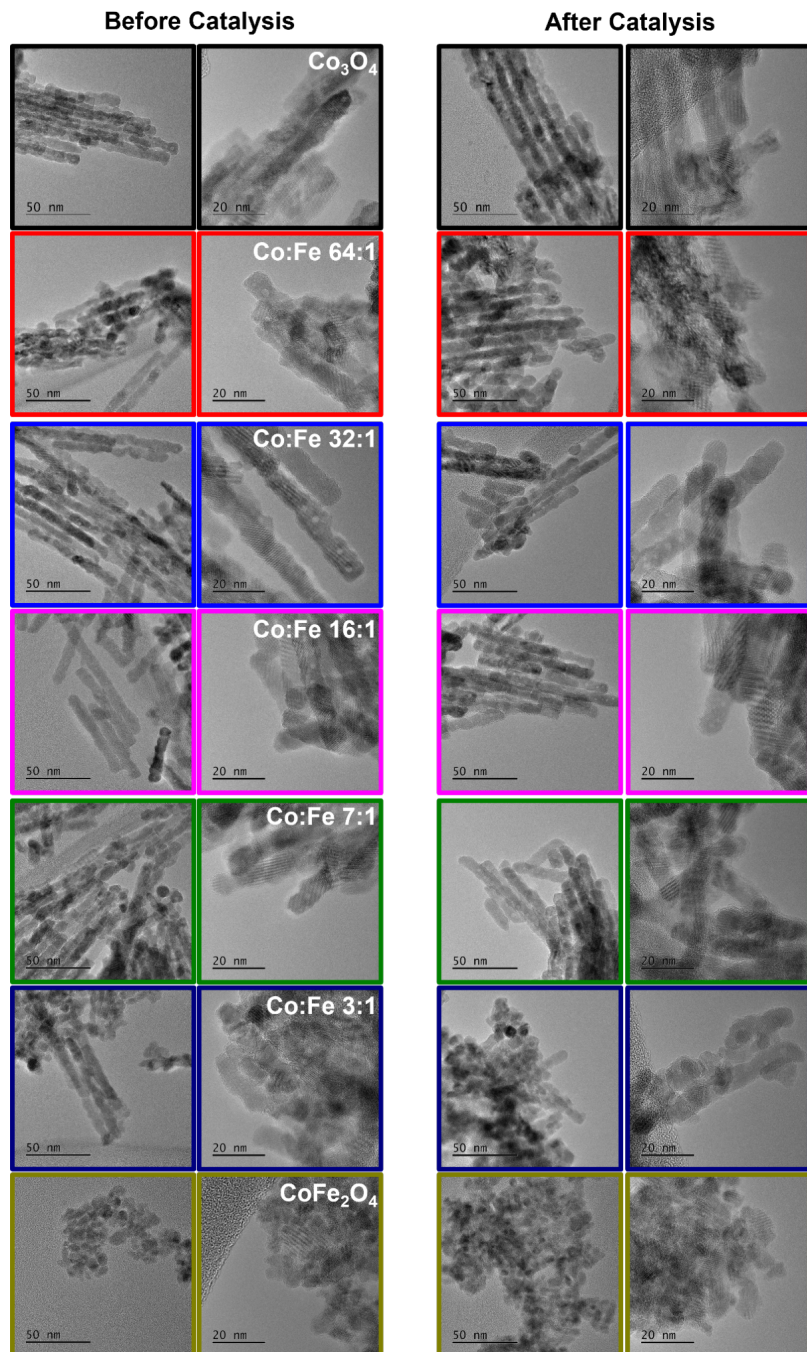


Figure S1: TEM micrographs before catalysis (left columns) and after catalysis (right columns) for the catalysts presented in the study.

S1

Table S1: BET surface areas from<sup>[1]</sup> and experimental Co/(Co+Fe) ratios determined by the catalysts' STEM-EDX and XPS.

Sample	S <sub>BET</sub> / m <sup>2</sup> g <sup>-1</sup>	Co/(Co+Fe) <sub>nominal</sub> / %	Co/(Co+Fe) <sub>EDX</sub> / %	Co/(Co+Fe) <sub>XPS</sub> / %
Co <sub>3</sub> O <sub>4</sub>	107 <sup>[1]</sup>	100.0	100.0	100.0
Co:Fe 64:1	128	98.5	97.2	98.4
Co:Fe 32:1	118 <sup>[1]</sup>	96.9	95.2	96.0
Co:Fe 16:1	103 <sup>[1]</sup>	94.1	93.1	93.7
Co:Fe 7:1	113 <sup>[1]</sup>	87.5	84.8	84.0
Co:Fe 3:1	125 <sup>[1]</sup>	75.0	75.9	76.8
CoFe <sub>2</sub> O <sub>4</sub>	178 <sup>[1]</sup>	33.3	27.8	46.6

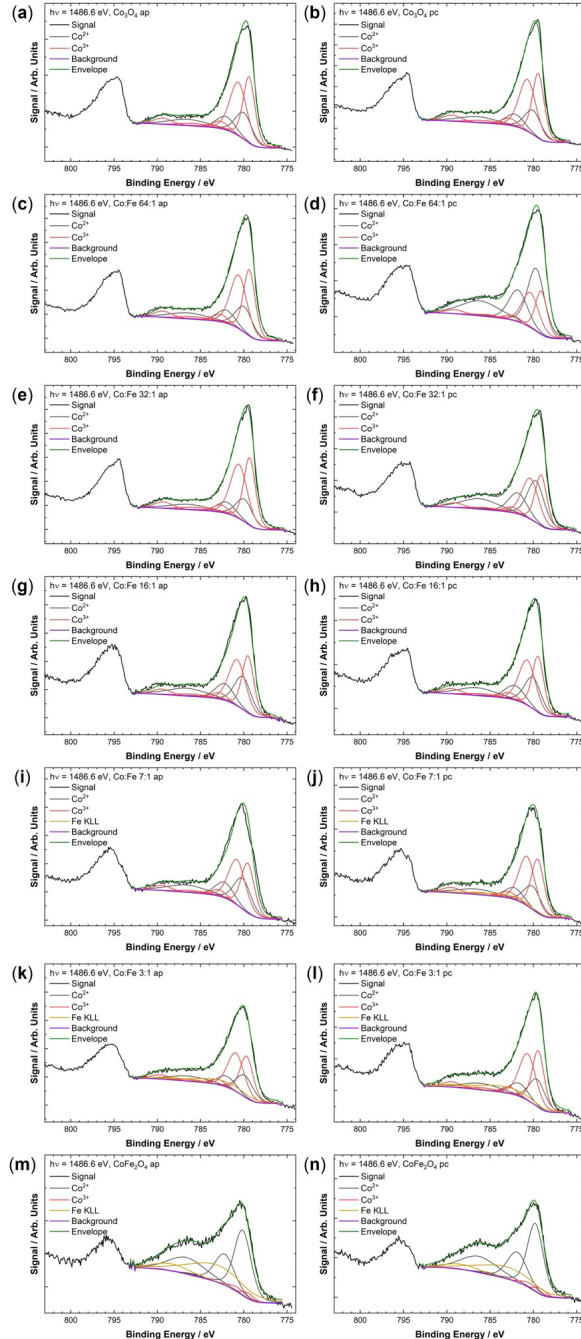


Figure S2: Co 2p XP spectra in the as-prepared state (left column) and in the post-catalysis state (right column) for (a) and (b)  $\text{Co}_3\text{O}_4$ , (c) and (d)  $\text{Co:Fe } 64:1$ , (e) and (f)  $\text{Co:Fe } 32:1$ , (g) and (h)  $\text{Co:Fe } 16:1$ , (i) and (j)  $\text{Co:Fe } 7:1$ , (k) and (l)  $\text{Co:Fe } 3:1$ , (m) and (n)  $\text{CoFe}_2\text{O}_4$ .

S3

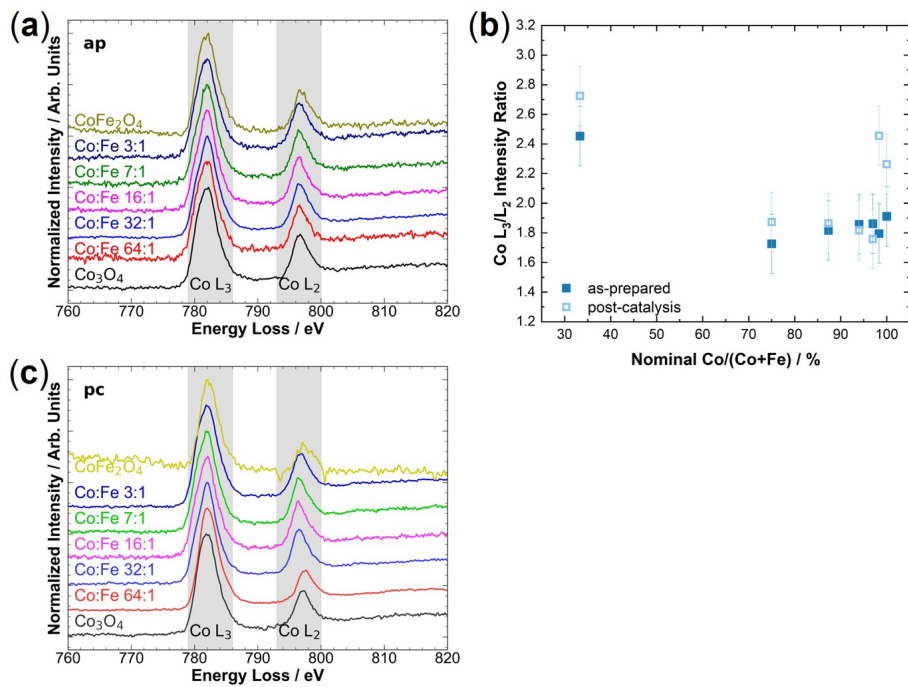


Figure S3: EELS spectra in the as-prepared (ap) state (a), Co L<sub>3</sub>/L<sub>2</sub> intensity ratios from integration of the EELS spectra (b), EELS spectra in the post-catalysis (pc) state (c).

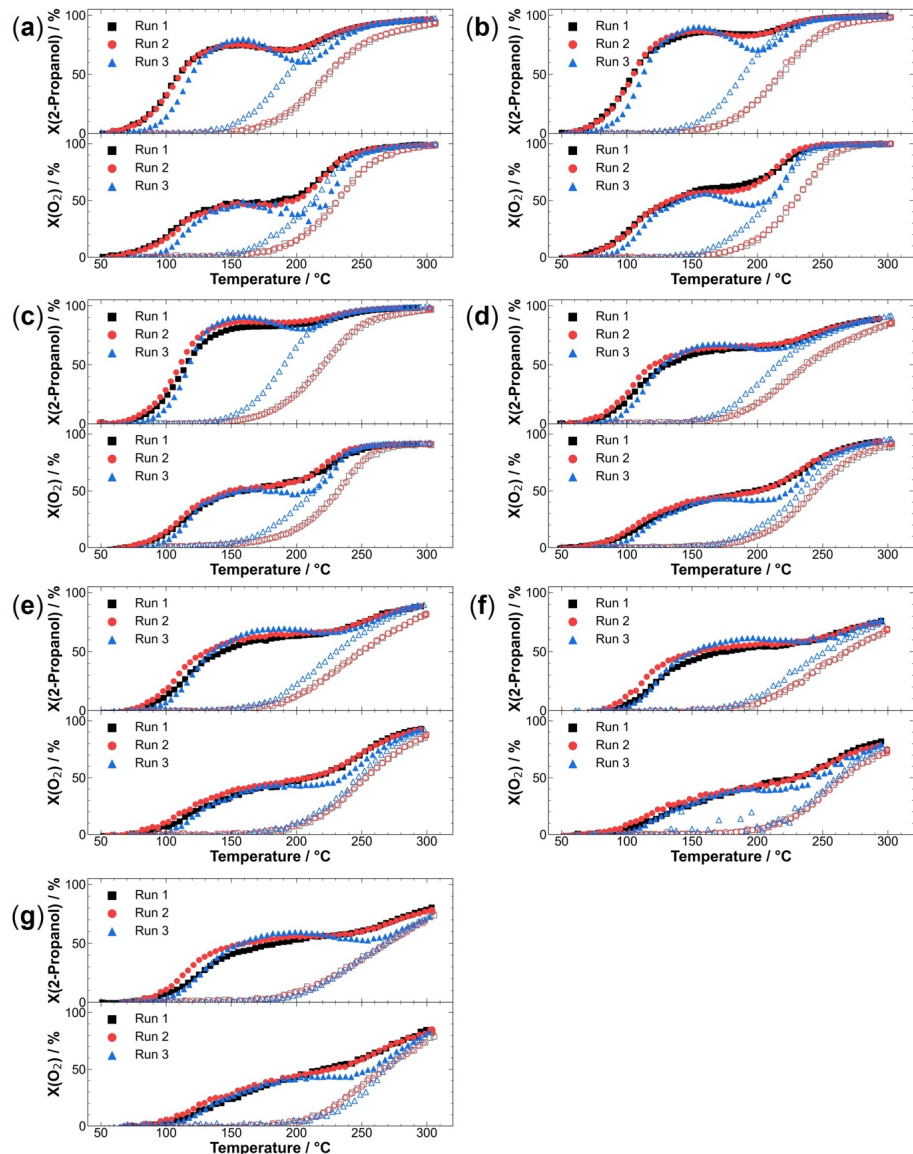


Figure S4: 2-Propanol and oxygen conversion during the dry (Run 1 and Run 2) and wet feed (Run 3) runs for (a)  $\text{Co}_3\text{O}_4$ , (b)  $\text{Co:Fe } 64:1$ , (c)  $\text{Co:Fe } 32:1$ , (d)  $\text{Co:Fe } 16:1$ , (e)  $\text{Co:Fe } 7:1$ , (f)  $\text{Co:Fe } 3:1$ , (g)  $\text{CoFe}_2\text{O}_4$ . Filled symbols show data points during heating. Empty characters show the behavior during cooling.

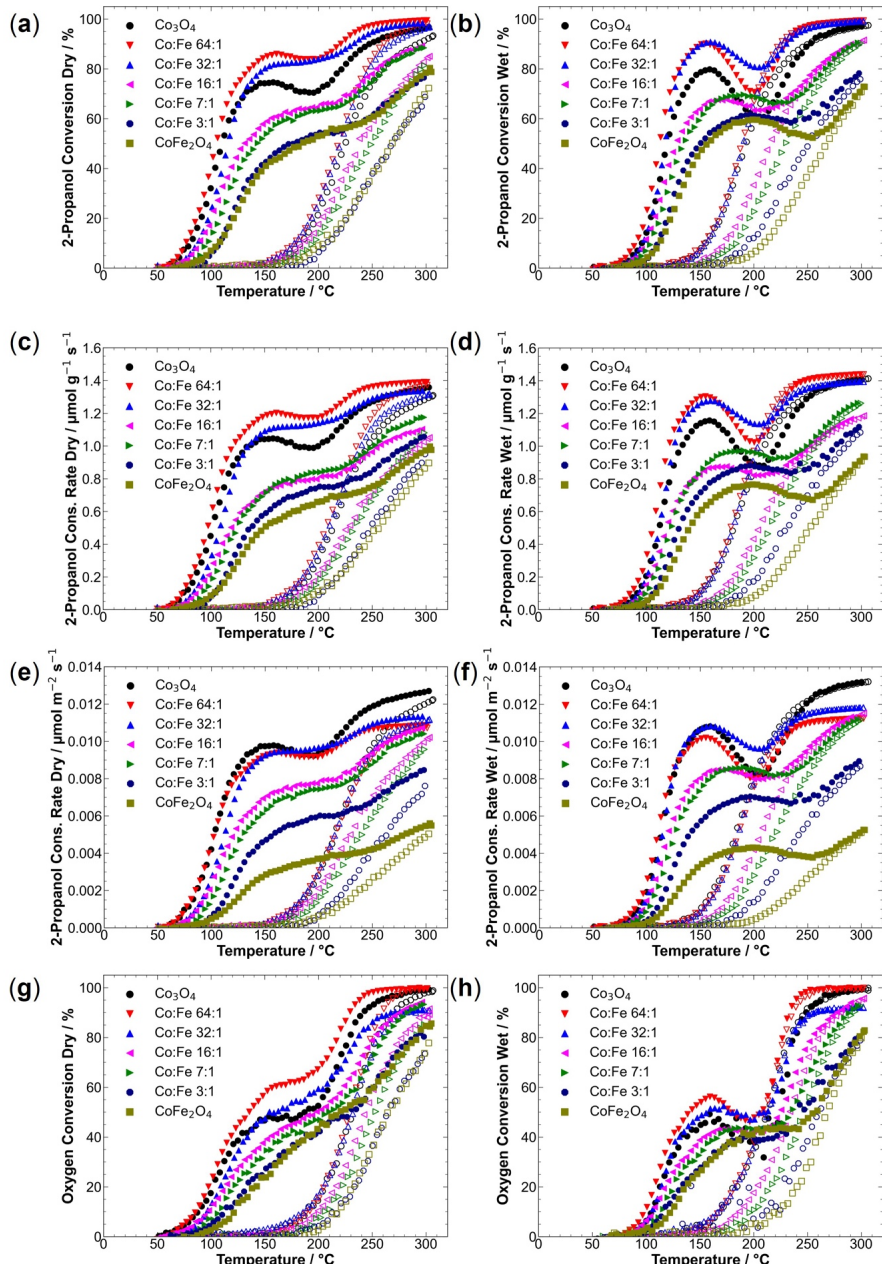


Figure S5: (a) 2-Propanol conversion in dry feed. (b) 2-Propanol conversion in wet feed. (c) Weight normalized 2-propanol consumption rate in dry feed. (d) Weight normalized 2-propanol consumption rate in wet feed. (e) Surface area normalized 2-Propanol consumption rate in dry feed. (f) Surface area normalized 2-propanol consumption rate in wet feed. (g) Oxygen conversion in dry feed. (h) Oxygen conversion in wet feed. Filled symbols show data points during heating. Empty characters show the behavior during cooling.

The conversion curve shapes in dry feed in Figure S5a differ. While  $\text{Co}_3\text{O}_4$  and Co:Fe 64:1 show clear maximums in the conversion curves at low temperature, the other catalysts show shoulders becoming less pronounced with decreasing Co content in the material except for pure  $\text{Co}_3\text{O}_4$ , which shows a surprisingly low conversion. The onset of the 2-propanol conversion shifts to higher temperatures with decreasing Co content. Oxygen conversions in Figure S5g show similar trends but no clear conversion maximum in dry feed even for  $\text{Co}_3\text{O}_4$  and Co:Fe 64:1. From product yields shown in Figure S6, oxidative dehydrogenation towards acetone is the main reaction pathway on all catalysts in the low-and HT reaction channels. However, the most active catalysts show a drop in acetone yield at temperatures above 260 °C favoring total oxidation. In the cooling segment, after an isothermal dwell period of 1 h at 300 °C, acetone remains the main product. During heating, the  $\text{CO}_2$  formation starts at around 120 °C for  $\text{Co}_3\text{O}_4$  and Co:Fe 32:1, while with increasing the Fe content, the  $\text{CO}_2$  formation onset shifts to higher temperatures. A two-step  $\text{CO}_2$  formation curve is observed for mixtures with minimum Co content of Co:Fe 16:1. Maximum  $\text{CO}_2$  yield is in the range of 28% for  $\text{Co}_3\text{O}_4$  and decreases with Co content in the materials, following the conversion data. During cooling, no multi-step behavior in  $\text{CO}_2$  formation is observed. However, after the isothermal dwell time, the decrease in  $\text{CO}_2$  yield is higher than the decrease in acetone yield, indicating a more favorable oxidative dehydrogenation pathway than total oxidation on partially deactivated catalysts. Propene and diisopropyl ether are detected in terms of products in minor fractions. Propene yield is most pronounced for  $\text{CoFe}_2\text{O}_4$ , which is in line with previous results and expectations based on the proposed surface Lewis-acidity of Fe-rich catalysts.<sup>[2]</sup> Ether formation is mainly observed on  $\text{CoFe}_2\text{O}_4$  and Co:Fe 3:1, which highlights the importance of Lewis-acidic surface sites for the ether formation.

In the wet feed, the onset of the reaction shifts to higher temperatures, which might be explained by the competitive adsorption of water and 2-propanol on the catalyst surface.<sup>[3]</sup> Another effect is the presence of an explicit conversion maximum for all catalysts, even with high Fe contents in the material. For the catalysts that featured a low-temperature maximum already in dry feed –  $\text{Co}_3\text{O}_4$  and Co:Fe 64:1 – a more pronounced maximum can be seen that is shifted to higher temperatures than dry feed. However, the drop in conversion after the low-temperature minimum is more significant. In the range between 150 and 170 °C, Co:Fe 32:1 is the most active 2-propanol consumption catalyst since it shows a less pronounced drop in conversion. In comparing dry and wet feed conversion curves, another feature becomes evident: the higher activity during cooling than heating for  $\text{Co}_3\text{O}_4$ , Co:Fe 64:1 and Co:Fe 32:1 in wet feed at

temperatures above 200 °C. Similar behavior was reported before for perovskite-based spinel catalysts, which contained a spinel-type secondary phase.

CO<sub>2</sub> formation onset shifts to higher temperatures in the wet feed than in dry feed, and the maximum CO<sub>2</sub> yield is decreased compared to dry conditions. As observed previously on perovskites, indications for water adsorption on Lewis-acidic surface sites were found, supported by a decrease of propene yield.<sup>[3b]</sup> However, the ether formation on CoFe<sub>2</sub>O<sub>4</sub> was slightly promoted but remained unchanged for Co:Fe 3:1 and Co:Fe 7:1.

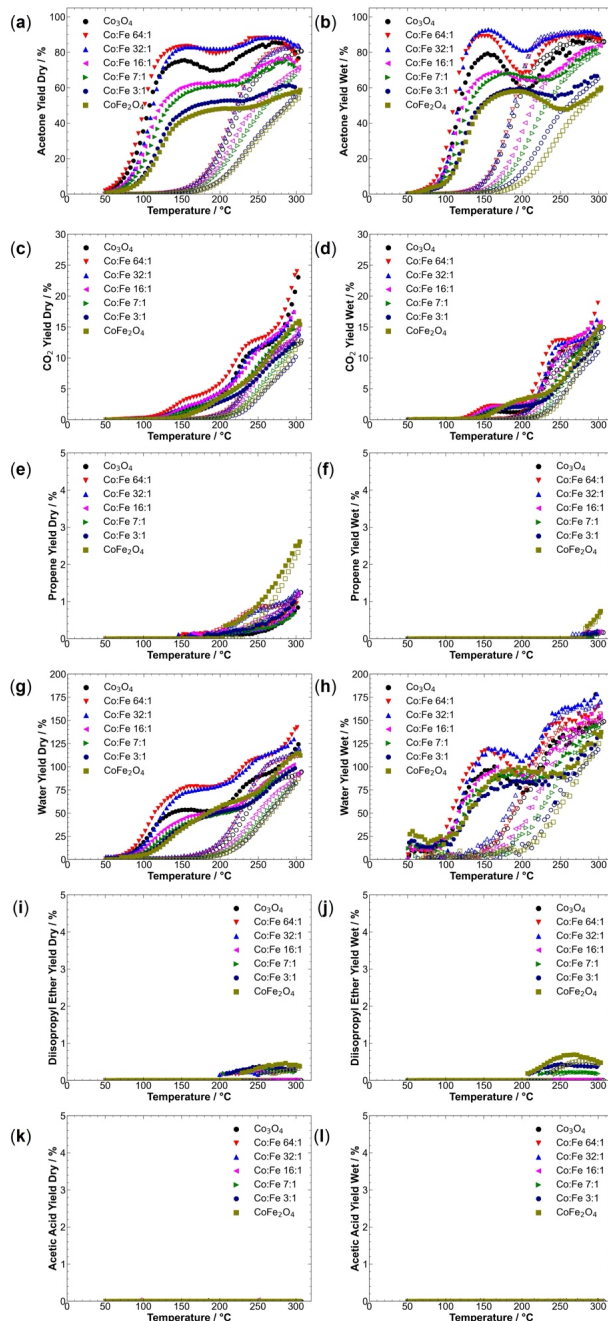


Figure S6: (a) Acetone yield in dry feed. (b) Acetone yield in wet feed. (c) CO<sub>2</sub> yield in dry feed. (d) CO<sub>2</sub> yield in wet feed. (e) Propene yield in dry feed. (f) Propene yield in wet feed. (g) Water yield in dry feed. (h) Water yield in wet feed. (i) Diisopropyl ether yield in dry feed. (j) Diisopropyl ether yield in wet feed. (k) Acetic acid yield in dry feed. (l) Acetic acid yield in wet feed. Filled symbols show data points during heating. Empty characters show the behavior during cooling.

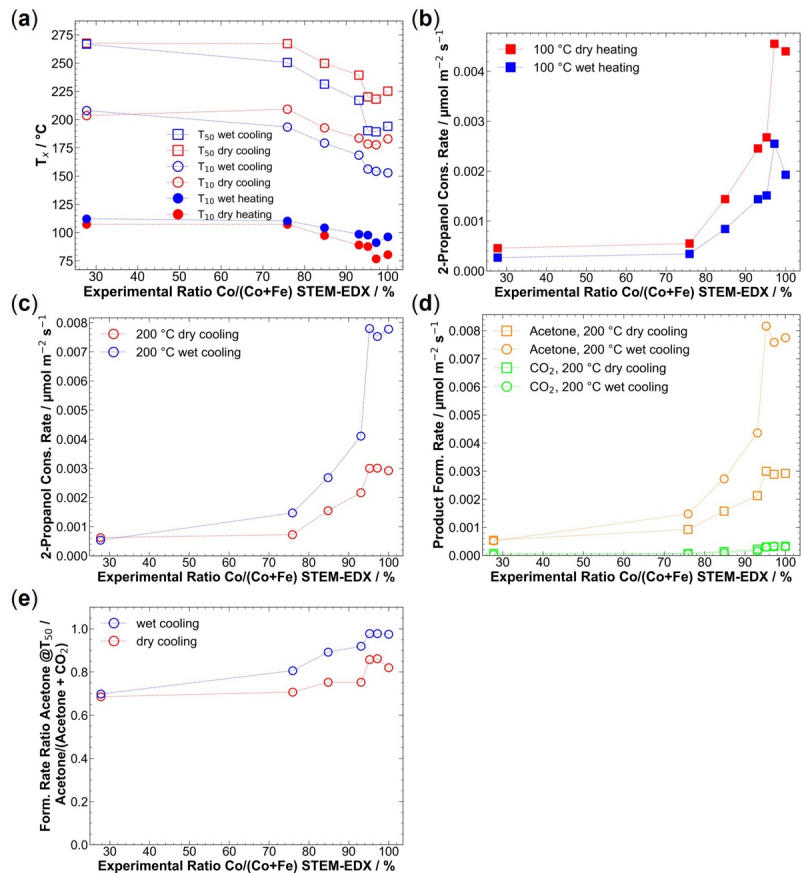


Figure S7: (a)  $T_{10}$  values during heating and cooling and  $T_{50}$  during cooling in dry and wet feed plotted against the experimental  $\text{Co}/(\text{Co}+\text{Fe})$  derived from STEM-EDX. (b) Surface-area normalized 2-propanol consumption rates at 100 °C during dry and wet feed heating. (c) Surface-area normalized 2-propanol consumption rates at 200 °C during dry and wet feed cooling.

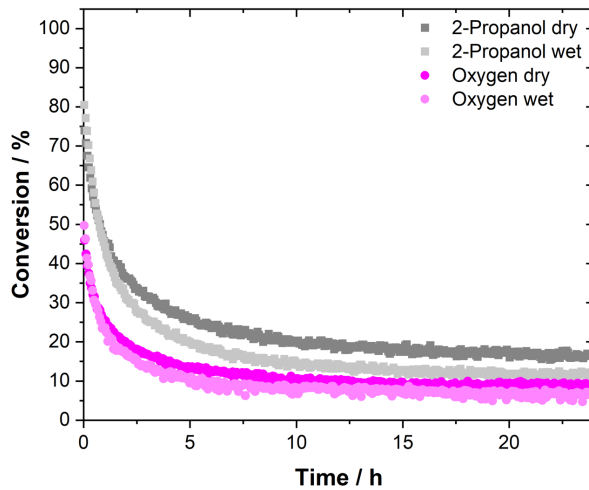


Figure S8: Steady-state conversions for  $\text{Co}_3\text{O}_4$  in dry and wet feed at the position of the low-temperature maximum at  $160^\circ\text{C}$ , reproduced from [4].

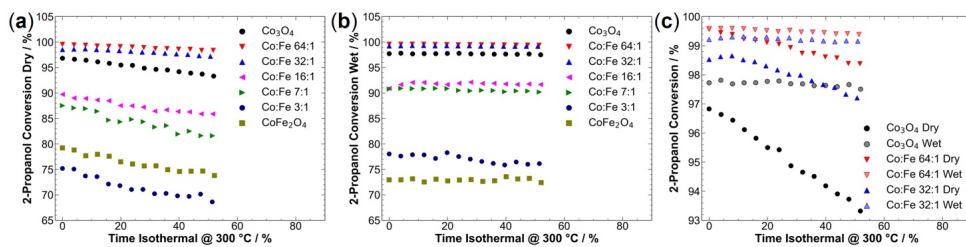


Figure S9: (a) Results of the CO pretreatment after TPO in  $20\% \text{O}_2$  and  $10\% \text{O}_2$ . (b) 2-Propanol conversions after the TPO and CO treatment. (c) Oxygen conversions after the TPO and CO treatment.

## References

- [1] M. Dreyer, A. Rabe, E. Budiyanto, K. Friedel Ortega, S. Najafishirtari, H. Tüysüz, M. Behrens, *Catalysts* **2021**, *11*, 1312.
- [2] N. Bahlawane, P. H. Ngamou, V. Vannier, T. Kottke, J. Heberle, K. Kohse-Hoinghaus, *Phys. Chem. Chem. Phys.* **2009**, *11*, 9224-9232.
- [3] a) R. Zhang, H. Alamdari, S. Kaliaguine, *Appl. Catal., B* **2007**, *72*, 331-341; b) M. Dreyer, D. Cruz, U. Hagemann, P. Zeller, M. Heidelmann, S. Salamon, J. Landers, A. Rabe, K. F. Ortega, S. Najafishirtari, H. Wende, N. Hartmann, A. Knop-Gericke, R. Schlögl, M. Behrens, *Chem. Eur. J.* **2021**, *27*, 17127-17144.
- [4] T. Falk, E. Budiyanto, M. Dreyer, C. Pfleiger, D. Waffel, J. Büker, C. Weidenthaler, K. F. Ortega, M. Behrens, H. Tüysüz, M. Muhler, B. Peng, *ChemCatChem* **2021**, *13*, 2942-2951.



## B. Publications

### Peer-Reviewed Publications

1. Angel, S.; Neises, J.; Dreyer, M.; Friedel Ortega, K.; Behrens, M.; Wang, Y.; Arandiyan, H.; Schulz, C.; Wiggers, H. *AIChE J.* **2019**, *10*, 441.
2. Falk, T.; Budiyanto, E.; Dreyer, M.; Pflieger, C.; Waffel, D.; Büker, J.; Weidenthaler, C.; Ortega, K. F.; Behrens, M.; Tüysüz, H.; Muhler, M.; Peng, B., *ChemCatChem* **2021**, *13* (12), 2942-2951.
3. Dreyer, M.; Krebs, M.; Najafishirtari, S.; Rabe, A.; Friedel Ortega, K.; Behrens, M., *Catalysts* **2021**, *11* (5), 550.
4. Füngerlings, A.\*; Koul, A.\*; Dreyer, M.\*; Rabe, A.; Morales, D. M.; Schuhmann, W.; Behrens, M.; Pentcheva, R., *Chem. Eur. J.* **2021**, *27* (68), 17145-17158. \*: Gleiche Beiträge
5. Dreyer, M.; Cruz, D.; Hagemann, U.; Zeller, P.; Heidelmann, M.; Salamon, S.; Landers, J.; Rabe, A.; Ortega, K. F.; Najafishirtari, S.; Wende, H.; Hartmann, N.; Knop-Gericke, A.; Schlögl, R.; Behrens, M., *Chem. Eur. J.* **2021**, *27* (68), 17127-17144.
6. Dreyer, M.; Rabe, A.; Budiyanto, E.; Friedel Ortega, K.; Najafishirtari, S.; Tüysüz, H.; Behrens, M., *Catalysts* **2021**, *11* (11), 1312.
7. Zerebecki, S.; Salamon, S.; Landers, J.; Yang, Y.; Tong, Y.; Budiyanto, E.; Waffel, D.; Dreyer, M.; Saddeler, S.; Kox, T.; Kenmoe, S.; Spohr, E.; Schulz, S.; Behrens, M.; Muhler, M.; Tüysüz, H.; Kampen, C.; Wende, H.; Reichenberger, S.; Barcikowski, S., *ChemCatChem*, **2022**, (e202101785), DOI: 10.1002/cetc.202101785.
8. Brix, A. C.; Dreyer, M.; Koul, A.; Krebs, M.; Rabe, A.; Hagemann, U.; Varhade, S.; Andronescu, C.; Behrens, M.; Schuhmann, W.; Morales, D. M., *ChemElectroChem* **2022**, *9* (e202200092), DOI: 10.1002/celc.202200092.
9. Klein, J.; Kampermann, L.; Korte, J.; Dreyer, M.; Budiyanto, E.; Tüysüz, H.; Friedel Ortega, K.; Behrens, M.; Bacher, G., *J. Phys. Chem. Lett.* **2022**. Accepted

### Peer-Reviewed Publications Included in this Thesis

1. Dreyer, M.; Krebs, M.; Najafishirtari, S.; Rabe, A.; Friedel Ortega, K.; Behrens, M., *Catalysts* **2021**, *11* (5), 550.

2. Füngerlings, A.\*; Koul, A.\*; Dreyer, M.\*; Rabe, A.; Morales, D. M.; Schuhmann, W.; Behrens, M.; Pentcheva, R., *Chem. Eur. J.* **2021**, 27 (68), 17145-17158. \*:  
Contributed equally
3. Dreyer, M.; Cruz, D.; Hagemann, U.; Zeller, P.; Heidelmann, M.; Salamon, S.; Landers, J.; Rabe, A.; Ortega, K. F.; Najafishirtari, S.; Wende, H.; Hartmann, N.; Knop-Gericke, A.; Schlögl, R.; Behrens, M., *Chem. Eur. J.* **2021**, 27 (68), 17127-17144.
4. Dreyer, M.; Rabe, A.; Budiyanto, E.; Friedel Ortega, K.; Najafishirtari, S.; Tüysüz, H.; Behrens, M., *Catalysts* **2021**, 11 (11), 1312.

### **Public Outreach Publications**

1. Dreyer, M.; Jansen, H.; Deitermann, M.; Busser, G. W.; Friedel Ortega, K.; Behrens, M.; Muhler, M. In *UNIKATE 57: Katalyse – alles andere als oberflächlich*, Universität Duisburg-Essen: Essen, 2021; Vol. 57, pp 63 - 71.

### **Posters and Oral Presentations**

1. 03/2021: Dreyer, M.; Najafishirtari, S.; Rabe, A.; Friedel Ortega, K.; Behrens, M. **Effect of water on the catalytic behavior of lanthanum iron cobalt perovskites in the selective oxidation of 2-propanol**; *54. Jahrestreffen Deutscher Katalytiker*, Online conference, Germany, 2021.
2. 09/2019: Dreyer, M.; Becker, S.; Friedel Ortega, K., Behrens, M. **Steady-state kinetic analysis of CO oxidation over transition metal oxides**; *EuropaCat 2019*, Aachen, Germany, 2019.
3. 06/2019: Dreyer, M.; Becker, S.; Friedel Ortega, K.; Behrens, M. **Steady-state kinetic analysis of CO oxidation over manganese oxide surfaces**; *21. JCF-Frühjahrssymposium in Bremen*, Bremen, Germany, 2019. |item 03/2019: Dreyer, M.; Becker, S.; Friedel Ortega, K.; Behrens, M. **Steady-state kinetic analysis of CO oxidation over manganese oxide surfaces**; *52. Jahrestreffen Deutscher Katalytiker*, Weimar, Germany, 2019.

## **Student Works**

The following student works were performed at the University of Duisburg-Essen in the Behrens group in the context of the presented thesis. Maik Dreyer participated in the definition of research questions, planning and conduction of experiments, their evaluation, interpretation and visualization within the scientific process.

1. Moritz Krebs, *Bericht zum Molekülteil*, Practical Course (08/2019 – 09/2019)
2. Moritz Krebs, *Synthesis of Hydroxycarbonates and Perovskites of the Lanthanum Iron Cobalt System by co-precipitation*, Advanced Lab Course (09/2019 – 02/2020)
3. Moritz Krebs, *Lanthanum Cobalt Iron Perovskites in Oxidation Catalysis*, Master Thesis (03/2020 – 11/2020), in cooperation with and co-supervised by the group of Prof. Dr. Matteo Cargnello (Stanford University, USA)
4. Nicolas Cosanne, *Einfluss von Morphologie und Komposition cobalthaltiger Spinelle auf Aktivität und Selektivität in der Isopropanoloxidation*, Advanced Lab Course (11/2020 – 03/2021), co-supervised by Anna Rabe
5. Nicolas Cosanne, *Investigation of the role of different cobalt species in the catalytic oxidation of 2-propanol*, Master Thesis (04/2021 – 09/2021), co-supervised by Dr. Sharif Najafishirtari

# **Curriculum Vitae**

Der Lebenslauf ist in der Online-Version aus Gründen des Datenschutzes nicht enthalten









## **D. Declaration of Authorship**

Hiermit bestätige ich, die vorliegende Arbeit mit dem Titel

“Exploring Structure- and Composition-Activity Correlations of Mixed Cobalt Iron  
Perovskites and Spinels in Oxidation Catalysis”

eigenständig verfasst und nur die angegebenen Quellen und Hilfsmittel verwendet zu haben.  
Alle benutzten Quellen sind wörtlich oder sinngemäß als solche kenntlich gemacht. Diese  
Arbeit wurde in dieser oder ähnlicher Form bisher bei keinem Prüfungsausschuss oder  
einer anderen Universität eingereicht.

---

Essen, den 7. April 2022, **Maik Dreyer**